FINITE ELEMENTS WITH DISCONTIGUOUS SUPPORT FOR ENERGY DISCRETIZATION IN PARTICLE TRANSPORT

A Dissertation

by

ANDREW THOMAS TILL

Submitted to the Office of Graduate and Professional Studies of
Texas A&M University
in partial fulfillment of the requirements for the degree of

DOCTOR OF PHILOSOPHY

Chair of Committee,	Marvin L. Adams
Co-Chair of Committee,	Jim E. Morel
Committee Members,	Jean-Luc Guermond
	Jean C. Ragusa
	Randal S. Baker
Head of Department,	Yassin A. Hassan

December 2015

Major Subject: Nuclear Engineering

ABSTRACT

The standard multigroup (MG) method for energy discretization of the transport equation can be sensitive to approximations in the weighting spectrum chosen for cross-section averaging. As a result, MG often inaccurately treats important phenomena such as self-shielding variations across a fuel pin. From a finite-element viewpoint, MG uses a single fixed basis function (the pre-selected spectrum) within each group, with no mechanism to adapt to local solution behavior. In this work, we introduce the Finite-Element-with-Discontiguous-Support (FEDS) method, an extension of the previously introduced Petrov-Galerkin Finite-Element Multigroup (PG-FEMG) method, itself a generalization of the MG method. Like PG-FEMG, in FEDS, the only approximation is that the angular flux is a linear combination of basis functions. The coefficients in this combination are the unknowns. A basis function is non-zero only in the discontiguous set of energy intervals associated with its energy element. Discontiguous energy elements are generalizations of bands introduced in PG-FEMG and are determined by minimizing a norm of the difference between sample spectra and our finite-element space. We present the theory of the FEDS method, including the definition of the discontiguous energy mesh, definition of the finite element space, derivation of the FEDS transport equation and cross sections, definition of the minimization problem, and derivation of a useable form of the minimization problem that can be solved to determine the energy mesh. FEDS generates cross sections that ordinary MG codes can use without modification, provided those codes can handle upscattering, allowing FEDS answers from existing MG codes.

FEDS requires that the energy domain is divided into elements, each in general a

collection of discontiguous energy intervals. FEDS solves a minimization problem to find the optimal grouping, in a certain sense, of hyperfine intervals into its elements. It generates accurate, convergent discretizations without need for accurate reference solutions. We show convergence in energy as energy elements are added for several types of problems, beginning with cylindrical pincell problems. Convergence is obtained for a variety of basis functions ranging from simple $(1/E)$ to more complicated (space-angle-averaged reference spectra), demonstrating robustness of the method.

We investigate four sets of problems. We first investigate the same pincell problems used when testing the PG-FEMG method. We use lessons learned from these pincell calculations to inform our implementation of the FEDS method on an energy-generalized version of the C5 problem, which we call the C5G$^{\infty}$ problem. We then apply FEDS to time-dependent neutronics problems, where correctly capturing streaming times in a time-of-flight problem becomes important. Finally, we compare the FEDS method to continuous-energy Monte Carlo one-dimensional slab pincell problem. We find FEDS to be superior in efficiency and accuracy to MG with the same weighting functions and number of energy unknowns. Whereas MG requires unknown counts commensurate with the number of resonances to be convergent, we find FEDS converges in energy even at low numbers of energy unknowns.

DEDICATION

> " 'Who is this that darkens counsel by words without knowledge? I will ask you, and you instruct Me!
> Where were you when I laid the foundations of the earth? Tell Me, if you have understanding. Who determined its measurements? Since you know.
> Where is the way to the dwelling of light? And darkness, where is its place, that you may take it to its territory, that you may know the paths to its home? By what way is light diffused? Do you know it, for you were born then, and the number of your days is great!' "
> (Job 38:2-5,19-21,24 NASB and NKJV)
> "[Even if I] understand all mysteries, and all knowledge, I am nothing. Whether there be knowledge, it shall vanish away. For we know in part, and we prophesy in part. But when that which is perfect is come, then that which is in part shall be done away. For now we see through a glass, darkly; but then face to face: now I know in part; but then shall I know even as also I am known."
> (1 Corinthians 13:2,8-10,12 KJV)

This dissertation is dedicated to my parents, Thomas and Kimberly Till, who have always encouraged my natural curiosity and who have unceasingly supported me in my academic endeavors, even when such endeavors led me far afield.

ACKNOWLEDGEMENTS

Though doing so in full would fill a volume larger than this already formidably sized document, I would like to acknowledge a few individuals and organizations who have made this work possible. First, to my co-chairs, Drs. Adams and Morel, who provided me with sufficient latitude in my research to investigate a topic outside the norm and who selflessly provide continual guidance, thank you. Secondly, to the rest of my committee, Drs. Guermond, Ragusa, and Baker, thank you for your insight on relevant, discriminating problems to try and theory to pursue. Thirdly, to Dr. Kord Smith at MIT, thank you for engaging with me and for pushing me to test my method against realistic problems. Penultimately, to my community at Texas A&M University, nuclear engineers, mathematicians and computer scientists alike, I have relished the opportunities and interactions you have fostered. Finally, to the Krell Institute and the Department of Energy Computational Science Graduate Fellowship program (DOE CSGF - grant number DE-FG02-97ER25308) for your funding and strong support of my professional development, I would like to offer particular gratitude.

NOMENCLATURE

FEDS	Finite Element with Discontiguous Support
MG	Multigroup
αMG	Adaptive Multigroup
sMG	Standard Multigroup
DOF	Degree of Freedom
QOI	Quantity of Interest
RRR	Resolved Resonance Region
URR	Unresolved Resonance Region
SCDT	Serial Cylindrical Deterministic Transport Code
PDT	Parallel Deterministic Transport Code
NJOY	Cross-Section Generation Code
MCNP	Monte Carlo N-Particle Transport Code
C5	Configuration 5 Reactor Benchmark
C5G$^{\infty}$	Configuration 5 Energy Resolution Problem
TOF	Time-of-Flight
PG-FEMG	Petrov-Galerkin Finite-Element Multigroup
MB	Multiband
ODF	Opacity Distribution Function
PT	Probability Table
SG	Subgroup
FE(M)	Finite Element (Method)
PWLD	Piecewise-Linear Discontinuous
GEM	Generalized Energy Mesh

IR	Intermediate Resonance (Approximation)
NR	Narrow Resonance (Approximation)
CP	Collision Probability
MC	Monte Carlo
MOC	Method of Characteristics
S_n	Discrete Ordinates
CE	Continuous-Energy
FSP	Fixed-Source Problem
HFG	Hyper-Fine Group
RI	Resonance Integral
XS	Cross Section
CED	Continuous Energy Domain
DED	Discontinuous Energy Domain
BP	Band-Preserving
MP	Moment-Preserving
BBC	Band-Boundary Calculation
CDF	Cumulative Density Function
PDF	Probability Density Function
RR	Reaction Rate
LWR	Light-Water Reactor
PWR	Pressurized Water Reactor
RT	Radiative Transfer (or Radiation Transport)
RH	Radiation Hydrodynamics
SPH	Superhomogénéisation (Factor)

TABLE OF CONTENTS

Page

LIST OF FIGURES

FIGURE Page

LIST OF TABLES

TABLE Page

1. INTRODUCTION

There is a practical need to accurately and efficiently simulate nuclear systems. This requires accurate and efficient treatment of the propagation of radiation and its interaction with its environment. The popular "deterministic method" of simulating these propagations and interactions discretizes the seven-dimensional phase space (space, angle, energy, and often time) upon which the radiation field depends and solves the discretized equations for the expected radiation distribution. Discretizing in energy has historically been a difficult problem due to the presence of resonances, which are sharp spikes in the cross sections that quantify the probability that a neutron interacts with a nucleus.

This work describes a novel discretization of the energy variable for radiation transport. Radiation, be it neutrons, gamma rays, thermal photons, etc., may be thought of as individual particles, where each particle has an associated energy / frequency. The interaction of a particle with its environment depends strongly on the energy of the particle. Within a cross section resonance, the probability of a neutron interacting with a nearby nucleus may change many orders of magnitude for a very small change in incident radiation energy due to quantum-mechanical effects. A resonant cross section is plotted in Fig. 1.1(a). Photon interactions are characterized by a similar strong dependence in the probability of interaction with atoms, quantified by opacities, which have lines that depend strongly on photon frequency.

While these resonances may be well-characterized, resolving them in their entirety using a deterministic method would be impractical. Resolving all the resonances requires an energy unknown count in excess of and proportional to the number of

resonances in the problem. Deterministic methods require a total unknown count proportional to the product of the number of spatial unknowns, the number of energy unknowns, and the number of angular (or moment) unknowns. This presents both memory and processing requirements that are impractical to meet even for foreseeable high-performance computing systems. Even if a computing system were able to store and solve such a problem, this would be an inefficient use of resources.

In practice, the energy dependence is often coarsened and averaged to create a reduced data size that is amenable to computation. This coarsening, a type of discretization, carries with it a necessary loss of fidelity. The loss of fidelity is especially apparent in the traditional "multigroup" (MG) treatment of the energy variable. This work describes a new method that allows increased resonance fidelity without substantial increase in computational cost. We apply our new method to neutron radiation problems.

Figure 1.1 shows the energy dependence of the cross section of the major resonant component (a) and the neutron-transport solution (b) to a simple pincell problem averaged over various spatial regions. High energy fidelity was attainable in this example because a simple geometry was used. Resonance shielding effects occur in the context of such nuclear reactor simulations. Neutrons are born from fission with high energy and downscatter through the resonance region. As the neutrons stream through a resonant material, absorptions in the resonances cause depressed fluxes near resonance energies; such depressions increase in magnitude as the neutrons penetrate more deeply into a resonant material such as fuel, a phenomenon known as spatial self-shielding. This implies that the energy profile depends upon where the neutrons are and where they came from; that is, the energy-dependent fluxes have spatial and angular dependencies. The flux dips rapidly for neutron energies near resonant energies of the fuel. The magnitude, but not location in the energy

domain, of these flux dips depends on spatial position (different colors of Fig. 1.1(b)) and direction (not shown) of the neutrons. These effects are important because they influence reaction rates, which determine depletion rates, power profiles, and system criticality.

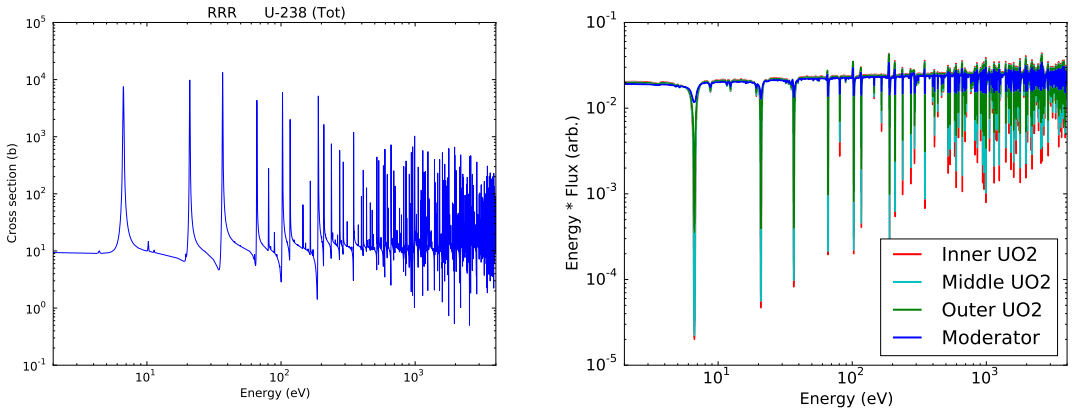

(a) Cross section (b) Flux spectrum

Figure 1.1: Component cross section (a) and scalar flux solution (b) of a simple infinite lattice of pincells with low-enriched uranium averaged over different pieces of the spatial domain.

In this work, we develop a new energy discretization method and apply it to problems of increasing complexity and importance. The method uses finite elements with discontiguous support to treat the energy variable. Clustering algorithms are used to solve a minimization problem whose solution is a discontiguous energy mesh. Our method naturally captures solution resonance behavior and achieves high fidelity with low numbers of degrees of freedom in the energy domain. Importantly, and unlike methods in use today, the new method converges predictably to the analytic solution as the number of unknowns increases. In addition, the method's equations have the same form as those of today's MG method, which means that standard MG

codes can, without modification, use the new method's parameters and obtain the new method's solutions.

In past work, we developed a new energy discretization scheme that we called Petrov-Galerkin Finite-Element Multigroup (PG-FEMG) [1]. PG-FEMG had a solid theoretical foundation, was found to be computationally efficient, and was shown to allow the within-group spectral shape of the solution to adapt to local conditions in the current problem. Previous work applied the method to one-dimensional pincells for reactor calculations. The current work introduces a new method based on PG-FEMG and applies it to several problem types, including multi-dimensional nuclear reactor cores.

While we implement and assess the new method in the context of nuclear reactor and neutron time-of-flight simulations, we stress that our method is sufficiently general as to apply to many photon-transport applications.

The following subsections characterize past work in the treatment of the energy variable, and introduce our generalized-MG method, which we call the Finite-Element-with-Discontiguous-Support (FEDS) method.

1.1 Energy Discretization Methods: Overview

In the context of deterministic particle transport, there are two classical schools of thought when it comes to discretization of the energy variable. The first school uses the multigroup (MG) concept of averaging over contiguous energy domains called groups [2]. To limit memory size and problem runtime, MG is often applied in the under-resolved regime where group widths span many resonances. Because such groups smear out fine structure, MG practitioners have been forced to develop clever methods involving calculations on smaller problems that yield averaged cross sections that approximately preserve reaction rates on the full problem.

The second school uses the multiband (MB) concept, which includes the probability table (PT), subgroup (SG)[1], and opacity density function (ODF) methods. Such methods discretize in cross section space instead of energy space.

The linear Boltzmann transport equation describes how neutrons move through and interact with a system. If $\mathbf{r}$ is the spatial location of a neutron (in $\mathbb{R}^3$), E is its kinetic energy (in $\mathbb{R}^+$), $\mathbf{\Omega}$ is its direction of travel (a unit vector in $\mathbb{R}^3$), t is time (in $\mathbb{R}$), $n(\mathbf{r}, E, \mathbf{\Omega}, t)$ is a differential number density (in $\mathbb{R}$), and d is a differential size, then $n(\mathbf{r}, E, \mathbf{\Omega}, t)\,\mathrm{d}\mathbf{r}\,\mathrm{d}E\,\mathrm{d}\mathbf{\Omega}$ is the number of neutrons in d$\mathbf{r}$ about $\mathbf{r}$, with energies in dE about E, traveling in directions d$\mathbf{\Omega}$ about $\mathbf{\Omega}$ at time t. The solution to the transport equation is called the angular flux and is the product of the expected neutron density and speed: $v(E)\,n(\mathbf{r}, E, \mathbf{\Omega}, t)$. The transport equation is a integro-differential equation in the given phase-space, which consists of space, energy, direction, and time ($\mathbf{r}$, E, $\mathbf{\Omega}$, and t). The transport equation has derivatives in space and time — and, in cylindrical and spherical coordinates, in the angle variables that describe direction — and integrals over direction and energy.

The vast majority of quantities of interest involve integrals over the angular and energy variables of the flux multiplied by a response function, usually a cross section. Examples include heating rates, absorption rates, fission rates, leakage rates, neutron-induced nuclide production / loss rates, and combinations thereof, such as the criticality eigenvalue or critical boron concentration.

There are two common classes of methods for solving the transport equation. One focuses on simulating individual particles and summing up the contribution of each particle to the quantity of interest (QOI), often called a tally. This former approach is known as Monte Carlo. The latter approach involves solving the linear Boltzmann

[1]While some researchers use the SG method as a MB method, others use the SG method as a means to generate MG cross sections. We refer to the former usage here.

transport equation for the expectation of the neutron density by discretizing the PDE and solving the resultant linear system. This is known as the deterministic approach. There exist numerous physical approximations and methods for transport discretizations. This research focuses on the discretization of the energy variable with applications to deterministic methods, though similar concepts can be used for energy-discretized Monte Carlo methods.

1.1.1 The Multigroup (MG) method

The traditional "multigroup" (MG) energy discretization approach is to combine particles with like energies into groups. Each group corresponds to all the particles in a contiguous energy range, say 1 to 5 eV. The unknowns associated with the discretization in energy are integrals of the flux over the energies within each group. Quantities of interest go from integrals over energy to sums over groups. Cross sections are averaged in energy over each group.

The process of integrating the transport equation over the energies within a group introduces approximations in practice. In theory, it is possible to define MG cross sections without any approximations as weighted averages of the pointwise cross sections, where the weighting is the angular flux (the solution). There are two problems with this approach. The first is that the solution is not known. The second is that this process would produce MG cross sections that depend continuously on space, angle, and time ($\mathbf{r}$, $\mathbf{\Omega}$, and t). The solution to the first problem is to use a shape function from a lower-order calculation that approximates the true flux. The solution to the second is to make this shape function depend only on energy and

material (i.e., piecewise constant in $\mathbf{r}$ and independent of $\mathbf{\Omega}$ and often t).[2]

There are three fundamental sources of approximation for the MG method. The first is applying the averaged cross sections to more complicated problems than those for which they were created. For example, it is common to create cross sections using a shape function that is the solution to an infinite (homogeneous) lattice of pincells / assemblies but to apply these cross sections to the full problem geometry, which is often a heterogeneous arrangement of pincells / assemblies. The second source of approximation is using approximate physics when doing the calculations to build the averaged cross sections. For example, the intermediate resonance (IR) approximation or the flat source approximation is often used to simplify the right-hand-side of the transport equation. The third source of approximation is that, while the MG cross sections may be calculated to preserve some energy-, space- and angle-integrated reaction rates, they often fail to capture differential / local reaction rates in space / angle / energy. For example, self-shielding is averaged over a material, which introduces errors in the spatial shape of reaction rates, including the fission rate in a reactor problem. This and other similar effects may impact spatial distributions of nuclides in depletion problems and power peaking factors.

Most of the errors associated with the MG method exist because of approximate resonance treatment. If the cross sections were smooth, two positive effects would occur. The first effect is that resolution of the energy variable would be possible with a reasonable number of groups. The second effect is that within-group spectrum changes due to absorption and scattering would be far smaller than is the case for

[2]The true temporal dependencies of the group-averaged microscopic cross sections depend on the details of the time-dependent angular flux. In time-dependent calculations where the cross sections depend on time, these time dependencies are often due to changes in atom densities that affect the macroscopic (and sometimes microscopic[3]) cross sections independently of angular flux effects.

[3]Microscopic cross sections often come from table lookups.[4] These lookups take arguments that depend on the densities of other nuclides present in the material.

[4]Cross section generation can be a convoluted process.

groups containing resonances. This second effect implies that if the correct MG cross sections / shape functions could be found, they would be correct differentially as well as in an average sense. The lack of resonance shielding and interference effects in this case would make the approximate, reduced-geometry calculations more representative of the actual problem, meaning the correct MG cross sections would be used for the full problem. The FEDS method produces cross sections with many of these desirable features.

1.1.2 The Multiband (MB) family of methods

The second school of thought uses the multiband (MB) concept to discretize the energy variable. While both MG and MB could be said to be concerned with accurately computing reaction rates — integrals over energy of cross sections multiplied by flux moments — whereas the MG approach seeks to approximate the Riemann form of the integral, the MB approach seeks to approximate the Lebesgue form of the integrals (Fig. 1.2(a)-(b)). Justification for MB often relies on invoking a narrow-resonance-like approximation to transform integrals of a flux-like quantity over energy into integrals over cross section space. MB methods create quadratures in this cross section space. MB works well for cases in which resonances can be treated as independent among nuclides.

The Lebesgue integration used by MB effectively transforms the energy discretization problem from one that must resolve many thin resonances in energy space (viz., MG) to one that must resolve a monotonic function in cross-section space (Fig. 1.2(c)). This allows the energy domain to be resolved indirectly by resolving cross section space with relatively few unknowns (Fig. 1.2(b)).

The name MB comes from early implementations that defined the quadrature by dividing up the cross section into bands based upon magnitude of the total cross

section (Fig. 1.2(b)). The quadrature weight for a band was the amount of the energy space represented by cross sections in the band. The quadrature points were averages of the total cross section over the band.

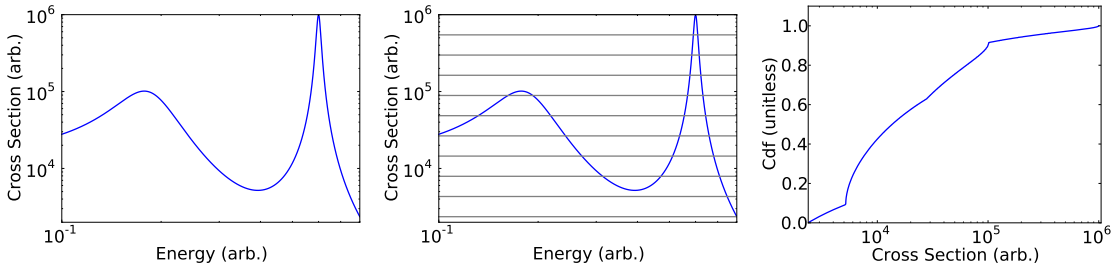

(a) Cross section in energy space (b) Dividing in bands (c) CDF of cross section

Figure 1.2: Examples of MB and its relationship to cross-section space. MB integrates cross sections (a) in a Lebesgue sense (b). The cumulative density function (CDF) of a cross section (c) is monotonic and easier to discretize than the cross section in energy space (a).

While discretization over cross section space allows proper treatment of resonances for a small number of quadrature points, the Achilles' heel of MB methods is their inability to treat multiple nuclides or cross sections well simultaneously. Most derivations rely on a transformation from lethargy space to total cross section space that becomes approximate if the flux depends more than one cross section. This is the case when the flux depends on partial cross sections or there are multiple total cross sections due to multiple, distributed resonant materials being present in the problem. MB methods commonly employ an approximate scattering treatment that uses a low-rank representation based on band probabilities instead of accurately representing the energy distributions of resonances within a group.

Another common problem is that it is not obvious which total cross section to use

when defining the bands. Using microscopic cross sections yields nuclide-dependent quadratures whose combination is not straightforward due to resonance interference effects.[5]

MB is often plagued by correlation issues among cross sections. The three most prominent issues are correlation among total cross section and partial cross sections for a given nuclide, correlation of cross sections at different temperatures for a given nuclide, and correlation of cross sections among nuclides. The first two issues may be solved by defining the bands based on a single total cross section at a preselected temperature and then defining band-wise partial cross sections for all temperatures and total cross sections for all other temperatures as the expectation values of those cross sections within the already chosen bands.[6] The last issue has been addressed by many authors, including Hébert [4] who developed correlation matrices that encode resonance interference effects.

More information on the MB method and its major contributors is given in Section 1.2.1 and in the first appendix (Appendix A).

1.1.3 The Petrov-Galerkin Finite-Element Multigroup (PG-FEMG) method

In this subsection we briefly outline our past work in the discretization of the energy variable for particle transport. Given the many fundamental difficulties inherent to MB methods, it was desirable to seek a method that did not live in cross section space. While remaining resolutely in energy space, in previous work we took inspiration from MB and relaxed the fundamental MG requirement of discretizing over contiguous energy ranges. Our resultant discontiguous energy elements were ex-

[5]Probability tables [3] often avoid this problem by restricting themselves to the unresolved resonance range and to Monte Carlo applications, where it is valid and possible, respectively, to sample cross sections for each nuclide independently of the other nuclides.

[6]This has similarities to our method: we first choose a partitioning of the energy domain and then consistently define cross sections averaged over each piece.

actly those that would be produced were one to transform a band from cross section space back to energy space (Fig. 1.3(a)).

Previous work [1] introduced a new method in the MB family that sought to overcome many of the issues mentioned previously without the need to introduce correlation matrices. The resultant PG-FEMG method was shown to successfully marry MB and MG. Like MG, the unknowns were defined in energy space. Like MB, unknowns were defined by banding a total cross section. Unlike typical MB, a single total cross section was chosen to represent to the entire problem, which led to global energy domains. Unlike typical MG, the energy domains became discontiguous. PG-FEMG was found to yield errors in several quantities of interest (QOI) — including k-eigenvalue and region-wise absorption rates — an order of magnitude or more lower than standard MG.

The fundamental deficiency of PG-FEMG was a theoretical limitation requiring the definition of a problem-wide effective total cross section from which to determine the energy elements. This was problematic for several reasons. First, solutions to transport problems do not depend solely on the total cross section, but on the partial cross sections as well. For example, elastic scattering peaks cannot be described by the total cross section. Second, it is not obvious how to construct an effective total cross section for problems with multiple resonant materials, or this is even possible (Fig. 1.3(c)). This limitation is stronger than it appears, because it applies to problems with one fuel type but multiple temperatures.

Recognizing the limitations of PG-FEMG, we focus on developing an improved method instead of testing PG-FEMG more thoroughly. In this work, we propose a new method, called Finite Element with Discontiguous Support (FEDS), that retains the positive attributes of PG-FEMG while addressing all of the listed limitations.

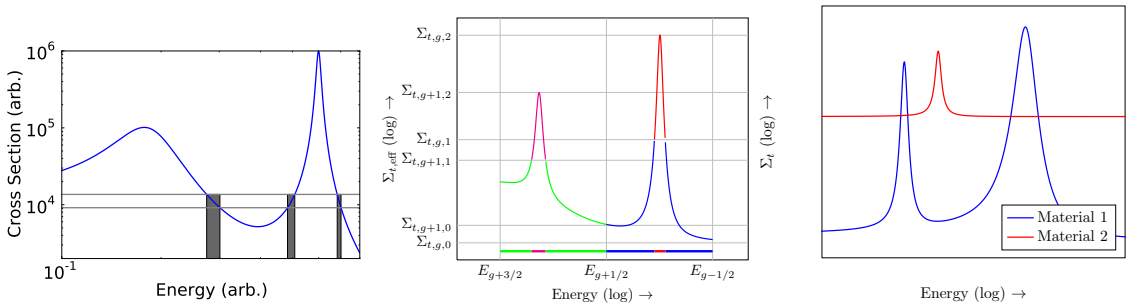

(a) One band (b) Multiple groups and bands (c) Multiple total cross sections

Figure 1.3: Band boundary calculation examples for PG-FEMG. (a) A discontiguous energy element is formed when mapping from a contiguous band in cross section space back to energy space. (b) Energy elements are defined by groups (two shown) and bands within a group (two shown for each group). Different colors indicate different energy elements. (c) Forming one effective total cross section is ambiguous when multiple resonant materials exist in the problem.

1.1.4 The Finite Element with Discontiguous Support (FEDS) method

In this work, we present our new FEDS method, a generalization of the PG-FEMG method. There are two important distinctions of FEDS compared to PG-FEMG. The first is that the finite element is defined with respect to a Generalized Energy Mesh (GEM), which generalizes the concept of groups and bands within a group to one of energy elements, which may be thought of as discontiguous groups. The second is that this GEM is constructed by solving a minimization problem, where the quantity to be minimized is the within-energy-element variance of a collection of spectra. These concepts are expounded upon in the following sections:

- Section 2: The Finite-Element-with-Discontiguous-Support (FEDS) method, including
  - A mathematical description of a generalized energy mesh (GEM) made up of discontiguous energy elements,

  - A finite element method that lives on the GEM,
  - A weak form of the transport equation that uses these finite elements,
  - The basis-function-weighted cross sections used in this transport equation,
  - A minimization problem that uses approximate spectra and yields the discontiguous energy elements that constitute the GEM,
  - Methods to solve the minimization problem using clustering algorithms from machine learning,
  - A different minimization problem that yields a contiguous (MG) energy mesh, and
  - An algorithm to partition energy unknowns among the coarse groups, within each of which a separate minimization problem is solved

- Section 3: Description and results for the one-dimensional cylindrical pincell problems, which use a MG reference over a subset of the resolved resonance range

- Section 4: Description and results for an energy-generalized C5 problem called the C5G$^\infty$ problem, which uses a MG reference over a subset of the resolved resonance range

- Section 5: Description and results for a streaming-dominated, time-dependent, time-of-flight (TOF) neutronics problem, which uses a hyperfine MG reference

- Section 6: Description and results for one-dimensional slab pincell problems, which use a continuous-energy Monte Carlo reference

- Section 7: Conclusions

- Appendix A: Addendum to Section 1. Description of several traditional MB implementations
- Appendix B: Addendum to Section 2, including
  - A discussion of the energy penalty implementation,
  - Derivations that show the apportioning algorithm used for partitioning energy unknowns among coarse groups satisfies useful properties,
  - Further comparisons between FEDS and PG-FEMG,
  - A workflow for running FEDS problems,
  - A detailed definition and exploration of the Bondarenko iteration process, and
  - A description of the method used to compute the hyperfine-group (HFG) spectra used in the minimization problem and for basis functions
- Appendix C: Addendum to Section 3
- Appendix D: Addendum to Section 4
- Appendix E: Addendum to Section 5, including quantification of the effect of varying the escape cross section on QOI error
- Appendix F: Addendum to Section 6
- Appendix G: Derivation of analytic solutions to a neutron advection problem used in Section 5
- Appendix H: Application of FEDS cross sections to Monte Carlo and interpretation as physics-based lossy data compression

1.2 Energy Discretization Methods: History and Current Status

1.2.1 Historical MB methods

Many authors have contributed to the development and evolution of MB methods. Such authors include Chandrasekhar [5], Strom and Kurucz [6], Carbon [7], Nikolaev and Filippov [8], Stewart [9], Cullen and Pomraning [10], Takeda et al. [11], Yamamoto [12], Huang et al. [13], Ribon and Maillard [14], Chiba and Unesaki [15], Hébert and Coste [16], Martin and Hébert [17]. Notable works include Shilkov [18] and Wray et al. [19], which introduce methods similar to the Petrov-Galerkin Finite-Element Multigroup (PG-FEMG) developed in previous work [1, 20], though all were developed independently.

The idea of subdividing an energy or frequency range within a group based on the total cross section or opacity dates back to Chandrasekhar in 1935 [5], when astrophysicists developed the opacity density function (ODF) method. Major contributors included Strom and Kurucz [6], Carbon [7], and Mihalas [21]. Modern work on the ODF method includes the work by Auer and Lowrie [22], Lowrie and Haut [23], Ripoll and Wray [24], and Wray et al. [19], the last of which has some similarities with the method presented in this paper, though both were developed independently.

Since 1935 there has been a proliferation of methods designed to give fidelity within a group. Different authors independently reinvented the ODF idea under new names and applied it to their physics regime. Three such sets of methods are: multiband (MB), which has seen application to both radiative transfer and neutronics; subgroup (SG), a new name to distinguish neutronics-specific applications of MB; and probability tables (PT), which were first introduced for the unresolved resonance range for neutronics. We briefly discuss each of these variants below.

Cullen [10] claims that Nikolaev [8, 25] and Stewart [9] were the first to propose using the MB framework for neutrons and photons, respectively, in the 1960's; Cullen himself did extensive work analyzing and implementing the method in the 1970's and 1980's [26, 27]. Other notable early MB work includes [28–30]. Modern work and implementation of the MB / SG method has been done by Yamamoto and Takeda [11, 12, 31–34], Huang et al. [13], Milošević [35], and others [36–42]. Due to its wide range of applicability in the literature and the fundamental similarities of all the methods, we will hereafter use MB to refer to any of the ODF, SG, PT, or MB methods generally.

The probability table (PT) method was developed by Levitt [3] for treating neutrons in the unresolved resonance range. Cullen [26] generalized PT to the resolved resonance region. Ribon and Maillard [14] were major contributors to PT theory and introduced a new moments-based approach to determine the band parameters. Modern work has been done on the PT method by Hébert and Martin [16, 17, 43, 44], and Chiba [15]. Since the output of the PT method is tables of correlated parameters that are straightforward to sample from, the probability table method sees substantial use in Monte Carlo calculations to treat the unresolved resonance range. Examples include codes such as MCNP from LANL [45], and RACER and MC21 from KAPL [46, 47]. Deterministic methods often use the PT method only when using SG to form MG cross sections, as explained below. As such, uses of the PT method for deterministic calculations have seen negligible use when performing full-core (or even assembly-level) calculations.

MB methods can be grouped into three families: band-preserving (BP), moment-preserving (MP), and discontiguous energy domain (DED). BP MB methods split up each microscopic total cross section into bands such that the total cross section is split up by its magnitude. These bands are used to define nuclide-specific dis-

contiguous energy meshes in the following sense. All energies that have total cross sections that are within a band (cross section range) are placed inside the element corresponding to that band. We refer to this process of determining the discontiguous energy mesh from bands as a band boundary calculation (BBC). The total and partial cross sections are condensed over each element to form band-wise microscopic cross sections. As each nuclide formally has its own set of element boundaries, resonance interference and correlation issues arise when combining microscopic band cross sections into macroscopic band cross sections. Most early ODF, MB, and PT methods were BP.

MP MB methods use quadrature to preserve moments of the nuclide-specific total (and sometimes partial) cross section(s). The quadrature consists of a set of probabilities and (microscopic) total cross sections for each band. While this method has desirable characteristics with respect to positivity of coefficients, and accuracy and convergence of integration for a single nuclide, it suffers from the same correlation problem as BP MB and further correlation problems because partial cross sections may not be perfectly correlated to the total cross section.

These correlation problems can be addressed by introducing correlation matrices between nuclides / reaction types and conditional band probabilities. Correlation matrices are straightforward to sample from for Monte Carlo simulations. For deterministic simulations, conditional band probabilities are often used in the context of producing MG cross sections via the SG method. Often, for each type of fuel pin encountered, separate collision probability calculations are performed for each band of each resonant nuclide of interest. Cross sections for the other nuclides are computed as the expectation value of those nuclides' cross sections using their own band-wise cross sections and the conditional band probabilities. Most correlation-preserving techniques have been inapplicable or not applied to deterministic methods such as

S_n and MOC due in part to the added complexity and unknown count of being forced to juggle multiple band structures for the different nuclides to account for band-wise cross section correlation among nuclides. More recent MB, SG, and PT methods have been MP.

DED MB methods are MG methods that use global energy element definitions. Such nuclide- and region-consistent discontiguous energy meshes resolve the mapping issues between regions and the correlation issues among nuclides within a region, but must be carefully constructed to preserve resonance features for all relevant nuclides / resonances in the problem. Oftentimes, a problem-wide effective total cross section is constructed to form bands in much the same way as BP MB. The difference is that these bands are not nuclide- or region-specific but global. These bands determine problem-wide element definitions over which to condense the cross sections, which are then used like normal MG cross sections. The FEDS method, the PG-FEMG method [1], [18], and [19] may all be classified as DED MB methods.

1.2.2 Traditional MG implementations

Modern reactor engineering calculations in the United States, Canada, and France have used a hierarchical solution methodology. The scheme begins with pointwise cross section data which is processed into many groups with a narrow-resonance (NR) / IR flux, e.g., $[1/(\sigma_t(E) + \sigma_0)]\ (1/E)$. This is done for several values of the background cross section, σ_0. On a pincell level, cross sections are mixed and NR / IR approximations with equivalence theory is used to determine the proper local background cross sections. One nuclide may use different background cross sections in different regions if it is mixed with different types and amounts of other nuclides in those regions or if one region is nearer to a boundary. Cross sections are then collapsed into an intermediate number of groups using a lattice cell calculation, usually

with a fixed source and reflective boundaries. Oftentimes, this coarsening is accompanied by a *superhomogénéisation* (SPH) factor [4] to ensure the coarse-group cross sections produce the same reaction rates as the fine-group cross sections. Few-group cross sections are then used for a full-core calculation, often nodal diffusion with discontinuity factors. Traditional references on this method include [48]. Modern references include [49–52]. Other notable works for computing better reaction-rate-preserving MG cross sections include [53–58].

The problem with the hierarchical approach is that resonance information is averaged out early in the hierarchy, even though the spectral shape of the correct final solution varies strongly with position and direction on the scale of individual resonances. This is especially problematic when spatial homogenization does not accompany energy condensation, because, in this case, cross sections that correspond to material averages of homogenous arrangements are used for the heterogeneous geometry. Additionally, the standard hierarchy has trouble taking into account heterogeneity effects on scales larger than individual pincells, including the effects of non-similar fuels in nearby pincells or, for fast systems, resonances in structural materials.

As an aside, the shape functions used for cross section condensation for MG are often used implicitly by defining the MG cross sections via lookup tables. To build such tables, computations are done on a variety of geometries and material compositions. These computations often involve two-region pincell collision probability problems and/or IR approximations. MG cross sections are defined to preserve the total and partial (e.g., scattering, absorption, fission) reaction rates for each problem. At the same time, background cross sections, moderator ratios, etc. for each problem are calculated. These cross sections and material parameters are combined into lookup tables that are later interpolated using the actual problem geometries

and material compositions. The fine-scale shape functions come into play in the calculation of the MG cross sections for each problem; they are often never explicitly stored.

1.2.3 Modern MG-like methods

Three novel treatments of the energy variable have been developed in the past 15 years. In 2002, Attieh and Pevey developed a generalized MG method that allowed an energy range to have partial membership in multiple groups using a combination of piecewise-constant square-tooth functions and linear hat-functions [59, 60]. The motivation was better energy spectra than piecewise-constant over a group available from MG. The result was a group spectral shape that was problem-adaptive. This method does not solve the energy discretization problem because within-group spectral shapes are not well approximated by polynomials of even moderate order.

Forget and Rahnema developed another generalized-MG method that expanded the neutron flux in terms of an orthogonal basis set [61, 62]. The 0th-order moment was shown to be equivalent to MG, producing the same integral quantities such as eigenvalues and reaction rates. Their technique allowed for estimation of the spectral shape within a group using a low-resolution energy (coarse-group) calculation; however, it suffered from an oscillatory interpolating polynomial that often went negative. Zhu and Forget later generalized this method to use discrete Legrendre orthogonal polynomials, which returned a fine-group flux estimate from a coarse-group calculation [63]. Further work developed the method as an iterative scheme using the unfolded flux from the current iteration to recondense the cross sections for the next iteration [64]. Under the constraints of using step-difference spatial finite difference, storing the angular flux, and computing cell-wise cross sections, the authors showed that their DGM (discrete generalized MG) method converged to the fine-

group eigenvector and eigenvalues for several k-eigenvalue problems. More recently, Gibson and Forget have recast their method as producing fine-group accuracy with coarse-group work [51].

Finally, Douglass and Rahnema have a method they call the Subgroup Decomposition Method (SDM) [52]. Though they do not describe it in these terms, SDM is a high-order low-order (HOLO) method where the HO calculation is fine-group MG with a fixed source and the LO calculation is a k-eigenvalue problem with coarse-group MG and a consistency term from the HO calculation. The SDM method shares the same aims as the DGM method.

The DGM and SDM methods offer incremental improvements and do not address the need for improved approximations at the resolution scale of individual resonances to deal with spatial self-shielding. Both methods work within the reactor calculation hierarchy mentioned above and at best allow one level finer of energy resolution to be used.

2. THE FINITE ELEMENT WITH DISCONTIGUOUS SUPPORT (FEDS) METHOD

2.1 Physical Model

The physical model underlying our work is the transport equation. Sometimes referred to as the linearized Boltzmann transport equation, it describes the movement of neutral particles under non-equilibrium conditions and is one of the workhorse equations of the nuclear engineering discipline.

Because FEDS uses the same energy finite element space for all positions and directions of travel, without loss of generality we begin with the continuous k-eigenvalue formulation of the transport equation for neutronics with anisotropic scattering and white boundary conditions:

$$\begin{aligned}\boldsymbol{\Omega}\cdot\nabla\psi(\mathbf{r},E,\boldsymbol{\Omega})+\Sigma_t(\mathbf{r},E)\psi(\mathbf{r},E,\boldsymbol{\Omega}) = \\ \int_{4\pi}\mathrm{d}\boldsymbol{\Omega}'\int_0^\infty \mathrm{d}E'\;\Sigma_s(\mathbf{r},E'\to E,\boldsymbol{\Omega}'\cdot\boldsymbol{\Omega})\psi(\mathbf{r},E',\boldsymbol{\Omega}')+ \\ \frac{\chi(\mathbf{r},E)}{4\pi\,k_{\text{eff}}}\int_0^\infty \mathrm{d}E'\;\nu\Sigma_f(\mathbf{r},E')\phi(\mathbf{r},E'),\end{aligned} \tag{2.1a}$$

$$\phi(\mathbf{r},E)=\int_{4\pi}\mathrm{d}\Omega\;\;\psi(\mathbf{r},E,\boldsymbol{\Omega}), \tag{2.1b}$$

$$\begin{aligned}\psi(\mathbf{r},E,\boldsymbol{\Omega})=\frac{1}{\pi}\int_{\boldsymbol{\Omega}\cdot\mathbf{n}>0}\mathrm{d}\Omega'\;\;|\boldsymbol{\Omega}'\cdot\mathbf{n}|\,\psi(\mathbf{r},E,\boldsymbol{\Omega}') \\ r\in\partial V,\;\boldsymbol{\Omega}\cdot\mathbf{n}(\mathbf{r})<0,\end{aligned} \tag{2.1c}$$

for $\psi(\mathbf{r},E,\boldsymbol{\Omega})$ the energy-dependent angular flux, $\phi(\mathbf{r},E)$ the energy-dependent scalar flux, $\mathbf{r}$ the spatial coordinate, $\boldsymbol{\Omega}$ the direction of travel, E the energy, $\Sigma_t(\mathbf{r},E)$ the local macroscopic total cross section, $\Sigma_s(\mathbf{r},E'\to E,\boldsymbol{\Omega}'\cdot\boldsymbol{\Omega})$ the angle-differential,

energy-differential scattering macroscopic cross section, $\chi(\mathbf{r}, E)$ the fission distribution function, $\nu\Sigma_f(\mathbf{r}, E')$ the neutron-production-from-fission macroscopic cross section, and k_{eff} the eigenvalue.

2.2 Energy Mesh Determination

2.2.1 Definition of the discontiguous energy mesh and elements

We use a generalized energy mesh (GEM) to define our partitioning of the energy domain into a discontiguous energy mesh. The GEM consists of two components, a list of energy subelement boundaries, $\mathcal{E}$, and a list of element memberships, $\mathcal{S}$, for some number of energy elements, N_e:

$$\mathcal{E} = \{E_{1/2}, E_{3/2}, \ldots, E_{G+1/2}\}, \quad 0 \leq E_{g-1/2} < E_{g+1/2}, \quad \forall g = 1, \ldots, G, \tag{2.2a}$$

$$\mathcal{S} = \{s_1, s_2, \ldots, s_G\}, \qquad s_g \in \{1, 2, \ldots, N_e\}, \qquad \forall g = 1, \ldots, G. \tag{2.2b}$$

For standard MG, $\mathcal{E}$ are just the group boundaries, $G = N_e$, and $\mathcal{S}_g = g$. For MG, groups, elements, and subelements are identical. Figure 2.1 shows example MG and FEDS meshes. FEDS allows for discontiguous energy elements.

We define energy subelements, Ξ_g, to be the contiguous energy ranges determined by the subelement boundaries:

$$\Xi_g = \left\{ E \,|\, E \in \left(E_{g-1/2}, E_{g+1/2}\right), E_{g\pm1/2} \in \mathcal{E} \right\}, \quad g = 1, \ldots, G. \tag{2.3}$$

Energy subelements are combined into energy elements, $\mathbb{E}_e$, using the element membership lists:

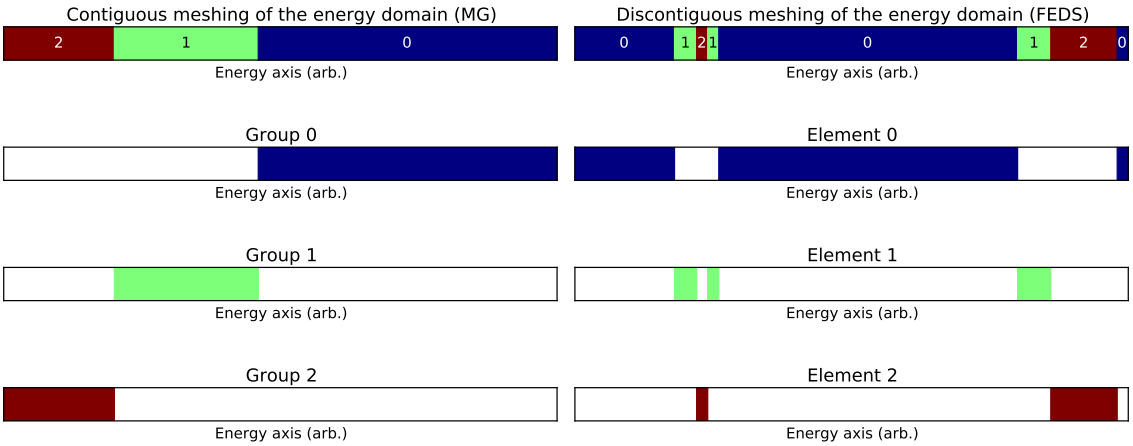

Figure 2.1: Example MG and FEDS generalized energy meshes.

$$\mathbb{S}_e = \{g \,|\, \mathcal{S} \ni s_g = e\}, \tag{2.4a}$$

$$\mathbb{E}_e = \bigcup_{g \in \mathbb{S}_e} \Xi_g. \tag{2.4b}$$

$\mathbb{S}_e$ holds the indexes of the sublements that belong to element e. $\mathbb{E}_e$ is a union of subelements determined by $\mathbb{S}_e$. That is, $\mathbb{E}_e$ is a set of discontiguous energy ranges.

For example, if

$$N_e = 2, \tag{2.5a}$$

$$\mathcal{E} = \{1, 2, 3, 4, 5, 6\} \text{ eV, and} \tag{2.5b}$$

$$\mathcal{S} = \{1, 2, 1, 2, 1\}, \tag{2.5c}$$

then,

$$\Xi_1 = (1, 2) \text{ eV},$$
$$\Xi_2 = (2, 3) \text{ eV},$$
$$\Xi_3 = (3, 4) \text{ eV},$$
$$\Xi_4 = (4, 5) \text{ eV},$$
$$\Xi_5 = (5, 6) \text{ eV}, \tag{2.5d}$$

and

$$\mathbb{S}_1 = \{1, 3, 5\}, \quad \mathbb{E}_1 = (1, 2) \cup (3, 4) \cup (5, 6) \text{ eV}, \tag{2.5e}$$
$$\mathbb{S}_2 = \{2, 4\}, \qquad \mathbb{E}_2 = (2, 3) \cup (4, 5) \text{ eV}. \tag{2.5f}$$

Because

$$\Xi_g \cap \Xi_\gamma = \emptyset, \quad g \neq \gamma, \tag{2.6a}$$

and

$$\mathbb{S}_e \cap \mathbb{S}_k = \emptyset, \quad e \neq k, \tag{2.6b}$$

our definition for $\mathbb{E}_e$ implies

$$\mathbb{E}_e \cap \mathbb{E}_k = \emptyset, \quad e \neq k. \tag{2.6c}$$

Additionally, because

$$\bigcup_{g=1}^{G} \Xi_\gamma = \left(E_{1/2}, E_{G+1/2}\right) \tag{2.7a}$$

and

$$s_g \in \{1, 2, \ldots, N_e\}, \quad \forall g = 1, \ldots, G, \tag{2.7b}$$

our definitions for $\mathbb{S}_e$ and $\mathbb{E}_e$ imply

$$\bigcup_{e=1}^{N_e} \mathbb{E}_e = \left(E_{1/2}, E_{G+1/2}\right). \tag{2.7c}$$

Our energy elements, $\mathbb{E}_e$, do not overlap and cover the full energy range. These properties are necessary to use them as a mesh. Notice further that $N_e \leq G$ and usually $N_e \ll G$. That is, the size of our GEM using discontiguous elements may be substantially smaller than the size of a MG energy mesh using contiguous subelements.

While both $(\mathcal{E}, \mathcal{S})$ and $\{\mathbb{E}_e, \mathbb{S}_e\}$, $e = 1, \ldots, N_e$, carry the same information, the former is a more efficacious for storing / representing the energy mesh, while the latter is more efficacious for defining the finite elements.

Using the GEM framework, standard MG chooses energy elements, $\mathbb{E}_e$, equal to the subelements, Ξ_g. That is, $N_e = G$, $\mathcal{S} = \{1, 2, \ldots, G\}$, $\mathbb{S}_e = \{e\}$, and $\mathbb{E}_e = \{E \,|\, E \in (E_{e-1/2}, E_{e+1/2})\}$. For FEDS, an energy element (aka a discontiguous group), $\mathbb{E}_e$, may contain multiple unconnected subelements, Ξ_g.

2.2.2 Mapping the minimization problem to a clustering problem

Our finite element definition relies, in part, on the definition of its underlying mesh, which we call the generalized energy mesh (GEM). We create this energy mesh by choosing the best possible definitions of the energy elements, where best is defined by solving a minimization problem. This minimization problem requires three ingredients: a hyperfine group (HFG) structure that resolves resonances, a set of spectra (fluxes) on this hyperfine structure that we want our finite element space to accurately represent, and a final number of elements. While there are many ways to define the HFG structure, we use an adaptive energy mesh that maximally resolves the features of the spectra using a minimal number of points. Appendix B gives more details. In the following derivation, we take our subelements to be the hyperfine groups.

Ideally, we would want to use several energy-resolved fluxes from the problem of interest as the spectra that we wish to capture with our finite element space. However, this would not be useful, because we want to solve the problem of interest without having to use a resolved energy mesh. Instead, we use approximate fluxes that come from inexpensive infinite-medium calculations. We may precompute and store many of these spectra, and then use those spectra which are characteristic of the problem of interest when computing the GEM for that problem. For example, if the problem of interest is a beginning-of-life PWR, we may wish to use three infinite-medium spectra: new UO_2, MOX, and control rod. This generality also allows us to reuse energy meshes for similar problems.

Once we have our spectra, we solve the following minimization problem to determine the energy mesh:

1. For a given set of spectra and a given set of energy subelements, pick a combi-

nation of the subelements into elements (choose an $\mathcal{S}$).

2. Compute the averages of the spectra in each element.

3. Compute the within-element variances. For each element and each spectrum, compute the difference between the hyper-fine spectrum and the element-averaged spectrum.

4. Sum these variances over all elements and spectra. This yields a variance / projection error that indicates how well the energy elements capture the resonance-scale behavior of the spectra. We call this error F.

5. Choose element definitions, $\mathcal{S}$, that minimize this projection error by looking at all possible combinations of subelements into elements.

There are efficient implementations of algorithms that solve the above problem, or closely related problems. Some definitions of the above problem do not require exhaustively searching for all possible combinations of subelements into elements, but may, for example, iteratively choose the elements.

We minimize the difference between a set of predetermined spectra and their projection onto energy elements. Minimizing this projection error is equivalent to minimizing the within-element variance because the projection of the spectra onto the energy elements is done via an average. We call this set of predetermined spectra a library.

There are many ways to determine the library of spectra we use as inputs to our minimization problem. The spectra may be hyperfine fluxes, or they may be more generally any quantity that is correlated with the flux or reaction rates. For example, the macroscopic total cross section is highly correlated with both the angular flux

and the reaction rates, especially at higher resonance energies, where the narrow resonance approximation better applies.

The notion of a point, p, in the library is very general and may refer to a material (e.g., if the spectra come from cross sections or infinite-medium-like slowing-down calculations), a spatial point (e.g., if the spectra come from the scalar flux at a point of a pointwise-in-energy pincell calculation), or a space/angle point (e.g., if the spectra come from an angular flux, as by ray tracing, or a partial current). We use an infinite-medium slowing down calculations for each material, as this produces effective spectra. This can be done for many material compositions of interest ahead of time and those that are deemed to be relevant to the problems for which the mesh is to be generated may be used during generation.

Mathematically, we may define a norm of the within-element variances, F, as follows:

$$F_1 = \left(\sum_p \omega_p \left[\sum_g \Delta E_g \left| \phi_{p,g} - \bar{\phi}_{p,g(e)} \right| \right]^M \right)^{1/M}, \tag{2.8}$$

where ω_p is the weight / importance of spectrum / point p, $\phi_{p,g}$ is the *average* hyperfine-group flux for point p and group g, $\bar{\phi}_{p,g(e)}$ is the average of $\phi_{p,g}$ over energy element e, and $M \in \mathbb{R}^+$ characterizes the norm used. For $M = \infty$, we use a maximum instead of the sum. We define the average more explicitly as:

$$\bar{\phi}_{p,g(e)} = \sum_e \bar{\phi}_{e,p} w_{e,g}, \tag{2.9}$$

where e is the energy element index, $w_{e,g}$ is an element membership function ($w_{e,g} = 1$ if $g \in \mathbb{S}_e$ and 0 otherwise) and $\bar{\phi}_{e,p}$ is the average of $\phi_{e,g}$ over element e for point p. Notice that $w_{e,g}$ does not depend on p, but applies to all points. Though some

algorithms never need to explicitly define the averages, $\bar{\phi}_{e,p}$, we include them for clarity of presentation.

The original minimization problem involves defining energy elements such that F_1 is minimized. That is, we choose how to combine hyperfine groups into elements such that the elements maximally preserve the spectra of interest.

Notice Eq. (2.9) may be thought of as using a finite element approximation for the energy dependence of the flux. This finite element uses basis functions that are piecewise constant within an element and zero elsewhere. When we later apply the FEDS method to a problem, we will again have a finite-element-in-energy representation for the flux, but with problem-dependent basis functions that capture solution behavior. (We cannot use these non-constant basis functions now because we calculate the GEM before we apply it to a given problem.) If, in the real problem, we use basis functions that look more like the solution, $b(\mathbf{r}, E) \simeq \phi(\mathbf{r}, E)$, we expect our within-element variance to be lower than that predicted by our minimization of F_1. That is, using less information at this phase does no harm and allows us to reuse energy meshes for multiple problems (for any and all problems for which the library of spectra applies).

Equation (2.8) is not in a useful or easily solvable form. We modify our definition of the minimization problem and map it to a problem that is easily solvable while maintaining the property that the energy elements it creates will still minimize within-element variance in some norm.

The first step in our mapping is to generalize the norm in energy to use the L^N norm, for some N, instead of the L^1 norm. This allows us to generalize our energy weights to be κ_g. If we think of $\phi_{p,g}$ as a pointwise representation of the flux at energy points instead of the average over a hyperfine energy group, it may make

sense to treat all groups with the same weight ($\kappa_g = 1$).

$$F_2 = \left(\sum_p \omega_p \left[\sum_g \kappa_g \left| \phi_{p,g} - \sum_e \bar{\phi}_{e,p} w_{e,g} \right|^N \right]^{M/N} \right)^{1/M}. \tag{2.10}$$

Our second step is to flip the norms. Instead of computing the error over all energy groups for each point and then taking a norm over points, we take the error over all points for each group and then take a norm over groups. We have:

$$F_3 = \left(\sum_g \kappa_g \left[\sum_p \omega_p \left| \phi_{p,g} - \sum_e \bar{\phi}_{e,p} w_{e,g} \right|^M \right]^{N/M} \right)^{1/N}, \tag{2.11}$$

Our third step is to split the sum over groups into two sums: one over the energy elements and another over the the hyperfine energy groups within an energy element.[1] We have:

$$F_3(\mathbb{S}) = \left(\sum_e \sum_{g \in \mathbb{S}_e} \kappa_g \left[\sum_p \omega_p \left| \phi_{p,g} - \sum_{e'} \bar{\phi}_{e',p} w_{e',g} \right|^M \right]^{N/M} \right)^{1/N},$$

$$F_3(\mathbb{S}) = \left(\sum_e \sum_{g \in \mathbb{S}_e} \kappa_g \left[\sum_p \omega_p \left| \phi_{p,g} - \bar{\phi}_{e,p} \right|^M \right]^{N/M} \right)^{1/N}, \tag{2.12}$$

where we have used $w_{e',g} = \delta_{e',e}$ for $g \in \mathbb{S}_e$ and made explicit F_3's dependence on $\mathbb{S}$.

We define a scaled flux that incorporates our weights:

$$\Phi_{p,g} = \kappa_g^{1/N} \omega_p^{1/M} \phi_{p,g}. \tag{2.13}$$

[1] Our errors, $F(\mathbb{S})$, are computed for a given partitioning of the groups into elements (for a fixed $\mathbb{S}$), so this sum splitting is valid. It is later that we minimize over all $\mathbb{S}$.

This simplifies our error expression:

$$F_3(\mathbb{S}) = \left(\sum_e \sum_{g \in \mathbb{S}_e} \left[\sum_p \left| \Phi_{p,g} - \bar{\Phi}_{e,p} \right|^M \right]^{N/M} \right)^{1/N} . \tag{2.14}$$

Our fourth step is to generalize our norms by allowing a different metric for hyperfine energy points in an element versus among elements:

$$F_4(\mathbb{S}) = \left\{ \sum_e \left(\sum_{g \in \mathbb{S}_e} \left[\sum_p \left| \Phi_{p,g} - \bar{\Phi}_{e,p} \right|^M \right]^{N_1/M} \right)^{N_2/N_1} \right\}^{1/N_2} . \tag{2.15}$$

Finally, we generalize our procedure to use simple functions of the fluxes. We often care about minimizing the variance across a wide range of flux magnitudes and hence we find it more practical to deal with $\log \phi$ instead of ϕ. Further, we take a page from MB and move to lethargy space, where the flux has less variance over long scales: $\phi(u) = E\phi(E)$. We define the term "observation" to mean the simple function of ϕ that we actually use for our minimization:

$$O_{p,g} = \kappa_g^{1/N} \omega_p^{1/M} \log \left(E_g \phi_{p,g} \right) . \tag{2.16}$$

Our final form of the mapped minimization problem minimization uses:

$$F_{M,N_1,N_2}(\mathbb{S}) = \left\{ \sum_e \left(\sum_{g \in \mathbb{S}_e} \left[\sum_p \left| O_{p,g} - \bar{O}_{e,p} \right|^M \right]^{N_1/M} \right)^{N_2/N_1} \right\}^{1/N_2} , \tag{2.17a}$$

or, equivalently,

$$F_{M,N_1,N_2}(\mathbb{S}) = \left\| O_{p,g} - \bar{O}_{e,p} \right\|_{\mathcal{W}_p(\{1,\ldots,P\}) \times \mathcal{W}_g(\mathbb{S}_e) \times \mathcal{W}_e(\{1,\ldots,N_e\})} . \tag{2.17b}$$

The minimization problem is: choose which elements each subelement belongs to (choose $\mathbb{S}$) such that $F_{M,N_1,N_2}(\mathbb{S})$ is minimized in Eq. (2.17). Minimization over observations from a library does not imply minimization of the projection error from the reference solution itself, but rather from something that is related to the solution, like an infinite-medium flux or a cross section. So long as the spectra used are representative or bounding for the problem of interest, the minimization based on them still combines into elements energies that behave similarly across the entire problem.

Algorithms that can solve Eq. (2.17) come from machine learning and are called clustering algorithms because they combine their inputs into clusters, that is, hyper-fine groups into energy elements. When we use a clustering algorithm to perform our minimization, we say we are clustering the data.

We note that using a spectrum of $\phi_{p,g} = \Sigma_{t,\text{eff},g}$, $P = 1$, $N_1 = \infty$, $N_2 = \infty$ and observations equal to logarithm of the spectra results in the band boundary calculation used for PG-FEMG. The results of that work [1] showed PG-FEMG worked well with up to six bands per group, implying we are allowed to use spectra that do not fully capture solution behavior. That said, the total cross section is a reasonable surrogate for the angular flux because its magnitude is correlated with the amount of self-shielding, which is a form of spectral change with varying space/angle.

We investigate two clustering methods, k-means and hierarchical agglomeration. Both solve the minimization problem and both are implemented in both SCIPY and SCIKIT-LEARN [65, 66]. Of the vector quantization options, these seemed the most applicable to our situation. K-means minimizes Eq. (2.17) using $M = N_1 = N_2 = 2$. Hierarchical agglomeration with the squared Euclidean distance metric and Ward linkage minimizes Eq. (2.17) using $M = N_1 = 2$ and $N_2 = \infty$.

Hierarchical agglomeration does not search the entire combinatoric space to de-

termine which groups should be part of which elements (the $\mathbb{S}_e$), but instead goes through $G - N_g$ stages. At the beginning of the calculation, each subelement belongs to its own element. In each stage, the two nearest two clusters / elements are merged together into one. At the end of the calculation, N_g elements remain.

The traditional implementation of k-means, Lloyd's algorithm, which is implemented in both SCIPY and SCIKIT-LEARN, iterates between defining the location of the elements' centers, the $\bar{O}_{e,p}$, as the average position of their constituent subelements and defining membership of the subelements as the element with the nearest center. If the iteration converges, the result can depend on the initial element center positions. For this reason, Lloyd's algorithm is often repeated for several random initial conditions and the choice that resulted in the smallest F is chosen. In practice, Lloyd's algorithm often results in an F that is very close to the minimal F.

The easiest way to generate the GEM is to define the subelements as the HFG structure, though this may lead to more points than are necessary to store the grid. Instead, all contiguous sets of energy points, g, that belong to the same energy element, e, should be grouped together, so only the boundaries between energy subelements need to be stored as the $E_{g+1/2}$ in the GEM. Once the GEM is formed, cross sections must be defined, which is tantamount to specifying the basis functions. This process is problem-dependent.

If the spectra represent fluxes at energy points instead of averaged over hyperfine groups, a straightforward way to generate the GEM is to associate each point, g, with the range $\Delta E_g = [E_{g-1/2}, E_{g+1/2}] = [\sqrt{E_{g-1}\,E_g}, \sqrt{E_g\,E_{g+1}}]$ and then build the GEM with this group structure.

There is still the issue of determining how many and which points to use. Though it may seem as though many space/angle points p would be required, especially for $M < \infty$, in practice this may be computationally intractable and is not guaranteed

to yield a better GEM than using several interesting bounding points. The optimal choice of space/angle points is an open question that is beyond the scope of this work. Conversely, we do know that many energy points e are required, because we wish to resolve the resonance structure.

We accumulate two sources of error when building our GEM. The first comes from using norms, spectra, observations, and material points that are approximate or that do not map well to the desired minimization problem (e.g., Eq. (2.8)). The second source of error comes from using a small / finite number of energy elements / clusters. Results show the latter to be more important for low to moderate numbers of elements / clusters. If that is the case, we should be able to get away with using inexpensive methods, spectra, observations, and points.

Our FEDS method is a two-step method. In the first step, we use infinite-medium spectra for several materials we expect to see in the problem of interest as inputs to a minimization problem whose solution is an energy mesh that uses discontiguous energy elements (groups). In the second step, we compute problem-specific basis functions with which we weight the continuous-energy cross sections to produce FEDS cross sections. These cross sections are flux-weighted averages over the discontiguous energy elements found in the first step. Once we have these cross sections, we may use them in any existing transport code without further modification to either cross section or code. The transport solver returns fluxes integrated over the discontiguous energy elements.

In addition to the infinite-medium spectra mentioned above, we often added an energy penalty of $\log(E_g)$ to our observations, weighted to be approximately the same magnitude as the other observations. Because our minimization combines hyperfine energy groups that have similar observations for all spectra, an observation of energy itself causes the minimization to separate groups with highly dissimilar energies into

separate elements. As the number of elements are increased, the energy range of an energy element decreases. A major conclusion of this work is that using energy penalties as the primary means to bound the extent of an element in energy is inferior to using coarse groups for the same purpose. More information on energy penalties may be found in the accompanying appendix, Appendix B.

2.2.3 Clustering algorithms that produce contiguous energy meshes

Machinery developed to solve the minimization problem to produce discontiguous energy elements can be reused with new algorithms that produce contiguous energy elements. This offers an automatic means of generating MG group structures. While the idea of adaptive energy mesh generation is not new, this formulation works with existing methods.

Table 2.1 gives an overview of the three types of meshes considered in this work. The first is sMG (standard MG), which uses equal-lethargy-spaced group structures. This subsection describes αMG, the adaptive MG option. Finally, FEDS uses a general clustering that produces discontiguous energy elements.

Table 2.1: Energy mesh family names and descriptions

Abbreviation	Description	Energy Contiguity
sMG	Standard MG (equal-lethargy spaced)	Contiguous
αMG	Adaptive MG	Contiguous
FEDS	FEDS	Discontiguous

Mosca et al. [57] developed a workflow for generating automatic MG boundaries that shares strong similarities to the methods we use for FEDS mesh generation, though each were developed separately. Both the Automatic Energy Mesh Con-

structor in [57] and our FEDS method create a reference hyperfine mesh that adequately resolves the flux and its resonance dips for several spectra of interest, choose these spectra as the infinite-medium-equivalent slowing-down solution in materials of interest, minimize error on the coarsened fine mesh, and generate meshes that are hierarchical with a coarse mesh. Their method computes error on reaction rates from the hyperfine mesh to those rates computed from a separate infinite-medium-equivalent slowing-down calculation on each proposed fine mesh. This requires an expensive nonlinear iteration on the fine group boundaries. We minimize a variance within an energy element with respect to the approximate spectra, which requires only one slowing-down calculation on the hyperfine mesh and one application of a clustering algorithm. Their method yields contiguous groups, where ours can be altered to either produce contiguous groups or discontiguous elements. They use importance weighting to determine how much error is tolerable in different nuclides and energy regions, while we work with the solution itself and do not assume energy regions have differing importances. They generalize their slowing down to fast systems where the fission source must be modeled accurately. We treat thermal systems or fast systems without fissionable nuclides. They use advanced weighting schemes within a group, such as the subgroup method. We use simpler, less accurate basis function shapes.

The basic idea for our adaptive MG is to limit the amount of solution variation within a group. Variation may be measured by a variety of norms that operate over spectra and hyperfine groups within the final MG fine group. We differentiate between the hyper-fine mesh that resolves the resonances and the fine mesh that is the mesh used by the adaptive MG method.

Three methods have been developed that rely on different norms. The first minimizes the squared error within a fine group by equally spacing the cumulative squared

error, which is defined as

$$S_e = \sum_{g'=1}^{e} \max_p \left| O_{g',p} - O_{g'-1,p} \right|^2. \tag{2.18}$$

The total cumulative squared error, S_{N_e} is divided by the desired number of final groups to determine the squared error per group. Group boundaries are placed at intervals of this per-group error. This method minimizes variance because it limits the amount of change in the spectra that can occur within a group. This method may be implemented without iteration, requiring only the computation of S_e and one iteration through it to determine coarse group boundaries.

The second method minimizes actual variance within a final group. Because this variance is not known ahead of time, this method requires an outer iteration on the variance per final group. Once that value is known, hyperfine groups are added to the fine group until its variance reaches the desired variance. This is repeated for all fine groups. Before convergence, there is the possibility that the group boundaries do not fit within the desired range. Because the results from this method were similar to those from the squared-error version, results from this method are not shown in this work.

The final method minimizes variance implicitly by dividing in index space. This method chooses final MG group boundaries by evenly dividing on the index of the hyperfine mesh. If the hyperfine mesh has N_e energy points and G final groups are desired, the group boundaries are $i(N_e/G)$, $i = 0, \ldots, G$, or the closest integers.

The final method requires an efficient hyperfine mesh. This third method treats all energy points as having equal information content about some aspect of the solution, and becomes inefficient if significant fractions of the hyperfine mesh resolve unimportant aspects of the solution and these unimportant points are not evenly

spaced. For example, if the hyperfine mesh is evenly spaced in lethargy, this method will yield a MG mesh evenly spaced in lethargy. Alternatively, if the hyperfine mesh spends most of its resources resolving variations in the spectra instead of variations in energy, this third method should be an efficient downsampling of the hyperfine mesh.

Our hyperfine mesh, described in Appendix B, is efficient and works well with the third adaptive MG method. Points on the hyperfine mesh are chosen to bound jumps in the solution:

$$r_{g,p} \equiv \max\left(\frac{\phi_{g,p}}{\phi_{g-1,p}}, \frac{\phi_{g-1,p}}{\phi_{g,p}}\right), \tag{2.19a}$$

$$\max_p r_{g,p} \leq c_1. \tag{2.19b}$$

At the same time, the hyperfine mesh is thinned where possible to reduce redundant points. Points are removed if the linear interpolation error made by removing those points is below a tolerance. This leads to the following condition:

$$c_2 \leq \max_p \left| \frac{\phi_{g,p} - \left[\phi_{g-1,p} + (\phi_{g+1,p} - \phi_{g-1,p})\left(\frac{E_g - E_{g-1}}{E_{g+1} - E_{g-1}}\right)\right]}{\phi_{g,p}} \right|. \tag{2.19c}$$

Equations (2.19b) and (2.19c) bound the jump in the flux from above and below. Notice that if the jump in the flux for all points were constant,

$$\max_p r_{e,p} \to c, \tag{2.20a}$$

then the difference in observation between two points would also be constant:

$$\max_p |\log \phi_{g,p} - \log \phi_{g-1,p}| = c, \tag{2.20b}$$

$$\max_p |O_{g,p} - O_{g-1,p}| = c. \tag{2.20c}$$

In this limit of constant jump, the third method reduces to the first method. In practice, the third method behaves similarly to the first method and is used for adaptive MG implementations in future sections.

2.2.4 Nested energy meshes with coarse groups and automatic apportioning

It is advantageous to perform hierarchical, or nested, partitioning of the energy domain. The outer level of the nesting is to divide energy into coarse groups. The inner level of the nesting is to divide the energies within a coarse group into energy elements, each of which may be discontiguous but may not include subelements outside of its coarse group.

Nested partitioning solves several problems. Reaction rate edits on a fraction of the full energy domain are simpler if the energy elements are hierarchical to the edit structure. Another problem solved is treating aspects of the solution that depend explicitly on energy, such as the scattering kernel and $1/v$ streaming. As will be explored in future sections, it is often impossible to generate accurate basis functions that are independent of neutron location, direction, and time for energy elements that span large ranges in energy. Dividing energy into coarse groups before dividing into elements solves these problems.

Although the energy discretization is often nested, energy index is treated as flat. This allows FEDS notation to more closely match MG notation. A notation of coarse group and element within that coarse group is often unnecessary and is unhelpful in

the context of the MG transport solver. Further, it calls to mind the group, band indexing using in MB and PG-FEMG. We wish to distinguish FEDS from MB and PG-FEMG and do not wish to be hampered by their notation.

The use of coarse groups adds two requirements to the FEDS method. The first requirement is determining the locations of the coarse group boundaries, which is explored in future sections. The second requirement is determining how many energy elements to use per coarse group. A method was developed, implemented and tested to determine this apportioning automatically.

The goal is to minimize the maximum variance within any energy element. For a fixed energy unknown count, this is accomplished if all elements have the same within-element variance. The problem is that variances within the coarse groups are in general not equal, so using an equal number of elements per coarse group will not satisfy our goal. Instead, we should bestow a number of energy elements to each coarse group proportional to the relative standard deviation in that coarse group. This conclusion relies on the following conditions and assumptions:

1. The true variance of the solution within a coarse group is well described by the variance of the spectra within the coarse group,

2. When a coarse group contains only one energy element, the energy element is the coarse group, meaning the variance within the energy element is the variance of the spectra within the coarse group,

3. Doubling the number of energy elements within a coarse group *often* halves the standard deviation within the energy elements that belong to this coarse group,

4. Variance is simply the square of standard deviation,

The third assumption is an observation that is true if the spectra data form lines when plotted against each other (as occurs in Fig. 2.8). If these Voronoi-like diagrams of spectra-vs-spectra are full, then more than a factor of two more elements must be added to decrease the standard deviation within the elements by a factor of two.

If a coarse group c begins at index $g_{c-1/2}$ and ends at index $g_{c+1/2}$ in the hyperfine energy mesh, then we compute its standard deviation, S_c, as:

$$N_c = g_{c+1/2} - g_{c-1/2} + 1, \tag{2.21a}$$

$$\bar{\Omega}_{p,c} = \frac{1}{N_c} \sum_{g=g_c-1/2}^{g_{c+1/2}} O_{g,p}, \tag{2.21b}$$

$$S_c = \sqrt{\frac{1}{N_c P} \sum_{g=g_{c-1/2}}^{g_{c+1/2}} \sum_{p=1}^{P} \left| O_{g,p} - \bar{\Omega}_{p,c} \right|^2}. \tag{2.21c}$$

The $1/N_g$ comes into play because the error within a coarse group or energy element is proportional to the average distance of the spectra from the mean, not the number of energy points within this group or element.

There is a wrinkle in the implementation of this apportioning to guarantee each coarse group receives at least one element. The full implementation is given in Appendix B.

An alternative, more complicated method would be to iterate on the number of energy elements per coarse group by computing the maximum variance of the elements within a coarse group, dividing by the sum of all coarse groups, and then reapportioning elements proportionally to this quantity. This level of sophistication was not found to be required.

Automatic apportioning can be applied for adaptive MG as well, though the method is different. The assumption that doubling the number of elements within a

coarse group halves the standard deviations of the elements within that coarse group does not apply to contiguous elements (groups) for small numbers of fine groups per coarse group because they will not resolve resonance structure. Instead, we look back to the squared error formula developed previously, Eq. (2.18). For adaptive MG, fine groups should be apportioned among coarse groups based on the relative L^1 error of each coarse group. This is based on the following observations and assumptions:

1. Minimizing the variation in the spectra for each fine group minimizes the error in each fine group and hence the solution,

2. The L^1 error, L_c, is a reasonable measure of the variation in the spectra for a group,

3. Doubling the number of fine groups per coarse group halves the variation in the L^1 error of the fine groups within that coarse group.

The L^1 error is

$$L_c = \sum_{g=g_{c-1/2}}^{g_{c+1/2}} \max_p \left| O_{g,p} - O_{g-1,p} \right| . \tag{2.22}$$

The L^1 error and not the squared error was used because of its proportionality to the number of energy points within a coarse group. Namely, if resolution is doubled, the individual differences in the $|O_{g,p} - O_{g-1,p}|$ will halve but there will be twice as many of them, so the error — and hence the number of fine groups within that coarse group — will stay the same, which is desired. If the coarse group is doubled in size and resolution kept constant, there will be twice as many $|O_{g,p} - O_{g-1,p}|$ terms of approximately the same magnitude, and the error — and hence the number of fine groups within that coarse group — will approximately double, which is also desired.

A final automatic apportioning method is to assign unknowns to coarse groups proportional to the maximum deviation of the spectrum within a coarse group, M_c:

$$M_c = \max_p \frac{\max\limits_{g\in c} \phi_{g,p}}{\min\limits_{g\in c} \phi_{g,p}} \tag{2.23}$$

because M_c is another measure of variation within a coarse group. In this work, adaptive MG used the L^1 apportioning and FEDS used the standard-deviation-based apportioning.

2.3 Method Definition and Derivation

2.3.1 Definition of the finite element space

In this subsection, we define our finite element in energy:

$$\begin{aligned} \varphi(\mathbf{r}, E, \mathbf{\Omega}) &\equiv \sum_{e=1}^{N_e} \Psi_e(\mathbf{r}, \mathbf{\Omega})\, b_e(\mathbf{r}, E), \\ &\simeq \psi(\mathbf{r}, E, \mathbf{\Omega}), \end{aligned} \tag{2.24}$$

such that, for some user-defined spatial region, V_i, and region-specific spectrum $f_i(E)$,

$$b_e(\mathbf{r} \in V_i, E) = \begin{cases} C_{i,e}\, f_i(E) & E \in \mathbb{E}_e, \\ 0 & \text{otherwise}, \end{cases} \tag{2.25}$$

with

$$C_{i,e} = \frac{1}{\int_{\mathbb{E}_e} \mathrm{d}E \;\; f_i(E)}, \tag{2.26}$$

for $e = 1, \ldots, N_e$. We note that approximating the true angular flux as a finite element in energy is our *only* approximation. The derivation to determine the FEDS

transport equation does not introduce further approximations.

We do not restrict the $\Psi_e(\mathbf{r}, \mathbf{\Omega})$ in this subsection, requiring only that they have similar regularity requirements to $\int_0^\infty \mathrm{d}E\ \psi(\mathbf{r}, E, \mathbf{\Omega})$. The next subsection will discuss a finite element method to define these coefficients.

There are several interesting properties satisfied by the basis functions, $b_e(\mathbf{r}, E)$. First, the basis functions are orthonormal because the $\mathbb{E}_e$ do not overlap. Second, the basis functions are piecewise-constant with respect to $\mathbf{r}$. They have no continuous dependence on space or direction ($\mathbf{r}$ or $\mathbf{\Omega}$). Third, the basis functions have the same spectral shape as the $f_i(E)$ within the energy element.

Our choice of finite element space is reasonable. If we choose $f_i(E) = 1$, our finite element space contains the constant solution $\psi(\mathbf{r}, E, \mathbf{\Omega}) = 1$ because the $\mathbb{E}_e$ span the entire energy domain. If the flux is separable in energy — i.e., if $\psi(\mathbf{r}, E, \mathbf{\Omega}) = g(E)\Phi(\mathbf{r}, \mathbf{\Omega})$ — and we choose $f_i(E) = g(E)$ and $\Psi_e(\mathbf{r}, \mathbf{\Omega}) = \Phi(\mathbf{r}, \mathbf{\Omega})$, then our finite element space contains $\psi(\mathbf{r}, E, \mathbf{\Omega})$.

It is acceptable for our finite element solution to be discontinuous in energy because we care about integrals over energy. Our basis functions are $L^p(E_{\min}, E_{\max})$ integrable so long as the spectral shapes, $f_i(E)$, are $L^p(E_{\min}, E_{\max})$ integrable, which is physical. Standard MG also produces solutions that are discontinuous in energy at group boundaries.

2.3.2 Derivation of the FEDS transport equation and cross sections

In this subsection, we derive, without approximation, equations for the coefficients of the FEM, the $\Psi_e(\mathbf{r}, \mathbf{\Omega})$, using a weak form of the transport equation. These equations will depend on element-averaged cross sections that we will find to be basis-function weighted.

Our weak form of the transport equation will use weight functions not equal

to the basis functions. This makes our FEM a Petrov-Galerkin FEM. The weight functions we choose are

$$w_e(E) = \begin{cases} 1 & \text{if } E \in \mathbb{E}_e, \\ 0 & \text{otherwise,} \end{cases} \tag{2.27}$$

for $e = 1, \ldots, N_e$. These weight functions have no spatial dependence, are orthonormal, and span the entire energy domain.

We begin with the space-, energy-, and angle-dependent linear neutron transport equation with fission and anisotropic scattering. The scattering term has been expanded in spherical harmonics moments, using the common assumption that the scattering kernel depends on $\mathbf{\Omega}' \cdot \mathbf{\Omega}$ only. We assume a finite but arbitrary truncation order to the scattering moments. The fission term has been assumed dyadic in energy, though this is not required by the method. We show here the white boundary condition, though it is straightforward to apply the method to many boundary conditions, including vacuum, reflective, specified current, etc. We begin with:

$$\begin{aligned} \big(\mathbf{\Omega} \cdot \nabla + \Sigma_t(\mathbf{r}, E)\big)\psi(\mathbf{r}, E, \mathbf{\Omega}) = \\ \int_0^\infty \mathrm{d}E' \sum_{l=0}^{L} \frac{2l+1}{4\pi} \Sigma_{s,l}(\mathbf{r}, E' \to E) \sum_{m=-l}^{l} Y_{l,m}(\mathbf{\Omega})\, \phi^{l,m}(\mathbf{r}, E') + \\ \frac{\chi(\mathbf{r}, E)}{4\pi\, k_{\text{eff}}} \int_0^\infty \mathrm{d}E'\, \nu\Sigma_f(\mathbf{r}, E')\phi(\mathbf{r}, E'), \end{aligned} \tag{2.28a}$$

$$\phi^{l,m}(\mathbf{r}, E) = \int_{4\pi} \mathrm{d}\Omega\ Y_{l,m}(\mathbf{\Omega})\, \psi(\mathbf{r}, E, \mathbf{\Omega}), \tag{2.28b}$$

$$\psi(\mathbf{r}, E, \mathbf{\Omega}) = \frac{1}{\pi} \int_{\mathbf{\Omega}\cdot\mathbf{n}>0} \mathrm{d}\Omega'\ \ |\mathbf{\Omega}' \cdot \mathbf{n}|\, \psi(\mathbf{r}, E, \mathbf{\Omega}'), \qquad r \in \partial V,\ \mathbf{\Omega} \cdot \mathbf{n}(\mathbf{r}) < 0, \tag{2.28c}$$

where $\phi(\mathbf{r}, E) \equiv \phi^{0,0}(\mathbf{r}, E)$ and $Y_{0,0}(\mathbf{\Omega}) = 1$.

To derive the weak form, we multiply by weight functions and integrate over

energy. We further use the definition of our finite element solution, φ, to give explicit dependence on the basis functions. We have:

$$\int_0^\infty \mathrm{d}E\; w_n(E)\Big\{\big(\mathbf{\Omega}\cdot\nabla+\Sigma_t(\mathbf{r},E)\big)\sum_e \Psi_e(\mathbf{r},\mathbf{\Omega})b_e(\mathbf{r},E)\Big\} =$$

$$\int_0^\infty \mathrm{d}E\; w_n(E)\Big\{\int_0^\infty \mathrm{d}E'\;\sum_{l=0}^{L}\frac{2l+1}{4\pi}\Sigma_{s,l}(\mathbf{r},E'\to E)\sum_{m=-l}^{l}Y_{l,m}(\mathbf{\Omega})\sum_{e'}\phi_{e'}^{l,m}(\mathbf{r})b_{e'}(\mathbf{r},E')\Big\}+$$

$$\int_0^\infty \mathrm{d}E\; w_n(E)\Big\{\frac{\chi(\mathbf{r},E)}{4\pi\,k_{\text{eff}}}\int_0^\infty \mathrm{d}E'\;\nu\Sigma_f(\mathbf{r},E')\sum_{e'}\phi_{e'}(\mathbf{r})b_{e'}(\mathbf{r},E')\Big\}, \tag{2.29a}$$

$$\int_0^\infty \mathrm{d}E\; w_n(E)\phi^{l,m}(\mathbf{r},E)=\int_0^\infty \mathrm{d}E\; w_n(E)\Big\{\int_{4\pi}\mathrm{d}\Omega\;Y_{l,m}(\mathbf{\Omega})\sum_e\Psi_e(\mathbf{r},\mathbf{\Omega})b_e(\mathbf{r},E)\Big\}, \tag{2.29b}$$

$$\int_0^\infty \mathrm{d}E\; w_n(E)\Big\{\sum_e\Psi_e(\mathbf{r},\mathbf{\Omega})b_e(\mathbf{r},E)\Big\} =$$

$$\int_0^\infty \mathrm{d}E\; w_n(E)\Big\{\frac{1}{\pi}\int_{\mathbf{\Omega}\cdot\mathbf{n}>0}\mathrm{d}\Omega'\;\;|\mathbf{\Omega}'\cdot\mathbf{n}|\sum_e\Psi_e(\mathbf{r},\mathbf{\Omega}')b_e(\mathbf{r},E)\Big\}$$

$$r\in\partial V,\;\mathbf{\Omega}\cdot\mathbf{n}(\mathbf{r})<0. \tag{2.29c}$$

We now rearrange terms by bringing the quantities that do not depend on energy

outside of the integrals:

$$\boldsymbol{\Omega}\cdot\nabla\sum_e \Psi_e(\mathbf{r},\boldsymbol{\Omega})\left[\int_0^\infty \mathrm{d}E\; w_n(E)\, b_e(\mathbf{r},E)\right] + \sum_e \Psi_e(\mathbf{r},\boldsymbol{\Omega})\left[\int_0^\infty \mathrm{d}E\; w_n(E)\,\Sigma_t(\mathbf{r},E)\, b_e(\mathbf{r},E)\right] = \sum_{l=0}^{L}\frac{2l+1}{4\pi}\sum_{m=-l}^{l} Y_{l,m}(\boldsymbol{\Omega})\sum_{e'}\phi_{e'}^{l,m}(\mathbf{r})\left[\int_0^\infty \mathrm{d}E'\; b_{e'}(\mathbf{r},E')\int_0^\infty \mathrm{d}E\; w_n(E)\,\Sigma_{s,l}(\mathbf{r},E'\to E)\right] + \frac{1}{4\pi\, k_{\text{eff}}}\sum_{e'}\phi_{e'}(\mathbf{r})\left[\int_0^\infty \mathrm{d}E\; w_n(E)\chi(\mathbf{r},E)\right]\left[\int_0^\infty \mathrm{d}E'\;\nu\Sigma_f(\mathbf{r},E')b_{e'}(\mathbf{r},E')\right], \tag{2.30a}$$

$$\left[\int_0^\infty \mathrm{d}E\; w_n(E)\phi^{l,m}(\mathbf{r},E)\right] = \int_{4\pi}\mathrm{d}\Omega\;\; Y_{l,m}(\boldsymbol{\Omega})\sum_e \Psi_e(\mathbf{r},\boldsymbol{\Omega})\left[\int_0^\infty \mathrm{d}E\; w_n(E)\, b_e(\mathbf{r},E)\right], \tag{2.30b}$$

$$\sum_e \Psi_e(\mathbf{r},\boldsymbol{\Omega})\left[\int_0^\infty \mathrm{d}E\; w_n(E)\, b_e(\mathbf{r},E)\right] = \frac{1}{\pi}\int_{\boldsymbol{\Omega}\cdot\mathbf{n}>0}\mathrm{d}\Omega'\;\; |\boldsymbol{\Omega}'\cdot\mathbf{n}|\sum_e \Psi_e(\mathbf{r},\boldsymbol{\Omega}')\left[\int_0^\infty \mathrm{d}E\; w_n(E) b_e(\mathbf{r},E)\right] \quad r\in\partial V,\;\boldsymbol{\Omega}\cdot\mathbf{n}(\mathbf{r})<0. \tag{2.30c}$$

We now use the definition of our basis functions and impose orthonormality:

$$\begin{aligned}\int_0^\infty \mathrm{d}E\; w_n(E)\, b_e(\mathbf{r},E) &= \int_0^\infty \mathrm{d}E\; w_n(E)\, w_e(E)\, C_{e,i}\, f_i(E)\\ &= \delta_{e,n}\, C_{e,i}\int_{\mathbb{E}_e}\mathrm{d}E\; f_i(E)\\ &= \delta_{e,n}.\end{aligned} \tag{2.31}$$

This orthonormality result implies the unknowns, $\Psi_e(\mathbf{r},\boldsymbol{\Omega})$, have a physical in-

terpretation as the angular flux integrated over (discontiguous) energy domains:

$$\begin{aligned}\Psi_n(\mathbf{r},\mathbf{\Omega}) &= \sum_e \Psi_e(\mathbf{r},\mathbf{\Omega}) \left[\int_0^\infty \mathrm{d}E\; w_n(E) b_e(\mathbf{r},E)\right] \\ &= \int_0^\infty \mathrm{d}E\; w_n(E)\, \varphi(\mathbf{r},E,\mathbf{\Omega}). \end{aligned} \tag{2.32}$$

This, in turn, gives us justification for defining:

$$\phi_e^{l,m}(\mathbf{r}) \equiv \int_0^\infty \mathrm{d}E\; w_e(E)\, \phi^{l,m}(\mathbf{r},E). \tag{2.33}$$

Our orthonormality property also helps us with our interaction terms:

$$\begin{aligned}\int_0^\infty \mathrm{d}E\; w_n(E)\, \Sigma_x(\mathbf{r},E)\, b_e(\mathbf{r},E) &= \int_0^\infty \mathrm{d}E\; w_n(E)\, w_e(E)\, C_{e,i}\, f_i(E)\, \Sigma_x(\mathbf{r},E) \\ &= \delta_{e,n} \int_0^\infty \mathrm{d}E\; C_{e,i}\, f_i(E)\, w_e(E)\, \Sigma_x(\mathbf{r},E) \\ &= \delta_{e,n} \int_0^\infty \mathrm{d}E\; b_e(\mathbf{r},E)\, \Sigma_x(\mathbf{r},E). \end{aligned} \tag{2.34}$$

We define spectrally-averaged interaction terms:

$$\Sigma_{t,e}(\mathbf{r}) \equiv \int_0^\infty \mathrm{d}E\; b_e(\mathbf{r},E)\, \Sigma_t(\mathbf{r},E), \tag{2.35a}$$

$$\chi_e(\mathbf{r}) \equiv \int_0^\infty \mathrm{d}E\; w_e(E)\, \chi(\mathbf{r},E), \tag{2.35b}$$

$$\nu\Sigma_{f,e}(\mathbf{r}) \equiv \int_0^\infty \mathrm{d}E\; b_e(\mathbf{r},E)\, \nu\Sigma_f(\mathbf{r},E), \tag{2.35c}$$

$$\Sigma_{s,l,e'\to e}(\mathbf{r}) \equiv \int_0^\infty \mathrm{d}E\; w_e(E) \int_0^\infty \mathrm{d}E'\; b_{e'}(\mathbf{r},E')\, \Sigma_{s,l}(\mathbf{r},E'\to E). \tag{2.35d}$$

The cross sections are weighted with the basis function, which has the shape $f_i(E)$. The cross sections are averaged over discontiguous energy domains, because both basis and weight functions have support restricted to one energy element, and all

energy elements are in general discontiguous.

We use orthonormality and our cross section definitions to simplify the transport equation to:

$$[\mathbf{\Omega}\cdot\nabla+\Sigma_{t,e}(\mathbf{r})]\,\Psi_e(\mathbf{r},\mathbf{\Omega})=\sum_{l=0}^{L}\frac{2l+1}{4\pi}\sum_{e'}\Sigma_{s,l,e'\to e}(\mathbf{r})\sum_{m=-l}^{l}Y_{l,m}(\mathbf{\Omega})\,\phi_{e'}^{l,m}(\mathbf{r})+\frac{\chi_e(\mathbf{r})}{4\pi\,k_{\text{eff}}}\sum_{e'}\nu\Sigma_{f,e'}(\mathbf{r})\phi_{e'}(\mathbf{r}),\tag{2.36a}$$

$$\phi_e^{l,m}(\mathbf{r})=\int_{4\pi}\mathrm{d}\Omega\;Y_{l,m}(\mathbf{\Omega})\,\Psi_e(\mathbf{r},\mathbf{\Omega}),\tag{2.36b}$$

$$\Psi_e(\mathbf{r},\mathbf{\Omega})=\frac{1}{\pi}\int_{\mathbf{\Omega}\cdot\mathbf{n}>0}\mathrm{d}\Omega'\;\;|\mathbf{\Omega}'\cdot\mathbf{n}|\,\Psi_e(\mathbf{r},\mathbf{\Omega}'),\qquad r\in\partial V,\;\mathbf{\Omega}\cdot\mathbf{n}(\mathbf{r})<0,\tag{2.36c}$$

for $e=1,\ldots,N_g$.

A common approximation is that cross sections are constant within a user-defined region, V_i. Though our method does not require this approximation, using it allows us to simplify our cross sections and equations. Our cross sections become, for $\mathbf{r}\in V_i$:

$$\Sigma_{t,e,i}\equiv\int_0^\infty\mathrm{d}E\;b_e(\mathbf{r},E)\,\Sigma_{t,i}(E),\tag{2.37a}$$

$$\chi_{e,i}\equiv\int_0^\infty\mathrm{d}E\;w_e(E)\,\chi_i(E),\tag{2.37b}$$

$$\nu\Sigma_{f,e,i}\equiv\int_0^\infty\mathrm{d}E\;b_e(\mathbf{r},E)\,\nu\Sigma_{f,i}(E),\tag{2.37c}$$

$$\Sigma_{s,l,e'\to e,i}\equiv\int_0^\infty\mathrm{d}E\;w_e(E)\int_0^\infty\mathrm{d}E'\;b_{e'}(\mathbf{r},E')\,\Sigma_{s,l,i}(E'\to E),\tag{2.37d}$$

where we make use of the fact that, $\forall\mathbf{r}\in V_i$, $b_e(\mathbf{r},E)=w_e(E)C_{e,i}f_i(E)$, i.e., our basis functions do not have continuous dependence on space within a material region.

With the approximation of piecewise-constant-in-space cross sections, our transport equation becomes, for $\mathbf{r} \in V_i$:

$$[\mathbf{\Omega} \cdot \nabla + \Sigma_{t,e,i}] \, \Psi_e(\mathbf{r}, \mathbf{\Omega}) = \sum_{l=0}^{L} \frac{2l+1}{4\pi} \sum_{e'} \Sigma_{s,l,e' \to e,i} \sum_{m=-l}^{l} Y_{l,m}(\mathbf{\Omega}) \, \phi_{e'}^{l,m}(\mathbf{r}) + \frac{\chi_{e,i}}{4\pi \, k_{\text{eff}}} \sum_{e'} \nu \Sigma_{f,e',i} \, \phi_{e'}, \tag{2.38a}$$

$$\phi_e^{l,m}(\mathbf{r}) = \int_{4\pi} \mathrm{d}\Omega \; Y_{l,m}(\mathbf{\Omega}) \, \Psi_e(\mathbf{r}, \mathbf{\Omega}), \tag{2.38b}$$

$$\Psi_e(\mathbf{r}, \mathbf{\Omega}) = \frac{1}{\pi} \int_{\mathbf{\Omega} \cdot \mathbf{n} > 0} \mathrm{d}\Omega' \;\; |\mathbf{\Omega}' \cdot \mathbf{n}| \, \Psi_e(\mathbf{r}, \mathbf{\Omega}'), \quad r \in \partial V, \; \mathbf{\Omega} \cdot \mathbf{n}(\mathbf{r}) < 0. \tag{2.38c}$$

Because FEDS uses orthonormal basis functions / orthogonal weights, interface conditions are trivial: $\Psi_e(\mathbf{r}^+, \mathbf{\Omega}) = \Psi_e(\mathbf{r}^-, \mathbf{\Omega})$ for $\mathbf{r}^- \in V_i$, $\mathbf{r}^+ \in V_j$, and $\mathbf{r} \in V_i \cap V_j$, $\forall e = 1, \ldots, N_e$.

Equation (2.38) is identical in form to the MG transport equation with spatially piecewise-constant cross sections. The only differences are in the definition of the cross sections, which are now basis-function averaged over discontiguous energy domains, and the physical interpretation of the unknowns, which are now integrals of the scalar flux over discontiguous energy domains.

2.4 Generating Cross Sections

Once we have the energy mesh, cross sections must be defined, which is tantamount to specifying the basis functions. This process is problem-dependent. Many existing methods that produce MG cross sections may be directly applied to produce FEDS cross sections, the sole difference being that the methods are applied to a discontiguous energy domain instead of a contiguous one. Even methods that

implicitly define basis functions, such as through lookup tables [50, 67] or by using unnormalized condensation / homogenization factors (e.g., SPH [4]), are acceptable. We are free to represent the cross sections and basis functions however we desire.

For the purposes of this work, we primarily use an infinite-medium slowing-down calculation with analytically-approximated escape cross section to determine the basis functions on a hyperfine energy mesh and use those basis functions to flux-weight the cross sections over the discontiguous energy mesh. We repeat this calculation in each material. As shown in our results, we do not require a pincell calculation to determine cross sections.

Unless otherwise stated, the estimate we use for our escape cross section is the average chord length, equal to the surface area of the fuel divided by four times its volume. Further details are given in the relevant sections. Justification for this expression is provided in Appendix B.

There are three components required to generate FEDS cross sections. These are given below and summarized in Fig. 2.2, which gives a workflow for the FEDS method in practice.

1. Generate the generalized energy mesh (GEM).

    (a) Use NJOY[2] [68] to generate resolved cross sections for each nuclide of interest.

    The total and elastic scattering cross sections will be needed. The energy grid from the PENDF file resolves the resonances for the represented nuclide. A union energy grid will be built over all nuclides and thinned as needed.

[2]NJOY is a cross section preparation code that was originally called MINX (Multigroup Interpretation of Neutron Cross Sections). Legend has it that an off-by-one error when printing the characters in MINX resulted in a printout of NJOY, which was kept in later versions of the code.

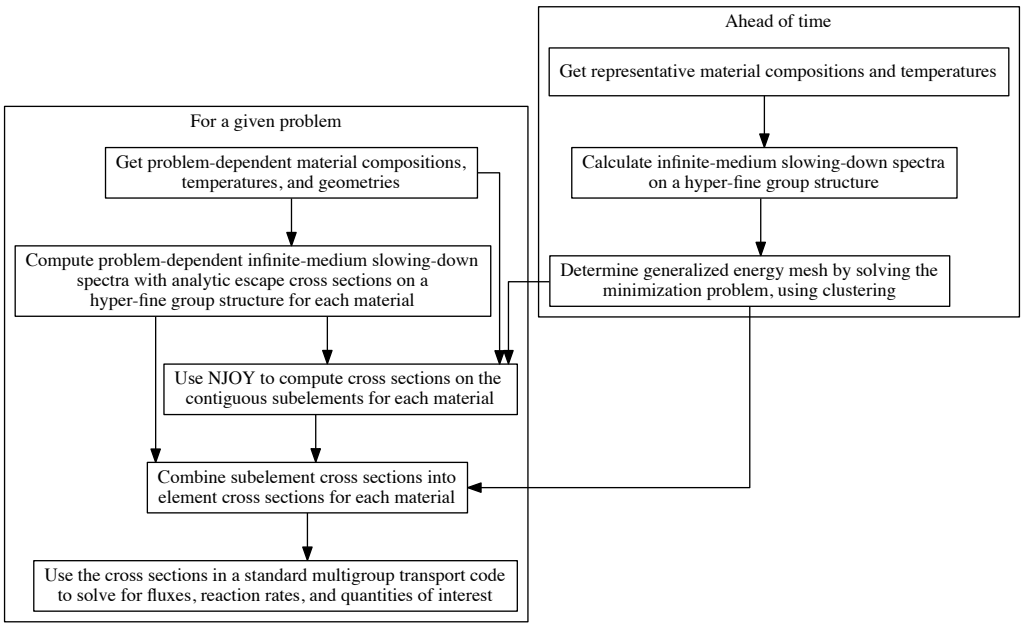

Figure 2.2: Workflow for the FEDS method, focusing on cross section preparation.

(b) Choose several material compositions and temperatures of interest in the problem.

These compositions will either correspond to actual material compositions in the problem of interest or be approximate compositions, in the case of depletion. Temperatures will always be assumed to be known ahead of time.

(c) Use those cross sections and material definitions to define infinite-medium spectra.

These spectra will consider only elastic scattering sources, and will use exact scattering kernels for each desired nuclide present in the material. This is sufficient for resolving spectra in the resolved resonance region of

heavy nuclides. Do this for each material and temperature on a hyper-fine union energy grid that resolves resonances.

(d) Use a clustering algorithm to combine energy ranges into energy elements.

The algorithm will combine, into elements, the energy ranges with similar spectra values. At the end of the process, all energy ranges will belong to exactly one energy element, though one element may contain multiple, potentially discontiguous, energy ranges. Energy elements are defined to minimize within-element variance for a given number of total elements. This means that all the spectra in an element are maximally nearby, for all materials, given the constraint that a fixed number of elements are to be used. As we have shown, choosing elements in this fashion minimizes the projection error when going from the pointwise representation of the spectra to the element (averaged) representation of the spectra, for a given number of elements.

(e) Use the definition of elements to define a generalized energy mesh.

A generalized energy mesh (GEM) has two components: a list of contiguous energy ranges called subelements and a list of which subelements belong to which elements. An element may include multiple, discontiguous subelements. If multiple contiguous hyperfine groups share the same element, they are combined into one (contiguous) energy subelement for reduced storage costs.

2. Generate cross sections on the subelements using standard MG techniques.

(a) Define a MG energy structure using the subelements.

The subelements are contiguous and so look the same as MG energy groups. For a given number of elements, the number of subelements may

be 1-2 orders of magnitude larger, depending on the definition of the elements. The ratio increases for higher energies because resonances become denser.

(b) Use NJOY and other standard cross section preparation techniques to generate MG cross sections and transfer matrices on the subelements.

This is identical to current MG procedures. Tables will be generated to store the cross sections as functions of background cross section and temperature for each reaction of each nuclide.

3. Generate cross sections on the elements by combining cross sections on the subelements.

(a) Use the GEM as a map to determine which subelements to combine into elements.

The condensation from subelements to elements is identical to the condensation from fine-group to coarse-group, except that the final cross sections on the elements cover discontiguous instead of contiguous energy ranges.

(b) Generate element-wise cross sections and transfer matrices.

As before, cross sections for each nuclide are represented as tables accessed by background cross section and temperature for each reaction.

The second and third steps of the above could be combined if the GROUPR routine in NJOY (or a similar code) were to be modified to condense into discontiguous instead of contiguous ranges. This combination would offer substantial memory savings, as the cross sections on the subelements would never need to be defined or stored. Such modification is beyond the scope of this work.

Using the separation of tasks listed above shows both the novel and preexisting

components of the FEDS method. The first component is novel. Although there have been various attempts at automatically generating MG group structures, none thus far have generated discontiguous energy structures and used them consistently for all nuclides. Further, using a clustering algorithm is novel and is a generalization of banding to multiple dimensions (i.e., multiple materials or space/angle points). The optimal way to implement the first component is an open question. For the purposes of this research, we have chosen to use an inexpensive, approximate method that uses only the infinite-medium fluxes for most of the calculations.

The second component is already done with MG calculations today. The first step of these calculations is to use NJOY or a similar code to determine fine-group cross sections from ENDF data. The method uses NJOY to determine subelement cross sections from ENDF data.

The third component is straightforward to implement. It requires an estimate of the flux on the subelements so that they may be properly averaged into an element. NJOY produces an estimate of this flux already. Instead, we prepose to use another set of infinite-medium calculations, with approximate analytic escape cross sections, to determine the flux on the subelements for condensation purposes.

Final storage costs for FEDS and for MG are identical when the same number of energy unknowns are used. There are two caveats to this. The first is, if the locations of the sublements are needed, either during post-processing or when analytically integrating a term in energy on-the-fly during the transport calculation[3], then FEDS will require additional storage proportional to the number of subelements.

The second caveat is that our implementation of FEDS requires temporary storage of cross sections on the subelements, which becomes expensive at high unknown counts. Such intermediate storage is not an intrinsic requirement of FEDS, but stems

[3]This is not the done for the fission spectrum or other quantities given in tabular form.

from our use of NJOY to initially process the cross sections. Cost is maximal for H-1, where the elastic scattering matrix is full and must be stored for all scattering moments, background cross sections and temperatures. For the reactor problems we studied, the subelement cross section file sizes for H-1 approached 5 GB[4] when using approximately 200 elements in the resolved resonance region (RRR), P_3 scattering, 10 background cross-section (σ_0) values, and 1 temperature.[5] For the same case, the final cross sections condensed onto the elements and interpolated in background cross section and temperature required around 5 MB of storage. Once the final FEDS cross sections are calculated, the temporary cross section file is deleted.

2.5 Properties of the FEDS Method

The FEDS method, like the PG-FEMG method before it, has several notable properties compared to the standard MG method. Integrals over energy once again become sums over energy unknowns (elements instead of groups). The only difference between FEDS cross sections / fluxes and MG cross sections / fluxes is the former represent averages / integrals over discontiguous energy domains, while the latter are over contiguous energy domains. A second property is that the FEDS method uses the same shape functions as are used by MG, meaning neither MG nor FEDS cross sections carry continuous spatial or any angular dependence. For this reason and because the finite element discretization is applied consistently, FEDS cross sections can be used in existing MG codes without modification to either the cross sections or the code. The only difference between MG and FEDS cross sections is that FEDS cross sections are defined over discontiguous elements instead of contiguous ones. The third notable property is that some energy elements become associated only

[4]This number could be reduced by approximately a factor of two by changing from an `ASCII` to binary file format.

[5]Cf. footnote 4 in section 1.

with resonances, leading to large cross sections in those energy elements. This forces robust spatial discretizations, because the FEDS method preserves boundary layers that are present in the true solution. Finally, FEDS cross sections, like MG cross sections, may be represented using lookup tables, which are memory-compact.

One interesting and undesirable feature of any method that uses discontiguous energy ranges is that they produce upper-diagonal terms in the scattering matrix. I call this effective upscattering and this phenomenon occurs for all problems that contain physical downscattering.[6]

Particles cannot upscatter unboundedly. If the scattering matrix were lower-triangular with a MG group structure, it would become block lower-triangular with a FEDS structure. That is, in each column of the scattering matrix, there is a column-dependent minimum row to which particles can upscatter. With FEDS, if coarse groups are used, multiple clustering calculations are done and stitched together to form the GEM, and the size of the upscattering blocks is bounded from above by the number of elements per coarse group. In energy instead of index space, the size of a block is limited to the energy range of the coarse group.

Effective upscattering also occurs in the PG-FEMG method. For PG-FEMG, the size of a block was the number of bands within a group and particles could not upscatter between groups. For FEDS, effective upscatter can only occur between elements whose subelements are interleaved, which is specified by the GEM. (As a notational note, I am deprecating the use of "groups" and "bands within a group" because they are misleading. I prefer the non-hierarchical definition of "energy element," even when coarse groups are used.)

[6]N.B. Scattering kernels that are characterized by no energy loss, such as coherent scattering, or by absorption-reemission, such as fission and or that occurs numerically in radiative transfer, do not experience effective upscattering.

2.6 Discussion

FEDS overcomes a major problem with MB and PG-FEMG, which is how to use handle multiple resonant materials. For MB, they are often handled inconsistently. For PG-FEMG, they are combined into one effective material. How to form this effective material is unclear. The different effective total cross sections in Fig. 2.3(b)-(d) will have different energy meshes.

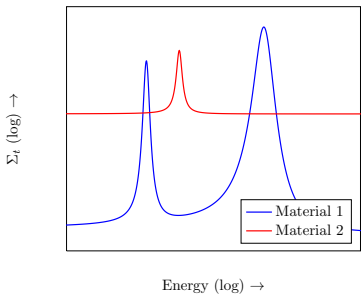

(a) Two resonant materials

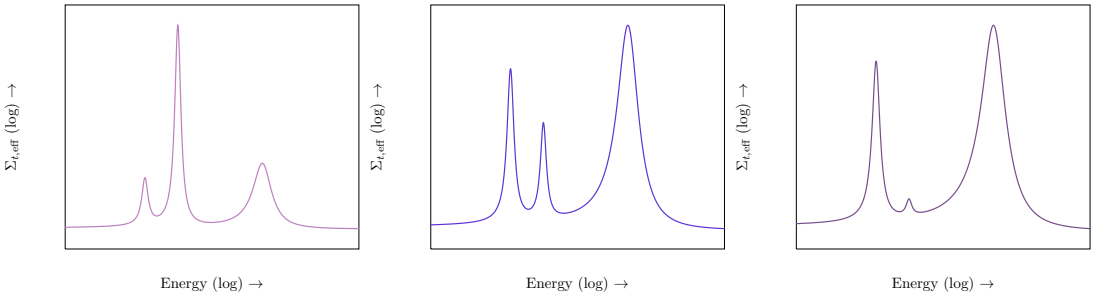

(b) Combination option 1 (c) Combination option 2 (d) Combination option 3

Figure 2.3: Example definitions of the effective total cross section required by PG-FEMG when multiple resonant materials are present

Figure 2.4 shows solution and cross section components for a reference MG solution of a pincell calculation. The solution depends on more than the total cross section alone, but is well-approximated by the scattering source divided by the local

total cross section. Infinite-medium fluxes overestimate flux dips near the edges of the fuel, but do well near the center. They capture scattering peaks, resonances, and their relative importances.

Figure 2.5 shows examples of the effect on clustering of using an energy penalty (a) versus using coarse groups (b). The energy penalty can create unexpected and undesirable splitting locations.

Figure 2.6 shows infinite-medium fluxes for the C5 problem on a coarse union energy grid suitable for clustering or a MG reference solution. It requires almost 10,000 groups to resolve all of the resonances, which is prohibitively expensive for the latter purpose. Instead, a portion of the resolved resonance range was chosen and the rest was not resolved by the group structure.

FEDS creates energy elements that handle multiple inputs. Figure 2.7 gives observations for a problem that includes multiple resonant materials and an energy penalty. The energy penalty is scaled to be less important than the solution, so it does not cause undue splitting in energy.

Figure 2.8 shows observations plotted against each other for the same problem as Fig. 2.7. Coloring indicates element membership, squares indicate element centers, and the dotted line is matching observations. Because clustering algorithms use L^2 distances to determine distances between observations and elements, Fig. 2.8 is what the clustering algorithm "sees."

Figure 2.9 shows spectra and their L^2 fits from the elements. Increasing the number of elements improves the fit, which is expected because the minimization problem was formulated to maximize the fits of the observations and the observations are simple functions of the spectra. The real FEDS basis functions are often not piecewise flat, so the fits here will be poorer than if the true basis functions were used. The infinite-medium spectra shown here are not the true solution, and the

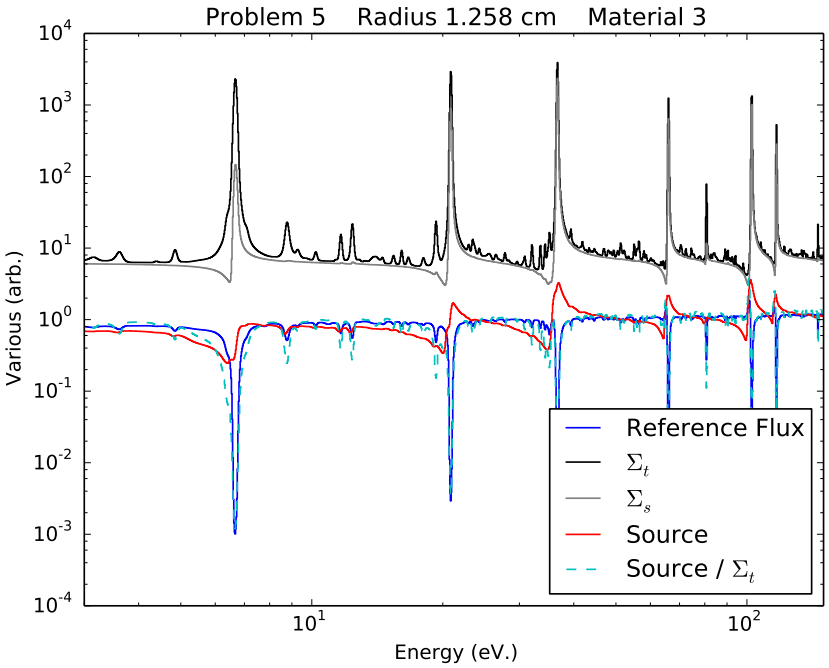

(a) Lower energies

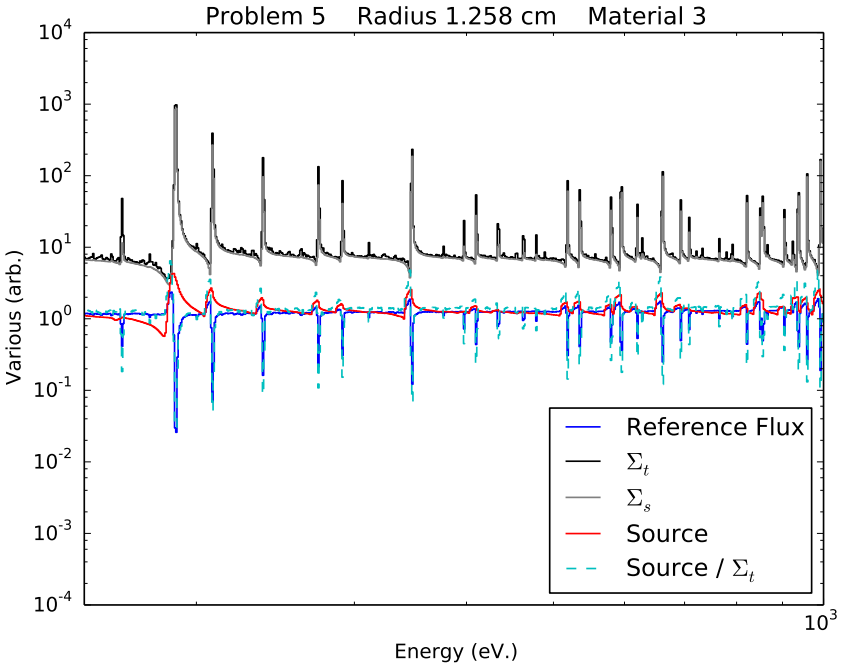

(b) Higher energies

Figure 2.4: Solution and cross section components for a pincell calculation

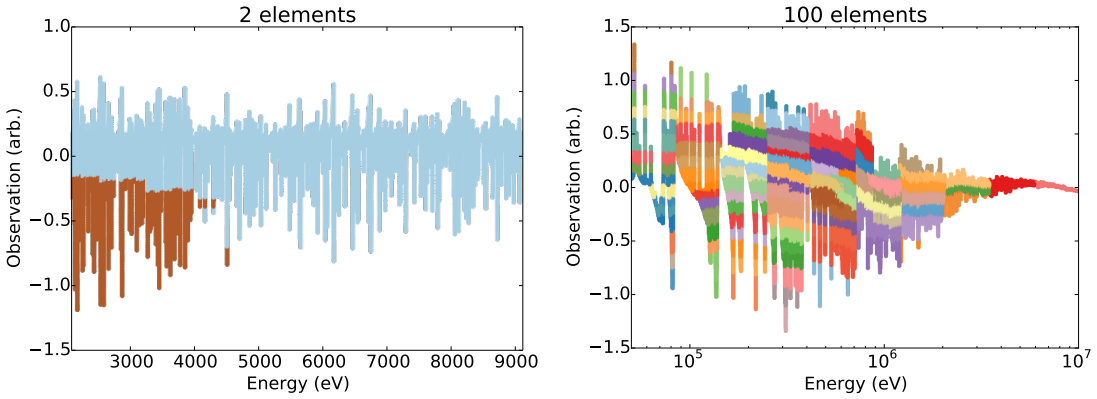

(a) Energy penalty effect

(b) Coarse groups example

Figure 2.5: Comparison of energy penalty versus coarse groups for controlling element size in energy. Energy ranges are colored by elements

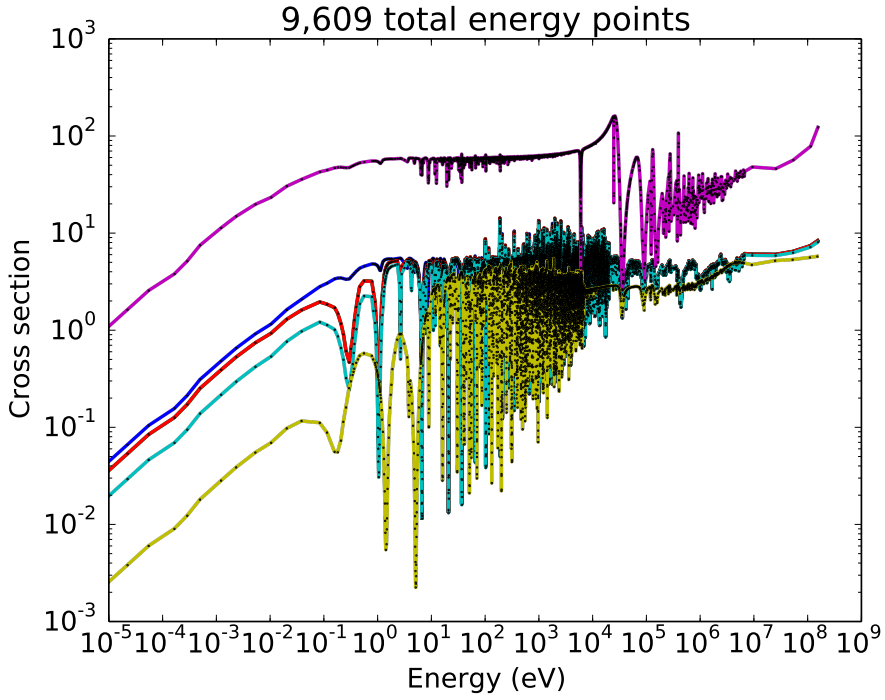

Figure 2.6: Example union energy mesh and approximate fluxes for the C5 problem. Different colors are different materials in the C5 problem, including UO_2 (blue), 4.3%-enriched MOX (green; covered by red), 7.0%-enriched MOX (red), 8.7%-enriched MOX (cyan), fission chamber (magenta), and control rod (yellow).

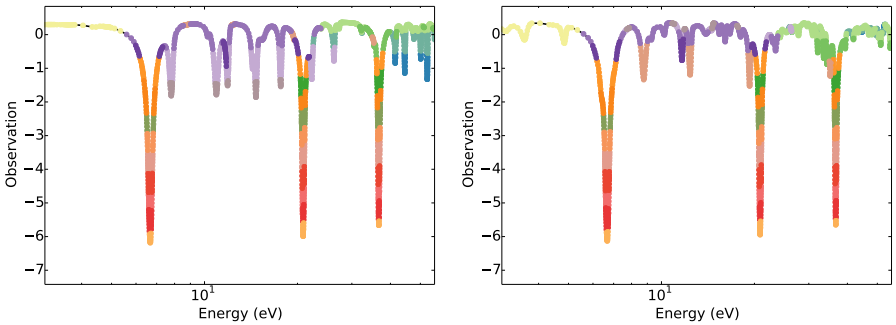

(a) MOX (b) UO_2

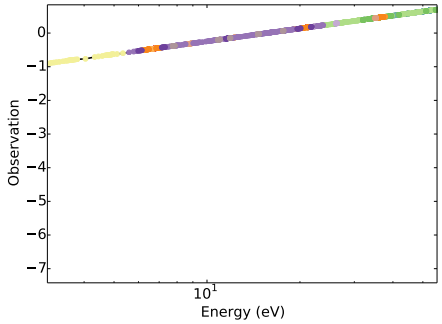

(c) Energy penalty

Figure 2.7: Observations plotted versus energy for multiple resonant materials and an energy penalty

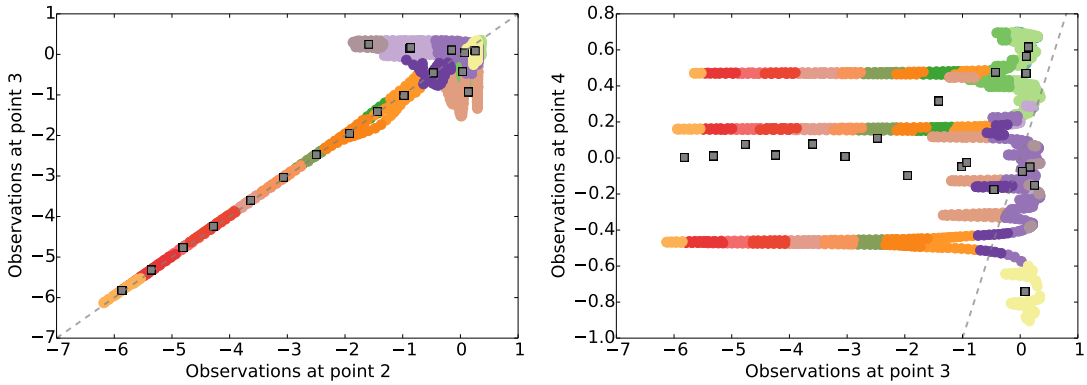

(a) UO_2 vs MOX (b) Energy penalty vs UO_2

Figure 2.8: Observations plotted against other observations

FEDS solution is not the L^2 projection of the true solution. Nevertheless, adding energy elements allows the FEDS solution to naturally self-shield.

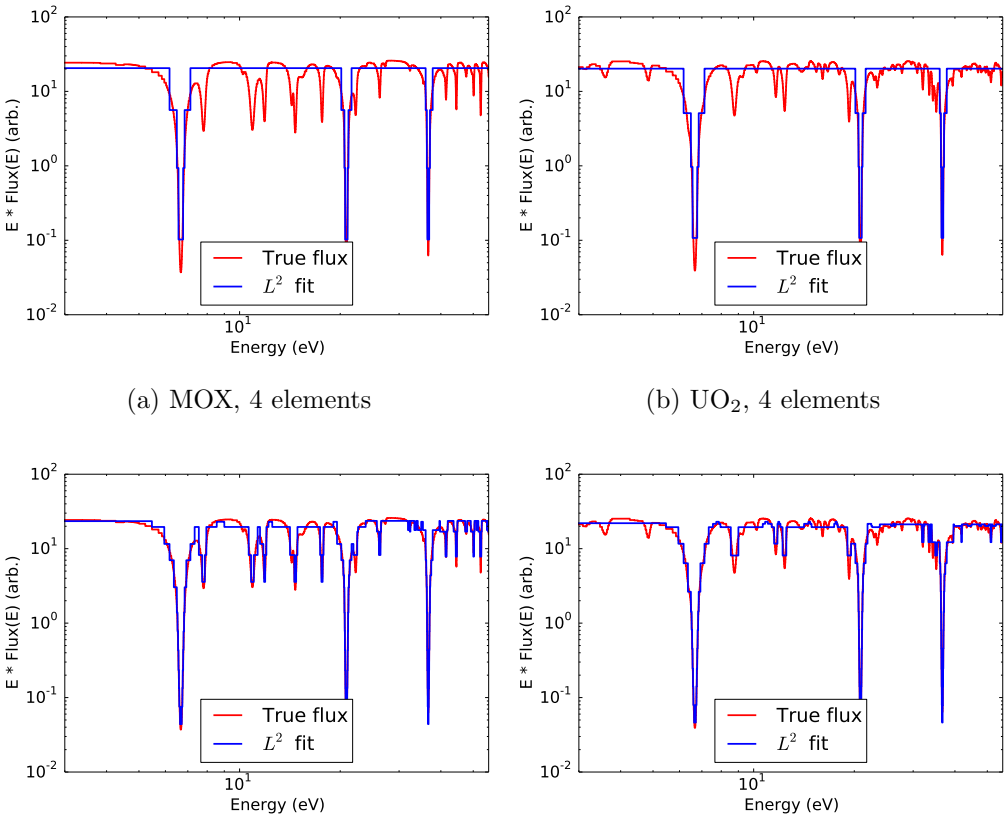

(a) MOX, 4 elements

(b) UO_2, 4 elements

(c) MOX, 20 elements

(d) UO_2, 20 elements

Figure 2.9: Observations and their L^2 fits using the elements

Figure 2.10(a) shows the L^2 projection error of the spectra on the elements and the k-eigenvalue error for a cyilndrical pincell problem using FEDS with k-means clustering. Both errors decrease with increasing resolution, which verifies our use of the minimization problem. Figure 2.10(b) shows the k-eigenvalue QOI error versus the L^2 projection error along with first- and second-order lines. Minimizing projec-

tion error minimizes solution error, though not always in a smooth way.

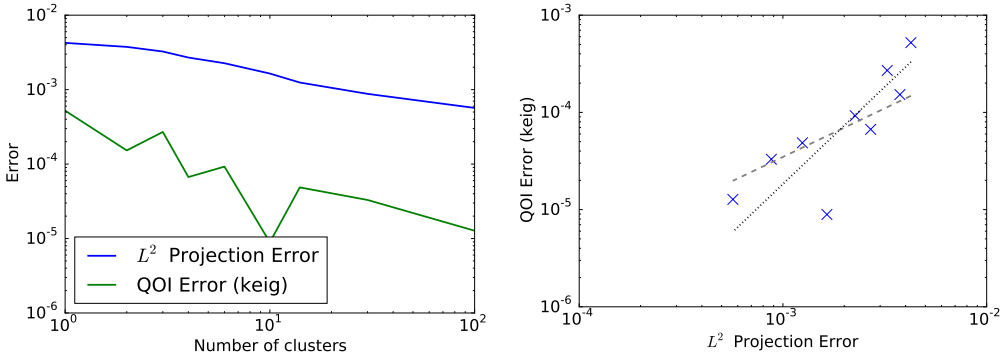

(a) Errors vs resolution

(b) Error vs error

Figure 2.10: Comparisons of projection error to QOI error

3. ONE-DIMENSIONAL PINCELL PROBLEMS

3.1 Problem Overview

In this section, we revisit the pincell calculations that were studied in [1]. These problems, while simple, allowed us to study the effect of numerous parameters on reaction rate errors. We vary the problem, effective resolved resonance range (RRR), clustering algorithm used to determine the GEM, basis functions used in cross section condensation, and the number of energy degrees of freedom (DOF) in the RRR. Testing on more realistic and more challenging problems, including multi-dimensional full-core simulations, is done in the next subsection.

Results in this section show FEDS to be accurate and convergent. FEDS is shown to be convergent for the reaction-rate-based QOI studied compared to a reference MG solution that resolved a third of the full RRR in lethargy space. Convergence is often approximately first-order in energy unknown, but is often uneven and sometimes convergent at a rate closer to half-order. The unevenness in convergence is attributed to using energy penalties to bound the size of an element in energy instead of using coarse groups, which were used by PG-FEMG in previous work and found again to work well in future sections. As expected, using higher-fidelity basis functions leads to better error constants. We found we could achieve target errors of 50 pcm in our QOI with fewer than 1,000 energy unknowns in our partial RRR, and often with fewer than 200 energy unknowns.

An adaptive MG was developed that attempted to maximally resolve resonance structure for a given number of groups. Results show adaptive MG (αMG; Table 2.1) to perform at lower errors than standard MG (sMG) that uses groups spaced equally in lethargy. Both adaptive MG and standard MG require their group structures to resolve the resonances before they begin converging appreciably.

3.2 Problem Description

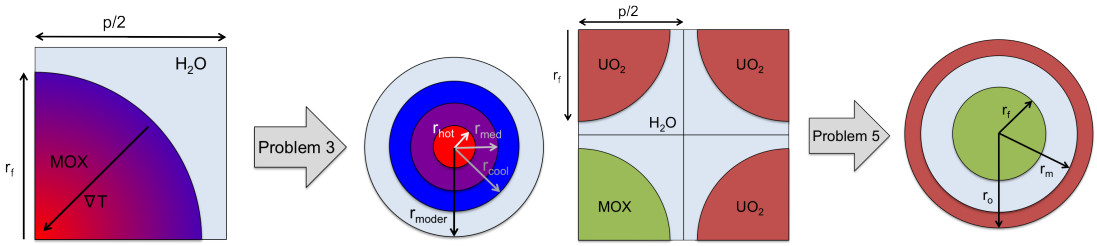

(a) Problem 3 (b) Problem 5

Figure 3.1: Pincell problem geometry cartoons

This section shows the results of our cylindrical pincell calculations. Figure 3.1 gives a cartoon of the geometries and materials used for two of the the cylindrical pincell problem. In problem 3, MOX in three rings of different temperatures (1000 K, 800 K, 700 K) is surrounded by cooler (550 K) moderator. In problem 5, MOX is surrounded by light-water moderator, which is itself surrounded by UO_2 (all at 400 K). Further details on the geometry, material, and solver specifications for the pincell problems may be found in [1, 20], where they are called problems 3 and 5, respectively. For the pincell problems, P_0 scattering and all reactions (including inelastic scattering and $S(\alpha, \beta)$ thermal scattering) were used. Due to the group-squared memory and calculation expenses of the reference solution, we did two separate sets of pincell

calculations per problem, one resolving the low-energy RRR while not resolving the medium-energy RRR, and vice versa.

We defined coarse chunks of the energy domain as thermal (< 3 eV), the "low-energy RRR" (3 – 55.6 eV), the "medium-energy RRR" (55.6 – 1060 eV), and the rest (> 1060 eV). For each problem, we defined a problem-specific RRR as the low- or medium-energy RRR chunks only. Outside of this problem-specific RRR, we used the SCALE 44-group energy boundaries [69].

Table 3.1 gives a description of how the energy mesh and cross sections were determined for the three cases studied. The spectra were only used to generate the energy mesh. The basis functions were only used to flux-weight the cross sections for a given energy mesh. The first two cases do not use any reference information while the latter case uses only reference information, representing an upper-bound on fidelity. The "infinite-medium" option for "spectra used" means we performed infinite-medium slowing-down calculations in the MOX (O-16, U-238 and Pu-239) and UO_2 (O-16, U-235, and U-238) to determine the spectra for clustering. $1/E$ basis functions means a spectrum with no resonance information was used to weight the cross sections.

We used partial currents from the reference solution for the spectra in case 3. This produced a slightly richer and more localized set of spectra: two half-currents per face and the partial current at the center of the pin versus one region-averaged scalar flux per material. The difference in fidelity between using partial currents and region-averaged scalar fluxes for the spectra was minimal. More important was using reference information for the basis functions used in cross section condensation.

For the infinite-medium with escape cross section calculation, we used a simple analytic estimate for the escape cross section of the chord length where possible. These calculations should approximately preserve flux dips and resonance interference ef-

fects. For the fuel pin in problem 3 and the center fuel in problem 5, the escape cross section was computed as the average chord length, $C/(4A)$, with $C = 2\pi r$, $A = \pi r^2$, and $r = 0.47$ cm, yielding 1.064 cm^{-1}. For the outer fuel in problem 5, the escape cross section was computed using the ratio of the partial current surface integral on the inner boundary ($r_m J_{g,\text{out}}$) to the volume integral in the outer fuel ($\int \mathrm{d}r\, r\phi_g(r)$). The median value over all groups was used. This method appears to be accurate even at low energy unknown count. This method produced an escape cross section of 0.8375 cm^{-1}, which is equivalent to using a pin with radius 0.597 cm.

Table 3.1: The different cases investigated for the pincell problem.

Case	Spectra Used	Basis Functions Used
1	Infinite-medium	$1/E$
2	Infinite-medium	Infinite-medium with escape XS
3	Reference-soln. partial currents	Reference-soln. material-averaged fluxes

Figure 3.2 shows energy meshes used with hierarchical agglomerative clustering and no reference information. The quantity plotted is the logarithm of the infinite-medium flux multiplied by energy. The left column is for problem 3 and a low-energy RRR. The right column is for problem 5 and a medium-energy RRR. For problem 5, the flux shown is in the UO_2. Individual dots give the resolution of the reference mesh, which resolves each resonance with several groups. Rows give the energy mesh at 10, 20, and 40 energy DOF in the RRR. Coloring indicates how the fine energy points are agglomerated into energy elements. Hierarchical agglomeration is noteworthy because meshes at lower DOF counts are always hierarchical to those at higher DOF counts. In Fig. 3.2, this is shown when one color splits into two or more colors evenly going down the rows.

An energy penalty is used to control element size in energy space. As energy DOF are added, the fine mesh is split into elements that occupy less flux and energy space. Energy penalties may not be the best way to accomplish the desired bounding of an energy element in energy space, because it leads to splitting that is not horizontal bands in Fig. 3.2. Other sections in this work use coarse groups instead of or in addition to an energy penalty. This is found to yield smoother convergence properties.

Four different clustering algorithms were used to solve the minimization problem. K-means (algorithm 1) and hierarchical agglomeration (alg. 2) resulted in discontiguous energy elements and used FEDS. Adaptive MG (alg. 3) produced contiguous groups and used MG. Standard MG (alg. 4) had an analytic solution of equally-spaced lethargy groups and used MG. Implementations for both k-means and hierarchical agglomeration were from SCIPY [65].

We investigated several quantities of interest (QOI), including absorption / fission production rates in the resonant nuclides (Pu-239, U-238, and U-235), criticality eigenvalue (k_{eff}), and power shape. Errors in QOI are relative errors with respect to a multigroup (MG) reference solution that resolves the resonances in our RRR. For the power shape, a relative L^2 error in space was used.

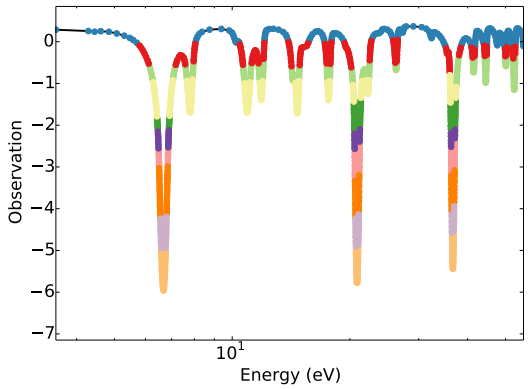

(a) Prob. 3, Low energy, 10 elements

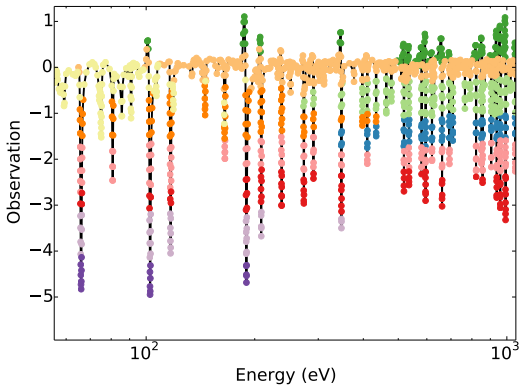

(b) Prob. 5, Med. energy, 10 elements

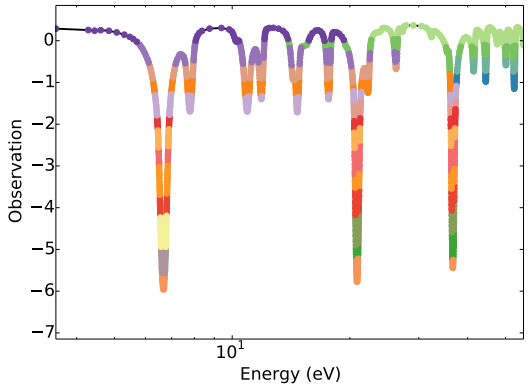

(c) Prob. 3, Low energy, 20 elements

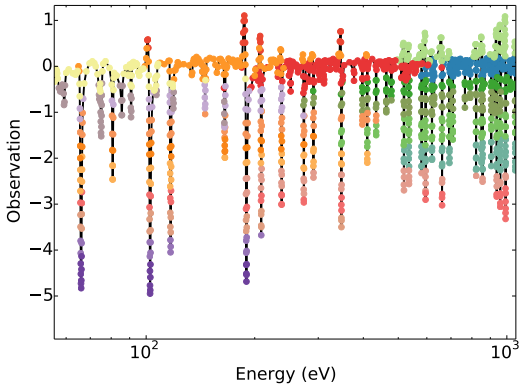

(d) Prob. 5, Med. energy, 20 elements

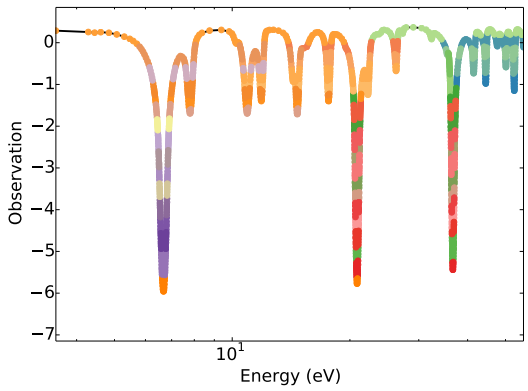

(e) Prob. 3, Low energy, 40 elements

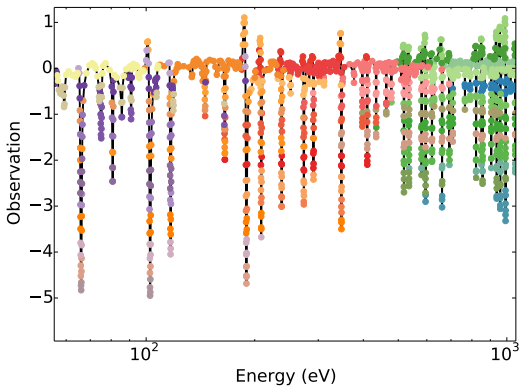

(f) Prob. 5, Med. energy, 40 elements

Figure 3.2: Energy meshes for several energy unknown counts and two problems for the one-dimensional cylinder pincell study.

3.3 Results

We plot errors in QOI in two ways. First, we show error in a specific QOI as a function of the number of energy elements in the RRR for all cases. These are given in Figs. 3.3 and 3.4. Colored lines are best-fits to the data, gray lines are at given convergence rates, and a green target of 5×10^{-4} (50 pcm) is given.

Second, we show errors in all the QOI as a function of the number of energy elements in the RRR for each case separately. These are given in Figs. 3.5 – 3.10. The red and blue lines give the maximum and minimum QOI error for all the QOI investigated. The black dots and cyan squares give measures of average QOI error. Gray lines are convergence rate fiducials.

Figure 3.3 shows errors in the k-eigenvalue QOI as a function of energy elements in the RRR for problem 3 with the low-energy portion of the RRR resolved. The different sub-figures use the three different condensing spectra (Table 3.1). Within each figure, the four algorithms are the different clustering methodologies, starting with k-means, then hierarchical agglomeration, then adaptive MG, then standard MG. Figure 3.4 shows the same things, except for problem 5 and the medium-energy portion of the RRR resolved.

Figures 3.5 – 3.7 shows errors in all QOI as a function of energy elements in the RRR for problem 3 with the low-energy portion of the RRR resolved, for condensing spectra cases 3, 2, and 1 respectively, for each of the four clustering algorithm methodologies. Figures 3.8 – 3.10 show the same things, except for problem 5 and the medium-energy portion of the RRR resolved. More results may be found in the accompanying appendix, Appendix C.

Figs. 3.5 – 3.10 collectively show that QOI error decreases with increasing numbers of energy elements for the low-energy RRR. For most QOI and cases, this

decrease is first-order, though case 1 is often more than first-order and case 2 is sometimes less than first-order. The convergence appears to be non-uniform, especially for cases 2 and 3. For case 2, we hypothesize that this non-uniformity is caused by using a weighting spectrum (basis function shape) that is not exact, and may incorrectly average cross sections over resonances significantly disparate in energy. For case 3, the errors are small in magnitude and near the target errors, so a poor convergence rate is acceptable so long as the errors do not stagnate or diverge, which they do not.

If a predictable and stable error convergence rate is desired when energy penalties are used, case 1 seems to be the best option studied. However, it begins with a larger error and requires more energy unknowns to reach the target error than either case 2 or 3. We claim that the goal is to use as few energy elements as possible to reach the target error without requiring reference information. Case 2 best satisfies these requirements and so we use it for the C5G$^{\infty}$ problem.

Taken together, Figs. 3.3 – 3.10 show promising and worrying properties concerning convergence rates and error magnitudes for FEDS. The worrying properties are related to uneven convergence rates and may be attributable to the use of an energy penalty, which is either not used or used in conjunction with coarse groups in later sections. While overall convergence for FEDS with both k-means and hierarchical agglomerative clustering are close to first-order, local convergence for a specific QOI can be uneven or even locally divergent. The latter we attribute to reductions in error cancellation with increasing DOF and note these regions occur either at DOF count below 10 or at errors around the single-digit pcm level. Uneven convergence, including convergence of individual QOI at half-order instead of first-order for significant spans of DOF count, are peculiar to this section. Other aspects peculiar to this section and the next section are strong reliance on energy penalty and low resolution

of the reference solution, especially at higher energies. An aspect peculiar to these results is defining cross sections by condensing the reference cross sections directly instead of returning to continuous-energy cross sections and condensing from there. This may compound errors in the poor resolution of the reference solution.

These results used a hand-tuned energy penalty in an attempt to naturally divide the elements in energy space. Future sections rely less or do not rely on this mechanism. The theoretical advantage of using an energy penalty is the ability to let the clustering algorithm do all of the splitting in energy automatically and at once. The practical results of energy penalties are less desirable. Energy penalties can cause the flux to produce energy elements with undesirable shapes (e.g., Fig. 2.5(a)). At low unknown counts, all of the resonances are effectively in one coarse group. As unknown counts rise, some elements that span multiple resonances are split because they have different energies. These splits, especially of the low-lying resonances explored with problem 3, can cause large reductions in error that show up as uneven convergence rates.

The promising properties shown in this section include convergence rates and error magnitudes. Convergence in the maximum error taken over all QOI is first-order for FEDS, even when other QOI error rates are not. This shows the method is able to determine where the error is and minimize it. FEDS begins converging immediately, while MG implementations require unknown counts proportional to the number of resolved resonances before convergence begins. FEDS is able to achieve the target error of 50 pcm in all QOI for all problems studied using fewer than 1,000 energy unknowns in the RRR, even with $1/E$ condensing spectrum.

The moderate-fidelity weighting spectrum (case 2) leads to lower errors than the $1/E$ condensing spectrum. Case 2 is especially useful for the medium-energy range, where FEDS is able to achieve low errors with around 20 energy unknowns in the

RRR.

While k-means and hierarchical agglomerative clustering overall yielded similar results, there are reasons to prefer hierarchical agglomeration to k-means clustering. Most implementations of k-means, including the one used here, have a stochastic element that is undesirable for reproduceability. Further, k-means results have a dependence on the hyperfine energy mesh used in the minimization problem. In my experience, k-means produces energy meshes of a higher quality for energy grids that have more resolution near the resonances as opposed grids that are equally spaced in lethargy. Finally, convergence for k-means is often less uniform than for hierarchical agglomeration in Figs. 3.3 – 3.10. For these reasons, hierarchical agglomeration is the clustering algorithm used in future sections.

Another promising development was the verification of the adaptive MG method. This method converges uniformly and rapidly once the unknown count is sufficient to resolve all of the important resonances. This property is useful if high energy resolution can be afforded, such as the low-energy portion of the RRR. Adaptive MG can achieve errors an order of magnitude lower than standard equally-lethargy-spaced MG for high energy unknown count, but behaves similarly at low energy unknown count. For these simple problems, adaptive MG can achieve almost second-order convergence in the asymptotic region.

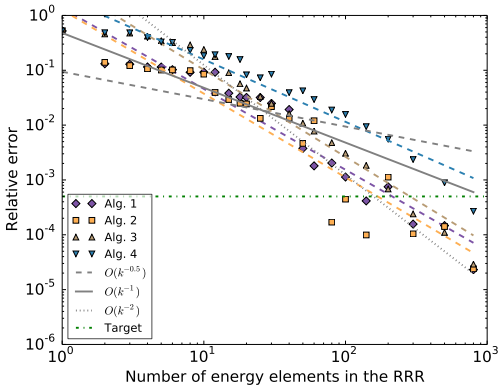

(a) Case 1

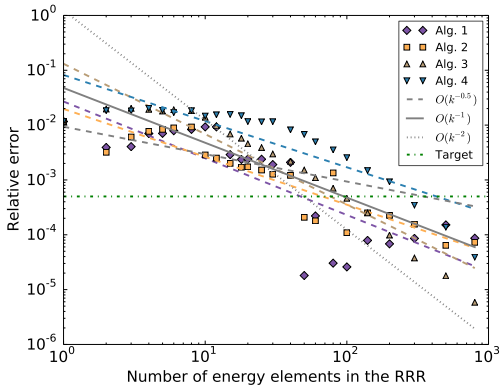

(b) Case 2

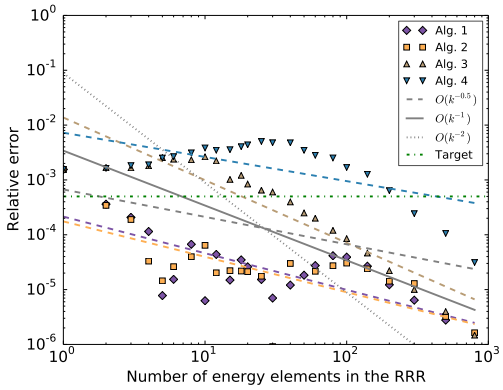

(c) Case 3

Figure 3.3: Errors for the k-eigenvalue QOI as a function of energy elements for problem 3 in the low-energy RRR for each case and all methods. Algorithms one through four in the legends refer to k-means, hierarchical agglomeration, adaptive MG, and standard MG, respectively. Cases one through three in the figure captions refer to the cases in Table 3.1.

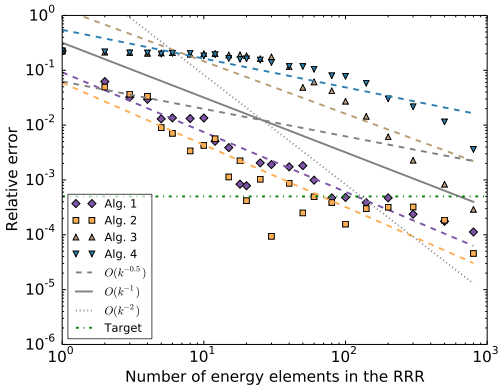

(a) Case 1

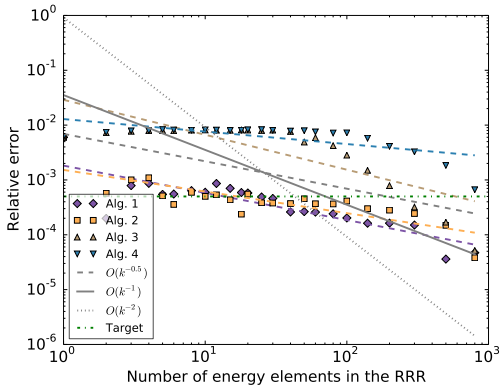

(b) Case 2

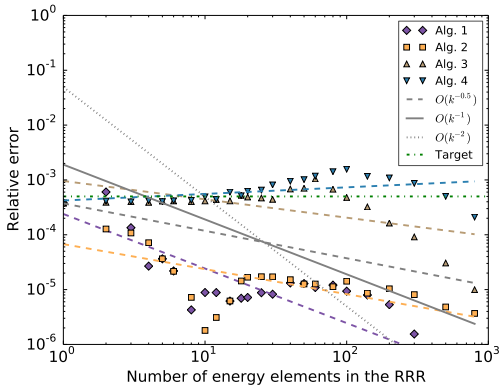

(c) Case 3

Figure 3.4: Errors for the k-eigenvalue QOI as a function of energy elements for problem 5 in the medium-energy RRR for each case and all methods. Algorithms one through four in the legends refer to k-means, hierarchical agglomeration, adaptive MG, and standard MG, respectively. Cases one through three in the figure captions refer to the cases in Table 3.1.

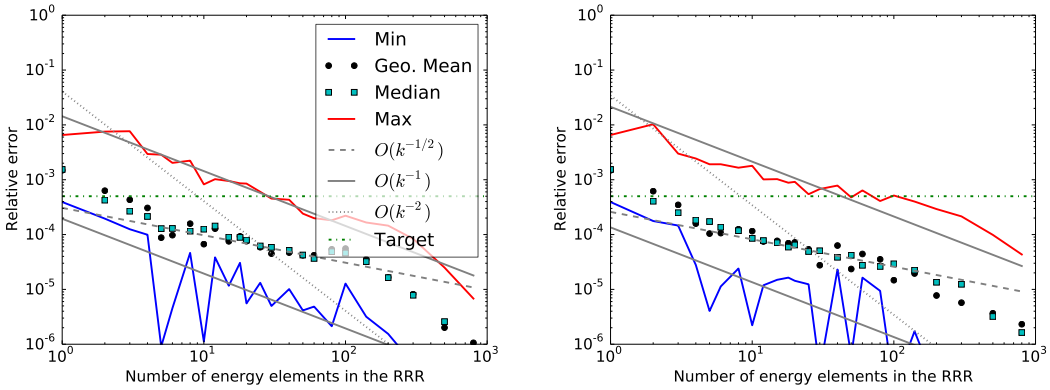

(a) Hierarchical agglomeration

(b) K-means

(c) αMG

(d) sMG

Figure 3.5: Errors for all QOI as a function of energy elements for problem 3 in the low-energy RRR for case 3 for each clustering method.

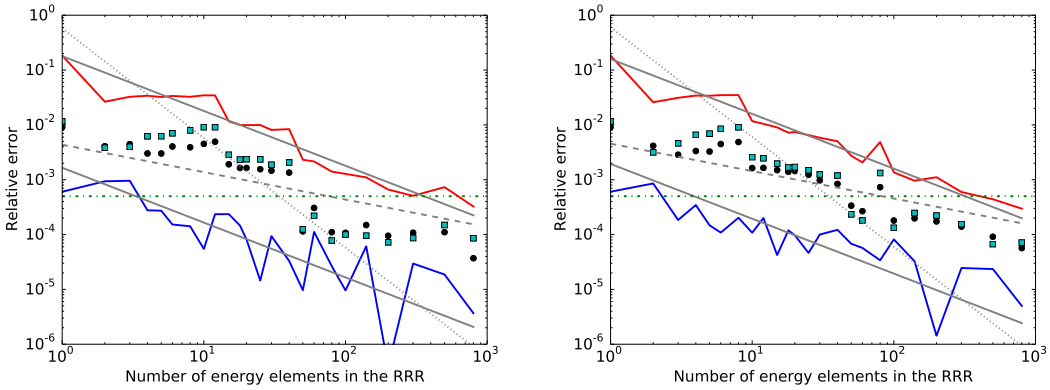

(a) Hierarchical agglomeration

(b) K-means

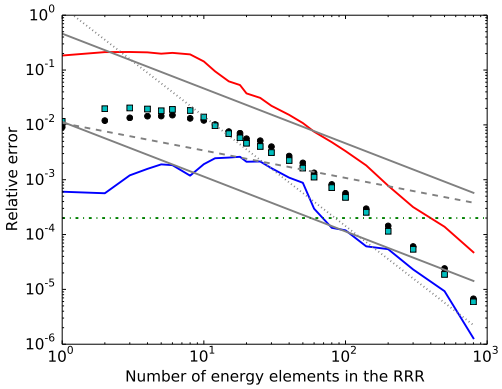

(c) αMG

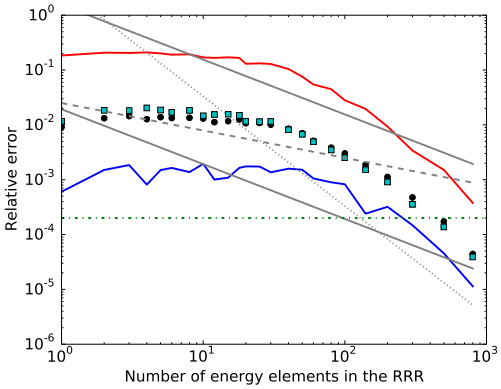

(d) sMG

Figure 3.6: Errors for all QOI as a function of energy elements for problem 3 in the low-energy RRR for case 2 for each clustering method.

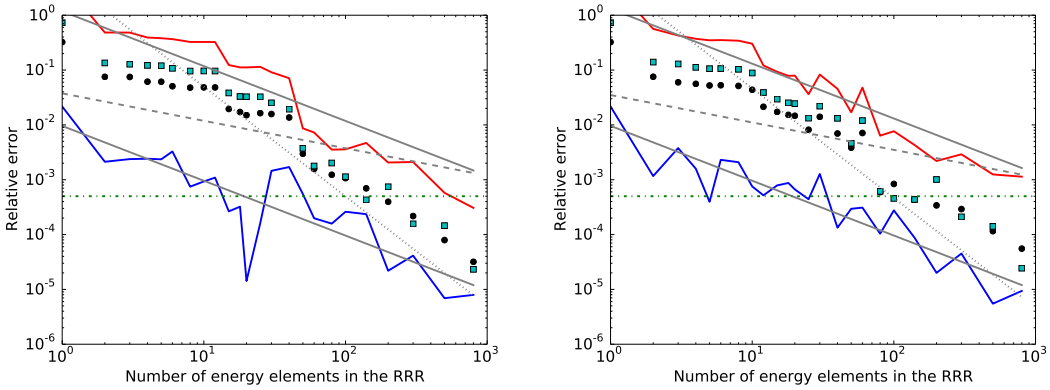

(a) Hierarchical agglomeration

(b) K-means

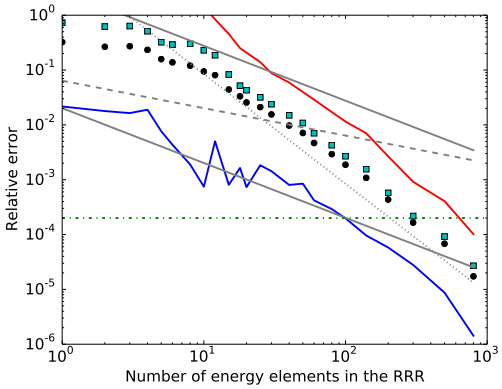

(c) αMG

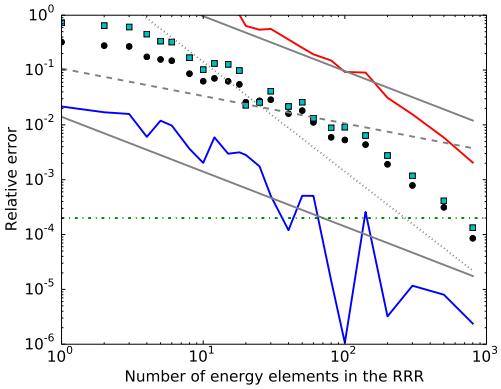

(d) sMG

Figure 3.7: Errors for all QOI as a function of energy elements for problem 3 in the low-energy RRR for case 1 for each clustering method.

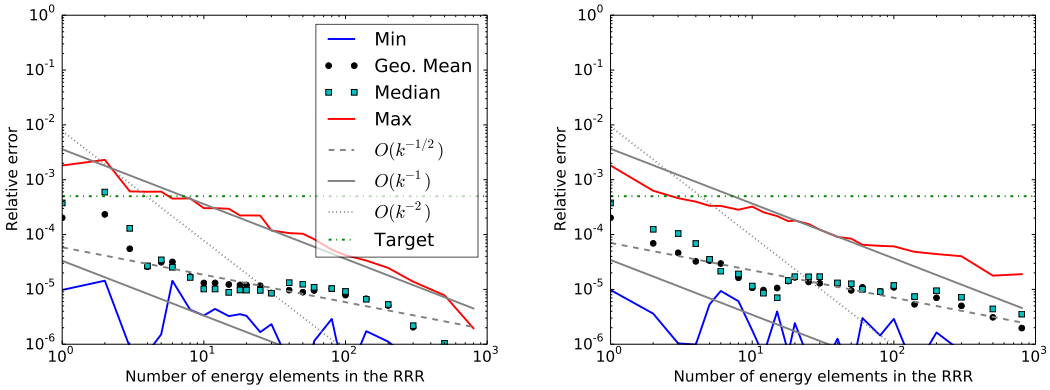

(a) Hierarchical agglomeration

(b) K-means

(c) αMG

(d) sMG

Figure 3.8: Errors for all QOI as a function of energy elements for problem 5 in the medium-energy RRR for case 3 for each clustering method.

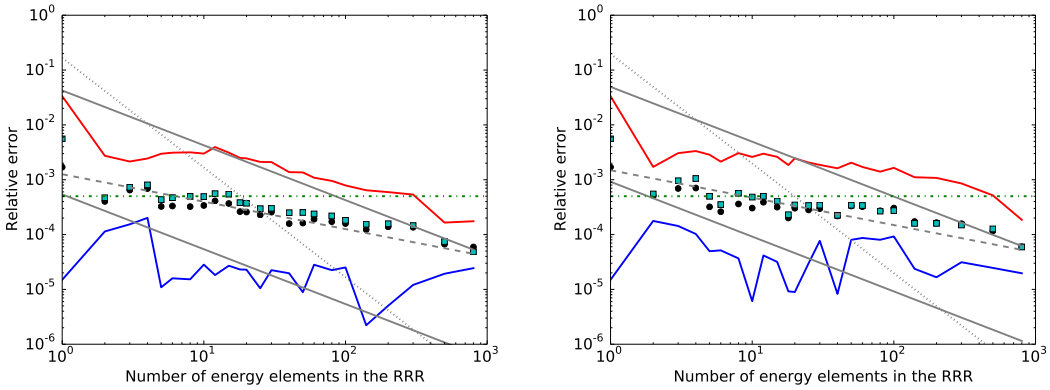

(a) Hierarchical agglomeration

(b) K-means

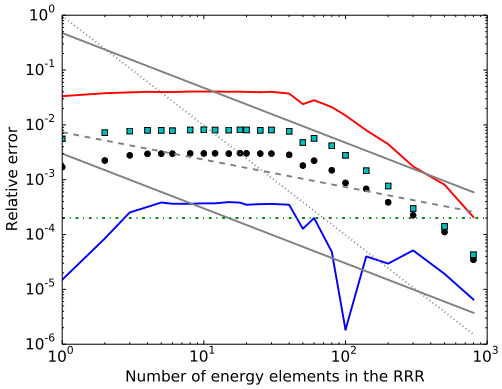

(c) αMG

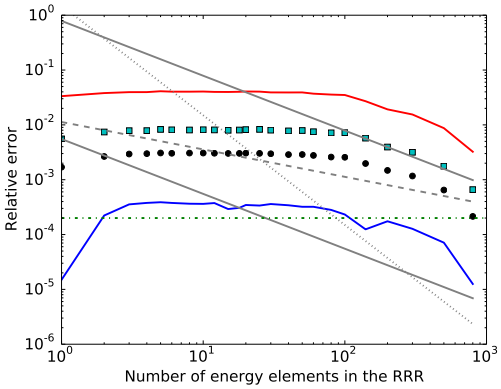

(d) sMG

Figure 3.9: Errors for all QOI as a function of energy elements for problem 5 in the medium-energy RRR for case 2 for each clustering method.

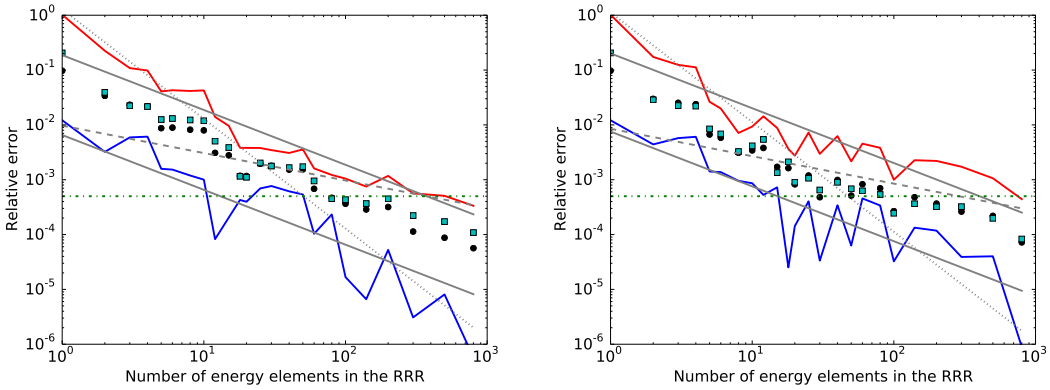

(a) Hierarchical agglomeration

(b) K-means

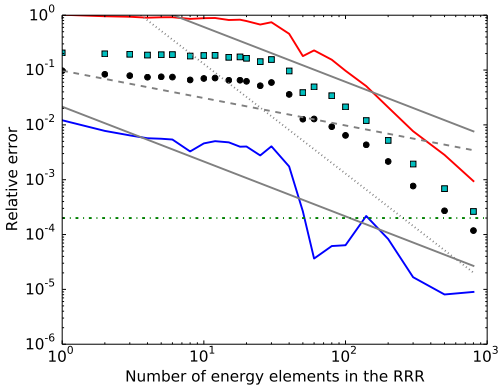

(c) αMG

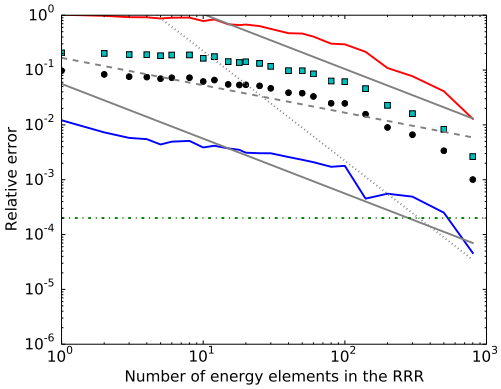

(d) sMG

Figure 3.10: Errors for all QOI as a function of energy elements for problem 5 in the medium-energy RRR for case 1 for each clustering method.

4. THE C5G$^\infty$ PROBLEM

4.1 Problem Overview

In this section, we move from simple cylindrical pincells with white boundaries to a two-dimensional reactor benchmark problem with cylindrical pins of varying composition in a square lattice. Multi-dimensional full-core problems introduce challenges not present in one-dimensional pincell problems. The most obvious is increased cost of solution due to increased dimensionality in space. Less obvious is the coupled dependence of the solution on neutron energy, direction and location.

The regular fuel lattices used in most nuclear reactors complicate the azimuthal dependence of the flux in angle due to shadowing. Particles traveling in different azimuthal directions have different distances between fuel pins, which causes self-shielding at resonance energies to have a fine-structure dependence in angle. This occurs regardless of the number of resonant materials. This phenomenon is not seen in one-dimensional pincell problems because white boundary condition are used and/or outer fuel pins are treated as annuli. Both of these approximations smear out angular dependence over the half-space (incoming or outgoing).

Real reactor cores contain more resonant nuclides than were treated previously. These nuclides are distributed heterogeneously in a manner that often exacerbates shadowing. Having more resonant nuclides and more variation in their combination stresses schemes that produce the GEMs and challenges methods that use approximate weighting spectra. For our multi-dimensional reactor case, we choose a standard benchmark problem in the two-dimensional C5 problem [70]. We emphasize our focus on energy discretization effects by calling our version of this problem the C5G$^\infty$ problem.

This section shares methodologies with the previous section. Once again, a reference MG solution that resolves only a portion of the resolved resonance region (RRR) is used, in this case 3 – 1060 eV. While this may be unsatisfying, it allows attribution of error to energy discretization effects. The RRR is split into two evenly-sized coarse groups but energy penalties are used to divide elements in energy space within each coarse group.

Results in this section are similar to the results of the previous section. FEDS is convergent in energy, even at low numbers of energy unknowns in the RRR. Convergence is approximately first-order and reaches target errors of 100 pcm in eigenvalue and 0.1 % in pin powers using fewer than 200 energy unknowns the RRR. An adaptive MG implementation requires sufficient groups to resolve the resonances before convergence begins. This section reiterates the result that energy penalties are inferior to using coarse groups alone for bounding element sizes in energy.

4.2 Problem Description

To create the C5G$^\infty$ problem, we reused the geometry and material specifications of the C5G7 problem, but created new cross sections. For each nuclide present in the C5G7 problem, we used NJOY99 [68] to generate cross sections for all reactions on a hyperfine energy grid that resolved our RRR, which for these results was 3 – 1060 eV. P_3 scattering was used. We formed our macroscopic cross sections using the material definitions of the C5G7 problem. We homogenized fuel and cladding (but not fuel and moderator) like the C5G7 specification. Unlike the C5G7 specification, we defined this homogenization to be atom-density-weighted, with no flux factors in fuel or cladding. We ran the C5G$^\infty$ problem using the PDT transport code [71] using our FEDS cross sections.

We defined coarse chunks of the energy domain as thermal (< 3 eV), the "low-

energy RRR" (3 – 1060 eV), and the rest (> 1060 eV). We resolved resonances within the low-energy RRR only. Outside of this problem-specific RRR, we used the SCALE 44-group energy boundaries [69]. For FEDS and adaptive MG, we used two coarse groups of equal lethargy size when calculating the energy mesh. A separate minimization problem, Eq. (2.17), was solved within each coarse group, meaning energy elements only contained subelements from one coarse group. This also means there is no effective upscattering outside of a coarse group.

To determine the spectra used for the energy mesh determination, we performed infinite-medium slowing-down calculations in the UO_2 (O, Al, Zr[1], U-235, and U-238) and the 8.7%-enriched MOX (O, Al, Zr, U-235, U-238, Pu-238, Pu-239, Pu-240, Pu-241, Pu-242, and Am-241). Due to our restriction of the RRR to below 1060 eV, we resolve few, if any, Zr resonances. The escape cross section was the fuel chord length, area / (4 * circumference), and was the same for all pins.

We believe it was valid to resolve energy while keeping spatial and angular resolutions fixed because the optical thicknesses of cells are bounded with the largest pointwise macroscopic total cross section, which is itself bounded for a given problem. Further details on the geometry, material, and solver specifications for the C5G$^\infty$ problem may be found by looking at C5G7 references [70, 71].

Figure 4.1(a) gives the physical layout for the C5 problem. The C5 problem consists of 4 assemblies surrounded by moderator, with each assembly containing a square lattice of 17-by-17 pincells with 20 guide tubes and one center fission chamber. The top and left boundaries are reflecting, while the bottom and right boundaries are vacuum. The top-left and bottom-right assemblies use one enrichment of UO_2

[1]We compute separately all the cross sections for the naturally occuring isotopes of Zr on a background cross section (σ_0) grid. The macroscopic UO_2 and MOX cross sections combine their component nuclides using the Bondarenko iteration to interpolate in background cross section. See Appendix B for more details.

fuel, while the other assemblies use three enrichments of MOX fuel.

Figure 4.1(b) gives pin powers for the C5G$^{\infty}$ problem from a FEDS calculation using 27 elements in the RRR. The unrodded C5 problem used here has a unphysical, large power peaking factor, with a ratio of maximum-to-minimum pin powers exceeding 10.

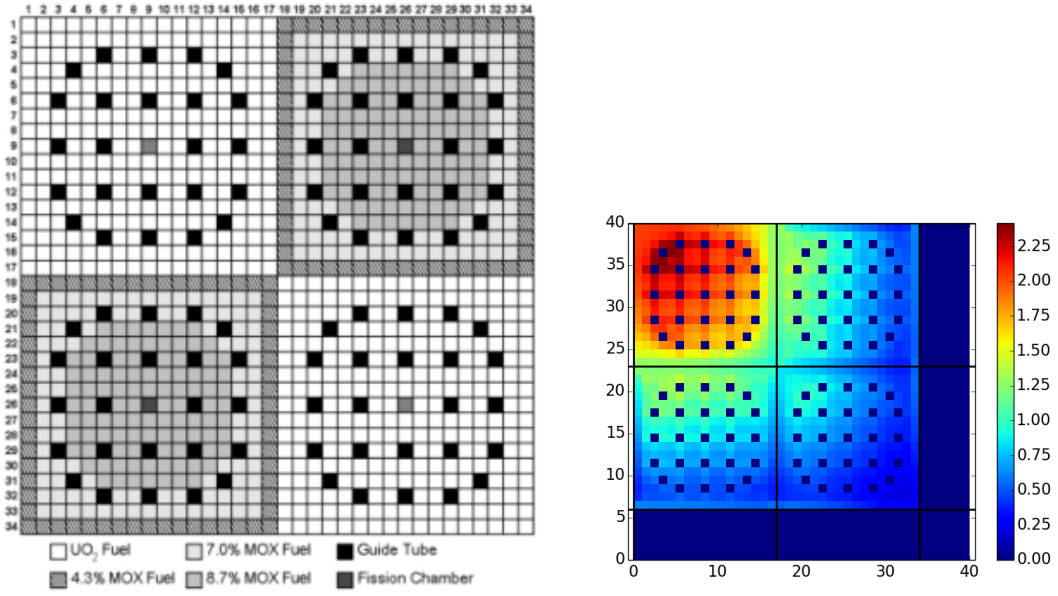

(a) C5 layout

(b) Pin powers

Figure 4.1: The NEA/NSC/DOC(2001)4 layout of the C5 problem and pin powers.

Figure 4.2 shows the spatial mesh we used for all runs of the C5G$^{\infty}$ problem. We placed three rings in the fuel/guide tube and one in the moderator. The outermost fuel ring was thin to resolve the flux dip in resonance energy elements. To increase robustness with this coarse spatial resolution, we used a lumped piecewise-linear discontinuous (PWLD) spatial discretization.[2] In angle, we used a Gauss-Chebyshev

[2]We use lumped PWLD because optical thicknesses in some of the fuel cells can be large for energy elements in the resolved resonance region and the thermal region for the spatial mesh used.

quadrature with 2 polar angles per half-plane (S_4) and 5 azimuthal directions per quadrant. Limitations in computer resources — especially for the reference solution — restricted us to these penurious spatial and angular resolutions.

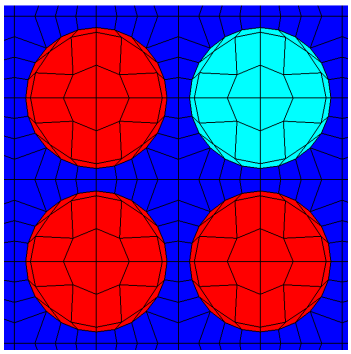

Figure 4.2: The low-resolution mesh used for the C5G$^\infty$ problem.

4.3 Results

Figure 4.3 shows element-integrated fluxes for selected energy elements for the C5G$^\infty$ problem solved with FEDS and 64 total energy elements. The colormap is proportional to the logarithm of the solution.

Figure 4.3(a) shows the fast flux, which peaks inside the fuel pins and dips slightly in the moderator-filled guide tubes. Figure 4.3(b) shows the flux in the URR, which is diffusive. Figure 4.3(c) shows the flux in the RRR for an energy element not corresponding to a resonance. This flux peaks in the moderator-filled guide tubes and moderator between pins, but overall has modest gradients. Figure 4.3(d) shows the flux in the RRR for an energy element at the tip of a resonance. This flux is strongly self-shielded, showing a steep gradient near the fuel-moderator boundaries of the pins. The flux in the moderator smoothly decreases from the center outward. Figure 4.3(e) shows the flux in an epithermal group with a low-lying Pu-239 resonance. The low-

frequency spatial mode of the flux is high in the center and decreases toward the outside. There is an interface near the MOX boundaries and large gradients within the MOX pins. Figure 4.3(f) shows the flux in a low-energy thermal group, where there is strong peaking in moderator regions overlaid on a peaking near the center UO_2 assembly and depression in the MOX assemblies.

Figure 4.4 gives three energy meshes used in the C5G$^\infty$ problem. The first row shows the FEDS mesh with 91 energy elements in the RRR. Energies that have the same color share the same element. The left and right columns are the observations taken from the MOX and UO_2 spectra. These and the energy penalty were the only spectra used in creating the energy meshes. The second row shows the energy mesh for adaptive MG with 91 resonance groups. The third row shows the reference MG energy mesh with 1499 resonance groups. The reference group structure used one coarse group in the RRR while the adaptive MG group structure used two.

We used pin powers and the criticality eigenvalue as QOIs for the C5G$^\infty$ problem. Table 4.1 shows how our QOI changed as a function of increasing the number of energy elements within the RRR. The first five QOI are pin powers, the latter three of which are sums over pins within an assembly. For the case of 2 energy elements, the energy mesh used two contiguous elements to cover the RRR and hence was similar to standard MG.

Table 4.2 gives relative errors in the QOI compared to the reference MG solution. The MG reference used 1,536 groups with adaptive spacing (1,499 groups in the RRR). Table 4.2 shows error in QOI decreases as energy elements are added to the RRR for all methods. Pin power errors are below 0.095% error when using 59 or more energy elements in the RRR (96 or more total energy elements) with FEDS. Errors in criticality eigenvalue quickly decrease as unknowns are added, until they saturate around 20 pcm for 91 or more DOF in the RRR for FEDS. This error stagnation

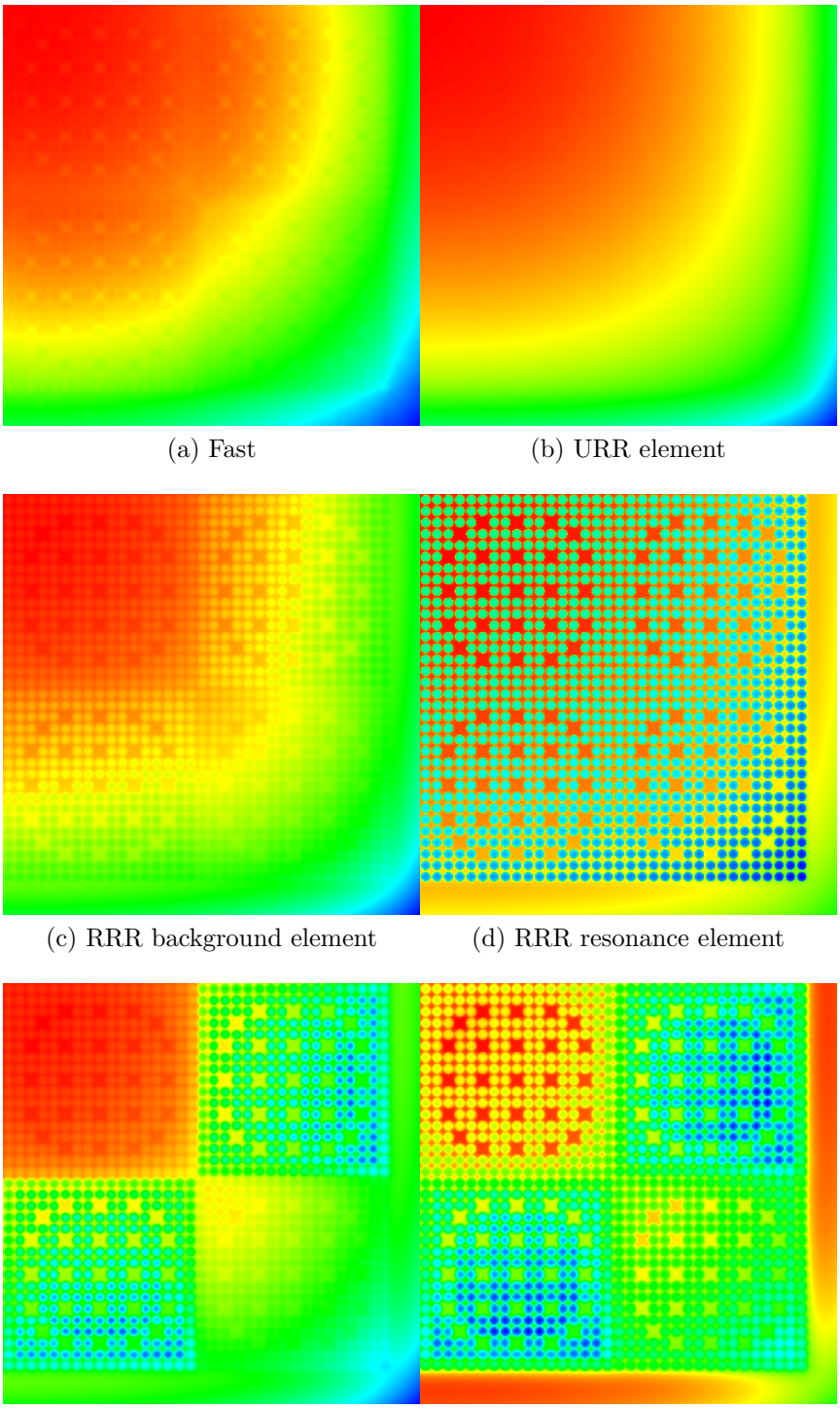

(a) Fast (b) URR element

(c) RRR background element (d) RRR resonance element

(e) Low-lying Pu-239 resonance (f) Thermal

Figure 4.3: C5G$^{\infty}$ fluxes for selected elements and 27 energy unknowns in the RRR.

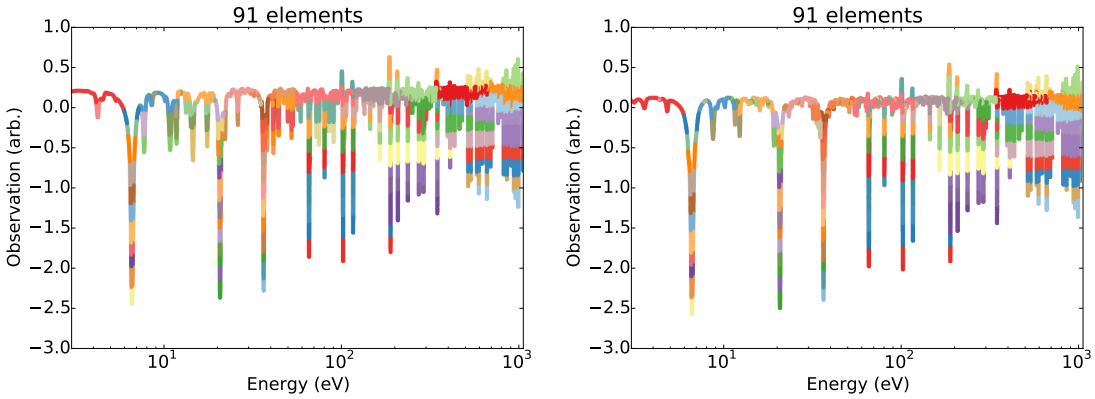

(a) FEDS, MOX

(b) FEDS, UO_2

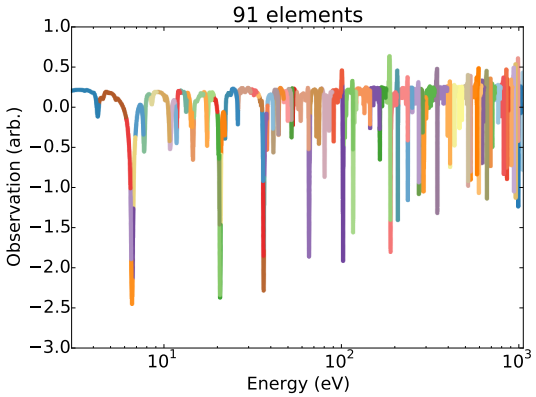

(c) αMG, MOX

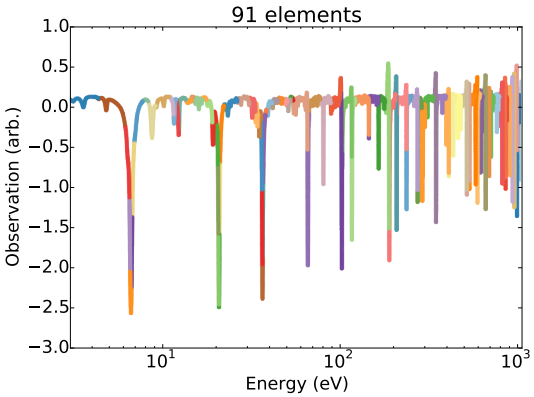

(d) αMG, UO_2

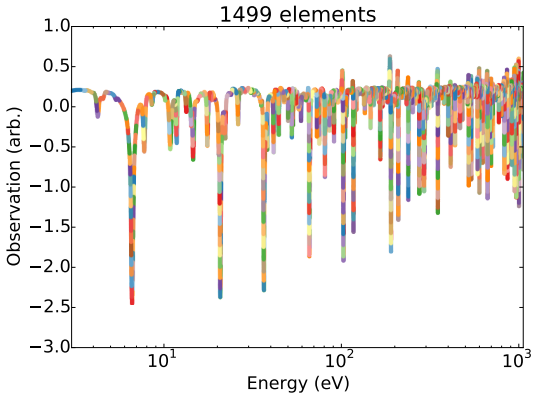

(e) Ref. MG, MOX

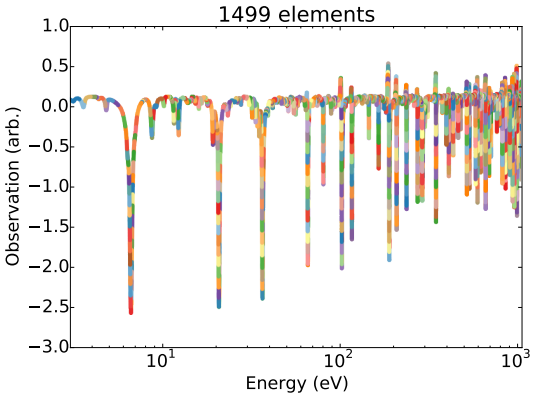

(f) Ref. MG, UO_2

Figure 4.4: Observations and energy meshes for the C5G$^{\infty}$ problem.

may have many causes, including the use of the energy penalty. Adaptive MG also converges, and has larger errors for a given number of energy unknowns. Standard MG has larger errors by a factor of 3 – 5 than adaptive MG. Both sMG and αMG (cf. Table 2.1) are non-convergent at low energy unknown counts. These results are similar to the one-dimensional results and indicate convergence in energy may be attainable with a reasonable number of unknowns (DOF) in energy.

The MG reference solution may be underresolved. Only 1,499 energy unknowns were used to resolve the partial RRR of 3 – 1060 eV. A FEDS reference solution was developed as an independent reference solution and to allow estimation of error in the MG reference solution. Wynn-epsilon extrapolation [72, 73] was used to accelerate the converging sequence of the FEDS existing solutions. The five highest resolutions of the FEDS run were extrapolated to form the FEDS reference solution. More information on Wynn's epsilon method may be found in the accompanying appendix, Appendix D.

Table 4.3 gives relative errors in the QOI compared to the Wynn-epsilon-accelerated FEDS reference solution. The bottom row shows the relative difference between the FEDS reference solution and the MG reference solution. If these are taken as uncertainty levels in either reference solution, pin powers are known to 0.04 to 0.09 % and k-eigenvalue is known to 40 pcm. These pin power uncertainties are larger than the pin power errors at the highest FEDS resolution in Table 4.2. This k-eigenvalue uncertainty is a factor of two smaller than than the eigenvalue error at the highest FEDS resolution. Comparisons to the FEDS reference solution as the preferred reference should be made warily, especially for the pin powers. Nevertheless, trends are similar for FEDS, αMG, and sMG in Table 4.3 compared to Table 4.2.

Figure 4.5 gives a graphical interpretation of the errors in the methods for both references. FEDS begins converging and then stagnates for many QOI compared

to the MG reference solution. Stagnation does not occur when compared to the FEDS-accelerated reference solution. Adaptive MG starts non-convergent when it has insufficient unknown count to resolve individual resonances, but then resolves in a first-order manner. Standard MG converges slowly and non-uniformly.

Figure 4.6 shows the same errors versus unknown count, but combines the pin-power errors into one average error. This clarifies the convergence. FEDS converges first-order in k-eigenvalue error for both reference solutions. It begins converging first-order in power error but stagnates compared to the reference solution. First-order convergence persists when compared to the FEDS reference solution, though this many only show the method is self-convergent. αMG requires approximately 20 unknowns before convergence begins, at which point it converges first-order in both eigenvalue and power error compared to the MG reference solution. Convergence in eigenvalue is similar compared to the FEDS reference solution. Unexpectedly, convergence in power error appears to be second-order with respect to the FEDS reference solution, which may indicate that this solution is accurate.

Figure 4.7 shows errors versus unknown count for k-eigenvalue error with all methods on the same plot. FEDS is able to achieve lower errors than αMG for the same unknown count by a factor of 3 or more for either reference solution.

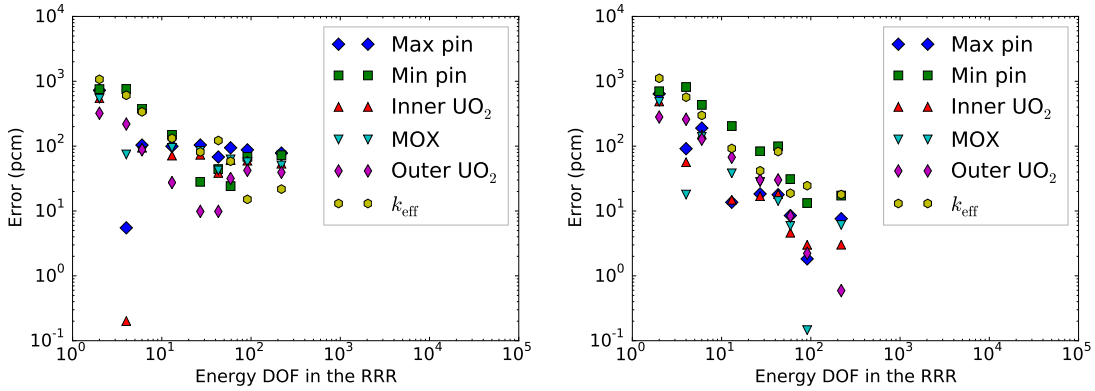

(a) FEDS with MG reference

(b) FEDS with FEDS reference

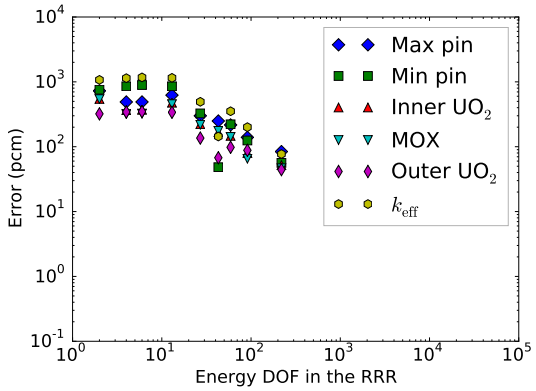

(c) αMG with MG reference

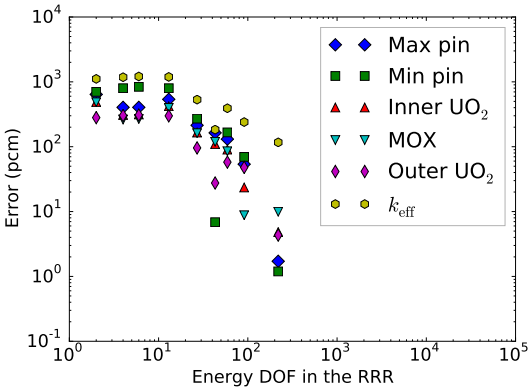

(d) αMG with FEDS reference

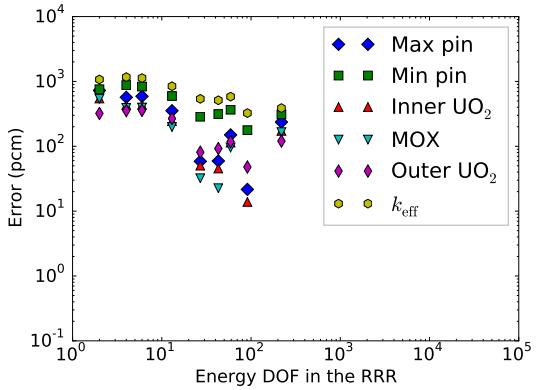

(e) sMG with MG reference

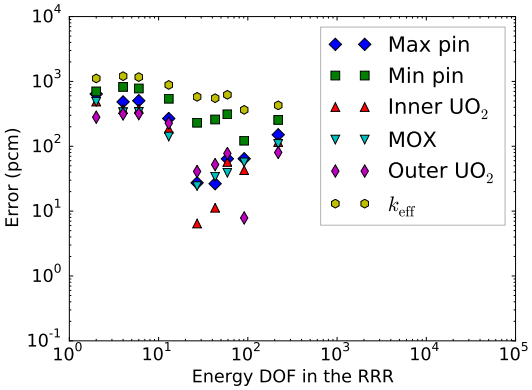

(f) sMG with FEDS reference

Figure 4.5: Errors for all QOI as a function of energy element number for the C5G$^{\infty}$ problem

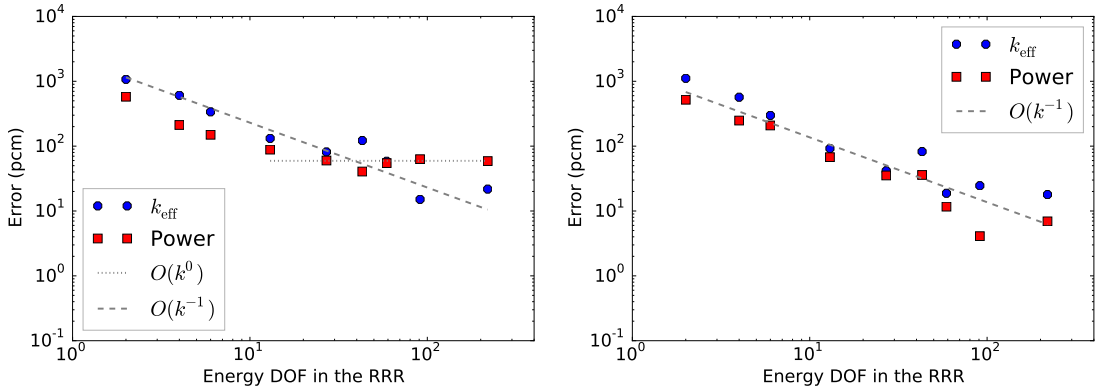

(a) FEDS with MG reference

(b) FEDS with FEDS reference

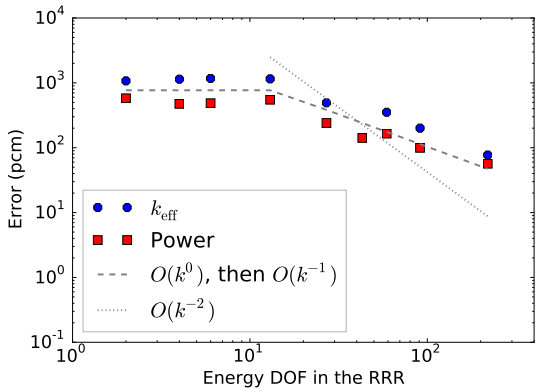

(c) αMG with MG reference

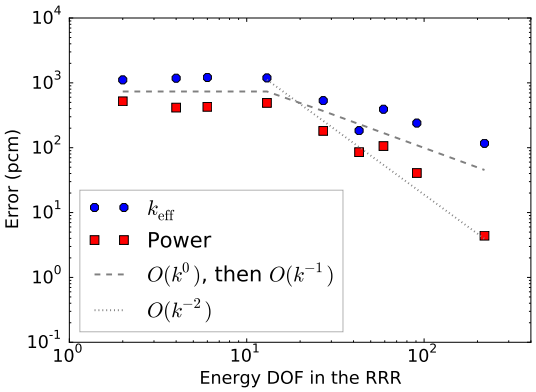

(d) αMG with FEDS reference

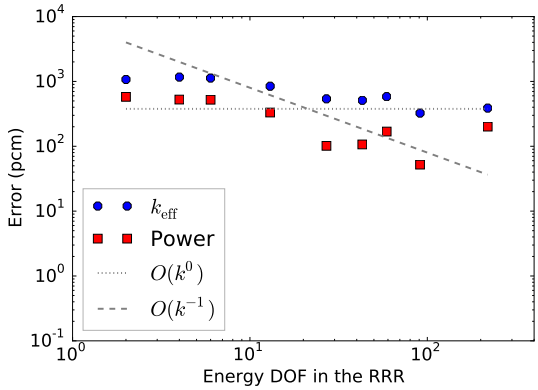

(e) sMG with MG reference

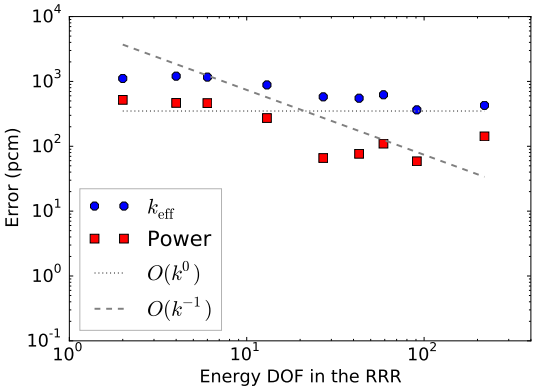

(f) sMG with FEDS reference

Figure 4.6: Errors for selected QOI as a function of energy element number for the C5G$^{\infty}$ problem

Table 4.1: QOI for the C5G$^{\infty}$ problem versus the number of energy elements in the RRR. The first five quantities are pin powers, the latter three of which are sums over pins within an assembly.

Method	RRR	Max Pin Power	Min Pin Power	Inner UO_2 Power	MOX Power	Outer UO_2 Power	k_{eff}
FEDS	2	2.52591	0.250210	494.534	209.476	142.514	1.132217
FEDS	4	2.54452	0.246440	497.246	208.503	141.747	1.151449
FEDS	6	2.54702	0.247390	497.718	208.174	141.933	1.148358
FEDS	13	2.54185	0.247960	496.891	208.545	142.019	1.145999
FEDS	27	2.54173	0.248260	496.881	208.524	142.072	1.145422
FEDS	43	2.54265	0.248220	497.055	208.436	142.072	1.145888
FEDS	59	2.54198	0.248390	496.942	208.478	142.103	1.145159
FEDS	91	2.54215	0.248500	496.950	208.466	142.118	1.144663
FEDS	219	2.54239	0.248510	496.980	208.453	142.114	1.144739
αMG	2	2.52591	0.250210	494.534	209.476	142.514	1.132217
αMG	4	2.53192	0.250450	495.429	209.013	142.545	1.131446
αMG	6	2.53191	0.250550	495.402	209.023	142.552	1.131080
αMG	13	2.52852	0.250450	494.876	209.292	142.540	1.131300
αMG	27	2.53676	0.249140	496.143	208.803	142.251	1.138854
αMG	43	2.53804	0.248450	496.418	208.714	142.154	1.142845
αMG	59	2.53887	0.248880	496.516	208.643	142.197	1.140460
αMG	91	2.54083	0.248640	496.848	208.484	142.183	1.142198
αMG	219	2.54224	0.248470	496.989	208.445	142.121	1.143608
sMG	2	2.52591	0.250210	494.534	209.476	142.514	1.132217
sMG	4	2.52990	0.250510	495.106	209.166	142.562	1.131144
sMG	6	2.52938	0.250400	495.088	209.172	142.567	1.131595
sMG	13	2.53539	0.249810	496.042	208.760	142.438	1.134836
sMG	27	2.54289	0.249040	496.997	208.415	142.173	1.138324
sMG	43	2.54287	0.249110	497.021	208.395	142.189	1.138634
sMG	59	2.54057	0.249240	496.680	208.547	142.225	1.137819
sMG	91	2.54383	0.248770	497.178	208.348	142.126	1.140773
sMG	219	2.53837	0.249100	496.387	208.692	142.229	1.140051
MG ref.	1499	2.54438	0.248330	497.247	208.348	142.058	1.144490
FEDS ref.	N/A	2.54220	0.248467	496.965	208.466	142.115	1.144944

Table 4.2: Relative errors for the C5G$^{\infty}$ problem compared to the reference MG solution. The first five errors are pin powers, the latter three of which are sums over pins within an assembly.

Method	RRR DOF	Max Pin (%)	Min Pin (%)	Inner UO_2 (%)	MOX (%)	Outer UO_2 (%)	k_{eff} (pcm)
FEDS	2	-0.7259	0.7571	-0.5456	0.5414	0.3210	-1,072
FEDS	4	0.0055	-0.7611	-0.0002	0.0744	-0.2189	608
FEDS	6	0.1038	-0.3785	0.0947	-0.0835	-0.0880	338
FEDS	13	-0.0994	-0.1490	-0.0716	0.0946	-0.0275	132
FEDS	27	-0.1042	-0.0282	-0.0736	0.0845	0.0099	81
FEDS	43	-0.0680	-0.0443	-0.0386	0.0422	0.0099	122
FEDS	59	-0.0943	0.0242	-0.0613	0.0624	0.0317	58
FEDS	91	-0.0876	0.0685	-0.0597	0.0566	0.0422	15
FEDS	219	-0.0782	0.0725	-0.0537	0.0504	0.0394	22
αMG	2	-0.7259	0.7571	-0.5456	0.5414	0.3210	-1,072
αMG	4	-0.4897	0.8537	-0.3656	0.3192	0.3428	-1,140
αMG	6	-0.4901	0.8940	-0.3710	0.3240	0.3477	-1,172
αMG	13	-0.6233	0.8537	-0.4768	0.4531	0.3393	-1,152
αMG	27	-0.2995	0.3262	-0.2220	0.2184	0.1359	-492
αMG	43	-0.2492	0.0483	-0.1667	0.1757	0.0676	-144
αMG	59	-0.2166	0.2215	-0.1470	0.1416	0.0978	-352
αMG	91	-0.1395	0.1248	-0.0802	0.0653	0.0880	-200
αMG	219	-0.0841	0.0564	-0.0519	0.0466	0.0443	-77
sMG	2	-0.7259	0.7571	-0.5456	0.5414	0.3210	-1,072
sMG	4	-0.5691	0.8779	-0.4306	0.3926	0.3548	-1,166
sMG	6	-0.5895	0.8336	-0.4342	0.3955	0.3583	-1,127
sMG	13	-0.3533	0.5960	-0.2423	0.1977	0.2675	-844
sMG	27	-0.0586	0.2859	-0.0503	0.0322	0.0810	-539
sMG	43	-0.0593	0.3141	-0.0455	0.0226	0.0922	-512
sMG	59	-0.1497	0.3664	-0.1140	0.0955	0.1176	-583
sMG	91	-0.0216	0.1772	-0.0139	0.0000	0.0479	-325
sMG	219	-0.2362	0.3101	-0.1730	0.1651	0.1204	-388

Table 4.3: Relative errors for the C5G$^{\infty}$ problem compared to the reference Wynn-epsilon-accelerated FEDS solutions. The first five errors are pin powers, the latter three of which are sums over pins within an assembly.

Method	RRR DOF	Max Pin (%)	Min Pin (%)	Inner UO_2 (%)	MOX (%)	Outer UO_2 (%)	k_{eff} (pcm)
FEDS	2	-0.6406	0.7015	-0.4892	0.4846	0.2809	-1,112
FEDS	4	0.0914	-0.8158	0.0565	0.0179	-0.2588	568
FEDS	6	0.1897	-0.4335	0.1515	-0.1399	-0.1280	298
FEDS	13	-0.0136	-0.2041	-0.0149	0.0380	-0.0674	92
FEDS	27	-0.0183	-0.0833	-0.0169	0.0280	-0.0301	42
FEDS	43	0.0178	-0.0994	0.0181	-0.0142	-0.0301	82
FEDS	59	-0.0085	-0.0310	-0.0046	0.0059	-0.0083	19
FEDS	91	-0.0018	0.0133	-0.0030	0.0001	0.0022	-25
FEDS	219	0.0076	0.0173	0.0030	-0.0061	-0.0006	-18
αMG	2	-0.6406	0.7015	-0.4892	0.4846	0.2809	-1,112
αMG	4	-0.4042	0.7981	-0.3091	0.2625	0.3027	-1,179
αMG	6	-0.4046	0.8383	-0.3145	0.2673	0.3076	-1,211
αMG	13	-0.5380	0.7981	-0.4203	0.3964	0.2992	-1,192
αMG	27	-0.2138	0.2708	-0.1654	0.1618	0.0958	-532
αMG	43	-0.1635	-0.0069	-0.1101	0.1191	0.0276	-183
αMG	59	-0.1308	0.1662	-0.0903	0.0851	0.0578	-392
αMG	91	-0.0538	0.0696	-0.0235	0.0088	0.0480	-240
αMG	219	0.0017	0.0012	0.0048	-0.0099	0.0043	-117
sMG	2	-0.6406	0.7015	-0.4892	0.4846	0.2809	-1,112
sMG	4	-0.4837	0.8222	-0.3741	0.3359	0.3146	-1,205
sMG	6	-0.5041	0.7780	-0.3777	0.3388	0.3182	-1,166
sMG	13	-0.2677	0.5405	-0.1857	0.1412	0.2274	-883
sMG	27	0.0273	0.2306	0.0064	-0.0243	0.0409	-578
sMG	43	0.0265	0.2588	0.0113	-0.0339	0.0522	-551
sMG	59	-0.0640	0.3111	-0.0573	0.0390	0.0775	-622
sMG	91	0.0643	0.1219	0.0429	-0.0565	0.0079	-364
sMG	219	-0.1505	0.2547	-0.1163	0.1086	0.0803	-427
MG ref.	1499	0.0859	-0.0552	0.0568	-0.0565	-0.0400	-40

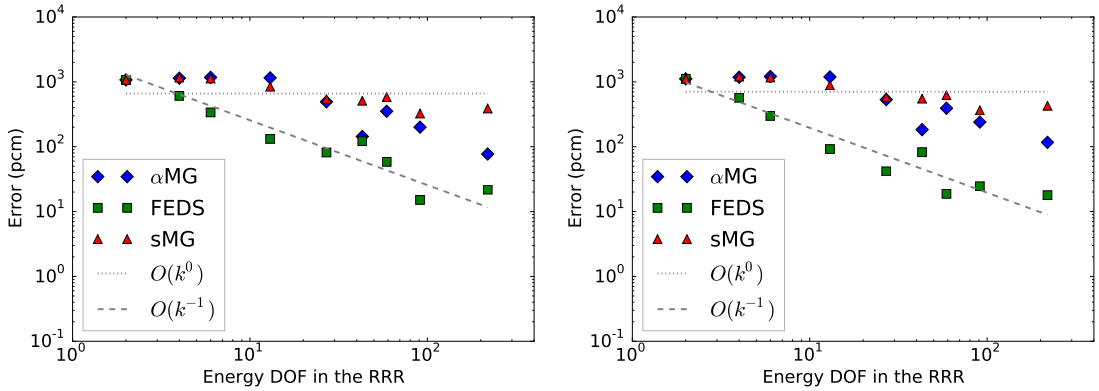

(a) MG reference

(b) FEDS reference

Figure 4.7: Criticality eigenvalue error for different energy discretization methods as a function of energy element number for the C5G$^\infty$ problem

5. A MODEL NEUTRON TIME-OF-FLIGHT PROBLEM

5.1 Problem Overview

In this section, we test the applicability of FEDS to a new type of neutronics problem, one that involves time dependence. In this problem, we pulse a fission source that is surrounded by a material with resonances and simulate a detector at various distances from the material. We record the energy-integrated detector response as a function of time. Neutrons travel at a speed that is a direct function of their energy. The time at which a neutron arrives at the detector is a direct function of its energy, and accurate detector responses requires accurate treatment of all neutron velocities. Because FEDS naturally defines energy elements with highly disparate subelement energies, unoptimized FEDS would yield inaccurate detector responses. We make FEDS competitive to standard MG by imposing coarse groups.

The main result of this section is that FEDS with coarse groups is a viable candidate for such time-of-flight (TOF) problems. Standard MG that uses groups equally spaced in lethargy does well at simulating the detector response but poorly at other relevant quantities of interest (QOI), such as absorption fraction in the material or in the cumulative detector response. FEDS is formulated with a knob to adjust the average number of energy elements per coarse group. For a fixed total number of energy unknowns, using few energy elements per coarse group means many coarse groups are used and FEDS acts similarly to standard MG. When many energy elements per coarse group are used and the total unknown count fixed, FEDS does worse at simulating detector response but better at simulating absorption fractions. Both effects are found to be first-order, meaning FEDS can be tuned to do well at a desired error. For sufficient energy resolution, FEDS can beat standard MG on

both detector response and absorption fraction for a fixed energy unknown count. Adaptive MG is also investigated, but behaves to within a factor of 2 of standard MG.

5.2 Problem Description

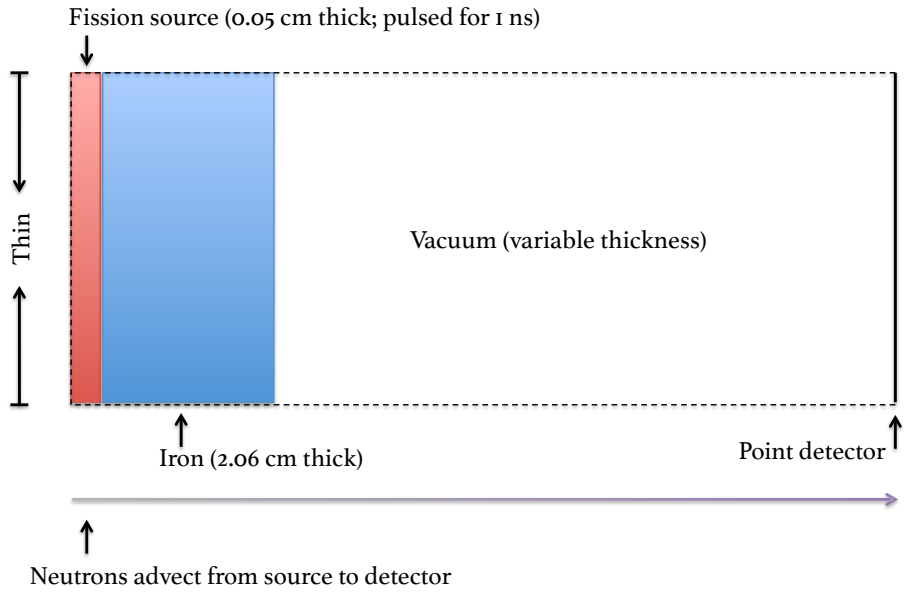

Figure 5.1: Layout of the neutron time-of-flight model problem. Neutrons are generated in the source and stream toward the point detector, where they are tallied as a function of time. Perfect collimation and a small detector are assumed.

Figure 5.1 gives the physical layout for the TOF problem. Neutrons are born in the left (fission source region) with a Watt fission spectrum in energy, isotropic distribution in direction, and uniform distribution in space and time. The source is pulsed and turns off at 1 ns. Perfect collimation and a small detector imply only uncollided neutrons traveling in direction $\mathbf{\Omega} = +\hat{x}$ reach the detector on the right. For this reason, angular versus scalar sources, fluxes, and reaction rates are used

interchangeably for the remainder of the section. We focus on the energies from 50 keV to 10 MeV, ignoring the small source contributions outside this range.

A solution analytic in space and time exists for this problem. The derivation is performed in Appendix G. This solution assumes neutrons are quantized such that every neutron energy has a uniquely associated total cross section and speed, but there are a finite number of allowable total cross sections and speeds. The differential angular flux solution is a pulse that advects in space-time from the source to the detector at its neutrons' associated speed, interacting with its neutrons' associated total cross section. Each pulse has a finite width in space/time determined by the finite extent of the source in space and time. The analytic solution is integrated over the set of energies that share the same speed and total cross section, as these neutrons advect identically. This set of neutrons has an effective source strength equal to the integral of the fission spectrum over its set of energies.

The reference solution uses a hyperfine MG group structure that resolves both the iron macroscopic total cross section and the neutron speeds for the detector distances of interest. As the point detector is moved farther from the source, the time between the fastest neutrons reaching the detector to the slowest neutrons reaching the detector increases, but the pulse width in space/time of each group remains constant. This causes less overlap among groups, forcing the use of smaller groups to maintain fidelity. The groups must be shrunk in energy width and cross section difference. For a given detector distance, the required energy fidelity may be determined using a resolution study in energy. More information on this study is provided in the accompanying appendix, Appendix E.

Different energy discretizations are compared against the reference solution. These discretizations, listed in Table 2.1, include standard MG, which defines groups as equally spaced in lethargy, an adaptive MG that puts more groups where the total

cross section has higher variance, and FEDS that is like the adaptive MG but is not forced to use contiguous energy elements. The infinite-medium flux in and the total cross section of iron were used as spectra when generating the energy meshes. It was discovered early on that groups or elements that included disparate energies would advect improperly, effecting error.

Attaining fidelity for this TOF problem required bounding the maximum group (MG) or element (FEDS) thickness in energy. This was automatically satisfied for standard MG. For adaptive MG and FEDS, this was solved by first imposing an equally-spaced lethargy mesh of coarse groups and then splitting the coarse groups into fine groups or energy elements, where the number of fine groups / energy elements per coarse group was determined automatically based on the variance of the total cross section within a coarse group.

This two-step process adds a knob: the ratio between the total number of energy degrees of freedom (DOF) and the number of coarse groups. If the ratio is one, the scheme reduces to standard MG. For a fixed total number of energy DOF, a large ratio means better cross section fidelity, but worse speed fidelity. Alternatively, one could imagine figuring out the required speed fidelity for a problem of interest and then increasing the total energy DOF until sufficient cross section fidelity is acquired. The first idea introduces the idea of maximizing fidelity by balancing different sources of error for given a fixed computational cost. The second introduces the idea of increasing computational cost to meet a desired fidelity. Either may be valid. This study looks at errors in QOI as the total number of energy unknowns (DOF) are increased for several ratios of energy DOF to coarse groups for both adaptive MG and FEDS methods within a coarse group.

The quantities of interest (QOIs) involve neutron reaction rates in the iron and at the detector. All QOIs are integrated over all energies (and are for the $\mathbf{\Omega} = \hat{x}$

direction). The first QOI, that of absorption fraction in the iron, is the space- and time-integrated total reaction rate in the iron, which represents total absorption in the iron. The third QOI, called detector response, is the time-binned total reaction rate at the point detector. This QOI uses a flat detector response, meaning the detector cross section is constant in energy. The second QOI, called cumulative detector response, is the cumulative sum in time of the third, that is, the sum of the detector response from time 0 to the end of the time bin for each bin. QOI errors for the latter two QOI are L^2 norms over the vector of time bins. Errors in the first QOI are typically smaller than errors in the second, which are themselves typically smaller than errors in the third. Different time bin sizes are investigated. Larger time bins allow for more within-bin error cancellation.

The error in the first QOI describes how well the total cross section is discretized. The exact expression for the first QOI is $\int_0^\infty \mathrm{d}E\; q(E)(1 - e^{-\Sigma_{t,\mathrm{iron}}(E)X})$, where $q(E)$ is the Watt fission spectrum and X is the thickness of the iron. The exact QOI does not depend on details of the speed discretization for the neutrons, but depends strongly on capturing the integral effect of the total cross section.

If the flux for the reference solution integrated in energy and binned over time bin b is r_b, and that of the FEDS or MG flux is m_b, then the detector response and

cumulative detector response errors are

$$e_{\text{det.}} = \lambda \sqrt{\frac{\sum_b \left| r_b - m_b \right|^2}{\sum_b \left| r_b \right|^2}}, \tag{5.1a}$$

$$e_{\text{cumul det.}} = \lambda \sqrt{\frac{\sum_b \left| \sum_{b' \leq b} (r_{b'} - m_{b'}) \right|^2}{\sum_b \left| \sum_{b' \leq b} r_{b'} \right|^2}}, \tag{5.1b}$$

$$\lambda \equiv \sum_b r_b, \tag{5.1c}$$

where λ represents the total transmission through the iron, and is approximately 0.58 for this problem. The detector response errors are multiplied by λ to normalize them per source particle.

In addition to total cross section fidelity, the error in the third QOI describes how well neutron speed is discretized. The L^2 error over time bins means that a neutron traveling at a sufficiently wrong speed will appear in the wrong time bin(s). This induces error both in the time bin(s) where it should have been and the time bin(s) where it scored. Another source of error in this QOI comes from errors in transmission from the iron, transmission being proportional to $q(E)e^{-\Sigma_{t,\text{iron}}(E)X}$. Physically, errors in this QOI represent neutrons imparting energy (heat) and momentum differentially at the wrong time, a property to which a set of coupled physics may be sensitive.

The error in the second QOI is similar to the third, except it has a different sensitivity to arrival times. Comparing cumulative reaction rates means neutrons that travel at the wrong speed and score to the wrong bin(s) will induce errors in all bins between the correct bin(s) and the scored bin(s). For large time bins or small errors in speed (and negligible error in transmission), only one bin will add error to this QOI, as opposed to both bins for the third QOI. Physically, errors in this

QOI represent neutrons imparting wrong integral amounts of energy and momentum, integral in the sense of $\int_0^t \mathrm{d}t'\ R(t')$, a property to which a potentially different set of coupled physics may be sensitive.

This problem setup is more difficult than the real time-of-flight experiments. No scattering means pulses are thinner than they would be realistically. Perfect collimation means only one angle makes it from the source to the detector. If an S_n calculation were performed for the experimental setup, there would be many angles within the solid angle of the detector, meaning each group would have multiple, smaller pulses. Approximate advection would add additional smoothing of pulses and hence detector response. Taking these real phenomena would smear the detector response curve in time, reducing error 3, probably substantially. Another way to think of error 3 is the differential angular error for a larger problem with more angles.

5.3 Solutions

5.3.1 The iron cross section and its impact on the source

Figure 5.2 shows sources, cross sections, and spectra for the TOF problem. The first (a) is the fission source, restricted to the energies of interest (50 keV – 10 MeV). The second (b) is the elemental iron total cross section. The third (c) is the absorption rate in the iron integrated over all times. The fourth (d) is the flux transmitted through the iron integrated over all times. This is the same flux seen by the detector.

Figure 5.2 shows three energy scales: the coarse scale of the fission source, $\chi(E)$; the fine scale of the fine resonances in the cross sections of the iron, and an intermediate scale of more slowly-varying resonance-like cross sections in the iron.

In future figures, the abscissa changes from neutron energy to detector time. The

two are related by $t \propto E^{-1/2}$, which flips and stretches the x-axis.

5.3.2 Detector responses for high DOF count in energy

What follows are a series of detector responses for our TOF problem. The detector response is the energy- and time-integrated signal at a point detector downstream of the fission source. Time integration is performed within a time bin at the location of the detector.

A caption of "1 m, 1600 elements, $r = 2$, FEDS" indicates that the point detector was 1 m away from the right edge of the iron and the solution came from a FEDS structure with 1600 total energy unknowns and a ratio (of total energy unknowns to number of coarse groups) of 2, meaning 800 coarse groups were used. For all problems, the solution is the uncollided flux only, and no scattering fill-in is taken into account.

Figure 5.3 shows that increasing detector distances increases intermediate structure in the detector response. At short distances, the pulses for individual groups overlap due to the finite size and time of the source. The first row of Fig. 5.3 is the detector response without iron at 12.06 cm from the right edge of the source (2.06 cm to leave space for the later addition of the iron, and 10 cm from the right edge of the to-be-inserted iron). The second row is the same response with the iron inserted. The third row is the response for a detector 1 m away from the right edge of the iron.

Figure 5.4 shows the detector response for various group structure definitions (cf.Table 2.1). Standard equal-lethargy spacing (sMG, top row) maximally captures intermediate-scale behavior. FEDS (bottom rows) uses discontiguous energy elements that maximally resolve resonance behavior while simultaneously restricting the energy elements in energy space using a set of coarse groups that limit the ratio

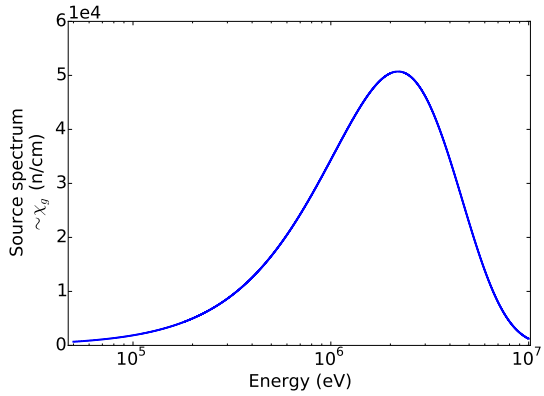

(a) Fission source

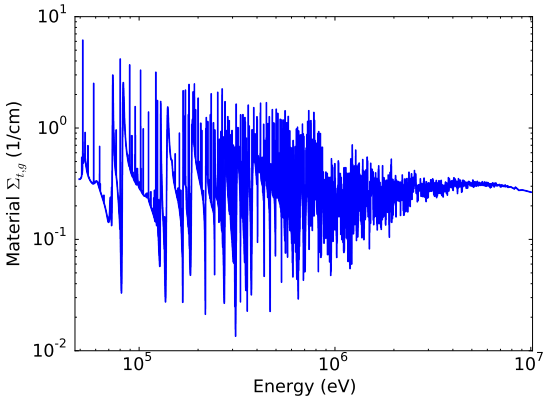

(b) Iron cross section

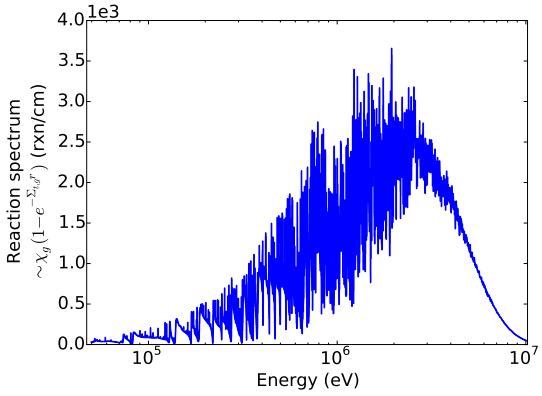

(c) Absorption in iron

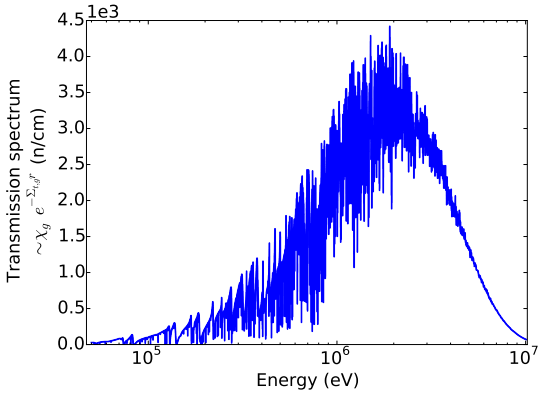

(d) Transmission through iron

Figure 5.2: Group-integrated fission source, total iron cross section, and group-integrated absorption and transmission as a function of energy for the TOF problem.

of the maximum to minimum energies represented within an energy element. The middle row uses a ratio of 2 and the bottom row a ratio of 4, with larger ratios meaning fewer coarse groups and often less accuracy in the detector response.

For a given number of degrees of freedom (DOF) in energy, the latter two rows / group structures spend more DOF getting the individual resonances correct. This means they have fewer DOF to spend on energy intervals that do not contain resonances. For the detector distances used, the pulses for individual resonances overlap. This leads to the following situation: some time bins will have contributions from many energy groups/elements, while others will have contributions from few or no energy groups/elements. This is what causes the spiky behavior in the bottom row of Fig. 5.4 that is not present in the top rows. For the top row, the sMG group structure essentially minimizes the maximum velocity spread within a group. This leads to a more uniform number of groups contributing to each time bin in the detector, meaning the top row has the most correct shape.

However, the top row (sMG) does not have the most correct magnitudes. Although sMG does well at resolving the intermediate energy scale, it does not resolve the finest (small resonance) energy scale. We do not expect sMG to do proper self-shielding for the fine resonances within each group, meaning the sMG transmission will not be correct until the group sizes are sufficiently small to resolve all fine resonances.

Figure 5.5 shows the effects of using a shorter detector distance. These figures add adaptive MG (middle row), which uses contiguous groups that maximally resolve fine-scale (resonance) behavior in addition to a base coarse group structure that resolves speeds.The first effect of using a shorter detector distance is that errors in group speed have smaller (absolute) effect on time-to-detector. The shorter distance implies a lower group dispersion, causing pulses of more groups to overlap in each

detector time bin. This smooths the detector response in time and results in αMG and FEDS (bottom rows) having more correct detector response shapes than in Fig. 5.4. At long times, errors are visible for αMG and FEDS that show up as noise in the detector response.

Alternatively, the same effect can be achieved at larger detector distances using coarser time bins. Figure 5.6 shows the same detector distance as Fig. 5.4 but a factor of 200 fewer time bins. Aside from late time bins where the flux is small, all three group structures (sMG, αMG, FEDS) agree to eye norm.

5.3.3 Detector responses for energy DOF counts in energy

Figure 5.7 shows the detector response for a large distance and fewer numbers of groups. All methods yield a poor differential detector response at this distance with this energy resolution. Far detector distance and fine time binning allow for the resolution of pulses for individual groups/elements. Notice that the ordinate limits on Fig. 5.7 (c,e) are expanded. As energy unknowns are added, detector response improves.

Figure 5.8 is the same as Fig. 5.7, except it uses a shorter detector distance. This yields substantially improved differential detector response.

Figure 5.9 is the same as Fig. 5.8, except with fixed group count and varying ratios of total energy unknowns to coarse groups. As fewer coarse groups are used, both methods develop worse differential detector response. For αMG, adding fine groups on top of the coarse groups improves speed fidelity in those coarse groups. This is not the case for FEDS (cf. Fig. 5.9 (f)). Notice that the ordinate limits on Fig. 5.9 (f) are expanded.

Figure 5.10 shows example energy meshes used for αMG and FEDS. For FEDS, the coarse groups discretize in energy while the elements within a coarse group dis-

cretize in cross section / flux.

Further figures are given in Appendix E.

5.4 Quantitative Comparisons to a Reference Solution

Tables 5.1 – 5.6 give selected results for errors in the three QOI compared to a finely resolved reference solution for sMG, αMG, and FEDS for various cases and ratios. A case has a unique distance to the detector, number of time bins, and number of total energy DOF. Ratios, r, are the number of total energy DOF divided by the number of coarse groups. The lowest errors for sMG, αMG, and FEDS for each case are in green, red, and blue, respectively. A fixed grid of ratios were investigated, though any ratio larger than unity is valid (a ratio of unity being by definition sMG). Further results are given in Appendix E.

The data have several interesting trends. sMG yields the lowest detector response errors (error 3) in cases with high bin counts and distances. For intermediate distances and/or low bin counts, where the error is around a few times 10^{-3}, FEDS can out-perform sMG for the detector response error, which was not expected, and is attributed to FEDS being more accurate in the transmission spectrum. FEDS and αMG yield lower absorption and cumulative detector response errors (errors 1 and 2) than sMG. While holding the total number of energy unknowns fixed, increasing the ratio generally decreases the absorption and cumulative detector response errors but increases the detector response error. FEDS can have a factor of 10 smaller error 1 and factor of 2-8 smaller error 2 than sMG for a fixed total number of energy DOF. αMG has a factor of 1.5 or less smaller error for errors 1 and 2 than sMG for a fixed total energy DOF. Increasing the total energy DOF while keeping a fixed ratio decreases all errors for all problems, including absorption fraction error for FEDS.

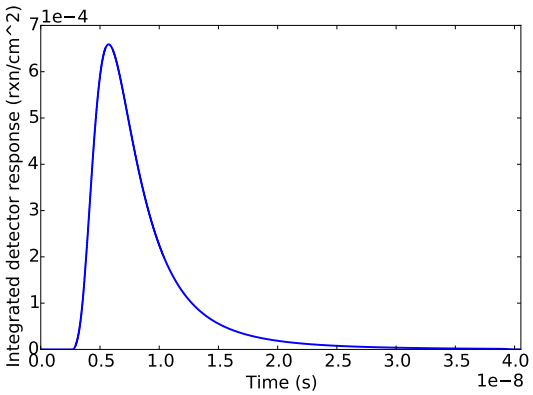

(a) 10 cm, 14,500 groups, no iron

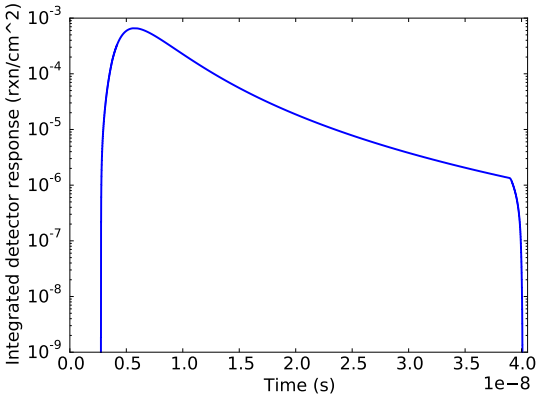

(b) 10 cm, 14,500 groups, no iron

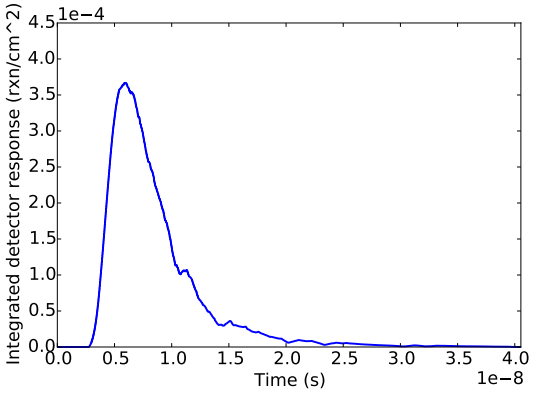

(c) 10 cm, 14,500 groups

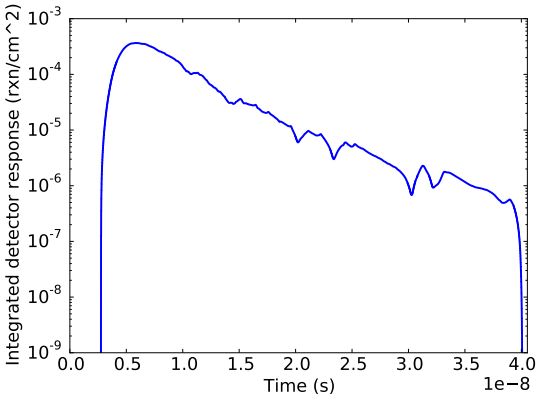

(d) 10 cm, 14,500 groups

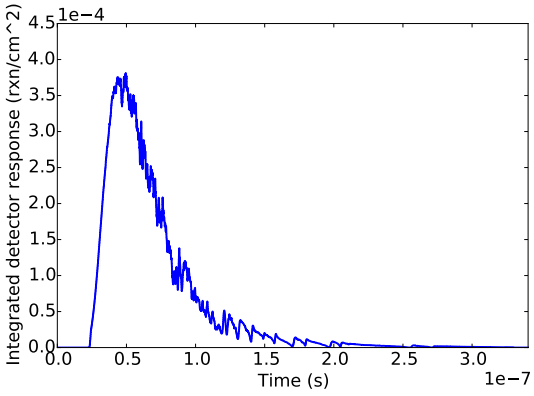

(e) 1 m, 14,500 groups

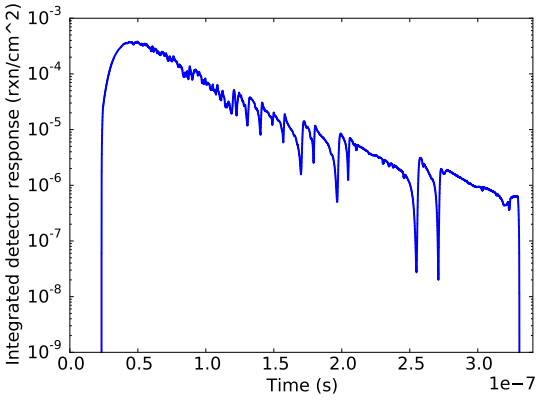

(f) 1 m, 14,500 groups

Figure 5.3: Reference energy-integrated differential detector response plotted against detector time using 10,000 time bins for different detector distances. Left column is linear-linear (x-y). Right column is linear-log.

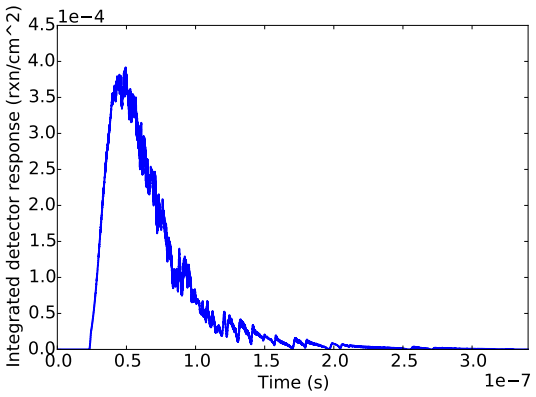

(a) 1 m, 1600 groups, sMG

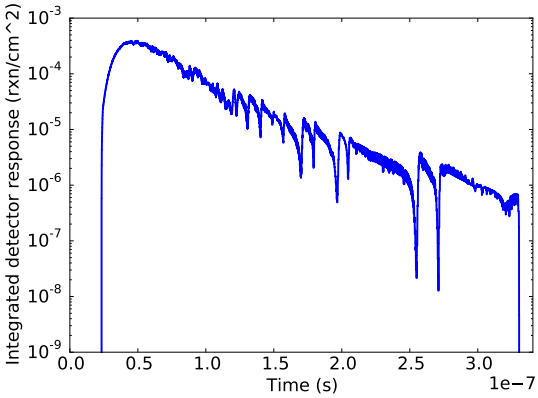

(b) 1 m, 1600 groups, sMG

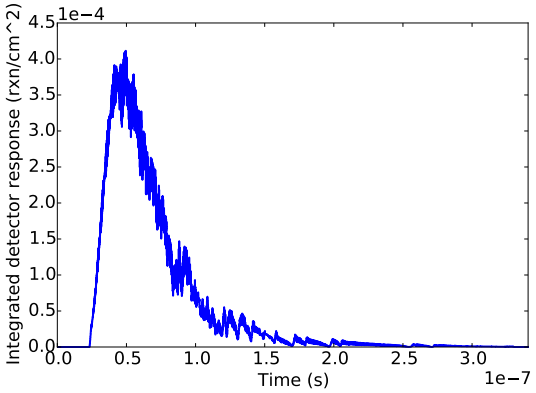

(c) 1 m, 1600 elements, $r = 2$, FEDS

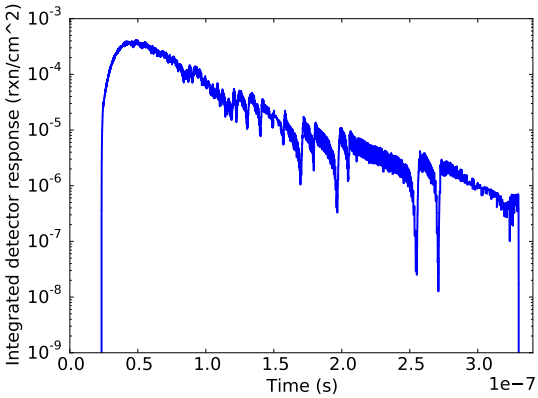

(d) 1 m, 1600 elements, $r = 2$, FEDS

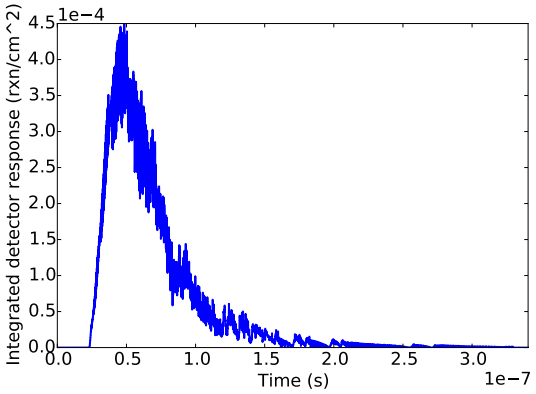

(e) 1 m, 1600 elements, $r = 4$, FEDS

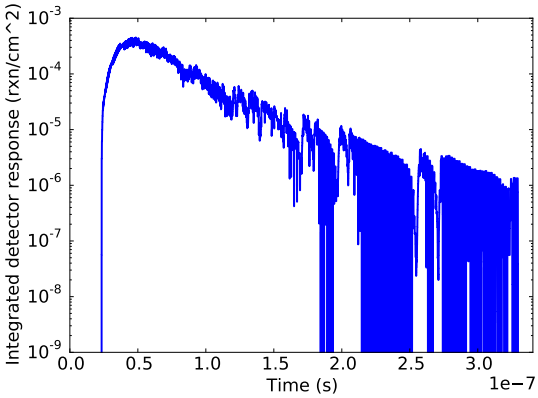

(f) 1 m, 1600 elements, $r = 4$, FEDS

Figure 5.4: Energy-integrated differential detector response plotted against detector time using 10,000 time bins at a detector distance of 1 m using 1600 unknowns in energy. Left column is linear-linear (x-y). Right column is linear-log.

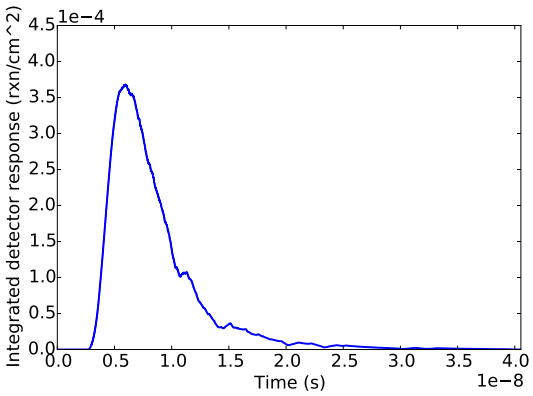

(a) 10 cm, 1600 groups, sMG

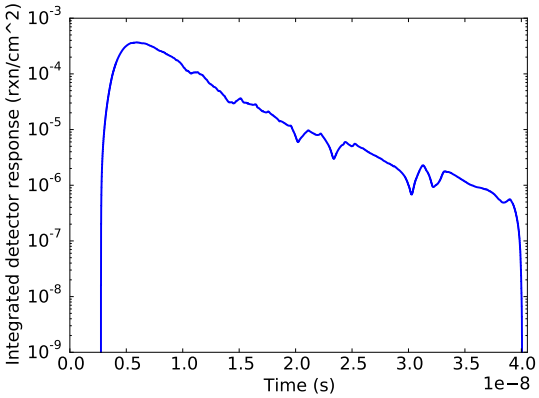

(b) 10 cm, 1600 groups, sMG

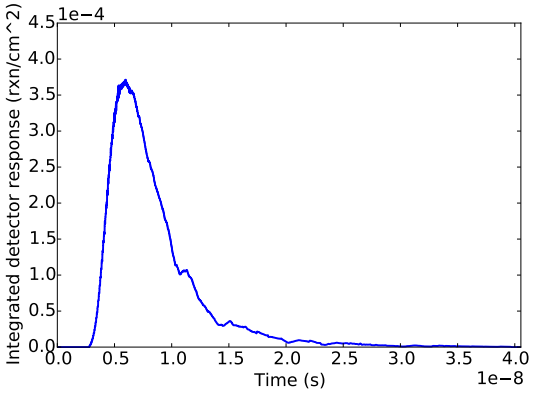

(c) 10 cm, 1600 groups, αMG

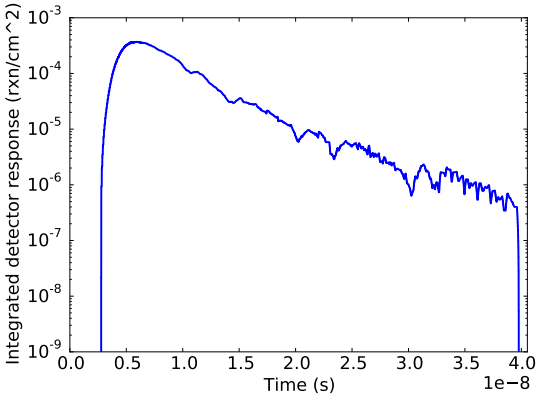

(d) 10 cm, 1600 groups, αMG

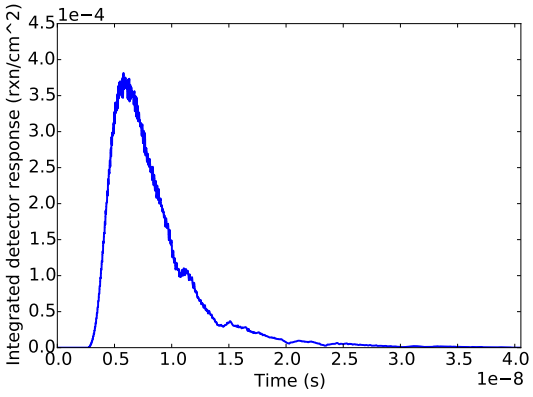

(e) 10 cm, 1600 elements, FEDS

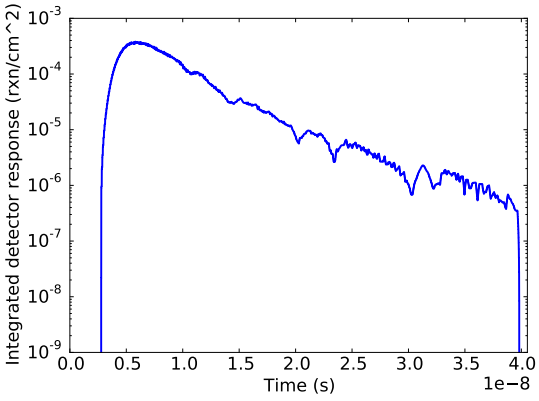

(f) 10 cm, 1600 elements, FEDS

Figure 5.5: Energy-integrated differential detector response plotted against detector time using 10,000 time bins at a detector distance of 10 cm with 1600 unknowns in energy. Left column is linear-linear (x-y). Right column is linear-log. A ratio of 10 was used for FEDS and αMG.

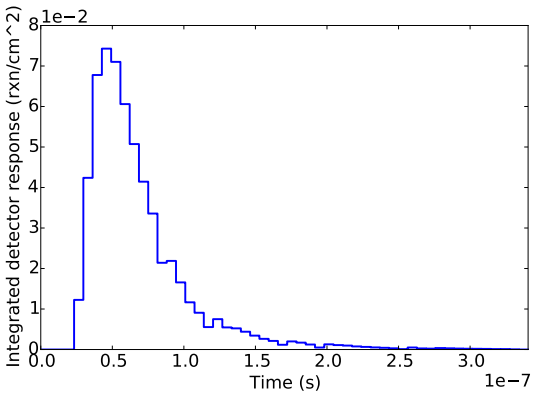

(a) 1 m, 1600 groups, sMG

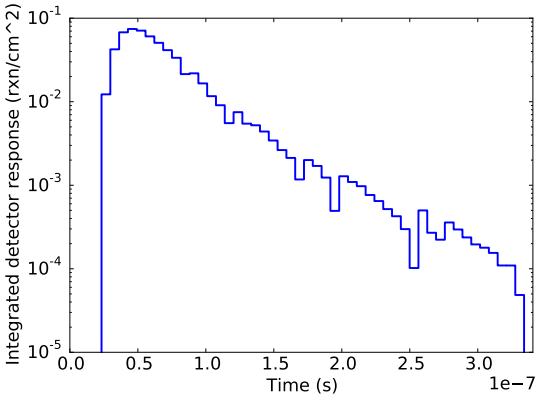

(b) 1 m, 1600 groups, sMG

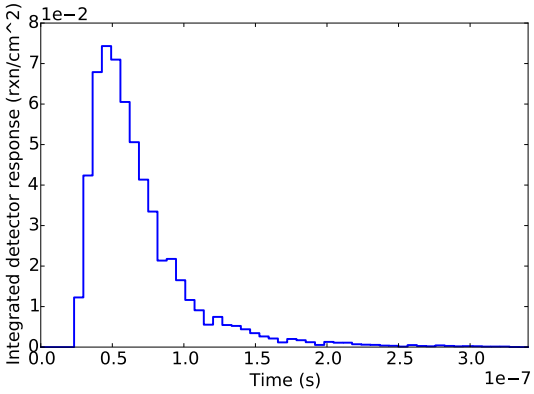

(c) 1 m, 1600 groups, αMG

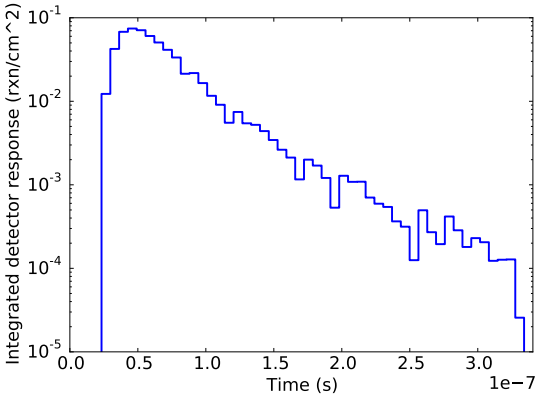

(d) 1 m, 1600 groups, αMG

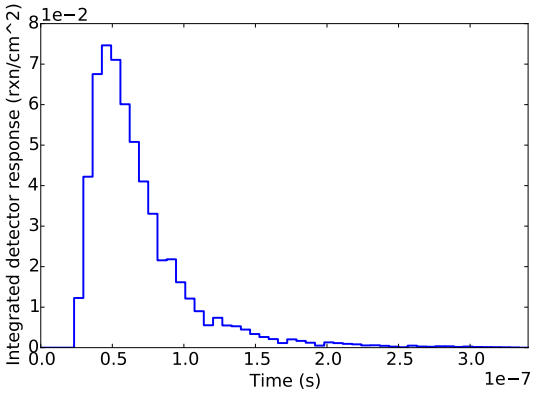

(e) 1 m, 1600 elements, FEDS

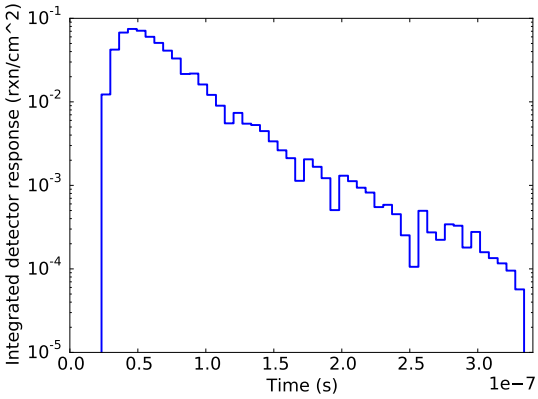

(f) 1 m, 1600 elements, FEDS

Figure 5.6: Energy-integrated differential detector response plotted against detector time using 50 time bins at a detector distance of 1 m using 1600 unknowns in energy. Left column is linear-linear (x-y). Right column is linear-log. A ratio of 10 was used for FEDS and αMG.

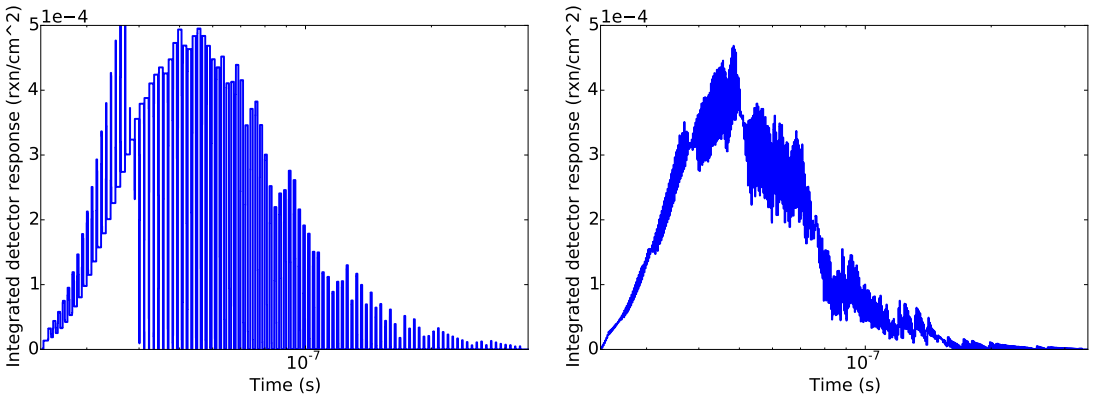

(a) 1 m, 100 groups, sMG

(b) 1 m, 400 groups, sMG

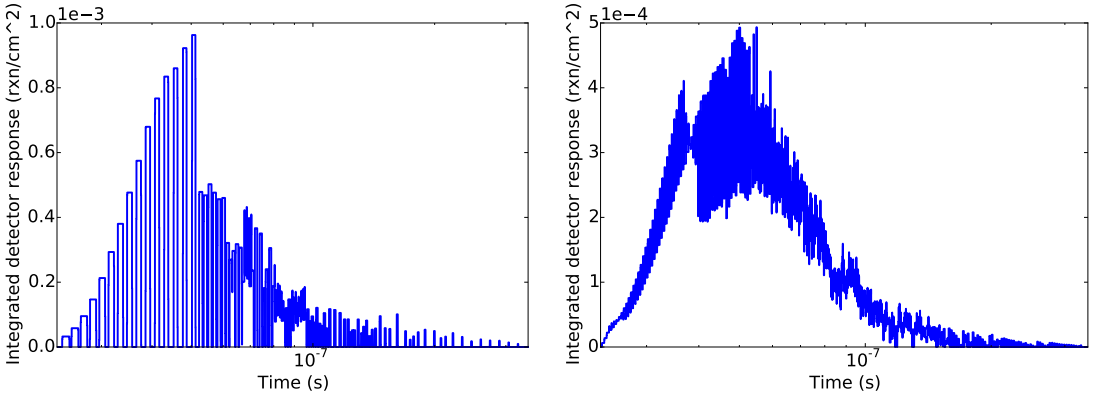

(c) 1 m, 100 groups, αMG

(d) 1 m, 400 groups, αMG

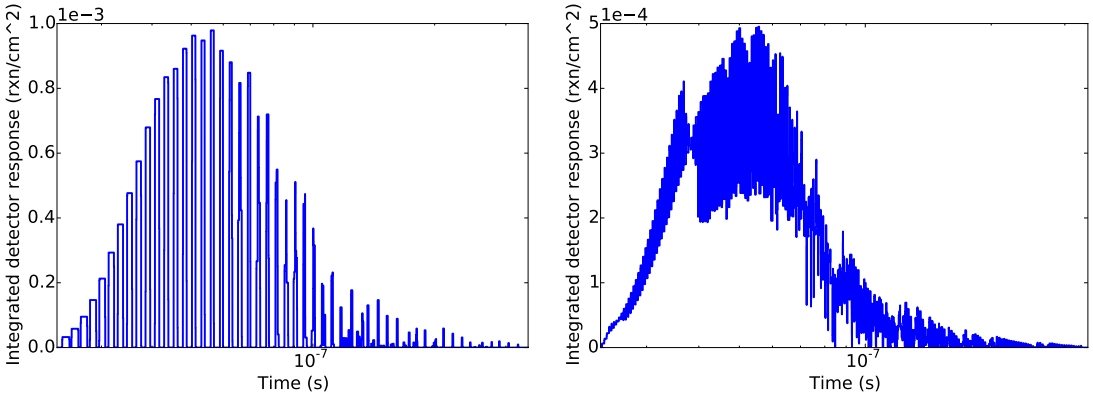

(e) 1 m, 100 elements, FEDS

(f) 1 m, 400 elements, FEDS

Figure 5.7: Energy-integrated differential detector response plotted against detector time using 10,000 time bins at 1 m using either 100 or 400 unknowns in energy. A log-linear scale was used. A ratio of 2 was used for FEDS and αMG.

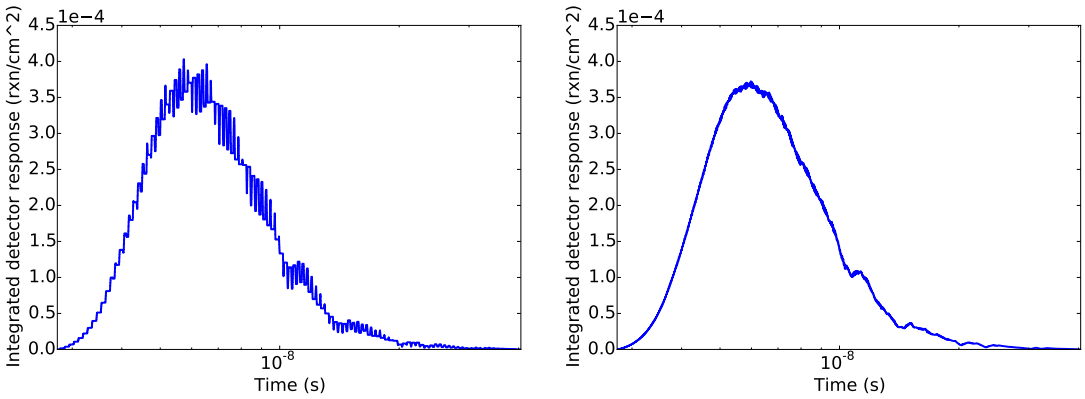

(a) 10 cm, 100 groups, sMG

(b) 10 cm, 400 groups, sMG

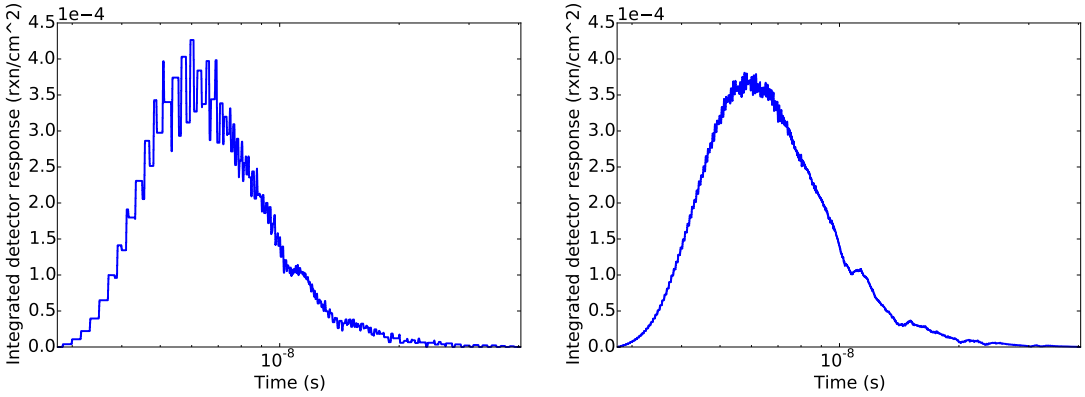

(c) 10 cm, 100 groups, αMG

(d) 10 cm, 400 groups, αMG

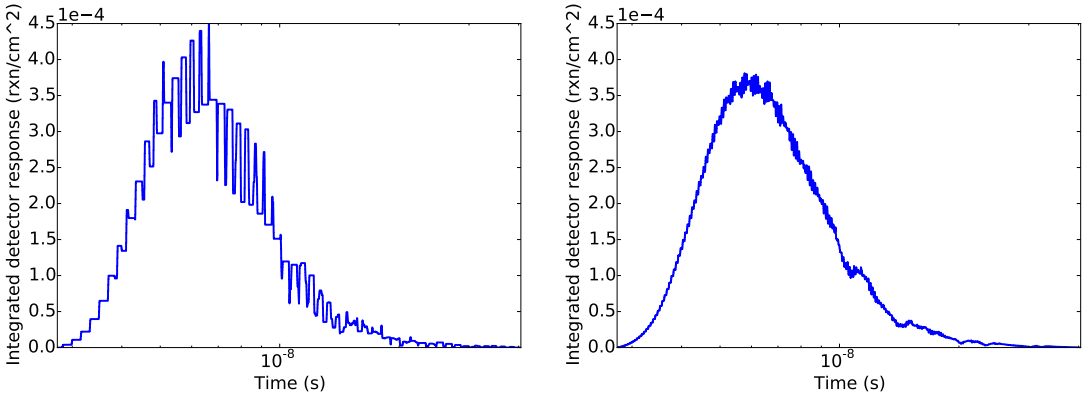

(e) 10 cm, 100 elements, FEDS

(f) 10 cm, 400 elements, FEDS

Figure 5.8: Energy-integrated differential detector response plotted against detector time using 10,000 time bins at 10 cm using either 100 or 400 unknowns in energy. A log-linear scale was used. A ratio of 2 was used for FEDS and αMG.

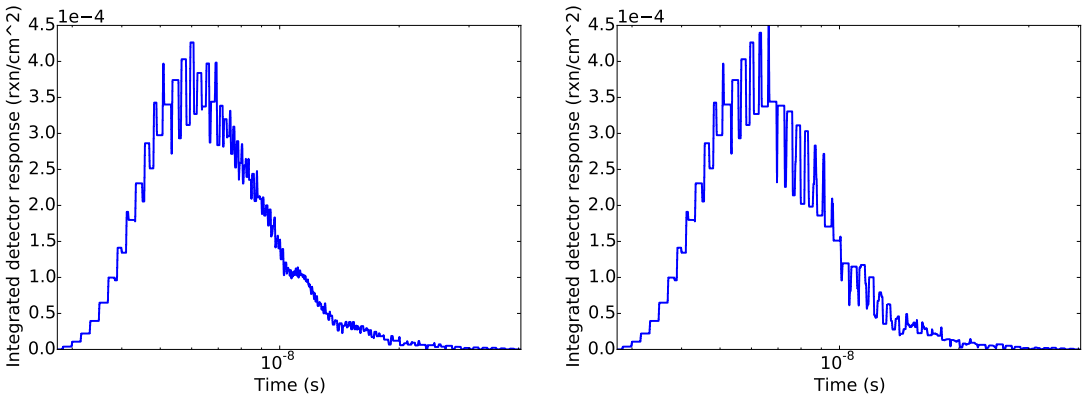

(a) 10 cm, 100 groups, $r = 2$, αMG

(b) 10 cm, 100 elements, $r = 2$, FEDS

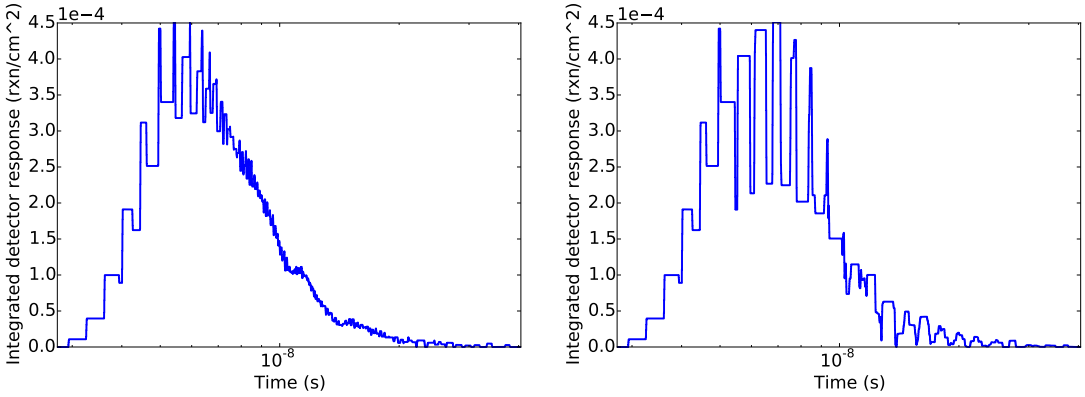

(c) 10 cm, 100 groups, $r = 4$, αMG

(d) 10 cm, 100 elements, $r = 4$, FEDS

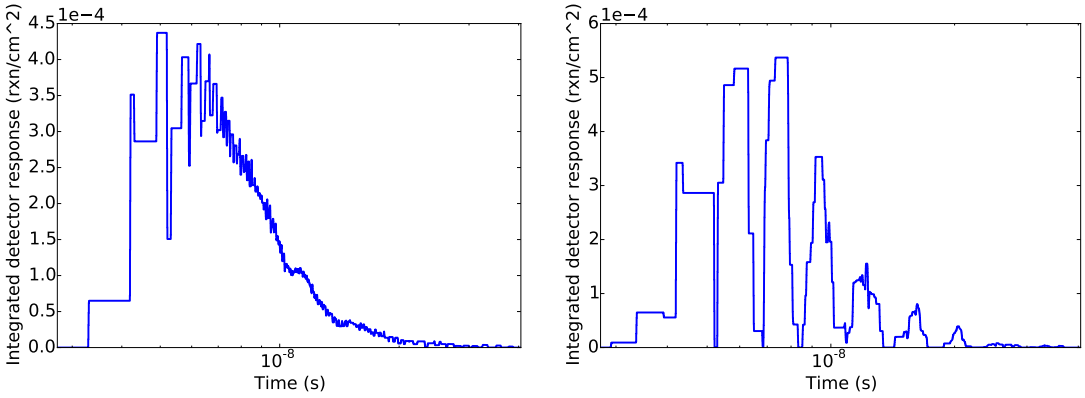

(e) 10 cm, 100 groups, $r = 10$, αMG

(f) 10 cm, 100 elements, $r = 10$, FEDS

Figure 5.9: Energy-integrated differential detector response plotted against detector time using 10,000 time bins at 10 cm using varying ratios and 100 energy unknowns. A log-linear scale was used.

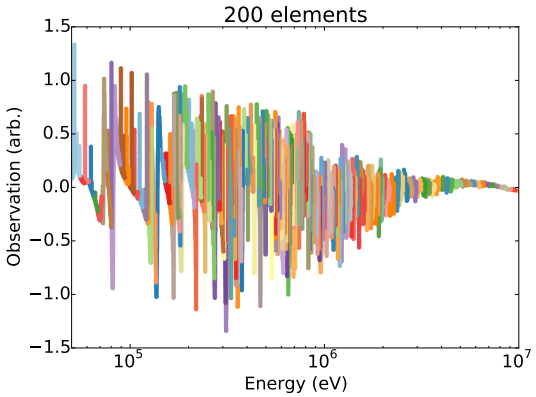

(a) 200 groups, $r = 2$, αMG

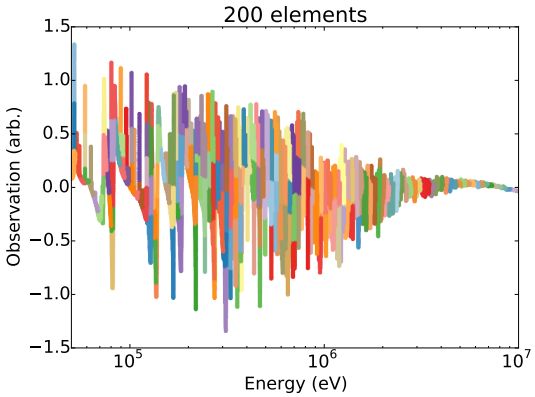

(b) 200 elements, $r = 2$, FEDS

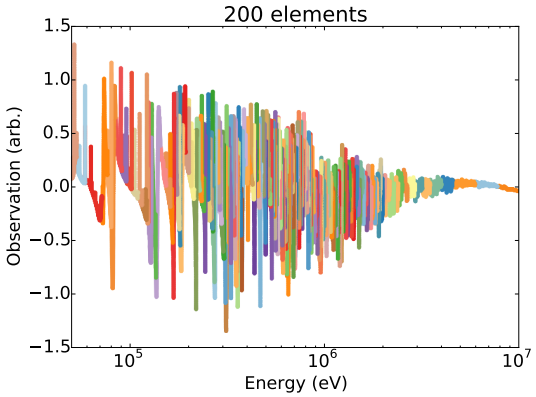

(c) 200 groups, $r = 10$, αMG

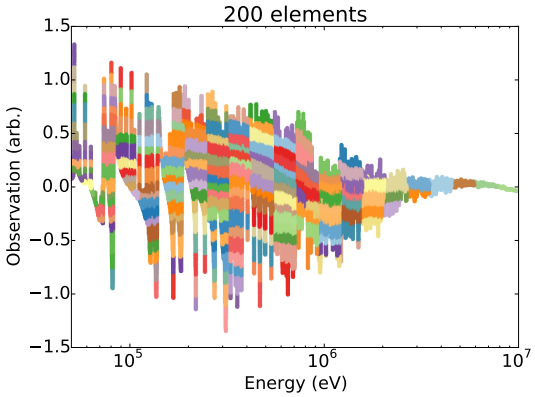

(d) 200 elements, $r = 10$, FEDS

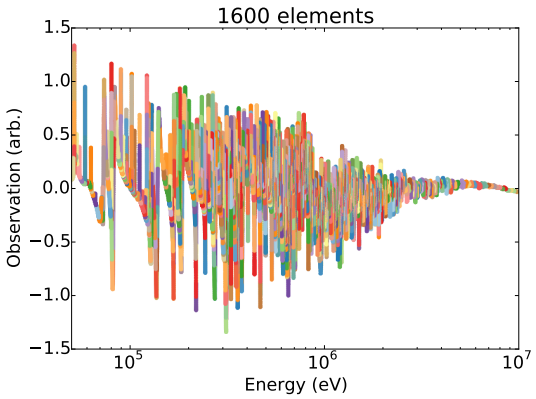

(e) 1600 groups, $r = 10$, αMG

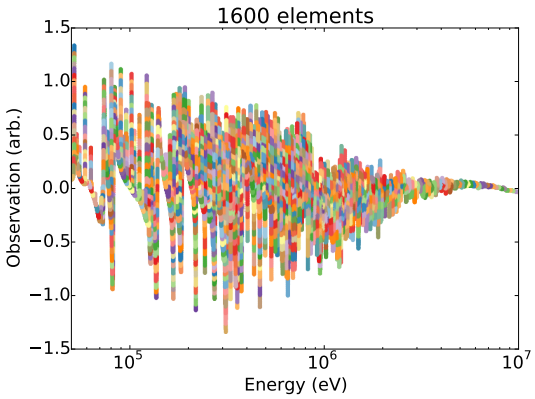

(f) 1600 elements, $r = 10$, FEDS

Figure 5.10: Energy element membership as a function of energy penalty. The plot is the total cross section of iron as a function of energy, colored so that each energy element has its own color.

5.5 Convergence Rates

There are two ways we studied to change resolution. In the first, the ratio was fixed and the total DOF was be increased.[1] In the second, the total number of energy DOF was fixed and the ratio was increased.[2] The rate of error reduction in general depends on which resolution pattern is used.

Figure 5.11 gives errors for the different methods as a function of total energy DOF for selected fixed ratios. For FEDS, ratios of 2 and 4 were chosen. Error values for other ratios may be found in tables in the appendices. There is no expectation of (first-order) convergence because the ratio for FEDS is fixed for each line. The plots show the effect of increasing groups while keeping the elements per group constant. The absolute errors and relative position of the lines are as important as the rates for these plots.

The top column of Fig. 5.11 is for the absorption error (error 1), which does not depend on the detector placement. Convergence rates are around $k^{1/2}$, where k is the total number of energy DOF. sMG does the worst for this QOI and FEDS with high ratio does the best. αMG is similar to sMG. Error magnitudes are small, below 1 %.

The second column of Fig. 5.11 is for the cumulative detector response error. It looks similar to the top absorption errors, with half-order convergence rates in total energy DOF.

The third column is for the detector response error. This error converges rapidly, between k^1 to $k^{3/2}$. Except at high unknown count, this error has the opposite ordering as the others, with sMG having the lowest error for a given unknown count. This is expected, as sMG uses all of its DOF to resolve the $1/v$ streaming to which

[1] This is equivalent to fixing the ratio and increasing the number of coarse groups.
[2] This is equivalent to fixing the total DOF and decreasing the number of coarse groups.

this QOI is sensitive, while FEDS and αMG also resolve the fine-scale solution behavior. Error magnitudes for this QOI may be large, above 10 %. This error is an upper-bound on expected advection error, because there is no error cancellation from numerical smoothing, scattering, or finite solid angle that would be present in a more realistic problem.

Figures 5.12 and 5.13 show the ratio of αMG or FEDS error to sMG for a fixed total energy DOF count but varying ratio (number of coarse groups) for several detector distances, numbers of time bins, and total energy DOF. Values above 1.0 mean αMG or FEDS does better than standard equally-lethargy-spaced MG. First-order and negative first-order fiducial lines of r^1 and r^{-1} are given.

The right column with FEDS shows expected behavior for the absorption error. Increasing the ratio (upping the elements per coarse group) decreases this error in a first-order manner, which shows up as a first-order increase in ratio of sMG error to FEDS error in Fig. 5.12. An accurate absorption QOI requires correct treatment of the total cross section, which occurs when more elements per coarse group are used.

Increasing the ratio is often found to increase the detector response error in a first-order manner, which was not expected, though seems reasonable. An accurate detector response requires accurate differential treatment of two components, that of particle advection (speed), and that of transmission fraction through the iron. Increasing the ratio decreases the number of coarse groups in a first-order manner, and it seems reasonable that coarse group width impacts advection fidelity in a first-order sense. The former component explains why decreasing coarse group count increases error relative to the sMG solution. The second component explains why, for high unknown count and/or low time bin count, the detector response error can decrease with increasing ratio for small ratios. In these cases, increased fidelity in the transmission fraction offsets decreased fidelity in the advection treatment. For

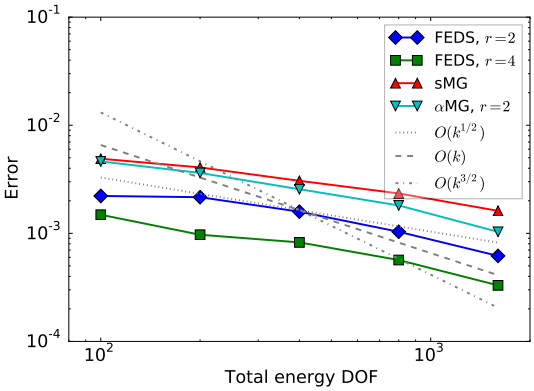

(a) Error 1 (abs.)

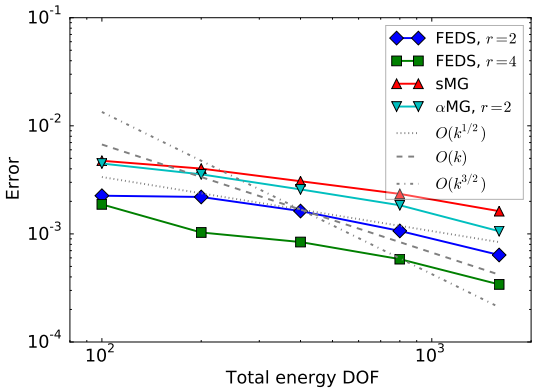

(b) Error 2 (cumul. det.), 10 cm

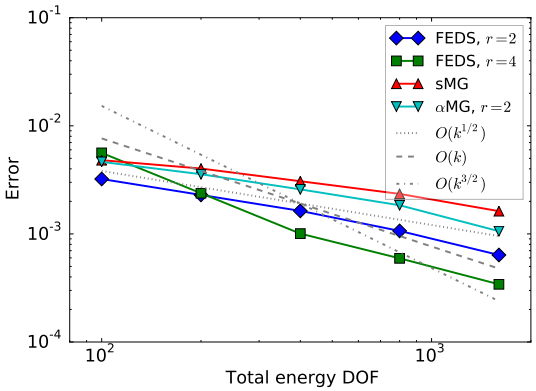

(c) Error 2 (cumul. det.), 1 m

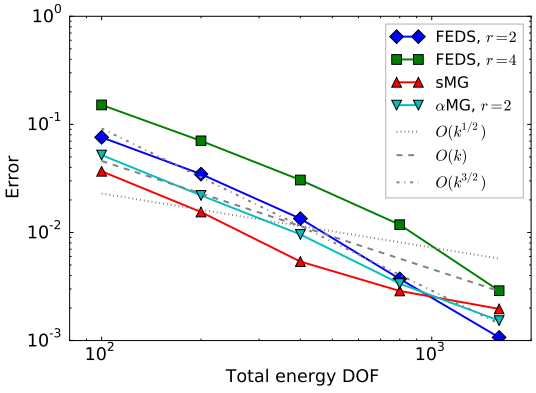

(d) Error 3 (det.), 10 cm

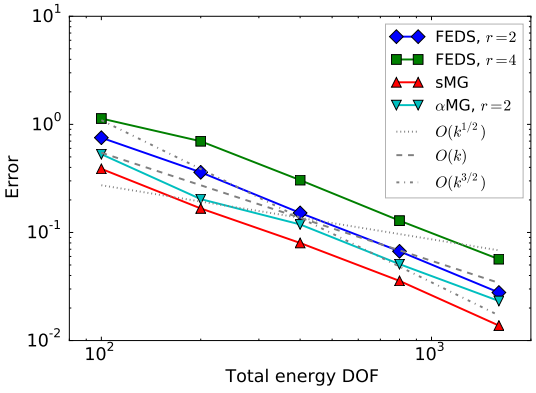

(e) Error 3 (det.), 1 m

Figure 5.11: Behavior of errors with fixed ratio and increasing total energy DOF for all errors at several distances and 10,000 time bins.

some 50 time bin cases, detector response error was seen to increase more rapidly than first-order. The cause may stem from decreased error cancellation within the thick time bins for reduced coarse group count.

Cumulative detector response seems to have the same two error components as detector response does. Treatment of transmission fraction through the iron is first-order in ratio while treatment of advection is negative first-order in ratio. The cumulative detector error tends to decrease (do better versus sMG) at first, then increase as advection errors begin to dominate, indicating that the cumulative detector response QOI is more sensitive to transmission treatment and less sensitive to advection treatment than the detector response QOI.

FEDS allows the user to tune the ratio to minimize the error of interest for a fixed cost, as measured in total energy DOF. If errors in absorption are more important, higher ratios should be used. If errors in differential detector response are more important, lower ratios should be used. αMG shows similar trends to FEDS, but at much lower rates, offering less error tradeoff ability than FEDS. αMG requires the group structure to be able to resolve the resonant spectral behavior within a fine group in order to decrease reaction error in that group. The numbers of fine groups per coarse group were insufficient to effect this. The absorption and cumulative detector errors for αMG were less than a factor of 2 smaller than the sMG errors, even at high ratios. Conversely, the detector response errors were up to a factor of 4 larger for αMG than for sMG for large ratios. αMG tends to do better with respect to sMG at high energy unknown counts, which are not shown here. These results show sMG to be superior to αMG for low energy unknown counts.

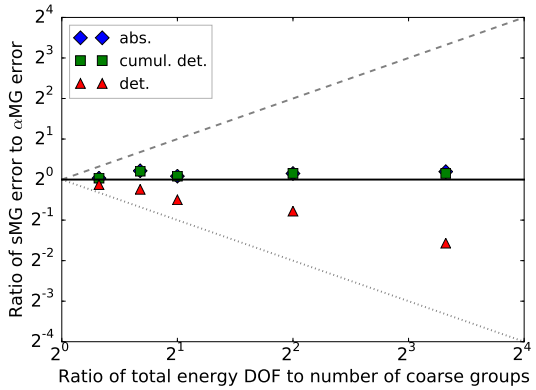

(a) αMG, 10 cm, 100 DOF

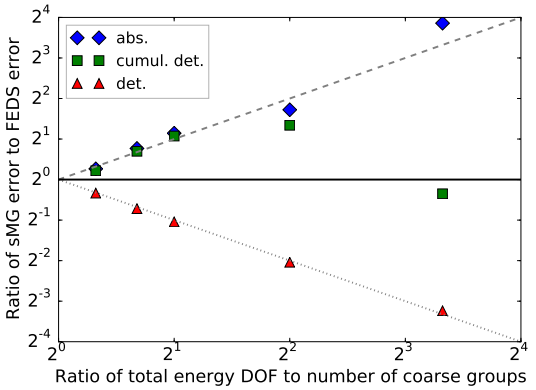

(b) FEDS, 10 cm, 100 DOF

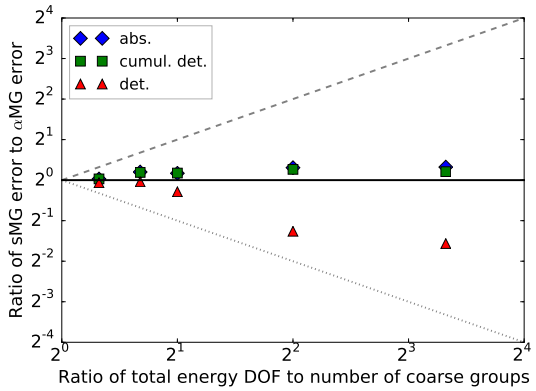

(c) αMG, 1 m, 200 DOF

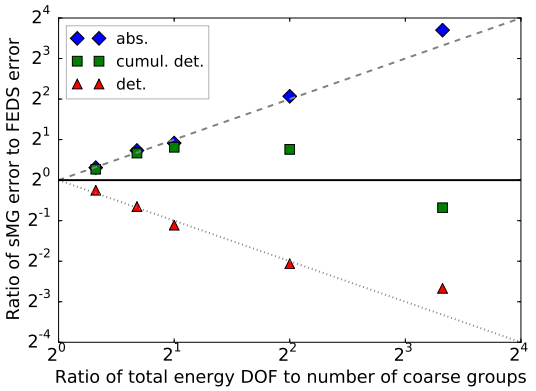

(d) FEDS, 1 m, 200 DOF

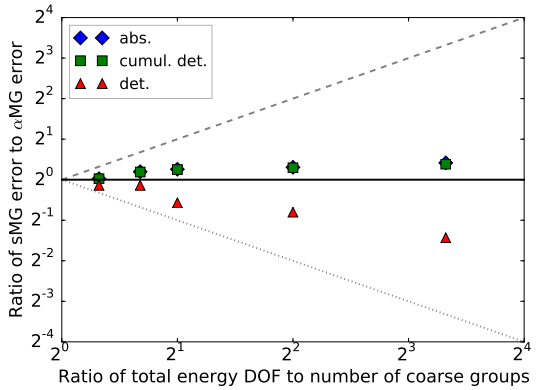

(e) αMG, 1 m, 400 DOF

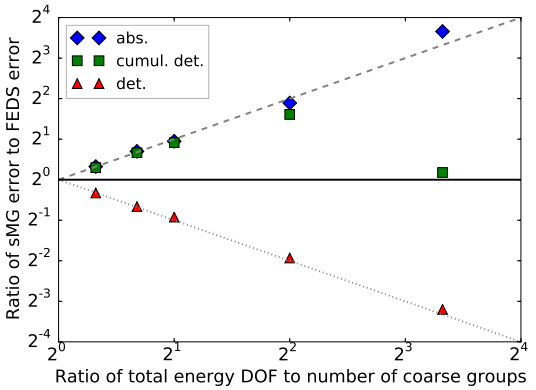

(f) FEDS, 1 m, 400 DOF

Figure 5.12: Behavior of errors with fixed total energy DOF and varying ratio for all errors and 10,000 time bins.

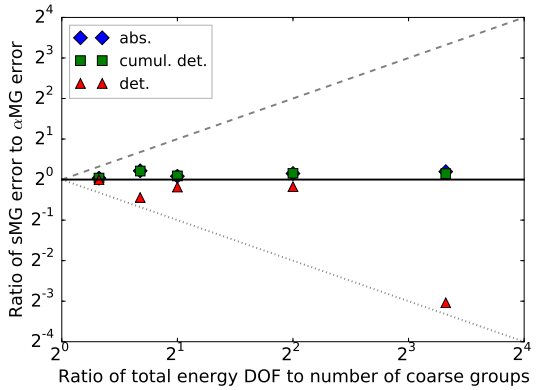

(a) αMG, 10 cm, 100 DOF

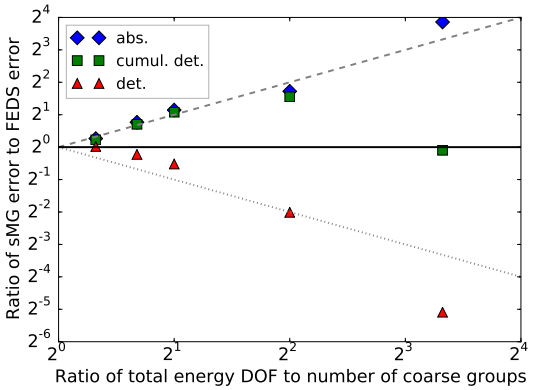

(b) FEDS, 10 cm, 100 DOF

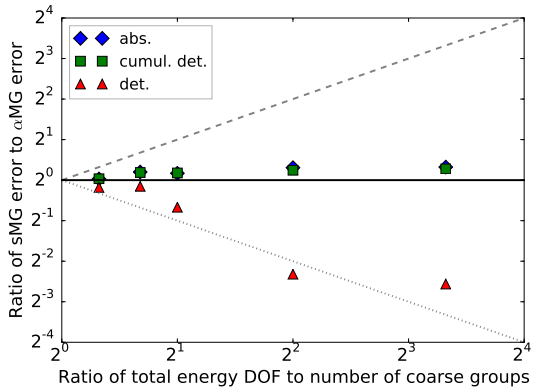

(c) αMG, 1 m, 200 DOF

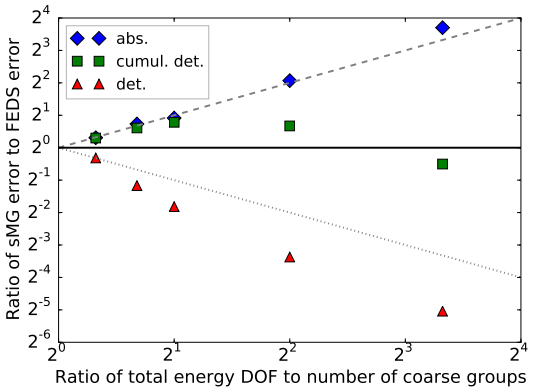

(d) FEDS, 1 m, 200 DOF

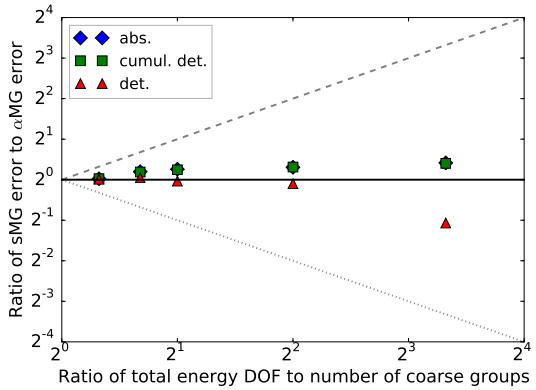

(e) αMG, 1 m, 400 DOF

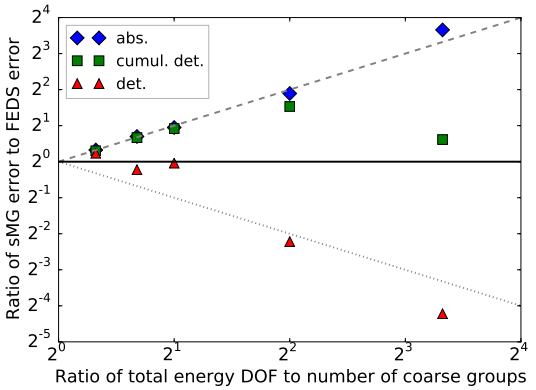

(f) FEDS, 1 m, 400 DOF

Figure 5.13: Behavior of errors with fixed total energy DOF and varying ratio for all errors and 50 time bins.

Table 5.1: Selected TOF QOI errors for vacuum distance 10 cm and 50 time bins

Method	Ratio	Coarse Groups	Total DOF	Error 1 (abs.)	Error 2 (cumul. det.)	Error 3 (det.)
sMG	1	100	100	4.90×10^{-3}	4.77×10^{-3}	5.59×10^{-3}
αMG	1.25	80		4.79×10^{-3}	4.65×10^{-3}	5.61×10^{-3}
	1.6	62		4.22×10^{-3}	4.12×10^{-3}	7.59×10^{-3}
	2	50		4.62×10^{-3}	4.48×10^{-3}	6.34×10^{-3}
	4	25		4.42×10^{-3}	4.28×10^{-3}	6.31×10^{-3}
	10	10		4.28×10^{-3}	4.31×10^{-3}	4.59×10^{-2}
FEDS	1.25	80		4.08×10^{-3}	4.08×10^{-3}	5.51×10^{-3}
	1.6	62		2.88×10^{-3}	2.92×10^{-3}	6.52×10^{-3}
	2	50		2.22×10^{-3}	2.26×10^{-3}	8.01×10^{-3}
	4	25		1.49×10^{-3}	1.63×10^{-3}	2.25×10^{-2}
	10	10		3.38×10^{-4}	5.09×10^{-3}	1.90×10^{-1}
sMG	1	200	200	4.07×10^{-3}	4.02×10^{-3}	4.50×10^{-3}
αMG	1.25	160		3.99×10^{-3}	3.94×10^{-3}	4.44×10^{-3}
	1.6	125		3.54×10^{-3}	3.52×10^{-3}	4.02×10^{-3}
	2	100		3.62×10^{-3}	3.56×10^{-3}	4.30×10^{-3}
	4	50		3.29×10^{-3}	3.25×10^{-3}	5.09×10^{-3}
	10	20		3.26×10^{-3}	3.20×10^{-3}	4.85×10^{-3}
FEDS	1.25	160		3.29×10^{-3}	3.33×10^{-3}	4.39×10^{-3}
	1.6	125		2.45×10^{-3}	2.50×10^{-3}	3.37×10^{-3}
	2	100		2.16×10^{-3}	2.20×10^{-3}	3.77×10^{-3}
	4	50		9.70×10^{-4}	1.02×10^{-3}	6.65×10^{-3}
	10	20		3.13×10^{-4}	1.42×10^{-3}	4.75×10^{-2}
sMG	1	400	400	3.06×10^{-3}	3.07×10^{-3}	3.48×10^{-3}
αMG	1.25	320		3.01×10^{-3}	3.02×10^{-3}	3.50×10^{-3}
	1.6	250		2.67×10^{-3}	2.69×10^{-3}	3.14×10^{-3}
	2	200		2.56×10^{-3}	2.58×10^{-3}	3.08×10^{-3}
	4	100		2.48×10^{-3}	2.50×10^{-3}	3.25×10^{-3}
	10	40		2.30×10^{-3}	2.33×10^{-3}	3.01×10^{-3}
FEDS	1.25	320		2.45×10^{-3}	2.50×10^{-3}	3.24×10^{-3}
	1.6	250		1.89×10^{-3}	1.94×10^{-3}	2.58×10^{-3}
	2	200		1.59×10^{-3}	1.63×10^{-3}	2.22×10^{-3}
	4	100		8.25×10^{-4}	8.47×10^{-4}	2.38×10^{-3}
	10	40		2.43×10^{-4}	4.03×10^{-4}	8.11×10^{-3}

Table 5.2: Selected TOF QOI errors for vacuum distance 10 cm and 10,000 time bins

Method	Ratio	Coarse Groups	Total DOF	Error 1 (abs.)	Error 2 (cumul. det.)	Error 3 (det.)
sMG	1	100	100	4.90×10^{-3}	4.75×10^{-3}	3.68×10^{-2}
αMG	1.25	80		4.79×10^{-3}	4.63×10^{-3}	4.01×10^{-2}
	1.6	62		4.22×10^{-3}	4.11×10^{-3}	4.35×10^{-2}
	2	50		4.62×10^{-3}	4.48×10^{-3}	5.21×10^{-2}
	4	25		4.42×10^{-3}	4.27×10^{-3}	6.31×10^{-2}
	10	10		4.28×10^{-3}	4.27×10^{-3}	1.09×10^{-1}
FEDS	1.25	80		4.08×10^{-3}	4.09×10^{-3}	4.64×10^{-2}
	1.6	62		2.88×10^{-3}	2.93×10^{-3}	6.05×10^{-2}
	2	50		2.22×10^{-3}	2.26×10^{-3}	7.59×10^{-2}
	4	25		1.49×10^{-3}	1.88×10^{-3}	1.51×10^{-1}
	10	10		3.38×10^{-4}	6.06×10^{-3}	3.47×10^{-1}
sMG	1	200	200	4.07×10^{-3}	4.02×10^{-3}	1.55×10^{-2}
αMG	1.25	160		3.99×10^{-3}	3.94×10^{-3}	1.82×10^{-2}
	1.6	125		3.54×10^{-3}	3.52×10^{-3}	1.97×10^{-2}
	2	100		3.62×10^{-3}	3.56×10^{-3}	2.20×10^{-2}
	4	50		3.29×10^{-3}	3.24×10^{-3}	3.58×10^{-2}
	10	20		3.26×10^{-3}	3.19×10^{-3}	4.66×10^{-2}
FEDS	1.25	160		3.29×10^{-3}	3.33×10^{-3}	2.03×10^{-2}
	1.6	125		2.45×10^{-3}	2.50×10^{-3}	2.67×10^{-2}
	2	100		2.16×10^{-3}	2.20×10^{-3}	3.47×10^{-2}
	4	50		9.70×10^{-4}	1.03×10^{-3}	7.04×10^{-2}
	10	20		3.13×10^{-4}	1.36×10^{-3}	1.53×10^{-1}
sMG	1	400	400	3.06×10^{-3}	3.07×10^{-3}	5.38×10^{-3}
αMG	1.25	320		3.01×10^{-3}	3.02×10^{-3}	6.65×10^{-3}
	1.6	250		2.67×10^{-3}	2.69×10^{-3}	7.52×10^{-3}
	2	200		2.56×10^{-3}	2.58×10^{-3}	9.59×10^{-3}
	4	100		2.48×10^{-3}	2.50×10^{-3}	1.67×10^{-2}
	10	40		2.30×10^{-3}	2.33×10^{-3}	2.23×10^{-2}
FEDS	1.25	320		2.45×10^{-3}	2.50×10^{-3}	7.34×10^{-3}
	1.6	250		1.89×10^{-3}	1.94×10^{-3}	1.00×10^{-2}
	2	200		1.59×10^{-3}	1.63×10^{-3}	1.34×10^{-2}
	4	100		8.25×10^{-4}	8.41×10^{-4}	3.06×10^{-2}
	10	40		2.43×10^{-4}	4.43×10^{-4}	7.97×10^{-2}

Table 5.3: Selected TOF QOI errors for vacuum distance 1 m and 50 time bins

Method	Ratio	Coarse Groups	Total DOF	Error 1 (abs.)	Error 2 (cumul. det.)	Error 3 (det.)
sMG	1	200	200	4.07×10^{-3}	4.04×10^{-3}	5.83×10^{-3}
αMG	1.25	160		3.99×10^{-3}	3.95×10^{-3}	6.60×10^{-3}
	1.6	125		3.54×10^{-3}	3.55×10^{-3}	6.48×10^{-3}
	2	100		3.62×10^{-3}	3.57×10^{-3}	9.27×10^{-3}
	4	50		3.29×10^{-3}	3.41×10^{-3}	2.91×10^{-2}
	10	20		3.26×10^{-3}	3.33×10^{-3}	3.45×10^{-2}
FEDS	1.25	160		3.29×10^{-3}	3.28×10^{-3}	7.26×10^{-3}
	1.6	125		2.45×10^{-3}	2.65×10^{-3}	1.31×10^{-2}
	2	100		2.16×10^{-3}	2.35×10^{-3}	2.05×10^{-2}
	4	50		9.70×10^{-4}	2.54×10^{-3}	6.03×10^{-2}
	10	20		3.13×10^{-4}	5.73×10^{-3}	1.92×10^{-1}
sMG	1	400	400	3.06×10^{-3}	3.08×10^{-3}	3.87×10^{-3}
αMG	1.25	320		3.01×10^{-3}	3.02×10^{-3}	3.84×10^{-3}
	1.6	250		2.67×10^{-3}	2.70×10^{-3}	3.75×10^{-3}
	2	200		2.56×10^{-3}	2.60×10^{-3}	3.96×10^{-3}
	4	100		2.48×10^{-3}	2.48×10^{-3}	4.14×10^{-3}
	10	40		2.30×10^{-3}	2.33×10^{-3}	8.12×10^{-3}
FEDS	1.25	320		2.45×10^{-3}	2.50×10^{-3}	3.29×10^{-3}
	1.6	250		1.89×10^{-3}	1.94×10^{-3}	4.52×10^{-3}
	2	200		1.59×10^{-3}	1.63×10^{-3}	3.98×10^{-3}
	4	100		8.25×10^{-4}	1.06×10^{-3}	1.80×10^{-2}
	10	40		2.43×10^{-4}	2.01×10^{-3}	7.22×10^{-2}
sMG	1	800	800	2.32×10^{-3}	2.33×10^{-3}	2.76×10^{-3}
αMG	1.25	640		2.10×10^{-3}	2.13×10^{-3}	2.66×10^{-3}
	1.6	500		1.83×10^{-3}	1.87×10^{-3}	2.41×10^{-3}
	2	400		1.78×10^{-3}	1.82×10^{-3}	2.49×10^{-3}
	4	200		1.56×10^{-3}	1.61×10^{-3}	2.58×10^{-3}
	10	80		1.48×10^{-3}	1.51×10^{-3}	3.22×10^{-3}
FEDS	1.25	640		1.68×10^{-3}	1.72×10^{-3}	2.28×10^{-3}
	1.6	500		1.30×10^{-3}	1.33×10^{-3}	1.90×10^{-3}
	2	400		1.03×10^{-3}	1.07×10^{-3}	2.17×10^{-3}
	4	200		5.66×10^{-4}	5.87×10^{-4}	3.17×10^{-3}
	10	80		1.74×10^{-4}	7.35×10^{-4}	2.24×10^{-2}

Table 5.4: Selected TOF QOI errors for vacuum distance 1 m and 10,000 time bins

Method	Ratio	Coarse Groups	Total DOF	Error 1 (abs.)	Error 2 (cumul. det.)	Error 3 (det.)
sMG	1	400	400	3.06×10^{-3}	3.07×10^{-3}	8.00×10^{-2}
αMG	1.25	320		3.01×10^{-3}	3.02×10^{-3}	8.80×10^{-2}
	1.6	250		2.67×10^{-3}	2.69×10^{-3}	8.80×10^{-2}
	2	200		2.56×10^{-3}	2.58×10^{-3}	1.19×10^{-1}
	4	100		2.48×10^{-3}	2.51×10^{-3}	1.39×10^{-1}
	10	40		2.30×10^{-3}	2.35×10^{-3}	2.16×10^{-1}
FEDS	1.25	320		2.45×10^{-3}	2.50×10^{-3}	1.00×10^{-1}
	1.6	250		1.89×10^{-3}	1.94×10^{-3}	1.27×10^{-1}
	2	200		1.59×10^{-3}	1.63×10^{-3}	1.52×10^{-1}
	4	100		8.25×10^{-4}	1.01×10^{-3}	3.05×10^{-1}
	10	40		2.43×10^{-4}	2.72×10^{-3}	7.34×10^{-1}
sMG	1	800	800	2.32×10^{-3}	2.33×10^{-3}	3.56×10^{-2}
αMG	1.25	640		2.10×10^{-3}	2.13×10^{-3}	4.16×10^{-2}
	1.6	500		1.83×10^{-3}	1.87×10^{-3}	4.60×10^{-2}
	2	400		1.78×10^{-3}	1.81×10^{-3}	5.09×10^{-2}
	4	200		1.56×10^{-3}	1.60×10^{-3}	7.76×10^{-2}
	10	80		1.48×10^{-3}	1.52×10^{-3}	1.05×10^{-1}
FEDS	1.25	640		1.68×10^{-3}	1.72×10^{-3}	4.57×10^{-2}
	1.6	500		1.30×10^{-3}	1.33×10^{-3}	5.55×10^{-2}
	2	400		1.03×10^{-3}	1.07×10^{-3}	6.70×10^{-2}
	4	200		5.66×10^{-4}	5.94×10^{-4}	1.29×10^{-1}
	10	80		1.74×10^{-4}	8.18×10^{-4}	3.76×10^{-1}
sMG	1	1600	1600	1.50×10^{-3}	1.51×10^{-3}	1.37×10^{-2}
αMG	1.25	1280		1.22×10^{-3}	1.25×10^{-3}	1.68×10^{-2}
	1.6	1000		1.11×10^{-3}	1.14×10^{-3}	2.07×10^{-2}
	2	800		1.00×10^{-3}	1.03×10^{-3}	2.32×10^{-2}
	4	400		8.96×10^{-4}	9.23×10^{-4}	4.14×10^{-2}
	10	160		8.45×10^{-4}	8.70×10^{-4}	5.09×10^{-2}
FEDS	1.25	1280		9.75×10^{-4}	1.00×10^{-3}	1.78×10^{-2}
	1.6	1000		7.82×10^{-4}	8.07×10^{-4}	2.28×10^{-2}
	2	800		6.19×10^{-4}	6.38×10^{-4}	2.78×10^{-2}
	4	400		3.30×10^{-4}	3.42×10^{-4}	5.66×10^{-2}
	10	160		9.50×10^{-5}	1.61×10^{-4}	1.27×10^{-1}

Table 5.5: Selected TOF QOI errors for vacuum distance 10 m and 50 time bins

Method	Ratio	Coarse Groups	Total DOF	Error 1 (abs.)	Error 2 (cumul. det.)	Error 3 (det.)
sMG	1	800	800	2.32×10^{-3}	2.34×10^{-3}	4.54×10^{-3}
αMG	1.25	640		2.10×10^{-3}	2.13×10^{-3}	3.79×10^{-3}
	1.6	500		1.83×10^{-3}	1.88×10^{-3}	6.94×10^{-3}
	2	400		1.78×10^{-3}	1.85×10^{-3}	8.86×10^{-3}
	4	200		1.56×10^{-3}	1.69×10^{-3}	1.39×10^{-2}
	10	80		1.48×10^{-3}	1.58×10^{-3}	1.18×10^{-2}
FEDS	1.25	640		1.68×10^{-3}	1.72×10^{-3}	4.55×10^{-3}
	1.6	500		1.30×10^{-3}	1.41×10^{-3}	9.01×10^{-3}
	2	400		1.03×10^{-3}	1.12×10^{-3}	1.28×10^{-2}
	4	200		5.66×10^{-4}	1.00×10^{-3}	2.96×10^{-2}
	10	80		1.74×10^{-4}	1.42×10^{-3}	5.07×10^{-2}
sMG	1	1600	1600	1.50×10^{-3}	1.51×10^{-3}	2.02×10^{-3}
αMG	1.25	1280		1.22×10^{-3}	1.24×10^{-3}	2.08×10^{-3}
	1.6	1000		1.11×10^{-3}	1.13×10^{-3}	2.32×10^{-3}
	2	800		1.00×10^{-3}	1.04×10^{-3}	2.53×10^{-3}
	4	400		8.96×10^{-4}	9.54×10^{-4}	4.99×10^{-3}
	10	160		8.45×10^{-4}	8.93×10^{-4}	4.70×10^{-3}
FEDS	1.25	1280		9.75×10^{-4}	1.00×10^{-3}	1.57×10^{-3}
	1.6	1000		7.82×10^{-4}	7.94×10^{-4}	1.87×10^{-3}
	2	800		6.19×10^{-4}	6.48×10^{-4}	3.04×10^{-3}
	4	400		3.30×10^{-4}	4.19×10^{-4}	6.09×10^{-3}
	10	160		9.50×10^{-5}	4.64×10^{-4}	1.57×10^{-2}

Table 5.6: Selected TOF QOI errors for vacuum distance 10 m and 10,000 time bins

Method	Ratio	Coarse Groups	Total DOF	Error 1 (abs.)	Error 2 (cumul. det.)	Error 3 (det.)
sMG	1	800	800	2.32×10^{-3}	2.33×10^{-3}	4.50×10^{-1}
αMG	1.25	640		2.10×10^{-3}	2.14×10^{-3}	5.29×10^{-1}
	1.6	500		1.83×10^{-3}	1.87×10^{-3}	5.63×10^{-1}
	2	400		1.78×10^{-3}	1.82×10^{-3}	6.20×10^{-1}
	4	200		1.56×10^{-3}	1.64×10^{-3}	8.08×10^{-1}
	10	80		1.48×10^{-3}	1.59×10^{-3}	9.07×10^{-1}
FEDS	1.25	640		1.68×10^{-3}	1.73×10^{-3}	5.60×10^{-1}
	1.6	500		1.30×10^{-3}	1.35×10^{-3}	6.56×10^{-1}
	2	400		1.03×10^{-3}	1.10×10^{-3}	7.44×10^{-1}
	4	200		5.66×10^{-4}	8.33×10^{-4}	1.02×10^{0}
	10	80		1.74×10^{-4}	1.53×10^{-3}	1.40×10^{0}
sMG	1	1600	1600	1.50×10^{-3}	1.51×10^{-3}	1.49×10^{-1}
αMG	1.25	1280		1.22×10^{-3}	1.25×10^{-3}	1.69×10^{-1}
	1.6	1000		1.11×10^{-3}	1.14×10^{-3}	2.22×10^{-1}
	2	800		1.00×10^{-3}	1.03×10^{-3}	2.81×10^{-1}
	4	400		8.96×10^{-4}	9.33×10^{-4}	4.72×10^{-1}
	10	160		8.45×10^{-4}	8.97×10^{-4}	5.69×10^{-1}
FEDS	1.25	1280		9.75×10^{-4}	1.00×10^{-3}	1.87×10^{-1}
	1.6	1000		7.82×10^{-4}	8.09×10^{-4}	2.64×10^{-1}
	2	800		6.19×10^{-4}	6.44×10^{-4}	3.44×10^{-1}
	4	400		3.30×10^{-4}	4.11×10^{-4}	6.30×10^{-1}
	10	160		9.50×10^{-5}	6.35×10^{-4}	9.19×10^{-1}

6. COMPARISONS TO CONTINUOUS-ENERGY MONTE CARLO

6.1 Problem Overview

In this section, we address an important question: can FEDS attain similar fidelity as continuous-energy Monte Carlo? Specifically, I address whether my FEDS implementation can attain sufficiently small errors in a simple-yet-relevant reactor problem compared with MCNP using the same initial cross sections. The results of this section constitute an existence proof that it is possible to attain MCNP-like accuracy with this method. The results give a upper bound on resolution required match MCNP for this problem, and quantify the closeness of this matching.

There are several interesting questions this section does not answer. Most importantly, it does not answer the question of required unknown count to achieve a desired resolution in energy. By specifying the number of energy elements per coarse group manually instead of automatically, I was able to decrease the error in k-eigenvalue in some cases, for example. Results in other sections show that much lower errors can be achieved if better basis functions are used when condensing the cross sections. I leave to future work applying and testing the various condensation schemes used in reactor engineering calculations today that have made unresolved MG capable of high accuracy.

The comparisons in this section to MG use an unoptimized MG. This section does not compare an unoptimized FEDS to an optimized MG because it is an unfair case. Many, if not all, methods to optimize MG cross sections to preserve reaction rates in heterogeneous geometries can be applied in a straightforward way to FEDS: they may be applied to the subelements, and the subelements can be combined using SPH-like methodologies. I leave to future work the interesting question of comparing

an optimized MG to an optimized FEDS.

I claim these results are valuable in convincing others try the FEDS method, especially in light of results in previous sections. The cylindrical pincell problems with MG reference solution quantify expected convergence rates. The C5 problem shows FEDS can handle complicated geometries with several heterogeneously positioned resonant nuclides. The time-of-flight problem shows FEDS is sufficiently flexible to tailor resolution to the energy or cross section / flux domain. This slab pincell problem with MCNP reference solution shows the method can get the "correct" answer with at most a reasonable number of unknowns in energy, at least for simple pincell problems.

This section addresses shortcomings in the methodologies of the cylindrical pincell and C5 sections in an attempt to be more compelling. Those previous sections used energy penalties for dividing energy space, which is shown to be inferior to the use of coarse groups in this section. Previous sections compared to a reference MG solution, while this section compares to the "right answer" of continuous-energy Monte Carlo. Previous sections used QOI that were energy-integrated, which may hide error cancellation. This section defines an edit structure of 12 coarse groups and does error comparisons on each coarse group, showing a more differential view of solution fidelity.

The results of this section are that FEDS attains correct fine-scale behavior of the solution at around 250 unknowns over the entire resolved resonance range (RRR). Error reduction rates are found to be first-order with respect to unknown count in the RRR until errors reach $10 - 50$ pcm, at which point errors in energy discretization are comparable to other numerical errors. In contrast to FEDS, a MG comparison does not converge as unknowns are added for the unknown counts used here, except for the low-lying resonances that are resolved by the group structure.

6.2 Problem Description

Table 6.1 gives a description of the problems studied. All problems used a one-dimensional (infinite by way of reflecting boundaries in x and y) infinite lattice of pincells made up of UO_2 fuel (10.29769 g/cm^3 in $z \in [0, 0.39218]$ cm) and H_2O moderator (0.740582 g/cm^3 in $z \in [0.39218, 0.62992]$ cm). Both MCNP and PDT used the same problem geometry and material compositions. A resolution study in space/angle/scattering moment was performed in PDT to determine when the reaction rates stopped changing. PDT used P_3 scattering, S_{32} Gauß-Legendre quadrature, and lumped PWLD spatial discretization with 20 (12) cells in the fuel (and its boundary) and 10 (5) cells in the moderator (and its boundary).

Varying energy discretizations were used for this problem. MCNP5 version 1.60 was used as the reference with ENDF/B-VII.1 cross sections at 293.6 K processed with NJOY 99.364 to create custom ACE files. PDT (circa version 928) was used as the test with the same ENDF/B-VII.1 cross sections at 293.6 K processed with NJOY 99.364 to create custom GENDF files, that were then converted to PDT-format cross section files by a custom Python script.

Four problems were investigated. The first problem (A) used only depleted uranium (U-238) and a spatially-flat, fixed fission source. The fission source was the thermal-neutron-induced Watt fission spectrum characterized by $a = 0.988$ MeV and $b = 2.249$ MeV^{-1}. PDT was given an analytically group-integrated version of this quantity. So not to double count the fission source, the `nonu` card was used in MCNP and the ν, $\nu\sigma_f$ and χ cross sections were manually removed from the PDT cross sections. The fixed fission source is a decent approximation to the true fission source within a pin and provided a level of additional consistency between MCNP and PDT. The second problem (B) added a fissile material (4% by atom U-235) but kept the

fixed fission source. This added the challenge of resonance interference effects. The third problem (C) was the same as B, except it was formulated as a k-eigenvalue problem and so had a spatially dependent source. Unlike MCNP, the PDT cross sections used a fixed fission spectrum, χ, for all incident neutron energies for problem C. The fourth problem (D) was the same as A, but incorrect chord lengths / escape cross sections were used. Namely, chord lengths for a 2D pincell with cylindrical fuel were used. This was meant to show the dependence of MG schemes on using accurate self-shielding parameters.

Reaction-rate-based quantities of interest (QOI) were compared between MCNP and PDT on a coarse energy grid. The energy grid was chosen based on conversations with Dr. Kord Smith at MIT and is given in Table 6.2. The highest-energy group is for fast neutrons. The second-highest-energy group is for the unresolved resonance range (URR) of U-238. The next eight groups are in the resolved resonance region (RRR) above 4 eV, where thermal effects start becoming important. The penultimate group contains low-lying resonances, and the final, lowest-energy group is for thermal neutrons. The edit structure is hierarchical with the SHEM-361 boundaries. All energy structures investigated in this section are hierarchical with the coarse energy grid. For FEDS energy meshes, all elements are restricted to live within one coarse group, which simplifies the process of projecting onto the coarse mesh.

Varying energy meshes were compared. Table 6.3 gives the number of groups used in the non-RRR coarse groups. All calculations in this section used the SHEM-361-group structure outside the RRR region. Table 6.4 gives the number of energy elements used within each of the RRR coarse groups.

The SHEM-361-group structure was developed in Canada to be accurate for several reactor types when using the subgroup (SG) method to generate cross sections [56]. For this study, the SG method was **not** used. Instead, the "lattice calculation"

was a Bondarenko iteration on background cross section using a analytically computed escape cross section of $S/(4V)$, where S is the surface area of the fuel and V is its volume. Because an approximate self-shielding calculation was used, the errors from the SHEM-361-group structure are higher than would be expected from cross sections produced by, for example, DRAGON [74].

New SHEM-244 and SHEM-166 group structures were created for this section. To create the SHEM-244 and SHEM-166 group structures, I began with the coarse group boundaries in Table 6.2. The SHEM-361 group structure [56] was used in the fast and thermal regions (coarse groups I, II, XI, and XII). For the SHEM-244 group structure, a lethargy width of approximately 0.2 was used for the higher-energy RRR where the resonances were not resolved by the group structure. For the lower-energy RRR, I attempted to resolve the lowest 3 resonances of U-238 and a few low-lying resonances of U-235. A lethargy thickness of approximately 0.027 was used to accomplish this. For the SHEM-166 group structure, 2 or 3 equally-spaced-in-lethargy groups were used in the higher-energy RRR. Lethargy spacings of approximately 0.18 and 0.10 were used in coarse groups IX and X, respectively. Group boundaries for all the SHEM meshes may be found in the accompanying appendix, Appendix F.

For the FEDS energy meshes, a two-step process was used. In the first step, the number of elements to use per coarse group was determined by making this number proportional to the relative standard deviation of the spectra the coarse group. The second step looped over coarse groups, determining a generalized (discontiguous) energy mesh per coarse group. These meshes were stitched into one mesh over all energies.

In this section, we focus on two types of errors, plotted for each coarse group.

The first error is absolute normalized error, in units of per-cent-mille (pcm):

$$\mathrm{E}_{t,g,\mathrm{pcm}} = (P_{t,g} - M_{t,g}) \frac{V_t}{N_{t,\mathrm{pcm}}} 10^5 \,\mathrm{pcm}, \tag{6.1a}$$

where $E_{t,g}$ is the error for tally t in coarse group g, V_t is the volume associated with the tally, $P_{t,g}$ is the volume-averaged value of the tally t integrated over group g given by PDT, $M_{t,g}$ is the volume-averaged value of the tally t integrated over group g given by MCNP, and $N_{t,\mathrm{pcm}}$ is either the total absorption or fission reaction rate for all nuclides integrated over the entire pincell. The second error is the relative error in percent:

$$\mathrm{E}_{t,g,\mathrm{rel}} = \frac{P_{t,g} - M_{t,g}}{M_{t,g}} \, 100\,\%. \tag{6.1b}$$

This total absorption rate gives the reaction rate of nuclide disappearance from neutron interaction. PDT defines the total absorption rate using a cross section equal to MT 1 - MT 2 - MT 4, where MT 1 is the total cross section, MT 2 is the elastic cross section, and MT 4 is the sum of the inelastic cross sections. These PDT cross sections are not the sums of the columns of their respective transfer matrices. MCNP defines the total absorption rate using an FM multiplier using cross sections "(-2:-6:16:17)." -2 means total neutron disappearance (absorption that does not produce another neutron), -6 means total fission, 16 is (n,2n), and 17 is (n,3n). This FM tally does not include reactions such as (n,4n), (n,αn), etc. in its absorption rate. Such additions are negligible for the materials used and the thermal spectrum present.

The total fission rate gives the reaction rate of nuclide disappearance due to fission. It does not include ν, the average number of neutrons produced per fission, because ν had to be "turned off" to do problems A, B, and D. PDT defines the total

fission rate using MT 18, the fission cross section. MCNP defines the total fission rate using an FM tally multiplier using cross section -6, the total fission cross section.

Table 6.1: Pincell problem definitions

Problem	Description
A	1D slab U-238 pincell with fixed fission source
B	1D slab U-238 and U-235 pincell with fixed fission source
C	1D slab U-238 and U-235 pincell in k-eigenvalue formulation
D	1D slab U-238 pincell with fixed fission source using 2D pin escape XS

Table 6.2: Coarse groups used for the edits

Coarse Group	Upper Energy (eV)	Uses FEDS?
I	2.00000×10^{7}	No
II	1.40000×10^{5}	No
III	2.26994×10^{4}	Yes
IV	9.11881×10^{3}	Yes
V	2.08410×10^{3}	Yes
VI	5.39204×10^{2}	Yes
VII	1.54176×10^{2}	Yes
VIII	5.17847×10^{1}	Yes
IX	2.78852×10^{1}	Yes
X	9.50002×10^{0}	Yes
XI	4.21983×10^{0}	No
XII	6.24999×10^{-1}	No

6.3 Results

Figure 6.1 plots the volume- and bin-averaged fluxes and absorption reaction rates for problem A. MCNP5 was used to calculate these values on a tally that used the SHEM-361-group structure. This is the "exact" answer projected onto a coarse

Table 6.3: Energy resolutions outside the RRR.

Coarse group	I	II	XI	XII	Total
Fine groups per coarse group	35	15	52	34	136

Table 6.4: Energy resolutions in the RRR for the slab pincell problem. "Resonant nuclides" refers to which nuclides were used as spectra when computing the energy mesh. Values given for each coarse group in the RRR are the number of energy elements within that coarse group.

Name	Resonant nuclides	III	IV	V	VI	VII	VIII	IX	X	Total
SHEM-166	N/A	2	3	3	3	3	3	5	8	30
$R_{1,d}$	U-238	1	2	3	3	4	5	6	6	30
$R_{1,e}$	U-238 + U-235	1	2	3	4	4	5	5	6	30
$R_{2,d}$	U-238	2	4	6	7	8	10	11	11	59
$R_{2,e}$	U-238 + U-235	2	4	6	7	8	10	11	11	59
SHEM-244	N/A	5	8	7	6	6	8	37	31	108
$R_{3,d}$	U-238	4	8	10	12	15	19	20	20	108
$R_{3,e}$	U-238 + U-235	4	8	10	12	15	19	19	21	108
SHEM-361	N/A	6	9	16	31	39	20	52	52	225
$R_{4,d}$	U-238	9	16	20	26	32	39	42	41	225
$R_{4,e}$	U-238 + U-235	9	16	21	25	32	39	40	43	225
$R_{5,d}$	U-238	11	19	26	32	40	49	52	52	281
$R_{5,e}$	U-238 + U-235	11	19	26	32	40	49	50	54	281

mesh (Table 6.2). Zoom-ins of the lower portion of the resolved resonance region (RRR) show the SHEM-361-group structure resolves the lower resonances of U-238, but not the larger ones.

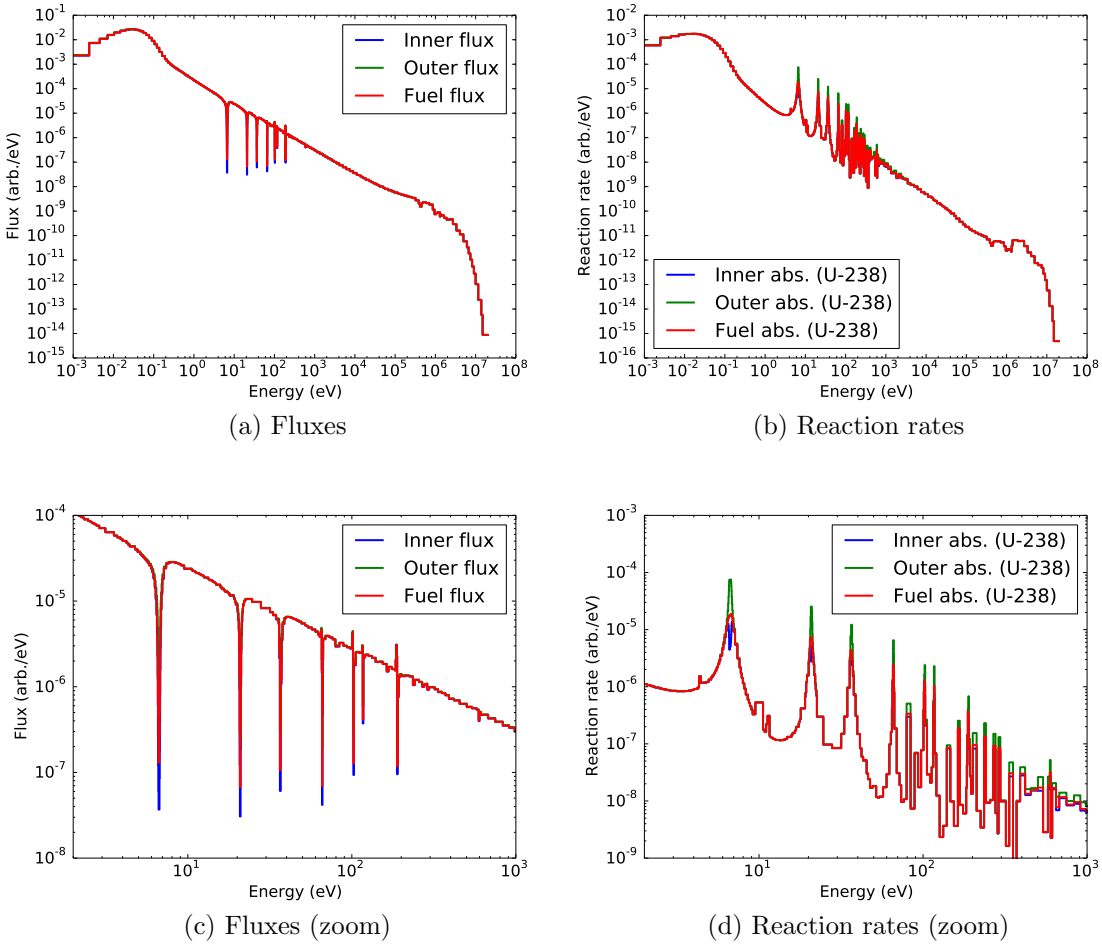

(a) Fluxes

(b) Reaction rates

(c) Fluxes (zoom)

(d) Reaction rates (zoom)

Figure 6.1: Flux and reaction rates tallied onto the SHEM-361-group structure using MCNP for problem A (cf. Table 6.1).

Figure 6.2 gives the unnormalized volume- and energy-averaged absorption rates for problem B for the three different SHEM group structures to show where the group

structures resolve resonance features. The left column is the entire energy range. The right column is a zoom of the lower RRR. Absorption rates in the inner and outer fuel are plotted. Spatial self-shielding causes flux depressions in the inner fuel that reduce resonance reaction rates. The effect of the self-shielding can be large: more than a factor of ten difference in average reaction rates between inside and outside.

6.3.1 Errors for problem C

Table 6.5 gives error in k-eigenvalue for problem C for the various energy discretizations studied. The errors in the SHEM MG family do not converge and end at several hundred pcm. SHEM-244 gets a low eigenvalue error through fortuitous error cancellation. Errors in the FEDS methods begin large but converge uniformly with increasing energy resolution in the RRR. Both the R_d family, which only uses U-238 when calculating the energy mesh, and the R_e family, which uses both U-238 and U-235, have approximately the same magnitude (and sign) of errors. This indicates either fortuitous error cancellation for the R_d family on U-235-related errors, or that U-238 is the dominant nuclide, and getting it right is necessary and sufficient for getting the flux, and hence reaction rates, correct.

The last column of Table 6.5 is efficiency, which is defined as the inverse of the error multiplied by the number of energy unknowns in the RRR. Efficiency should be constant if the method is first-order convergent. Efficiency decreases for the SHEM MG case because increasing resolution is not decreasing the error because the group structures are insufficient to resolve all of the resonances. Efficiency is approximately constant for the FEDS methods, starting around 4, and dipping to around 3 before climbing to around 5.5. The dip may be due to increases in fidelity causing decreases in error cancellation while not affecting the integral eigenvalue error.

Tables 6.6 – 6.9 give errors in all the QOI for problem C for the $R_{5,e}$ energy

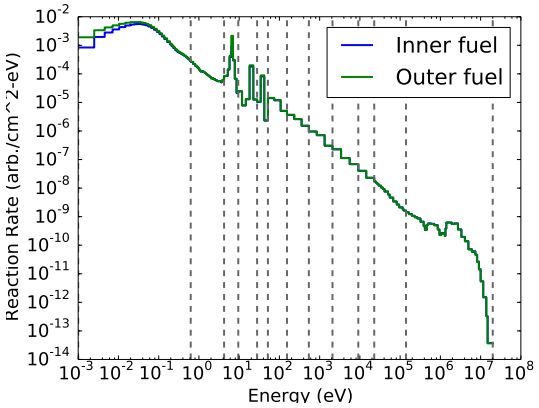

(a) SHEM-166

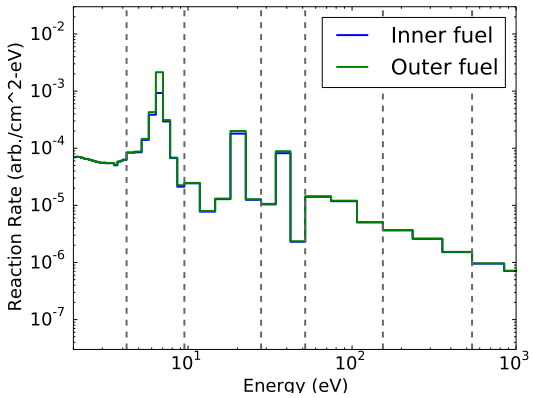

(b) SHEM-166 (zoom)

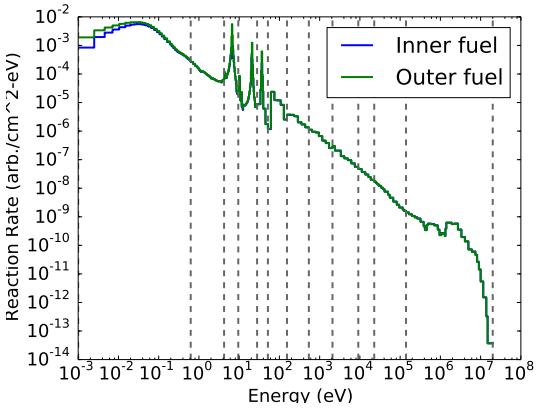

(c) SHEM-244

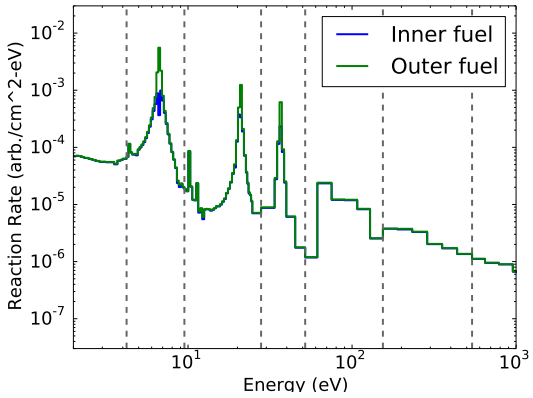

(d) SHEM-244 (zoom)

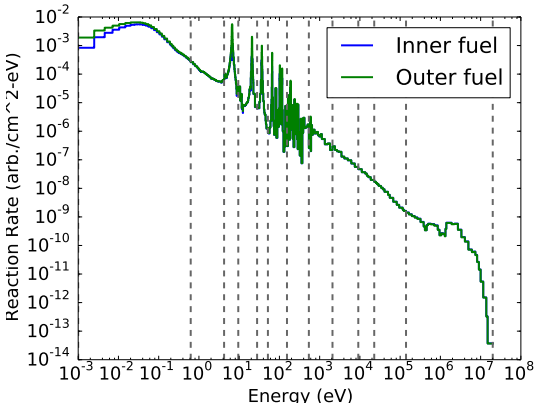

(e) SHEM-361

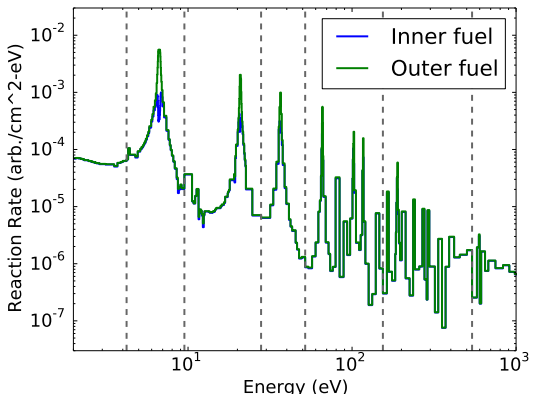

(f) SHEM-361 (zoom)

Figure 6.2: Reaction rates with the SHEM group structures using PDT for problem B

discretization, which represents the highest fidelity energy discretization used. Errors for many differential QOI are given on the coarse group mesh. Relative errors in percent and absolute errors in pcm are given. These results show FEDS can get differential behavior correct with a minimal number of DOF in the RRR. Most relative errors are under 0.5 % and most absolute errors are under 20 pcm for coarse groups in the RRR. U-238 absorption errors in coarse group VI are still large, but are within 1.3 %.

Errors for other problems are similar and are not given in table format. Errors in FEDS tend to converge with increasing resolution. Differential errors in MG using the SHEM group structures are large and do not tend to converge with increasing resolution for the resolutions studied.

Table 6.5: Errors in k-eigenvalue for various energy resolutions for problem C

Name	Error (pcm)	Efficiency (1/[error×DOF])
SHEM-166	-202 ± 2	16.5
SHEM-244	-93 ± 2	9.9
SHEM-361	-587 ± 2	0.8
$R_{1,d}$	762 ± 2	4.4
$R_{2,d}$	493 ± 2	3.4
$R_{3,d}$	317 ± 2	2.9
$R_{4,d}$	116 ± 2	3.8
$R_{5,d}$	69 ± 2	5.2
$R_{1,e}$	757 ± 2	4.4
$R_{2,e}$	506 ± 2	3.4
$R_{3,e}$	313 ± 2	3.0
$R_{4,e}$	89 ± 2	5.0
$R_{5,e}$	63 ± 2	5.6

Table 6.6: Errors for energy discretization $R_{5,e}$ for problem C.

Coarse Group	PDT (rxn. frac.)	MCNP mean (rxn. frac.)	sigma (%)	(P-M) /M (%)	(P-M) (pcm)
		Total absorption			
I	1.04269×10^{-1}	1.04128×10^{-1}	0.00	0.14	14
II	2.88655×10^{-2}	2.88853×10^{-2}	0.00	-0.07	-2
III	1.98683×10^{-2}	1.97710×10^{-2}	0.01	0.49	10
IV	3.99224×10^{-2}	3.98728×10^{-2}	0.01	0.12	5
V	4.98174×10^{-2}	4.98341×10^{-2}	0.01	-0.03	-2
VI	6.26583×10^{-2}	6.30235×10^{-2}	0.01	-0.58	-37
VII	7.37969×10^{-2}	7.39168×10^{-2}	0.01	-0.16	-12
VIII	5.71912×10^{-2}	5.74328×10^{-2}	0.01	-0.42	-24
IX	7.98188×10^{-2}	7.99493×10^{-2}	0.01	-0.16	-13
X	7.76790×10^{-2}	7.78452×10^{-2}	0.01	-0.21	-17
XI	5.70235×10^{-2}	5.67182×10^{-2}	0.01	0.54	31
XII	3.49220×10^{-1}	3.48623×10^{-1}	0.01	0.17	60
Total	1.00013×10^{0}	1.00000×10^{0}	0.00	0.01	13
		Total fission			
I	1.42551×10^{-1}	1.42704×10^{-1}	0.00	-0.11	-15
II	1.15503×10^{-2}	1.15456×10^{-2}	0.00	0.04	0
III	6.35742×10^{-3}	6.33496×10^{-3}	0.01	0.35	2
IV	1.48349×10^{-2}	1.48181×10^{-2}	0.00	0.11	2
V	2.47220×10^{-2}	2.47963×10^{-2}	0.01	-0.30	-7
VI	3.98580×10^{-2}	3.99442×10^{-2}	0.01	-0.22	-9
VII	4.66445×10^{-2}	4.65741×10^{-2}	0.01	0.15	7
VIII	3.30419×10^{-2}	3.30459×10^{-2}	0.01	-0.01	-0
IX	4.87366×10^{-2}	4.86913×10^{-2}	0.01	0.09	5
X	2.66386×10^{-2}	2.68131×10^{-2}	0.01	-0.65	-17
XI	6.93492×10^{-2}	6.89325×10^{-2}	0.01	0.60	42
XII	5.36665×10^{-1}	5.35800×10^{-1}	0.01	0.16	87
Total	1.00095×10^{0}	1.00000×10^{0}	0.01	0.10	95

Table 6.7: Errors for energy discretization $R_{5,e}$ for problem C (cont.).

Coarse Group	PDT (rxn. frac.)	MCNP mean (rxn. frac.)	sigma (%)	(P-M) /M (%)	(P-M) (pcm)
		Inner absorption (U-238)			
I	6.83657×10^{-2}	6.83019×10^{-2}	0.00	0.09	6
II	1.75628×10^{-2}	1.75707×10^{-2}	0.00	-0.04	-1
III	1.27617×10^{-2}	1.26883×10^{-2}	0.01	0.58	7
IV	2.40863×10^{-2}	2.40416×10^{-2}	0.01	0.19	4
V	2.46261×10^{-2}	2.45685×10^{-2}	0.01	0.23	6
VI	2.52666×10^{-2}	2.54792×10^{-2}	0.01	-0.83	-21
VII	2.82720×10^{-2}	2.83475×10^{-2}	0.01	-0.27	-8
VIII	2.12401×10^{-2}	2.14664×10^{-2}	0.02	-1.05	-23
IX	2.62440×10^{-2}	2.63835×10^{-2}	0.01	-0.53	-14
X	3.59815×10^{-2}	3.60029×10^{-2}	0.01	-0.06	-2
XI	1.00480×10^{-2}	1.00132×10^{-2}	0.01	0.35	3
XII	2.62318×10^{-2}	2.61838×10^{-2}	0.01	0.18	5
Total	3.20687×10^{-1}	3.21047×10^{-1}	0.00	-0.11	-36
		Outer absorption (U-238)			
I	1.50927×10^{-2}	1.51016×10^{-2}	0.00	-0.06	-1
II	3.93380×10^{-3}	3.94888×10^{-3}	0.00	-0.38	-2
III	2.90693×10^{-3}	2.89808×10^{-3}	0.01	0.31	1
IV	5.80774×10^{-3}	5.81693×10^{-3}	0.01	-0.16	-1
V	7.12959×10^{-3}	7.15933×10^{-3}	0.01	-0.42	-3
VI	8.85728×10^{-3}	8.96788×10^{-3}	0.02	-1.23	-11
VII	1.13607×10^{-2}	1.14666×10^{-2}	0.02	-0.92	-11
VIII	9.43902×10^{-3}	9.44095×10^{-3}	0.02	-0.02	-0
IX	1.24264×10^{-2}	1.24397×10^{-2}	0.02	-0.11	-1
X	1.95071×10^{-2}	1.95413×10^{-2}	0.02	-0.17	-3
XI	2.28902×10^{-3}	2.28017×10^{-3}	0.01	0.39	1
XII	6.58048×10^{-3}	6.55816×10^{-3}	0.01	0.34	2
Total	1.05331×10^{-1}	1.05619×10^{-1}	0.01	-0.27	-29

Table 6.8: Errors for energy discretization $R_{5,e}$ for problem C (cont.).

Coarse Group	PDT (rxn. frac.)	MCNP mean (rxn. frac.)	sigma (%)	(P-M) /M (%)	(P-M) (pcm)
		Fuel absorption (U-238)			
I	8.34585×10^{-2}	8.34036×10^{-2}	0.00	0.07	5
II	2.14966×10^{-2}	2.15196×10^{-2}	0.00	-0.11	-2
III	1.56687×10^{-2}	1.55863×10^{-2}	0.01	0.53	8
IV	2.98941×10^{-2}	2.98585×10^{-2}	0.01	0.12	4
V	3.17557×10^{-2}	3.17279×10^{-2}	0.01	0.09	3
VI	3.41238×10^{-2}	3.44470×10^{-2}	0.01	-0.94	-32
VII	3.96327×10^{-2}	3.98139×10^{-2}	0.01	-0.46	-18
VIII	3.06792×10^{-2}	3.09073×10^{-2}	0.01	-0.74	-23
IX	3.86704×10^{-2}	3.88232×10^{-2}	0.01	-0.39	-15
X	5.54886×10^{-2}	5.55445×10^{-2}	0.01	-0.10	-6
XI	1.23370×10^{-2}	1.22934×10^{-2}	0.01	0.35	4
XII	3.28122×10^{-2}	3.27420×10^{-2}	0.01	0.21	7
Total	4.26017×10^{-1}	4.26667×10^{-1}	0.00	-0.15	-65
		Fuel absorption (U-235)			
I	1.69156×10^{-2}	1.68705×10^{-2}	0.00	0.27	5
II	7.34548×10^{-3}	7.34257×10^{-3}	0.00	0.04	0
III	4.18261×10^{-3}	4.16801×10^{-3}	0.01	0.35	1
IV	9.98246×10^{-3}	9.96902×10^{-3}	0.00	0.13	1
V	1.79838×10^{-2}	1.80289×10^{-2}	0.01	-0.25	-5
VI	2.84092×10^{-2}	2.84522×10^{-2}	0.01	-0.15	-4
VII	3.39935×10^{-2}	3.39335×10^{-2}	0.01	0.18	6
VIII	2.63867×10^{-2}	2.64012×10^{-2}	0.01	-0.05	-1
IX	4.08524×10^{-2}	4.08311×10^{-2}	0.01	0.05	2
X	2.19127×10^{-2}	2.20235×10^{-2}	0.01	-0.50	-11
XI	4.32494×10^{-2}	4.29946×10^{-2}	0.01	0.59	25
XII	3.09153×10^{-1}	3.08655×10^{-1}	0.01	0.16	50
Total	5.60367×10^{-1}	5.59671×10^{-1}	0.01	0.12	70

6.3.2 Errors for problem A

We compare reaction rate errors for MG and FEDS using the same number of degrees of freedom for each. This provides an apples-to-apples comparison of resolution versus cost. Element structures with 30, 108, and 225 unknowns in the RRR are compared. Problems A, B, and D are compared (Table 6.1). Results for problem C were similar to problem B and so are not shown, aside from errors given above in Tables 6.5 – 6.9. Fuel-integrated total absorption and fission reaction rates are compared. Statistical uncertainties from MCNP are shown as shading around the lines.

Figure 6.3 gives the errors in absorption rate for problem A over the entire problem for several energy discretizations compared to continuous-energy Monte Carlo. Resolution increases left to right. The top row shows MG, using the SHEM group boundaries. As resolution is increased, differential errors stay approximately constant around 200 pcm for the higher portion of the RRR where the resonances are not resolved by the group structure. The errors in the lower portion of the RRR decrease with increasing resolution because the group structure begins to resolve the low-lying resonances (cf. Fig. 6.2). The normalization for problem A is on total absorption rate, meaning the sum of the errors is zero.[1] The absorption rate in the lowest coarse group may be regarded as a cumulative error of its upstream errors. This error does not converge for the SHEM group structures.

The middle row of Fig. 6.3 uses FEDS with energy meshes in the R_d family. In this family, the only resonant nuclide used in determining the energy mesh is U-238. At the lowest resolution, with 30 energy unknowns in the RRR, differential errors

[1]Differences in the cross sections used to define absorption rate and inconsistencies in the one-dimensional cross sections versus the column sums of the transfer matrices may make the sum of the errors non-zero, though this was measured as a small effect.

are upwards of 200 pcm and the cumulative error above 500 pcm. As resolution is increased to 225 unknowns, differential errors decrease to around 60 pcm or less and cumulative error to around 100 pcm. These FEDS energy structures are getting a better integral answer without relying on error cancellation.

The bottom row of Fig. 6.3 uses FEDS with energy meshes in the R_e family. In this family, the resonant nuclides used in determining the energy mesh include both U-235 and U-238. There is no U-235 in problem A, so this family of energy meshes should be less efficient than the R_d family. Figure 6.3 shows similar errors for both R_d and R_e families, indicating the loss in efficiency is negligible for this problem.

6.3.3 Errors for problem D

Figure 6.4 gives the errors in absorption rate for problem D, which is like problem A, except it uses 2-D pincell escape cross sections instead of 1-D slab escape cross sections. Using the wrong escape cross section should increase error in resonances not resolved by the energy mesh. The SHEM group boundaries show differential errors in excess of 700 pcm and cumulative errors in excess of 1000 pcm. The cumulative errors converge for the MG comparison. This is likely caused by resolution of the lower RRR at higher energy unknown count.

Both the R_d and R_e families converge with increasing energy unknown count. Even at the coarsest unknown count of $R_{1,d}$, differential errors are below 200 pcm in all coarse groups. As energy unknown count is increased, differential errors converge. At 225 unknowns in the RRR, the FEDS differential and cumulative errors are similar to those of problem A, where the proper escape cross section was used. This is another demonstration that FEDS is insensitive to basis function / condensing spectrum.

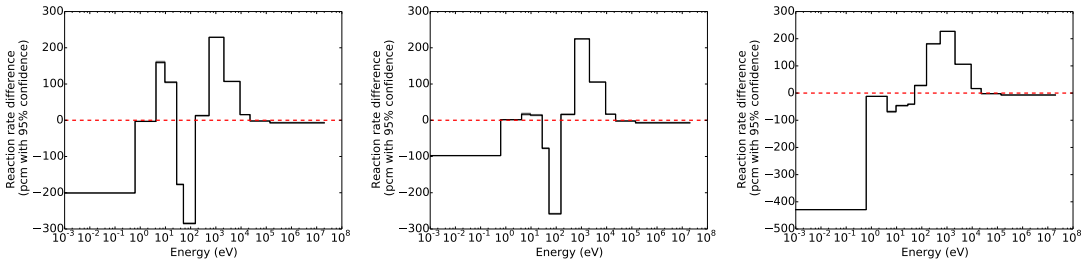

(a) SHEM-166 (b) SHEM-244 (c) SHEM-361

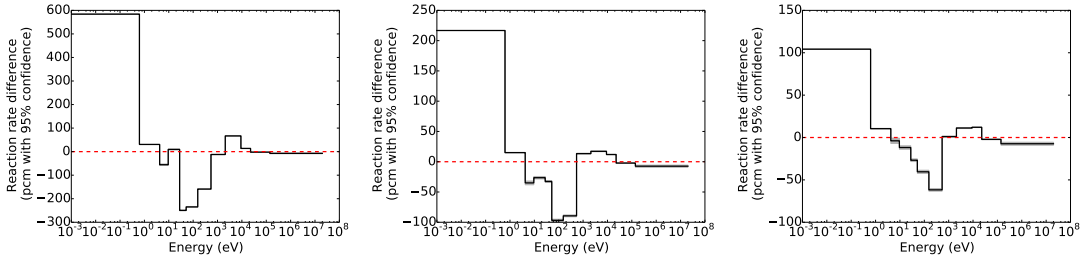

(d) $R_{1,d}$ (e) $R_{3,d}$ (f) $R_{4,d}$

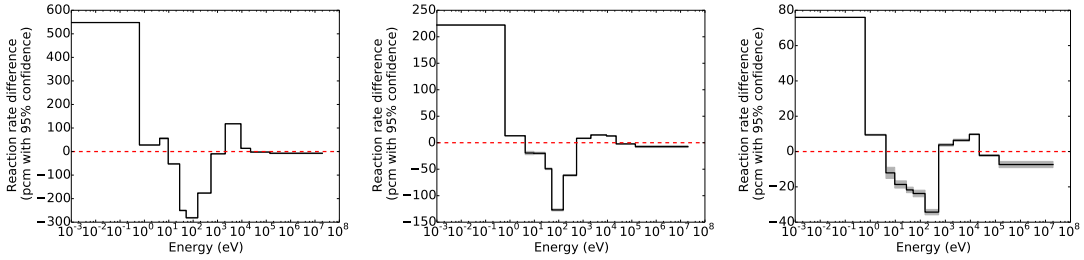

(g) $R_{1,e}$ (h) $R_{3,e}$ (i) $R_{4,e}$

Figure 6.3: Total absorption errors between MCNP and PDT for different energy structures for problem A in pcm, normalized to the total absorption rate

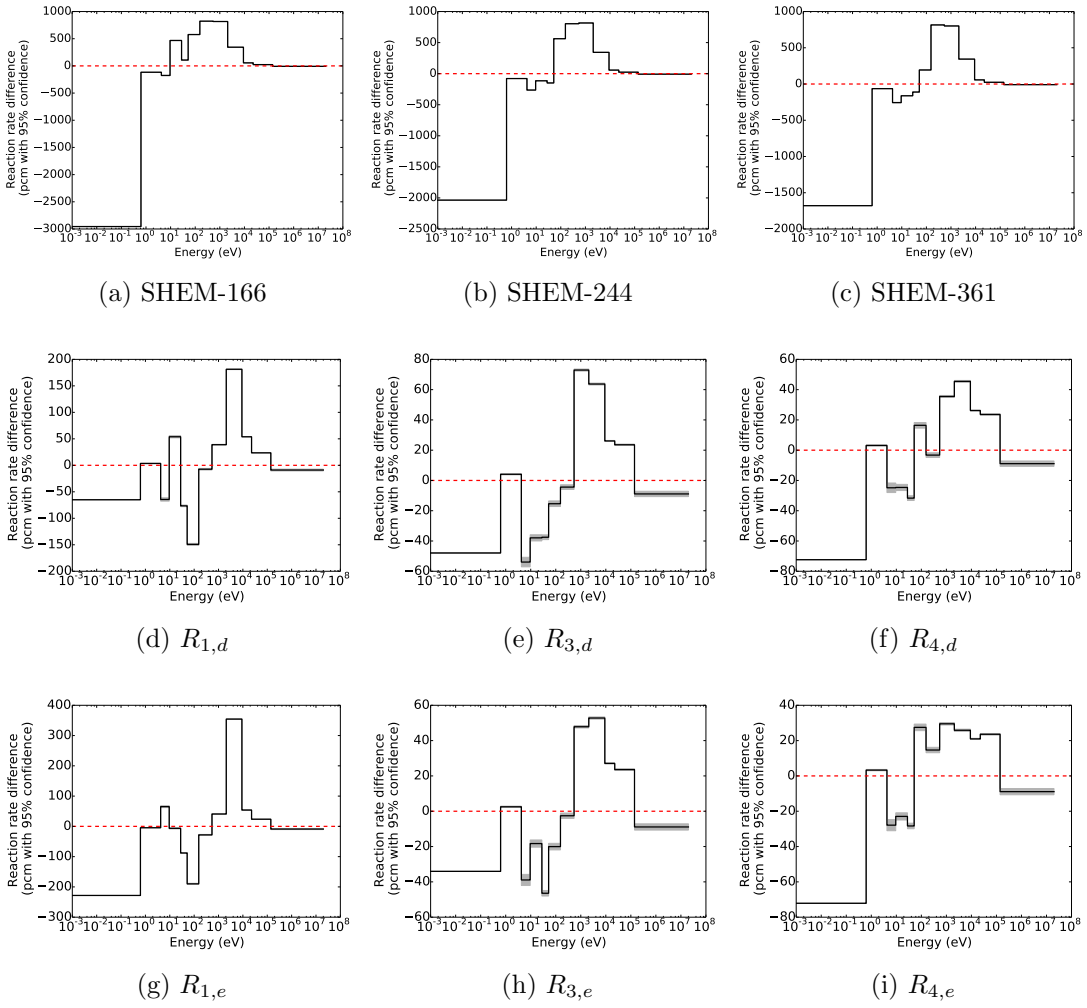

(a) SHEM-166 (b) SHEM-244 (c) SHEM-361

(d) $R_{1,d}$ (e) $R_{3,d}$ (f) $R_{4,d}$

(g) $R_{1,e}$ (h) $R_{3,e}$ (i) $R_{4,e}$

Figure 6.4: Total absorption errors between MCNP and PDT for different energy structures for problem D in pcm, normalized to the total absorption rate

6.3.4 Errors for problem B

Figures 6.5 and 6.6 give the total absorption and fission rate errors for problem B. Fission errors do not include ν. Results are similar to problem A, except problem B has U-235, and so the R_e family is expected to be more efficient than the R_d family, which will not resolve U-235 resonances in its energy mesh. This is seen in Fig. 6.6, where the differential errors in the R_e family decrease more quickly than differential errors in the R_d family. The differential errors in $R_{4,e}$ are a factor of 2 to 4 smaller than those in $R_{4,d}$, which are less than 80 pcm. The cumulative errors are approximately the same, due to favorable error cancellation for $R_{4,d}$. This shows FEDS can handle disparate resonant nuclides but also shows FEDS can do well when not all resonant nuclides are accounted for. The SHEM MG family does not appreciably converge at the resolutions used because the group structure does not resolve resonance behavior.

6.3.5 Component errors for problem B

Figure 6.7 shows errors on further tallies for problem B using the SHEM-361 energy mesh, which uses 225 unknowns in the RRR. The tallies explored are more differential in space and nuclide. Figure 6.7(a)-(c) give errors in absorption in U-238 in the inside, outside, and totality of the fuel, respectively. Spatial self-shielding is larger near the inside of the fuel. The condensation used for the SHEM MG cross sections was formulated to get the reaction rate correct averaged over the entire fuel pin, not portions of the pin. Figure 6.7(a)-(c) show that MG makes a large (over 200 pcm) spatial error, having more reactions in the center than the outside of the fuel. There is large error cancellation to get approximate rates correct over the entire fuel.

Figure 6.7(d) and (e) give the U-235 absorption and fission rate errors over the entire fuel, respectively. Differential errors are around 50 pcm per coarse group.

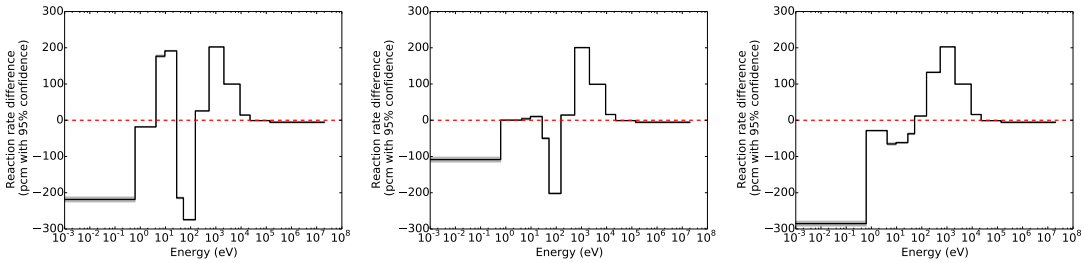

(a) SHEM-166 (b) SHEM-244 (c) SHEM-361

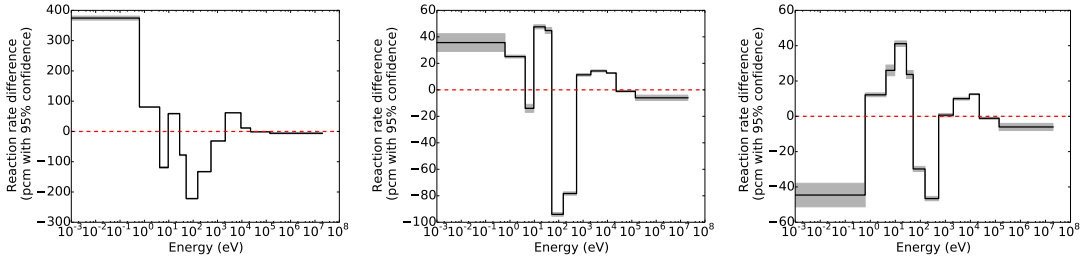

(d) $R_{1,d}$ (e) $R_{3,d}$ (f) $R_{4,d}$

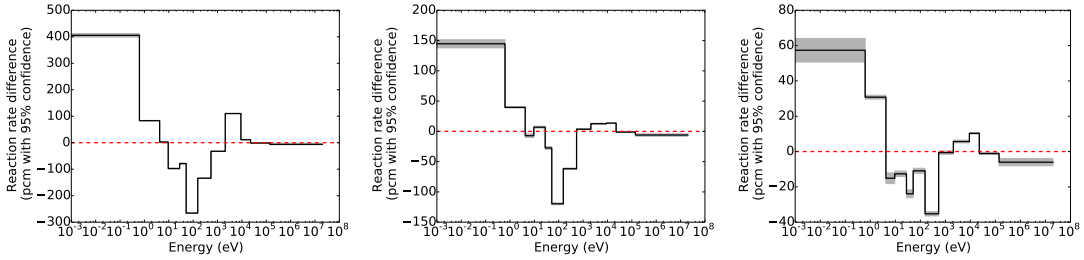

(g) $R_{1,e}$ (h) $R_{3,e}$ (i) $R_{4,e}$

Figure 6.5: Total absorption errors between MCNP and PDT for different energy structures for problem B in pcm, normalized to the total absorption rate

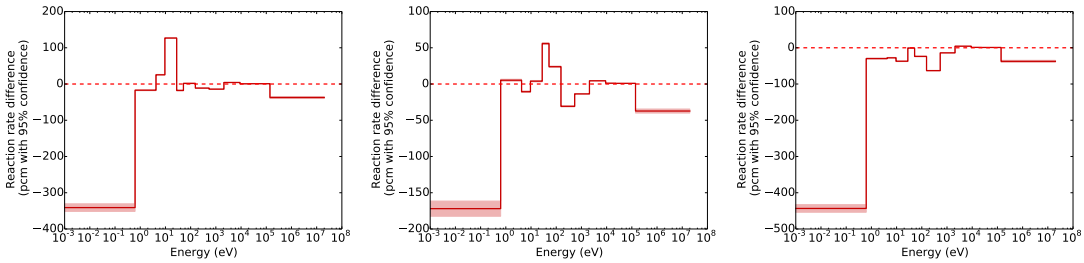

(a) SHEM-166 (b) SHEM-244 (c) SHEM-361

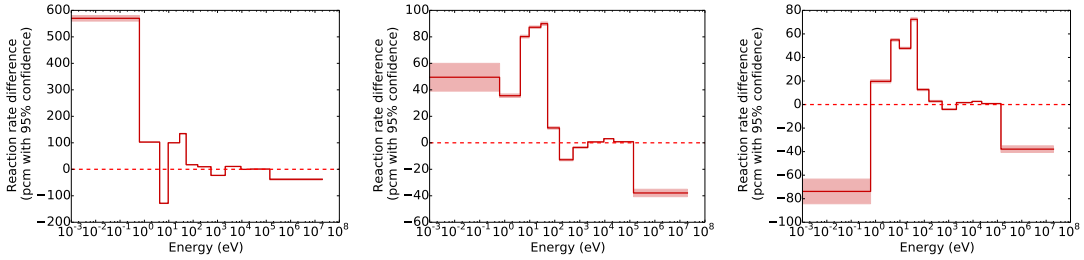

(d) $R_{1,d}$ (e) $R_{3,d}$ (f) $R_{4,d}$

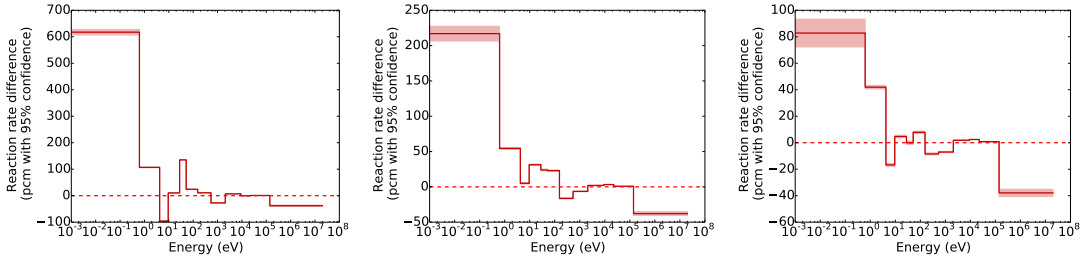

(g) $R_{1,e}$ (h) $R_{3,e}$ (i) $R_{4,e}$

Figure 6.6: Total fission errors between MCNP and PDT for different energy structures for problem B in pcm, normalized to the total fission rate

Cumulative errors are large, above 250 pcm. This is at the highest resolution of MG studied.

Figure 6.8 shows errors on further tallies for problem B using the $R_{4,e}$ energy mesh, which uses 225 unknowns in the RRR and includes U-235 resonances when generating the energy mesh. Figure 6.8(a)-(c) give errors in absorption in U-238 in the inside, outside, and totality of the fuel, respectively. They show FEDS correctly treats spatial self-shielding, leading to differential errors below 25 pcm in each coarse group in (a) and (b).

Figure 6.8(d) and (e) give the U-235 absorption and fission rate errors over the entire fuel, respectively. Differential errors are below 20 pcm per coarse group. Cumulative errors are below 90 pcm. Errors in $R_{5,e}$, which uses 281 unknowns in the RRR, are smaller yet, indicating FEDS converges correctly on differential quantities.

Other figures show the same general trends, and may be found in Appendix F.

6.3.6 Error convergence for problems A and B

Figure 6.9 shows convergence rates in the U-238 absorption rate in inner fuel and coarse group VI (a), U-238 absorption rate in outer fuel and coarse group VI (b), total U-235 fission rate (c), and U-235 fission rate in coarse group VI (d). The convergence rate is approximately first-order for several QOI except at low unknown count or low error magnitudes. For low unknown count, error cancellation or insufficient DOF within the coarse group may lead to non-convergence. When QOI error decreases to around 10 – 20 pcm, numerical errors not related to the energy discretization begin to dominate, ending convergence (Fig. 6.9(d)). This behavior is typical. See tables and figures above and in Appendix F for more convergence rate examples.

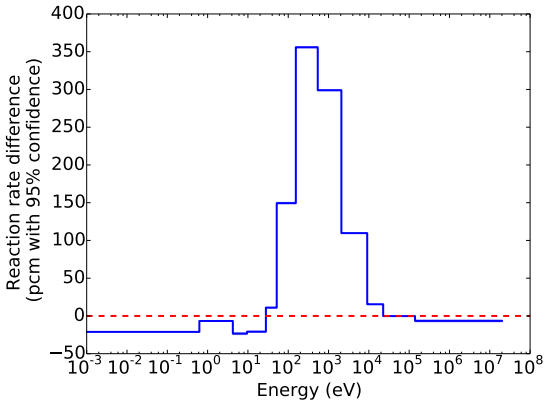

(a) Inner fuel U-238 absorption differences

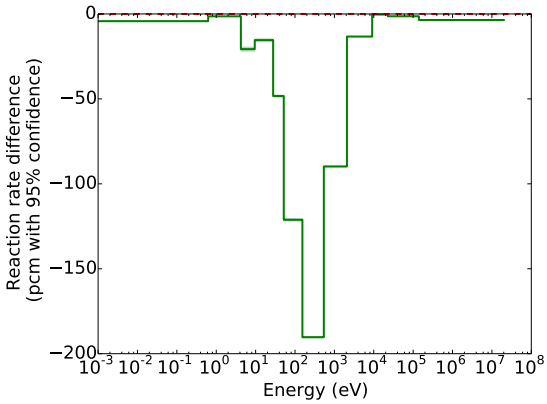

(b) Outer fuel U-238 absorption differences

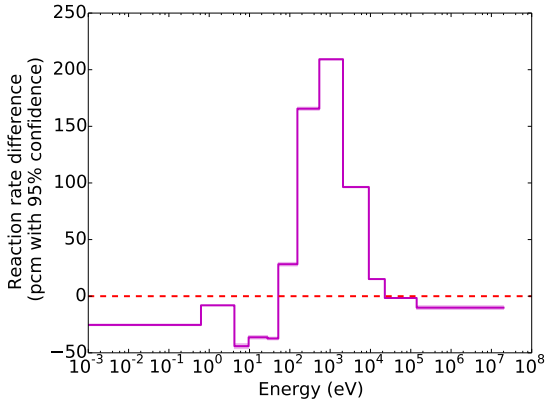

(c) Total fuel U-238 absorption differences

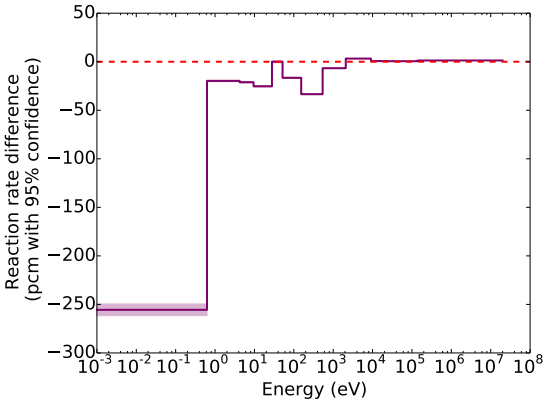

(d) Total fuel U-235 absorption differences

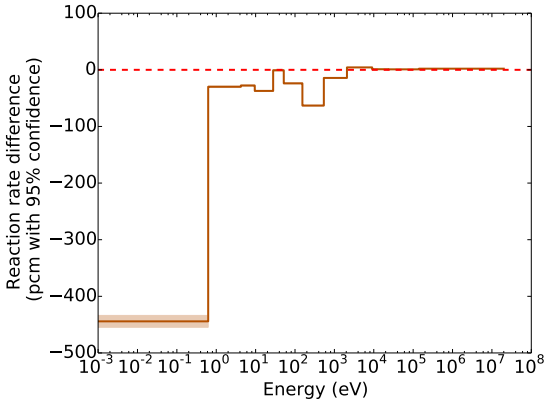

(e) Total fuel U-235 fission differences

Figure 6.7: Component errors between MCNP and PDT using the 361-group SHEM structure for problem B in pcm, normalized to the total absorption or fission rate

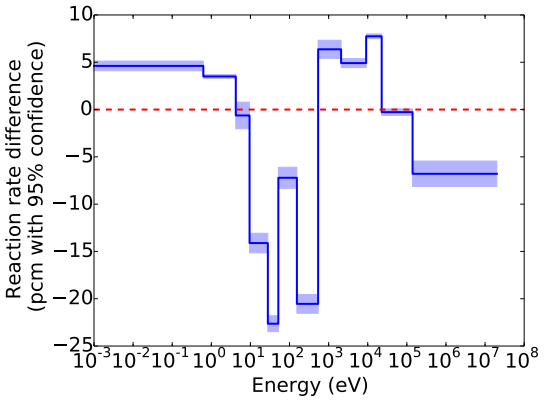

(a) Inner fuel U-238 absorption differences

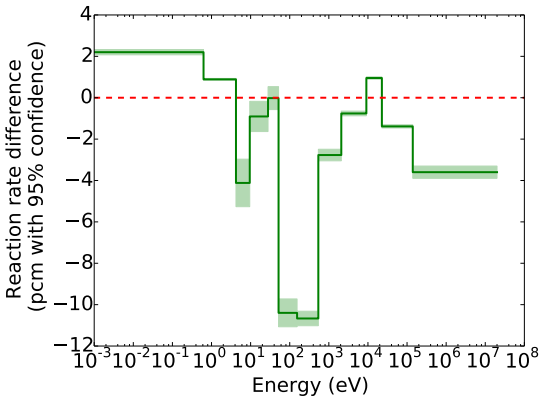

(b) Outer fuel U-238 absorption differences

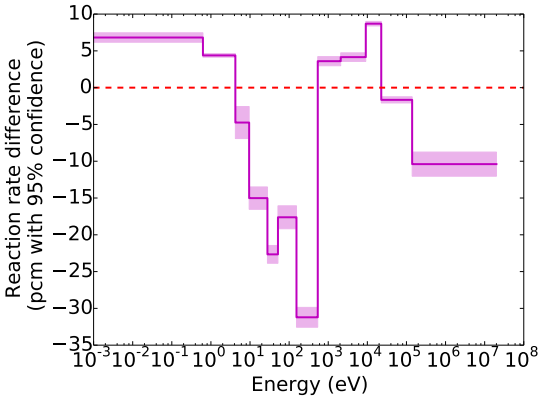

(c) Total fuel U-238 absorption differences

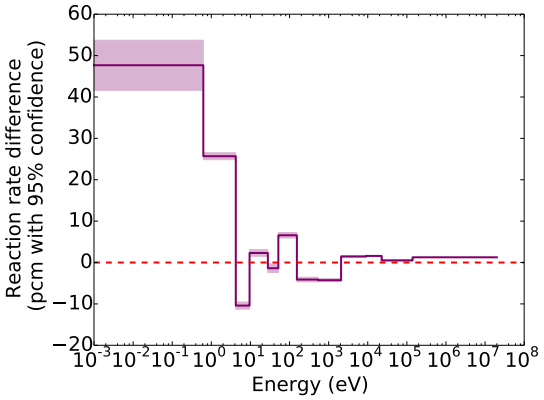

(d) Total fuel U-235 absorption differences

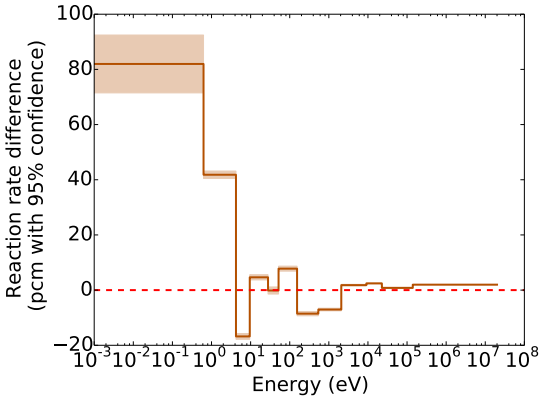

(e) Total fuel U-235 fission differences

Figure 6.8: Component errors between MCNP and PDT using the $R_{4,e}$ structure for problem B in pcm, normalized to the total absorption or fission rate

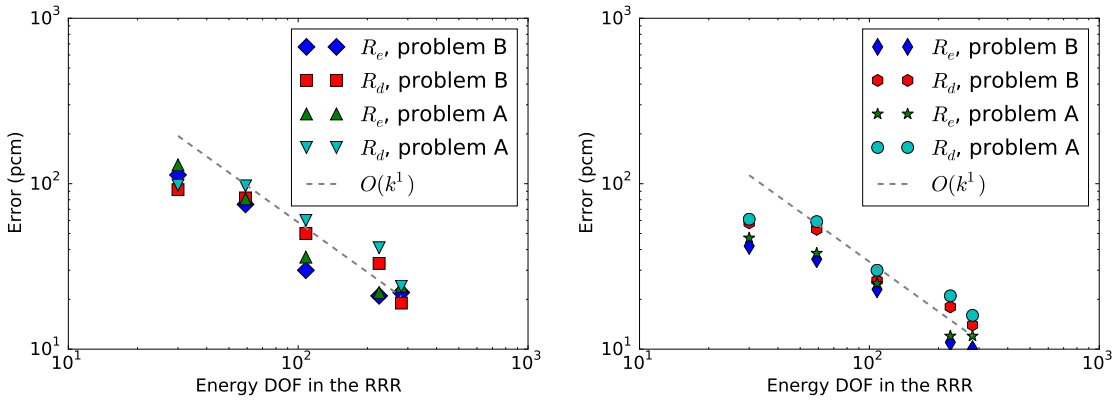

(a) U-238 inner absorption, VI

(b) U-238 outer absorption, VI

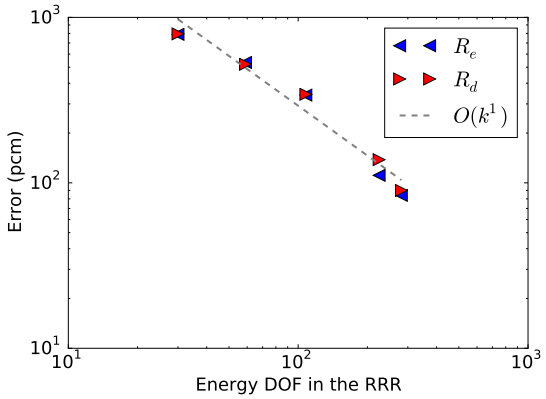

(c) U-235 fission, total

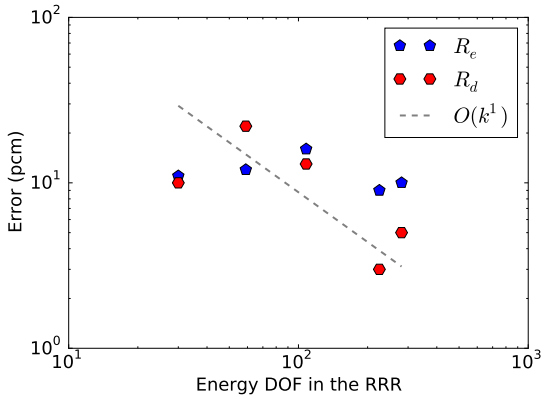

(d) U-235 fission, VI

Figure 6.9: Errors in selected QOI as a function of energy unknowns for different mesh families. R_e and R_d refer to the mesh family. VI refers to the coarse group.

Table 6.9: Errors for energy discretization $R_{5,e}$ for problem C (cont.).

Coarse Group	PDT (rxn. frac.)	MCNP mean (rxn. frac.)	sigma (%)	(P-M) /M (%)	(P-M) (pcm)
		Fuel fission (U-235)			
I	3.09515×10^{-2}	3.08718×10^{-2}	0.00	0.26	8
II	1.15388×10^{-2}	1.15343×10^{-2}	0.00	0.04	0
III	6.35385×10^{-3}	6.33149×10^{-3}	0.01	0.35	2
IV	1.48322×10^{-2}	1.48157×10^{-2}	0.00	0.11	2
V	2.46520×10^{-2}	2.47263×10^{-2}	0.01	-0.30	-7
VI	3.98576×10^{-2}	3.99446×10^{-2}	0.01	-0.22	-9
VII	4.66444×10^{-2}	4.65747×10^{-2}	0.01	0.15	7
VIII	3.30419×10^{-2}	3.30463×10^{-2}	0.01	-0.01	-0
IX	4.87364×10^{-2}	4.86919×10^{-2}	0.01	0.09	4
X	2.66385×10^{-2}	2.68135×10^{-2}	0.01	-0.65	-18
XI	6.93491×10^{-2}	6.89334×10^{-2}	0.01	0.60	42
XII	5.36665×10^{-1}	5.35809×10^{-1}	0.01	0.16	86
Total	8.89261×10^{-1}	8.88093×10^{-1}	0.01	0.13	117

7. CONCLUSIONS

7.1 Conclusions

I have developed, implemented, and tested the Finite-Element-with-Discontiguous-Support (FEDS) method, a novel energy discretization scheme for radiation transport that can capture resonance behavior in the solution with a modest unknown count that does not depend on the number of resonances. This property is characteristic of multiband (MB) methods, which discretize the solution in a Lebesgue sense, but is not shared by multigroup (MG) methods, which require multiple unknowns per resonance to capture fine-scale behavior in energy. FEDS generalizes the MB notion of discretizing the solution by banding a single resonant total cross section to discretizing the solution by minimizing the variance of several infinite-medium spectra within an energy element. Like MG methods, FEDS defines its unknowns in energy space, though unlike MG, its energy elements become discontiguous. By using one energy mesh for the entire problem, FEDS overcomes the primary weakness of MB, which is an approximate handling of band interface conditions between regions with disparate materials or temperatures. FEDS is less sensitive than unresolved MG to condensing spectrum because resonances are resolved by the energy elements.

Mathematically, FEDS is a Petrov-Galerkin Finite Element Method whose weight functions are membership functions[1] that have support only within the corresponding discontiguous energy element and whose basis functions have the same support and a user-defined shape that accounts for short-range resonance self-shielding effects and long-range solution behavior, where "range" refers to distance along the energy axis.

[1]Membership functions are square-tooth functions that vary discontinuously between unity in some regions and zero in other regions. Mathematically, they may be generated by sums of Heaviside step functions.

The FEDS method uses cross sections that are basis-function-weighted in a transport equation that can be solved by traditional MG transport solvers, provided they can handle upscattering.

In addition to the FEDS method, this work introduced two novel techniques. The first was a family of clustering algorithms that solve the minimization problem but produce contiguous groups, resulting in an adaptive MG method that achieves higher fidelity than standard equal-lethargy-spaced MG for the same group count and condensing spectrum. The second was a method that allowed efficient hierarchical energy structures to be used. A coarse group structure is defined and each coarse group is further split into energy elements or groups. The second technique was an algorithm to automatically apportion unknowns among the coarse groups based on a relative variance-like metric within a coarse group.

FEDS performs favorably on a variety of problems and for a variety of quantities of interest (QOI). FEDS demonstrated first-order convergence as energy unknowns were added, even at relatively low unknown counts. FEDS was able to achieve errors on the order of 10 – 50 pcm for 200 – 300 energy unknowns in the resolved resonance region (RRR) in the reactor-inspired problems on which it was tested. Convergence was demonstrated with a variety of basis function fidelities and clustering algorithms; for heterogeneous reactor-type problems with several resonant components; and in a time-dependent problem where $1/v$ streaming effects were important. FEDS solutions were evaluated in comparison to continuous-energy Monte Carlo simulations for pincell-scale problems.

7.2 Future Work

This work has demonstrated the viability of the FEDS method. Along the way, new opportunities for further research were discovered. This subsection distills such

unanswered questions into suggestions for future work.

Section 6 performed comparisons to continuous-energy Monte Carlo for a simple slab pincell problem. This should be extended to more complicated geometries and material compositions, including a standard two-dimensional pincell and typical burnup compositions / temperature gradients.

The FEDS method requires the locations in energy of the cross sections to be defined. This is not possible in the unresolved resonance region (URR). Integrating concepts from MB, especially probability tables, for the URR may allow FEDS to be expanded to cover the entire resonance range. One challenge here is that the URR for one nuclide may overlap the RRR for other nuclides. The number of nuclides that may simultaneously receive an URR treatment might need to be limited to avoid combinatorically large energy unknown counts.

Although FEDS has been developed for neutrons in a static medium, the concept can be generalized to other physics. The presence of spatially-dependent material motion complicates the method, as resonances effectively shift position in the laboratory reference frame depending on the material velocity.

Thermal radiation problems depend on opacities much like neutronics problems depend on cross sections. Opacities have lines which are similar in effect to resonances. An interesting area for future work is the application of FEDS to thermal radiation problems and problems of photon transport in the atmosphere.

Using a nested energy mesh with energy elements within coarse groups was found to be efficient and convergent. Determining the optimal number and location of the coarse group boundaries is an open question. The use of many coarse groups at low energy unknown count forces the method to act more like unresolved MG, reducing convergence and efficiency. In the limit of energy unknown counts sufficient to resolve all of the resonances, use of one element per coarse group may be desirable.

For downscattering-dominated problems, studying the downscattering kernel with respect to resonance widths and downscattering widths may be useful in deriving a theory for coarse group boundary placement.

Resolution of the solution in some coarse groups may be less important than in others for an accurate quantity of interest. Weighting the standard deviations of the coarse groups with importance information based on an adjoint calculation on the coarse groups may yield higher efficiency of energy element placement.

The FEDS method transforms downscattering kernels into block-full element-to-element scattering matrices. The MG method, in contrast, has lower-diagonal group-to-group scattering matrices for such kernels. Previous work using Gauß-Seidel in energy showed the increased work to solve the block-full scattering matrices was less than a factor of 2 increase in the number of required sweeps. Block-Gauß-Seidel iterative techniques with an inner Jacobi iteration in energy should be tested and quantified, as they offer increased parallelism opportunity and efficiency.

Energy mesh generation can be improved. There are questions of the best way to generate the mesh given resource constraints such as computer time, memory, and available parallelism. The proposed spectra do not take into account heterogeneity effects directly, relying on the minimization problem to take care of such correlations in the norm over materials. It is unclear whether this produces the best energy meshes.

Cross section generation and condensation can be optimized. Currently, NJOY is used in addition to a Bondarenko iteration on background cross section and an analytic escape cross section. While inexpensive, this may be inaccurate, as it does a poor job handling resonance interference or the effects of heterogeneous lattices.

There is the opportunity to study how to incorporate the resonances of important nuclides not present in the chosen bounding materials. For example, what is the best

way to incorporate the effects of zirconium (thermal reactors) or stainless steel (fast reactors) cladding on the spectra when generating the energy mesh? One idea would be to include them as separate materials, perhaps weighted to be less important. Another idea would be to include them as separate homogenized materials (combined fuel and cladding, e.g.). A final idea would be to include their effects from a finite-dimensional (say, 1-D pincell) slowing-down calculation directly. I ignored their effects when generating the energy meshes in this work.

Current cross section definitions are inconsistent. NJOY by default uses nuclide-specific spectra, either $(1/E)$ $[1/(\sigma_t + \sigma_0)]$ or the result of a single-nuclide slowing-down calculation. These imply an inconsistent basis function among nuclides, making re-expansion of the flux unclear. Further consistency issues arise when using different region-averaged weighting spectra, $f_i(E)$, when defining the observations and when running NJOY. When doing reconstructions, $f_i(E)$ could be used for the assumed within-group shape.

The above topics are relevant and important and I bring them up to indicate the rich potential for future research.

7.3 How To Break FEDS

FEDS is not a perfect method and it is possible to make it yield poor results. This subsection presents some lessons learned during development of FEDS to serve as a guide for potential future researchers on what aspects should be given additional care. The order of this subsection is approximately the order in which the method is implemented.

The first thing a would-be user must do is determine which materials to use when generating the spectra. The problems studied in this work used only a handful of resonant nuclides and material definitions. For realistic problems, one must deter-

mine a way to select which materials to use, where a material is composed of a set of nuclides, their densities, a temperature, and a background source. We used either $1/E$ or a Watt fission spectrum for the source, depending on energy, though this may not be appropriate for all problems. All our problems used at most a small number of known temperatures, though real problems may need to use materials at bounding or representative temperatures. The same is true for material compositions, which is especially important for burnup studies.

I would caution against using microscopic cross sections instead of spectra as inputs to the minimization problem. Using spectra instead of cross sections is grounded in the theory of minimizing the variance of the solution across the element, at least in the infinite-medium limit, which makes the solution less sensitive to errors in the shape of the basis functions. The solution is not proportional to individual microscopic cross sections, but to scattering sources divided by macroscopic total cross sections. Further, using many unweighted microscopic cross sections would dilute the energy elements and would spend computational resources on resolving resonances to which the solution is not sensitive. Using microscopic cross sections adds additional complexity. Users must decide whether they wish to use partial cross sections or the total. If microscopic cross sections are used, they should be weighted so "important" nuclides receive more resolution. This would require researching weighting strategies. One potential advantage to using microscopic cross sections is that, if both the flux and the individual cross sections are used, the resulting energy mesh may minimize reaction rate variance within an energy element, accurate reaction rates being the ultimate goal. It is dubious that this uncertain advantage would outweigh the known disadvantages.

The next task is to compute infinite-medium spectra on a union hyperfine grid that resolves all the spectral features. This means the grid must resolve all the

resonance dips and scattering peaks. Insufficient resolution of resonances on this grid will prevent the minimization problem from assigning energy unknowns to those resonances. The grid should be kept small so that the clustering algorithms may be solved rapidly. Less intuitively, the type of union hyperfine grid may impact the final energy mesh. An equally-spaced grid in lethargy has many grid points that are not on resonances. Clustering algorithms like k-means use L^2 norms over hyperfine groups and put more energy elements where the grid points are compared to more expensive methods like hierarchical agglomerative clustering. Using a hyperfine grid that puts more unknowns where the solution is changing may lead to better results from the clustering algorithms and hence better energy meshes.

The hyperfine grid used for clustering is not used in the same way as a typical grid. When building a hyperfine grid for continuous-energy cross sections, for example, points are added to bound the linear interpolation error from the grid. For the clustering application, points should be added to bound solution jump between points. This is because clustering combines like values and needs sufficient resolution of values when it divides into elements. Imagine the solution were perfectly linear in energy. Then two points would be enough for a continuous-energy representation of the grid. A FEDS or MG grid using a constant condensing spectrum would not be accurate with one or two energy elements, and the clustering algorithm would require a hyperfine grid with more than two points to yield more than two elements, because the clustering does not subdivide points.

The spectra must be converted to observations, which are then fed to the clustering algorithm to solve the minimization problem. Many clustering algorithms use unweighted L^2 norms over the different observations present. This means all spectra and all relevant features in the spectra should have similar magnitudes. This is why I used a logarithm of the fine-group-averaged spectra to define the observations. Not

dividing by the ΔE_g of a hyperfine group will lead to energy elements that combine hyperfine groups of the same sizes, which is not useful. It is desirable to limit cross section variance within an energy element in addition to solution variance, because cross sections are averaged over an energy element with an approximate weighting spectrum (the basis function). This requires energies with similar total cross section have similar observation values. Spectra are often proportional to $M(E)/\Sigma_t(E)$, where $M(E)$ is a shape function that may be Maxwellian in the thermal range, $1/E$ in the resonance range, and a Watt spectrum in the fast range. I divided my spectra by $M(E)$ to effect this second property. While one-dimensional cylindrical pincell results not included in this work show an insensitivity to observation definition, their definition should nevertheless be given careful consideration.

The user must select an efficient clustering algorithm. Clustering algorithms often trade speed for fidelity. If on-the-fly clustering is performed, an efficient, approximate algorithm such as Birch, mini-batch-k-means, or k-means may be desirable [66]. Most implementations of (mini-batch-)k-means use a random initialization of centroids, which causes the final energy mesh to be stochastic as well. Similarly, Birch is often optimized for machine-specific parameters, such as cache size, and this will cause different results on different machines. On the other side of fidelity, unoptimized hierarchical agglomeration is $O(G^3)$ expensive, where G is the size of the hyperfine grid on which the spectra are defined. Optimizations exist to limit searches to a small number of nearest neighbors, which decreases cost substantially, but which may impact solution. Hierarchical agglomeration was chosen because its result is deterministic and repeatable, and the Scikit-Learn implementation usually takes less than two minutes on a typical single computing core[2] for a hyperfine mesh that is appropriate for the RRR in a typical thermal reactor.

[2]At the time of this writing.

One of the most important aspects is bounding element extent in energy. FEDS will yield poor results if one large coarse group is used because energy elements will span large lethargy widths. This will increase sensitivity to the long-range behavior in energy of the basis functions, which is not the case for MG. Basis functions are often inaccurate at such long-range behavior, which will lead to loss in fidelity for the scattering kernel and other energy-explicit terms, such as the $1/v$ streaming term.

Energy penalties do not work as well as coarse groups for explicitly dividing in energy. Further, energy penalties add another free parameter for how much to divide in energy versus dividing in flux. Optimizing this parameter was often ad hoc and problem-dependent.

The final energy mesh is sensitive to the coarse group boundaries. Boundaries should not occur within a resonance. Coarse group boundary placement may require expert guidance. Existing coarse MG group structures may work well for coarse group boundaries.

If coarse groups are used, the user must determine how to determine how many energy elements to use within each coarse group. Optimal apportioning may be manual, though this again requires expert judgement and introduces another free parameter. Automatic apportioning relies on determining a functional that approximates the total variance within each coarse group. Using the wrong functional will assign a non-optimal number of elements to the coarse groups, reducing efficiency.

Once an energy mesh has been determined, cross sections are generated. The current implementation is to generate cross sections on the contiguous subelements in NJOY and to combine these into cross sections on the discontiguous elements in a post-processing step. This implementation requires temporary storage of the scattering matrices on the subelements, which for hydrogen requires MG^2 floating-point numbers, where M is the number of Legendre moments and G is the number of

subelements. This limits resolution by requiring large processing times and storage costs. Some versions of NJOY have a compile-time limit on the number of groups that may be handled, providing a harder limit on resolution. Alternative implementations would require development of improved cross-section preparation software.

FEDS accuracy depends on basis function fidelity. FEDS cross sections are basis-function weighted, and more accurate basis functions yield more accurate cross sections, especially for low energy unknown counts. Accurate basis functions are obligatory if the energy mesh does not resolve all of the resonances present within the problem. This occurs for minor nuclides that do not affect the spectrum, because the energy mesh is determined by minimizing variance of spectra, not individual cross sections. We used equivalence theory to implicitly define basis functions based on escape cross sections. Using escape cross sections that were wrong by a factor of 2 was observed to decrease QOI fidelity by a similar factor, indicating some sensitivity to basis function.

Due to the complexity of the transport equation with its myriad microscopic cross section and scattering kernel contributions, we have not developed theory on expected convergence order. While such theory may be possible to compute for simple problems that depend on one resonant cross section and for some clustering algorithms, its extension to more complicated, heterogeneous problems is not straightforward. We have observed first-order convergent behavior with increasing energy element count for a fixed number of coarse groups. While this behavior was widely observed, we did not develop a theoretical basis for it and the convergence rate was often bumpy, especially when energy penalties instead of coarse groups were used to divide in energy. Local convergence rates of half-order or less were observed when energy penalties were used.

Finally, care must be taken when considering how FEDS affects resolution re-

quirements elsewhere in the phase space and how it affects solver requirements. The transport solver must be able to handle the effective upscattering FEDS creates. The problems studied where such artificial upscattering was present were eigenvalue problems with an outer iteration on the fission source. The use of groupsets in PDT and this additional outer iteration were sufficient to handle the upscattering without incurring noticeable overhead in solve time.

With respect to the resolution requirements, FEDS produces energy elements that have large cross sections, in excess of 100 cm^{-1}. This forces finer space-angle resolutions and / or a spatial discretization robust to unresolved absorptive boundary layers. Spatial and angular mesh resolutions that worked for MG may be insufficient for FEDS.

Failure to account for the above may lead to poor FEDS performance or efficiency. My goal in airing these implementation stipulations is to make future research on FEDS accessible and fruitful.

REFERENCES

[1] A. T. Till, A Generalized Multigroup Method, Master's thesis, Texas A&M University (May 2014).

[2] E. E. Lewis, W. F. Miller, Computational Methods of Neutron Transport, American Nuclear Society, La Grange Park, Illinois, 1993.

[3] L. B. Levitt, Probability Table Method for Treating Unresolved Neutron Resonances in Monte Carlo Calculations, Nucl. Sci. Eng. 49 (4) (1972) 540–457.

[4] A. Hébert, The Ribon Extended Self-Shielding Model, Nucl. Sci. Eng. 151 (2005) 1–24.

[5] S. Chandrasekhar, The Radiative Equilibrium of the Outer Layers of a Star, with Special Reference to the Blanketing Effect of the Reversing Layer, Mon. Not. R. Astr. Soc. 96 (1935) 21–41.

[6] S. E. Strom, R. L. Kurucz, A Statistical Procedure for Computing Line-Blanketed Model Stellar Atmospheres with Applications to the F5 IV Star Procyon, J. Quant. Spectrosc. Radiat. Transfer 6 (1966) 591–607.

[7] D. F. Carbon, A Comparison of the Straight-Mean, Harmonic-Mean, and Multiple-Picket Approximations for the Line Opacities in Cool Model Atmospheres, The Astrophysical Journal 187 (1974) 135–145.

[8] M. N. Nikolaev, V. V. Filippov, Measurement of the Resonance Parameters for Total Cross Sections of Some Elements in the Energy Region 0.3-2.7 MeV, Atom. Energ. 6 (6) (1963) 493, (in Russian).

[9] J. C. Stewart, Non-Grey Radiative Transfer, J. Quant. Spectrosc. Radiat. Transfer 4 (1964) 723–729.

[10] D. E. Cullen, G. C. Pomraning, The Multiband Method in Radiative Trans-

fer Calculations, Journal of Quantitative Spectroscopy and Radiative Transfer 24 (2) (1980) 97 – 117.

[11] T. Takeda, H. Fujimoto, K. Sengoku, S. Shiroya, H. Unesaki, K. Kanda, Application of Multiband Method to KUCA Tight-Pitch Lattice Analysis, Journal of Nuclear Science and Technology 28 (9) (1991) 863–869.

[12] T. Yamamoto, Background-Cross-Section-Dependent Subgroup Parameters, Journal of Nuclear Science and Technology 40 (6) (2003) 370–375.

[13] S.-E. Huang, K. Wang, D. Yao, An Advanced Approach to Calculation of Neutron Resonance Self-Shielding, Nuclear Engineering and Design 241 (8) (2011) 3051 – 3057.

[14] P. Ribon, J. M. Maillard, Probability Tables and Gauss Quadrature: Application to Neutron Cross-Sections in the Unresolved Energy Range, in: ANS Topical Meeting on Advances in reactor Physics and Safety, ANS, Saratoga Springs, New York, 1986.

[15] G. Chiba, H. Unesaki, Improvement of Moment-based Probability Table for Resonance Self-Shielding Calculation, Annals of Nuclear Energy 33 (13) (2006) 1141 – 1146.

[16] A. Hébert, M. Coste, Computing Moment-based Probability Tables for Self-shielding Calculations in Lattice Codes, Nucl. Sci. Eng. 142 (2002) 245–257.

[17] N. Martin, A. Hébert, A Monte Carlo Lattice Code with Probability Tables and Optimized Energy Meshes, Nucl. Sci. Eng. 167 (2011) 177–195.

[18] A. V. Shilkov, Generalized Multigroup Approximation and Lebesgue Averaging Method in Particle Transport Problems, Transport Theory and Statistical Physics 23 (6) (1994) 781–814.

[19] A. A. Wray, J.-F. Ripoll, D. Prabhu, Investigation of the Opacity Binning Approach for Solving the Shock-Generated Radiation of the Apollo AS-501 Re-

entry, Tech. rep., Center for Turbulence Research (2006).

[20] A. T. Till, M. L. Adams, J. E. Morel, A Generalized Multigroup Method Based on Finite Elements, in: International Conference on the Physics of Reactors (PHYSOR) - The Role of Reactor Physics toward a Sustainable Future, American Nuclear Society, Kyoto, Japan, 2014.

[21] D. M. Mihalas, B. Mihalas, Foundations of Radiation Hydrodynamics, Dover Publications, Inc., Mineola, New York, 1999.

[22] L. H. Auer, R. B. Lowrie, Dispersion Analysis of Radiation/Thermal Fronts with Fully Resolved Spectral Opacity Variation, Tech. Rep. LA-UR-00-6094, Los Alamos National Laboratory, Los Alamos, New Mexico (Oct. 2000).

[23] R. B. Lowrie, T. S. Haut, Reconstructing Opacities for Multigroup Thermal Radiative Transport, Tech. Rep. LA-UR-14-24608, Los Alamos National Lab (2014).

[24] J.-F. Ripoll, A. A. Wray, A 3D Multiband Closure for Radiation and Neutron Transfer Moment Models, Journal of Computational Physics 227 (4) (2008) 2212 – 2237.

[25] V. V. Sinitsa, M. N. Nikolaev, Analytical Determination of Subgroup Parameters, Sov. At. Energy 35 (6) (1973) 1129–1131, translated from At. Energ. (USSR).

[26] D. E. Cullen, Application of the Probability Table Method to Multigroup Calculations of Neutron Transport, Nucl. Sci. Eng. 55 (4) (1974) 387–400.

[27] D. E. Cullen, E. F. Plechaty, R. J. Doyas, C. R. Weisbin, J. E. White, Cross Section Probability Tables in Multigroup Transport Calculations, Tech. rep., Lawrence Livermore National Laboratory, Livermore, California (Mar. 1978).

[28] Y. B. Zel'dovich, Y. P. Raizer, Physics of Shock Waves and High-Temperature Hydrodynamic Phenomena, Courier Dover Publications, 2012.

[29] G. C. Pomraning, The Equations of Radiation Hydrodynamics, Courier Dover Publications, 1973.

[30] M. N. Nikolaev, Comments on the Probability Table Method, letter to the Editor (Jun. 1975).

[31] T. Takeda, Y. Kanayama, A Multiband Method with Resonance Interference Effect, Nucl. Sci. Eng. 131 (3) (1999) 401–410.

[32] T. Yamamoto, T. Takeda, Reaction Rate Calculation in Fast Reactor Blanket Using Multiband S_n Theory, Journal of Nuclear Science and Technology 37 (5) (2000) 428–435.

[33] T. Yamamoto, A Generalized Approach to Optimize Subgroup Parameters, Journal of Nuclear Science and Technology 41 (4) (2004) 425–431.

[34] T. Yamamoto, T. Takeda, Subgroup Parameters based on Orthogonal Factorization, Journal of Nuclear Science and Technology 44 (1) (2007) 36–42.

[35] M. J. Milošević, A New Subgroup Method for Resolved Resonance Treatment, Nucl. Sci. Bull. 2 (1) (1997) 9–13.

[36] M. Tatsumi, A. Gihou, T. Takeda, Space and Angular Dependence of Interface Currents in the Multiband-CCCP Method, Journal of Nuclear Science and Technology 37 (7) (2000) 572–580.

[37] G. Chiba, A Combined Method to Evaluate the Resonance Self Shielding Effect in Power Fast Reactor Fuel Assembly Calculation, Journal of Nuclear Science and Technology 40 (7) (2003) 537–543.

[38] R. N. Hwang, Nuclear Computational Science: A Century in Review, Springer, 2010, Ch. 5: Resonance Theory in Reactor Applications, pp. 217–290.

[39] L. Cao, H. Wu, Q. Liu, Q. Chen, Arbitrary Geometry Resonane Calculation Using Subgroup Method and Method of Characteristics, in: International Conference on Mathematics and Computational Methods Applied to Nuclear Science

and Engineering (M&C 2011), Rio de Janeiro, Brazil, 2011.

[40] Z. Gao, Y. Xu, T. J. Downar, The Treatment of Resonance Interference Effects in the Subgroup Method , Annals of Nuclear Energy 38 (5) (2011) 995 – 1003.

[41] S. Peng, X. Jiang, S. Zhang, D. Wang, Subgroup Method with Resonance Interference Factor Table, Annals of Nuclear Energy 59 (0) (2013) 176 – 187.

[42] P. Mosca, C. Mounier, P. Bellier, I. Zmijarevic, Improvements in Transport Calculations by the Energy-Dependent Fission Spectra and Subgroup Method for Mutual Self-Shielding, Nuclear Science and Engineering 175 (3) (2013) 266–282.

[43] A. Hébert, Development of the Subgroup Projection Method for Resonance Self-Shielding Calculations, Nucl. Sci. Eng. 162 (2009) 56–75.

[44] N. Martin, J. Miss, A. Hébert, Moment-based Probability Tables for Angular Anisotropic Scattering, Annals of Nuclear Energy 38 (5) (2011) 1125 – 1132.

[45] X-5 Monte Carlo Team, MCNP - A General Monte Carlo N-Particle Transport Code, Version 5 Volume I: Overview and Theory, Los Alamos National Laboratory, lA-UR-03-1987 (February 2008).

[46] T. M. Sutton, F. B. Brown, Implementation of the Probability Table Method in a Continuous-Energy Monte Carlo Code System, Tech. Rep. Conf-981003, KAPL, Schenectady, New York, 12301 (Oct. 1998).

[47] T. M. Sutton, T. J. Donovan, P. S. Dobreff, E. Caro, D. P. Griesheimer, L. J. Tyburski, D. C. Carpenter, H. Joo, The MC21 Monte Carlo Transport Code, in: Joint International Topical Meeting on Mathematics & Computation and Supercomputing in Nuclear Applications, American Nuclear Society, Monterey, California, 2007.

[48] J. J. Duderstadt, L. J. Hamilton, Nuclear Reactor Analysis, John Wiley & Sons, 1976.

[49] Y. Liu, B. Collins, B. Kochunas, W. Martin, K.-S. Kim, M. Williams, Resonance Self-Shielding Methodology in MPACT, in: International Conference on Mathematics and Computational Methods Applied to Nuclear Science and Engineering, American Nuclear Society, 2013.

[50] Y. Liu, B. Collins, B. Kochunas, W. Martin, K.-S. Kim, M. Williams, Modeling Resonance Interference by 0-D Slowing-Down Solution with Embedded Self-Shielding Method, in: International Conference on Mathematics and Computational Methods Applied to Nuclear Science and Engineering, American Nuclear Society, 2013.

[51] N. A. Gibson, B. Forget, On the Stability of the Discrete Generalized Multigroup Method, Annals of Nuclear Energy 65 (2014) 421–432.

[52] S. Douglass, F. Rahnema, Subgroup Decomposition Method, Annals of Nuclear Energy 48 (0) (2012) 84 – 101.

[53] R. J. Stamm'ler, M. J. Abbate, Methods of Steady-State Reactor Physics in Nuclear Design, Vol. 111, Academic Press London, 1983.

[54] C. Wemple, R. Stamm'ler, A. Ferri, Improved Temperature-Dependent Resonance Treatment in HELIOS-1.9, Transactions of the American Nuclear Society 96 (2007) 657–659.

[55] R. Roy, Nuclear Computational Science: A Century in Review, Springer, 2010, Ch. 4: Reactor Core Methods, pp. 167–216.

[56] A. Hébert, A. Santamarina, Refinement of the Santamarina-Hfaiedh Energy Mesh Between 22.5 eV and 11.4 keV, in: International Conference on the Physics of Reactors (PHYSOR), American Nuclear Society, Interlaken, Switzerland, 2008.

[57] P. Mosca, C. Mounier, R. Sanchez, G. Arnaud, An Adaptive Energy Mesh Constructor for Multigroup Library Generation for Transport Codes, Nuclear

Science and Engineering 167 (1) (2011) 40–60.

[58] S. Yasseri, F. Rahnema, Subgroup Decomposition Method in Diffusion Theory, Annals of Nuclear Energy 60 (2013) 235–241.

[59] I. Attieh, R. Pevey, An Adaptive General Multigroup Method, in: Proc. 27th Annual CNS-CAN Student Conference, Toronto, Ontario, Canada, 2002.

[60] I. K. Attieh, Generalized Multigroup Method, Ph.D. thesis, The University of Tennessee (2004).

[61] B. Forget, F. Rahnema, A Spectral Unfolding Method, Trans. Am. Nucl. Soc. 96 (2007) 669.

[62] F. Rahnema, S. Douglass, B. Forget, Generalized Energy Condensation Theory, Nucl. Sci. Eng. 160 (2008) 41–58.

[63] L. Zhu, B. Forget, A Discrete Generalized Multigroup Energy Expansion Theory, Nucl. Sci. Eng. 166 (2010) 239.

[64] L. Zhu, B. Forget, An Energy Recondensation Method Using the Discrete Generalized Multigroup Energy Expansion Theory, Annals of Nuclear Energy 38 (8) (2011) 1718 – 1727.

[65] E. Jones, T. Oliphant, P. Peterson, et al., SciPy: Open-Source Scientific Tools for Python, [Online; accessed 2014-12] (2001–).

[66] F. Pedregosa, G. Varoquaux, A. Gramfort, V. Michel, B. Thirion, O. Grisel, M. Blondel, P. Prettenhofer, R. Weiss, V. Dubourg, J. Vanderplas, A. Passos, D. Cournapeau, M. Brucher, M. Perrot, E. Duchesnay, Scikit-learn: Machine Learning in Python, Journal of Machine Learning Research 12 (2011) 2825–2830.

[67] M. L. Williams, K. S. Kim, The Embedded Self-Shielding Method, in: Conference on the Physics of Reactors (PHYSOR) - Advances in Reactor Physics, The American Nuclear Society, Knoxville, Tennessee, USA, 2012.

[68] R. E. MacFarlane, D. W. Muir, The NJOY Nuclear Data Processing System,

Version 91, Los Alamos National Laboratory, Los Alamos, New Mexico, report LA-12750-M (1994).

[69] S. M. Bowman, SCALE 6: A Comprehensive Nuclear Safety Analysis Code System, Nuclear technology 174 (2) (2011) 126–148.

[70] E. Lewis, M. Smith, N. Tsoulfanidis, G. Palmiotti, T. Taiwo, R. Blomquist, Benchmark Specification for Deterministic 2-D/3-D MOX Fuel Assembly Transport Calculations without Spatial Homogenization (C5G7 MOX), Tech. rep., NEA/NSC (2001).

[71] C. N. McGraw, M. L. Adams, W. D. Hawkins, M. P. Adams, T. Smith, Accuracy of the Linear Discontinuous Galerkin Method for Reactor Analysis with Resolved Fuel Pins, in: International Conference on the Physics of Reactors (PHYSOR) - The Role of Reactor Physics toward a Sustainable Future, American Nuclear Society, Kyoto, Japan, 2014.

[72] A. Sidi, Practical Extrapolation Methods: Theory and Applications, Vol. 10, Cambridge University Press, 2003.

[73] B. D. Ganapol, The Response Matrix Discrete Ordinates Solution to the 1D Radiative Transfer Equation, Journal of Quantitative Spectroscopy and Radiative Transfer 154 (2015) 72–90.

[74] G. Marleau, R. Roy, A. Hébert, A User's Guide for DRAGON Version 5, Tech. Rep. IGE-335, Institut de génie nucléaire, Ecole Polytechnique de Montréal, Montréal, Québec (December 2014).

[75] P. K. Romano, B. Forget, The OpenMC Monte Carlo Particle Transport Code, Annals of Nuclear Energy 51 (2013) 274–281.

APPENDIX A

HISTORICAL MULTIBAND METHODS DERIVATIONS

There are many flavors of MB. This appendix seeks to describe some common variants and their advantages and shortcomings. This appendix also describes a possible extension of FEDS to the unresolved-resonance region (URR).

We desire subgroup fidelity that will allow the within-group flux shape to adapt to local shielding effects. We do this by assuming the resonance within-group shape flux shape in energy is $1/E$ multiplied by a shielding factor that depends on the local macroscopic total cross section only:

$$\psi(\mathbf{r}, E, \mathbf{\Omega}) \simeq \Psi(\mathbf{r}, \mathbf{\Omega})\, f_{\text{ss}}(\Sigma_t(E))\, \frac{1}{E}. \tag{A.1}$$

More generally, methods express f_{ss} as a function of macroscopic resonance absorption (or total) cross sections and a background cross section (XS): $f_{\text{ss}} = f_{\text{ss}}(\Sigma_{a/t}(E), \Sigma_0)$. The background cross section accounts for non-resonant nuclides such as moderators, for the equivalence cross section, and possibly potential resonance scattering. The equivalence cross section takes into account limited heterogeneity effects (see books on equivalence theory). The point is that f_{ss} is a function of the local macroscopic absorption (or total) resonance cross section only.

We do quadrature on reaction-rate-like terms:

$$\begin{aligned}
\int_{\Delta E_g} \mathrm{d}E\ \psi(\mathbf{r}, E, \mathbf{\Omega})\Sigma_t(E) &\simeq \Psi(\mathbf{r}, \mathbf{\Omega}) \int_{\Delta E_g} \frac{\mathrm{d}E}{E} f_{\mathrm{ss}}(\Sigma_t(E))\Sigma_t(E) \\
&= \Psi(\mathbf{r}, \mathbf{\Omega}) \int_{\Delta u_g} \mathrm{d}u\ f_{\mathrm{ss}}(\Sigma_t(u))\Sigma_t(u) \\
&= \Psi(\mathbf{r}, \mathbf{\Omega}) \int_{\Delta \sigma} \mathrm{d}\sigma\ p(\sigma) f_{\mathrm{ss}}(\sigma)\sigma \\
&\simeq \Psi(\mathbf{r}, \mathbf{\Omega}) \sum_{m=1}^{M} p_m f_{\mathrm{ss}}(\sigma_m)\sigma_m \\
&= \sum_{m=1}^{M} \Psi_m(\mathbf{r}, \mathbf{\Omega})\sigma_m. \qquad \text{(A.2)}
\end{aligned}$$

Here, $p_m \sim |\Delta u_m|$ is a quadrature weight corresponding to a lethargy area, $\Psi_m(\mathbf{r}, \mathbf{\Omega}) = \Psi(\mathbf{r}, \mathbf{\Omega}) p_m f_{\mathrm{ss}}(\sigma_m)$ is a MB flux, and σ_m is a quadrature point in XS space.

This quadrature idea applies to any function of total cross section; we can generate our quadratures to be exact for select powers of total cross section:

$$\int_{\Delta u_g} \mathrm{d}u\ g(\Sigma_t(u)) \simeq \sum_{m=1}^{M} p_m g(\sigma_m), \qquad \text{(A.3a)}$$

$$\int_{\Delta u_g} \mathrm{d}u\ \Sigma_t^l(u) = \sum_{m=1}^{M} p_m \sigma_m^l, \quad l = 0, \ldots, L(M). \qquad \text{(A.3b)}$$

So long as Eq. (A.1) is correct and we have an accurate quadrature scheme, we can capture reaction rates, flux values, and cross section moments of the true solution.

Partial reaction rates can similarly be treated with quadrature by incorporating

the idea of expectations:

$$\int_{\Delta E_g} \mathrm{d}E\ \psi(\mathbf{r}, E, \mathbf{\Omega})\Sigma_x(E) \simeq \psi(\mathbf{r}, \mathbf{\Omega}) \sum_{m=1}^{M} p_m f_{\mathrm{ss}}(\sigma_m) E(\sigma_x|\sigma_m) = \sum_{m=1}^{M} \Psi_m(\mathbf{r}, \mathbf{\Omega}) x_m, \tag{A.4}$$

where $E(\sigma_x|\sigma_t)$ is the expectation of the partial cross section given the total cross section and $x_m = \sigma_{x,m} = E(\sigma_x|\sigma_t = \sigma_m)$. The interpretation of x_m as an expectation is accurate in the URR.

In general, the angular flux is not a function of the local total macroscopic cross section only. It depends upon the local scattering kernel (which determines the source, Q) and non-local macroscopic cross sections (which determine the boundary flux into the region). For radiative transfer (RT) problems and problems with fast neutron fluxes, the angular flux also depends on the spectrum of the local source, which may not be smooth in energy or correlated to the local absorption XS.

Equation (A.1) is not the most egregious approximation made for MP MB. There are often correlation approximations within a group that affect how the macroscopic XS are formed from microscopic XS or resonance integrals (RI), there are approximations to the scattering kernel, and there are approximations for region interface conditions. These will be explained below.

A.1 Method 1: Different Flux Shielding Moments

Physically, near the edge of a material, the flux is unshielded. Near the inside, it becomes increasingly shielded. The unshielded flux goes as $1/E$. The NR flux goes as $(1/E)\ [1/(\sigma_t(E) + \sigma_0)]$. This progression inspires us to define cross section

moments with respect to different amounts of flux shielding:

$$f_m(\Sigma_t(u)) = \frac{1}{(\Sigma_t(u) + \Sigma_0)^m}, \tag{A.5a}$$

$$f_m(\Sigma_{t,n}) = \frac{1}{(\Sigma_{t,n} + \Sigma_0)^m}, \tag{A.5b}$$

$$(\Sigma_x)_m = \frac{\int\limits_{\Delta u_g} \mathrm{d}u \;\; f_m(\Sigma_t(u))\; \Sigma_x(u)}{\int\limits_{\Delta u_g} \mathrm{d}u \;\; f_m(\Sigma_t(u))}. \tag{A.5c}$$

Here we use macroscopic cross sections because they are the correct flux shapes. Σ_0 represents the equivalence XS or any (non-resonance) XS not included in Σ_t.

Using these definitions, we define band-wise total macroscopic cross sections and band probabilities which preserve moments of the total macroscopic cross section, similar to the quadrature idea in Eq. (A.2):

$$(\Sigma_t)_m = \frac{\sum\limits_{n=1}^{N} \Sigma_{t,n} P_n f_m(\Sigma_{t,n})}{\sum\limits_{n=1}^{N} P_n f_m(\Sigma_{t,n})} \quad m = 0, \ldots, M-1, \tag{A.6a}$$

$$\sum_{n=1}^{N} P_n = 1. \tag{A.6b}$$

Equation (A.6) consists of $M+1$ equations for $2N$ unknowns. The equations are M moment equations (Eq. (A.6a)) and 1 conservation equation (Eq. (A.6b)). The unknowns are N band macroscopic total cross sections, $\Sigma_{t,n}$, and N band probabilities, P_n. N is specified, so $M = 2N - 1$ is the number of required moments to be satisfied.

The system in Method 1 is nonlinear, as the unknowns appear together in the term $\Sigma_{t,n}P_n$ and nonlinearly in the term $f_m(\Sigma_{t,n})$. The system can be shown to be ill-posed unless we require $\Sigma_{t,n} \leq \Sigma_{t,n+1}$. There is no guarantee that the probabilities

are positive or that $\Sigma_{t,\min} \leq \Sigma_{t,n} \leq \Sigma_{t,\max}$.

Physically, $m = 0$ corresponds to unshielded, $m = 1$ corresponds to totally shielded flux, and $m = 2$ corresponds to totally shielded current [10].

Once the $\Sigma_{t,n}$ and P_n are known, the following system can be used to get the $\Sigma_{x,n}$:

$$(\Sigma_x)_m = \frac{\sum_{n=1}^{N} \Sigma_{x,n} P_n f_m(\Sigma_{t,n})}{\sum_{n=1}^{N} P_n f_m(\Sigma_{t,n})} \quad m = 0, \ldots, M' - 1, \tag{A.7}$$

for $x = c, f, s$, etc., where c is capture (n, γ), f is fission (n, f), and s is scattering, e.g. (n, n), (n, n'). Since the P_n are known, Eq. (A.7) is a set of M' linear equations for N unknowns, requiring $M' = N$.

The result of Method 1 is a set of band-wise macroscopic total cross sections, $\Sigma_{t,n}$, band-wise macroscopic partial cross sections, $\Sigma_{x,n}$, and band-wise probabilities, P_n, for each group g. We have suppressed the group subscript for readability.

Scattering is treated approximately within a group as

$$\Sigma_{s,(g',b')\to(g,b)} = \Sigma_{s,g',b'} T_{g'\to g} P_{g,b}, \tag{A.8}$$

where $\Sigma_{s,g',b'}$ is a $\Sigma_{x,n}$, $P_{g,b}$ is a P_n, and $T_{g'\to g}$ is the group-to-group scattering probability.

This ensures that

$$\sum_{b=1}^{B_g} \Sigma_{s,(g',b')\to(g,b)} = \Sigma_{s,g',b'} T_{g'\to g}, \tag{A.9a}$$

$$\sum_{g=1}^{G} \sum_{b=1}^{B_g} \Sigma_{s,(g',b')\to(g,b)} = \Sigma_{s,g',b'}, \tag{A.9b}$$

which upholds the definition of $\Sigma_{s,(g',b')\to(g,b)}$ as an energy-differential cross section.

There are two bounds on subgroup interface conditions. The first assumes complete correlation, and is given by

$$\psi_{g,b,\text{in}} = \psi_{g,b,\text{out}}. \tag{A.10a}$$

The other assumes no correlation and is given by

$$\psi_{g,b,\text{in}} = P_{g,b,\text{in}} \sum_{b'=1}^{B_g} \psi_{g,b',\text{out}}. \tag{A.10b}$$

Equation (A.10b) assumes that the flux is flatly redistributed within a group at a material interface such that the average downwind flux is the same for each band.

Implementing Eq. (A.10b) would require rewriting existing MG transport codes to advect bands within agroup together so interface conditions could be treated without lagging information. Such rewriting would allow more efficient treatment of within-group scattering: Eq. (A.8) may strongly couple all bands within a group.

Note that $P_{g,b}$ represents the normalized size of the band in energy space or lethargy space:

$$P_{g,b} \sim \frac{|\Delta E_{g,b}|}{|\Delta E_g|}, \tag{A.11a}$$

while $\psi_{g,b}$ represents the integrated angular flux over a band:

$$\psi_{g,b} \sim \int\limits_{\Delta E_{g,b}} \mathrm{d}E\ \psi(E). \tag{A.11b}$$

Here $\Delta E_{g,b}$ is the set of energies corresponding to the band. With MP MB, the $\Delta E_{g,b}$ are never actually constructed as they are with BP MB.

A.1.1 Implementation

As a matter of implementation, resonance integrals are normally computed ahead of time, often for the microscopic cross sections. A common practice is to have a code such as NJOY compute

$$\mathrm{RI}_{x,i,m} = \int\limits_{\Delta u_g} \mathrm{d}u \; \frac{\sigma_{x,i}(u)}{\left(\sigma_{t,i}(u) + \sigma_0\right)^m} \tag{A.12a}$$

or, if material information is known or can be approximated,

$$\mathrm{RI}_{x,i,m} = \int\limits_{\Delta u_g} \mathrm{d}u \; \frac{\sigma_{x,i}(u)}{\left(\Sigma_t(u) + \Sigma_0\right)^m} \tag{A.12b}$$

for several σ_0 or Σ_0 values and several m values ahead of time. Care must be taken when converting from microscopic to macroscopic cross resonance integrals, as the proper denominator involves the macroscopic quantities. One instance where Eq. (A.12a) and Eq. (A.12b) are equivalent is when there is only one resonant nuclide in a material, a case often used in the literature.

For ease of notation, we define $\sigma_{x=0,i} \equiv 1$, such that

$$\mathrm{RI}_{0,i,m} = \int\limits_{\Delta u_g} \mathrm{d}u \; \frac{1}{\left(\Sigma_t(u) + \Sigma_0\right)^m}. \tag{A.13}$$

One idea which preserves the spirit of non-correlation is to use the approximation that the current resonant nuclide is the only resonant nuclide when computing the resonance integrals. In this case,

$$\mathrm{RI}_{x,i,m} = \int\limits_{\Delta u_g} \mathrm{d}u \; \frac{\sigma_{x,i}(u)}{\left(\Sigma_t(u) + \Sigma_0\right)^m} \simeq \frac{1}{N_i^m} \int\limits_{\Delta u_g} \mathrm{d}u \; \frac{\sigma_{x,i}(u)}{\left(\sigma_{t,i}(u) + \lambda_i\right)^m}, \tag{A.14a}$$

where

$$\lambda_i \equiv \sum_{j \neq i} \frac{N_j}{N_i} \bar{\sigma}_{t,j} + \frac{1}{N_i} \Sigma_e, \tag{A.14b}$$

$$\bar{\sigma}_{t,j} \simeq \frac{\mathrm{RI}_{t,j,1}}{\mathrm{RI}_{0,j,1}}. \tag{A.14c}$$

The approximation in $\bar{\sigma}_{t,j}$ comes about because the background, not the average, value should be used in λ_i. The above equations require a Bondarenko iterative process to find the λ_i, which play the role of background cross sections.

If using several flux moments, several resonance integrals will be required. It might be easiest to use one λ_i, determined by the $m = 1$ flux, as shown above.

Once the λ_i and $\bar{\sigma}_{t,j}$ have been computed, one must calculate the $(\Sigma_x)_m$ from the RI. This is non-trivial because

$$\frac{1}{(\Sigma_t(u) + \Sigma_0)^m} \neq N_i^{-m} \frac{1}{(\sigma_{t,i}(u) + \lambda_i)^m} \tag{A.15}$$

in general.

There are several options, including

A Ignore Eq. (A.15) and define

$$(\Sigma_x)_m = \sum_i N_i \frac{\mathrm{RI}_{x,i,m}}{\mathrm{RI}_{0,i,m}}. \tag{A.16a}$$

This term-by-term division of the RI may minimize the error from Eq. (A.15) by using a nuclide-consistent numerator and denominator RI.

B Approximate the left-hand of Eq. (A.15) by defining

$$(\Sigma_x)_m = \frac{\sum_i N_i \, \mathrm{RI}_{x,i,m} \, n_{i,m}}{\sum_i w_i \, \mathrm{RI}_{0,i,m} \, n_{i,m}}, \tag{A.16b}$$

$$n_{i,m} = N_i^{-m}, \tag{A.16c}$$

$$\sum_i w_i = 1. \tag{A.16d}$$

The $n_{i,m}$, which divide out term-by-term in Eq. (A.16a), can be adjusted to include any differences in normalization among the disparate nuclides.

The w_i simply provide a way of averaging the distinct $\mathrm{RI}_{0,i,m}$. Two obvious choices would be a straight average or to use $w_i = \delta_{i,r}$ for dominant resonant nuclide r.

C Ignore all correlation assumptions and define

$$(\sigma_{x,i})_m = \frac{\mathrm{RI}_{x,i,m}}{\mathrm{RI}_{0,i,m}}, \tag{A.16e}$$

$$(\sigma_{x,i})_m = \frac{\sum_{n=1}^{N} \sigma_{x,i,n} P_{i,n} f_m(\sigma_{t,i,n})}{\sum_{n=1}^{N} P_{i,n} f_m(\sigma_{t,i,n})}, \tag{A.16f}$$

This yields nuclide-specific band-dependent cross sections and band probabilities. Such data are used, for example, in MC calculations or for deterministic calculations where the number of unknowns is increased to be dependent on the number of resonant nuclides (see Section A.6).

Notice that this may not be useful for Method 1, as formation of the λ_i and hence $\bar{\sigma}_{t,j}$ are required for this method, meaning the nuclides need to be coupled before the band calculation from the moments anyway.

If region-independent microscopic XS are desired, set $\lambda_i = 0$. This is a rather

severe approximation, but allows each nuclide to be computed independently. What should not be done, but what I have noticed in the literature, is to sum the band-dependent cross sections:

$$\Sigma_{x,n} = \sum_i N_i \sigma_{x,n} \quad \text{(bad)}. \tag{A.16g}$$

Equation (A.16g) implicitly assumes the microscopic cross sections have the same band structure. A band refers to a set of energies within the group that have similar total cross section. (In MP MB, this energy range is never explicitly formed, but its concept still exists.) If different total cross sections are used, as in Eq. (A.16f), this implies different band structures. Further, the band probabilities, $P_{i,n}$, refer to the size of the band in lethargy or energy space. When different nuclides have different band probabilities, it is impossible to combine them without blatantly ignoring correlation effects.

To be specific, Eq. (A.16g) assumes full correlation between the bands, which is not the case for MP MB. This is why Eqs. (A.6a) and (A.7) are defined with respect to macroscopic cross sections, so that they are consistent within a material.

D Preserve Eq. (A.15) and use the macroscopic total cross section in the denominator of the RI. That is, use Eqs. (A.12b) and (A.13). Notice this requires forming the total cross section as a function of energy, which involves knowledge of both the material and detailed cross sections. This option is more expensive and may not allow some of the memory and time savings of the previous methods. However, this method does not require computation or iteration of the λ_i or $\bar{\sigma}_{t,j}$, as the true macroscopic cross section is explicitly formed as a function of energy.

An algorithm for options A and B above might look something like

1. Preprocess in NJOY:

   Compute microscopic resonance integrals (Eq. (A.12a)) for several values of σ_0 and m (and possibly temperature) for each group for each nuclide independently.

2. Begin problem-specific XS preparation:

   (a) Guess the background cross sections, the λ_i.

   (b) Compute escape XS using Dancoff factors or a similar method.

   (c) Interpolate the resonance integrals and compute the $\bar{\sigma}_{t,j}$ using Eq. (A.14c).

   (d) Compute background cross sections using Eq. (A.14b) with equivalence XS from above.

   (e) Iterate between 2c and 2d.

3. Once the converged, material-specific background XS are known, combine resonance integrals to form macroscopic XS moments using Eq. (A.16a) or Eq. (A.16b).

4. For each material, determine band probabilities, and total and partial band XS using Eq. (A.6) and Eq. (A.7).

Instead of storing the RI for several σ_0 and T, one could store coefficients for a functional approximation, which could save substantial data.

An algorithm for option D above might look something like

1. Preprocess in NJOY by computing hyperfine-group (HFG) XS, possibly for several temperatures.

2. Determine equivalence XS using Dancoff factors or an HFG fixed-source slowing-down problem (FSSDP).

3. Replace integrals in Eq. (A.5c) with sums over the HFG structure, using only the equivalence XS for the background XS term. Compute macroscopic XS moments using material composition.

4. For each material, determine band probabilities, and total and partial band XS using Eq. (A.6) and Eq. (A.7).

Note that this algorithm is more expensive, as it requires storage and manipulation of the HFG XS. Aside from more rigorous math and a potentially more exact quadrature set, the advantage of the MP method over the BP method is avoiding the expense of computing and storing the HFG representation of the XS. Since MP MB is already approximate with regard to scattering kernel and material interface conditions, the extra work required for option D may not be justified.

A resonance interference factor (RIF) [50] should be used to get the shielded scattering matrix from an unshielded matrix for option D. This would allow the scattering matrix to only be stored in coarse form, not in HFG representation.

Option D could alternatively use CE instead of HFG.

A.1.2 Method 1a: Recalculated band probabilities

Since $M' < M$, there are multiple choices of sets of moments to preserve the partial XS. Some authors claim this makes the band probabilities and partial cross sections inconsistent. A common remedy is to use Eq. (A.6) to calculate the $\Sigma_{t,n}$ and P_n, and then to calculate P'_n by preserving moments $m = 0, \ldots, M' - 1$ of Eq. (A.6a) using the previously calculated $\Sigma_{t,n}$. This is a linear solve. The P'_n then replace the P_n before the calculation in Eq. (A.7) and are used thereafter as the band

probabilities. Notice this does not guarantee that $\sum_{n=1}^{N} P'_n = 1$.

A.1.3 Method 1b: Evenly-weighted band probabilities

A common early variant of Method 1 is to set the P_n ahead of time (e.g., [26]). Method 1b sets

$$\hat{P}_n = \frac{1}{N}. \tag{A.17}$$

Since the probabilities are already determined, solving Eq. (A.6) requires $M = N$ moments.

This linearizes the system and is similar to the Russian approach, [25], except the latter is potentially iterated. Ribon and Maillard [14] points out that this is less accurate than allowing the P_n to vary by band and that it preserves fewer moments.

A.1.4 Method 1c: Intermediate resonance approximation

Our derivation of Method 1 involved using the NR approximation. This can easily be extended to the IR approximation, which many authors claim is superior. In the IR approximation, only some of the resonant nuclide's scattering cross section is assumed to be resonant (the rest is treated as background). Caution must be taken when doing so, as the IR simply provides a knob that varies from NR to WR (wide resonance). Neither of these limits is correct, especially in heterogeneous systems. The same approximations that the flux only depends on the local macroscopic cross section still apply.

A.1.5 Method 1d: Planck and Rosseland moments

A variant of Method 1 for radiative transfer is to preserve Planck and Rosseland moments of the cross section. If Method 1 is used, $M = 2N - 1$ and is always odd. A third moment must be added, usually a "super-Rosseland" mean (cf. [10]). If

Method 1b is used, $M = N$, and only the two moments are required.

In RT applications, there is often a single material in a region, simplifying the implementation of Method 1d. This is equivalent to the simplifying case of the macroscopic XS having only one resonant component above.

A.2 Method 2: Different Background XS

Another method to capture the different flux environments seen within a material due to self-shielding is to use multiple background XS for the XS moments. Low background XS correspond to highly shielded environments seen, for example, in the center of fuel pins. High background XS correspond to less shielded or unshielded environments seen, for example, at the edge of fuel pins.

Method 2 is highly similar to Method 1, differing in the definition of the flux factor used for the moments:

$$F_l(\Sigma_t(u)) = \frac{1}{\Sigma_t(u) + \Sigma_{0,l}}, \tag{A.18a}$$

$$F_l(\Sigma_{t,n}) = \frac{1}{\Sigma_{t,n} + \Sigma_{0,l}}, \tag{A.18b}$$

$$\Sigma_{0,l} = \bar{N} 10^l, \tag{A.18c}$$

$$[\Sigma_x]_l = \frac{\int\limits_{\Delta u_g} \mathrm{d}u \; F_l(\Sigma(u))\Sigma_x(u)}{\int\limits_{\Delta u_g} \mathrm{d}u \; F_l(\Sigma_x(u))}, \tag{A.18d}$$

where $\bar{N}$ is a representative atom density for the material. Method 2, like Method 1, normally uses microscopic RI that are combined into macroscopic moments which are used to determine the band parameters. As in Method 1, this introduces approximations not present if the macroscopic XS are used throughout.

Background XS are conventionally used with the microscopic (per-nuclide) application of the NR approximation. To preserve this interpretation (and units) when

dealing with macroscopic XS, we have introduced $\bar{N}$, which should be the atom density of the resonant nuclides or dominant resonance nuclide in the material.

As in Method 1, a quadrature representation is used to preserve $M = 2N - 1$ background XS moments to determine the band-dependent total XS, $\Sigma_{t,n}$, and band probabilities, P_n, using Eq. (A.6) with $[\Sigma_t]_l$ instead of $(\Sigma_t)_m$. Once these are known, the band-dependent partial XS, $\Sigma_{x,n}$ are calculated through Eq. (A.7) in the same manner as Method 1, again with $[\Sigma_x]_l$ replacing $(\Sigma_x)_m$.

Method 2 has similar variants as Method 1. The recalculated band probabilities (Method 1a, Section A.1.2), evenly-weighted band probabilities (Method 1b, Section A.1.3), and intermediate-resonance approximation (Method 1c, Section A.1.4) map directly to Method 2. Using Planck and Rosseland moments (Method 1d, Section A.1.5) does not easily map, as there is no background XS for those moments.

In Method 1, the background cross sections are iterated to consistency in a Bondarenko fashion using the λ_i's and $\bar{\sigma}_{t,j}$'s (Eqs. (A.14b) and (A.14c)). In traditional implementations of Method 2, no such iteration is performed. We now make the argument for why this is disadvantageous and introduce a scheme that reintroduces this concept.

Not using the λ_i's leads to a lack of consistency. To see why, take two hypothetical nuclides, $\mathcal{A}$ and $\mathcal{B}$. Both are resonant nuclides and but nuclide $\mathcal{A}$ has a high background XS while $\mathcal{B}$ has a low background XS. Say we are in a regime where the NR approximation is valid. For simplicity, the material only contains the two above nuclides in equal atom densities. Say we want to add in a very small background XS. Then the flux moment we would use is

$$F(u) = \frac{1}{\sigma_{\mathcal{A}}(u) + \sigma_{\mathcal{B}}(u) + \epsilon}, \tag{A.19a}$$

for some small ϵ.

Using independence and the NR approximation, we could instead use

$$F_{\mathcal{A}}(u) = \frac{1}{\sigma_{\mathcal{A}}(u) + \bar{\sigma}_{\mathcal{B}} + \epsilon} = \frac{1}{\sigma_{\mathcal{A}}(u) + \sigma_{0,\mathcal{A}}} \tag{A.19b}$$

for nuclide $\mathcal{A}$, and

$$F_{\mathcal{B}}(u) = \frac{1}{\bar{\sigma}_{\mathcal{A}} + \sigma_{\mathcal{B}}(u) + \epsilon} = \frac{1}{\sigma_{\mathcal{B}}(u) + \sigma_{0,\mathcal{B}}} \tag{A.19c}$$

for nuclide $\mathcal{B}$, where $\bar{\sigma}_{\mathcal{A}}$ and $\bar{\sigma}_{\mathcal{B}}$ are the background XS for nuclides $\mathcal{A}$ and $\mathcal{B}$ chosen to make $F(u) \simeq F_{\mathcal{A}}(u) \simeq F_{\mathcal{B}}(u)$ in some sense.

Because $\bar{\sigma}_{\mathcal{A}} \gg \bar{\sigma}_{\mathcal{B}} \gg \epsilon$ by assumption, then $\sigma_{0,\mathcal{A}} \gg \sigma_{0,\mathcal{B}}$. However, Method 2 requires us to use the same background XS, $\sigma_{0,l}$, for both nuclides:

$$F_{\mathcal{A},l}(u) = \frac{1}{\sigma_{\mathcal{A}}(u) + \sigma_{0,l}}, \tag{A.19d}$$

$$F_{\mathcal{B},l}(u) = \frac{1}{\sigma_{\mathcal{B}}(u) + \sigma_{0,l}}. \tag{A.19e}$$

This equates to using a different flux for each nuclide: $F_{\mathcal{A},l} \neq F_{\mathcal{B},l}$. This poses problems when the microscopic XS moments are added together to form macroscopic XS moments, as the moments *should* use the same weighting fluxes but do not.

Another problem is over-shielding the current resonant nuclide. The amount of background that nuclide $\mathcal{A}$ sees should always be at least $\bar{\sigma}_{\mathcal{B}}$. However, there is nothing stopping someone from picking $\sigma_{0,l} \ll \bar{\sigma}_{\mathcal{B}}$ in Eq. (A.19d). This argument becomes more cogent if nuclide $\mathcal{B}$ were a moderator.

A potential fixup for both of these difficulties would be to add two sources of

background XS:

$$F_{i,l}(u) = \frac{1}{\sigma_i(u) + \kappa_i + \frac{\tilde{N}}{N_i}\sigma_{0,l}}, \tag{A.20}$$

with $\kappa_i = \sum_{j \neq i} N_j / N_i \sigma_{t,j}$. κ_i and the $\sigma_{0,l}$ term can be combined into $\lambda_{i,l}$ and a Bondarenko-like iteration as in Method 1 (Eqs. (A.14b) and (A.14c)) can be used.

Equation (A.20) would give consistency between the microscopic implementations of Method 2 and the macroscopic implementation. I have not seen this done in the literature.

While the flux generally does not become more shielded than $1/(\sigma_i(u) + \kappa_i)$, it does become less shielded, say near the edge of the fuel for incoming fluxes. Equation (A.20) preserves these physics.

This is one area where Method 2 outperforms Method 1. In Method 1, all higher moments are more shielded than the $m = 1$ moment, which is the maximum amount of shielding desired. In Method 2, using Eq. (A.20), $\sigma_{0,l}$ provides a knob to go between fully shielded ($\sigma_{0,l} = 0$) and fully unshielded ($\sigma_{0,l} \to \infty$). Additionally, different $\sigma_{0,l}$ now represent different escape XS.

If we wish to use microscopic RI for our implementation, we use Eq. (A.20) to

define the flux instead of Eq. (A.18a). We define our microscopic RI as

$$\mathrm{RI}_{x,i,l} = \int\limits_{\Delta u_g} \mathrm{d}u \; \frac{\sigma_{x,i}(u)}{\sigma_{t,i}(u) + \lambda_{i,l}}, \tag{A.21a}$$

$$\mathrm{RI}_{0,i,l} = \int\limits_{\Delta u_g} \mathrm{d}u \; \frac{1}{\sigma_{t,i}(u) + \lambda_{i,l}}, \tag{A.21b}$$

$$\lambda_{i,l} = \sum_{j \neq i} \frac{N_j}{N_i} \bar{\sigma}_{t,j} + \frac{\bar{N}}{N_i} \sigma_{0,l}, \tag{A.21c}$$

$$\sigma_{0,l} = 10^l, \tag{A.21d}$$

$$\bar{\sigma}_{t,j} = \frac{\mathrm{RI}_{t,j,-\infty}}{\mathrm{RI}_{0,j,-\infty}}, \tag{A.21e}$$

for several values of $\sigma_{0,l}$. We can once again use NJOY or a similar code to precompute RI for several values of λ and interpolate during the Bondarenko iteration.

Using Eq. (A.21) to define the RI, we reuse the implementations from Section A.1.1. For option A, simply replace m terms with l terms. For option B, again replace m's with l's and set $n_{i,m} = N_i^{-1}$. For option C, iterate to consistency, or take $\lambda_{i,l} = \sigma_{0,l}$ and do no iteration. Option D in Section A.1.1, which uses macroscopic RI, is essentially the same for Method 1 and Method 2, differing only in the definition of the flux weighting, $f_m(\Sigma_t)$ vs. $F_L(\Sigma_t)$.

As a final note, instead of exactly preserving quadrature integrals as in Eqs. (A.6) and (A.7) for a certain number of moments, many authors minimize the L^2 error by approximately preserving many more moments. A common way to do this is to fit $[\Sigma_t](\sigma_{0,l})$ to a functional form and then choose a quadrature scheme that approximates this function either at discrete values of the function or in an L^2 sense over the entire domain. In the former case, this could allow the same moments for $[\Sigma_t]_l$ and $[\Sigma_x]_l$ to be approximately preserved. Depending on how the non-linear iteration were carried out, this scheme might yield strictly positive band probabilities. Care

must be taken such that $\sum_n P_n = 1$ still holds. See [41] for an example of using L^2 error minimization with physical constraints such as positivity on XS and band probabilities.

A.3 Method 3: Different XS Moments

By far the most popular method in the recent literature is to preserve moments of the cross sections directly:

$$\langle \Sigma_t^m \rangle = \frac{1}{\Delta E_g} \int\limits_{\Delta E_g} \mathrm{d}E \; \Sigma_t^m(E), \qquad m = -M^-, \ldots, 0, \ldots, M^+, \tag{A.22a}$$

$$\langle \Sigma_t^m \rangle = \sum_{n=1}^{N} p_n \sigma_n^m, \qquad m = -M^-, \ldots, 0, \ldots, M^+, \tag{A.22b}$$

$$\langle \Sigma_x \Sigma_t^m \rangle = \frac{1}{\Delta E_g} \int\limits_{\Delta E_g} \mathrm{d}E \; \Sigma_x(E) \Sigma_t^m(E), \qquad m = -M'^-, \ldots, 0, \ldots, M'^+, \tag{A.22c}$$

$$\langle \Sigma_x \Sigma_t^m \rangle = \sum_{n=1}^{N} p_n x_n \sigma_n^m, \qquad m = -M'^-, \ldots, 0, \ldots, M'^+, \tag{A.22d}$$

where $\Sigma_t^m(E) = (\Sigma_t(E))^m$ and $x_n = E(\Sigma_x | \Sigma_t = \sigma_n)$.

The rationale behind this is to preserve the Laurent series of functions that depend

solely on the total cross section:

$$f(\sigma) = \ldots + \frac{a_{-2}}{\sigma^2} + \frac{a_{-1}}{\sigma} + a_0 + a_1\sigma + a_2\sigma^2 + \ldots,$$

$$f(\sigma) = \sum_{i=-\infty}^{\infty} a_i \sigma^i, \tag{A.23a}$$

$$f(\sigma) \simeq \hat{f}(\sigma) = \sum_{i=-M^-}^{M^+} a_i \sigma^i, \tag{A.23b}$$

$$\begin{aligned}
\frac{1}{\Delta E_g} \int\limits_{\Delta E_g} \mathrm{d}E\ f(\Sigma_t(E)) &= \sum_{i=-\infty}^{\infty} a_i \frac{1}{\Delta E_g} \int\limits_{\Delta E_g} \mathrm{d}E\ \Sigma_t^i(E), \\
&\simeq \sum_{i=-M^-}^{M^+} a_i \frac{1}{\Delta E_g} \int\limits_{\Delta E_g} \mathrm{d}E\ \Sigma_t^i(E), \\
&= \sum_{i=-M^-}^{M^+} a_i \int\limits_{\Delta\sigma} \mathrm{d}\sigma\ p(\sigma)\sigma^i, \\
&= \sum_{i=-M^-}^{M^+} a_i \sum_{n=1}^{N} p_n \sigma_n^i, \\
&= \sum_{n=1}^{N} p_n \hat{f}(\sigma_n), \\
&\simeq \sum_{n=1}^{N} p_n f(\sigma_n).
\end{aligned} \tag{A.23c}$$

Notice the approximation here is not in the quadrature representation of the integral but in the truncation of the expansion of f. Recall that $p(\sigma)$ acts as a Jacobian when going from energy space to XS space and is physically positive.

As in the previous methods, if the groupwise total flux depends solely on local macroscopic total cross section, then Method 3 will preserve integrals of this quantity such as group fluxes and reaction rates. We repeat that this is assumption is not justified for real systems.

The moments method was first introduced by Ribon and Maillard [14] in a paper

that is often the foundation of MB work done by authors today.

With a technique reminiscent of the previous methods, N macroscopic total XS quadrature points and N band probabilities (quadrature weights) are chosen to preserve Eq. (A.22b) for $2N$ moments. Normally, the moments used are $-(N-1), \ldots, 0, 1, \ldots, N$, implying $M^- = N-1$ and $M^+ = N$. It is useful to use moments 0 and 1 in particular because they correspond to conservation and correct integral of the total reaction rate with constant flux, respectively.

The algorithm to implement the required nonlinear solve is discussed below. Method 3 was developed so that the nonlinear portion of the algorithm only involved finding the roots of a polynomial from a Padé expression.

Once the total XS band values and probabilities have been found, a linear solve is often done to define N partial XS quadrature points by preserving N moments through Eq. (A.22d). This is done for each partial XS. More details are given below. For now, just take $M'^{\pm} < M^{\pm}$, and $M'^{\pm} \geq 1$.

The following gives an algorithm to compute the band parameters from the XS moments using Padé forms. It is reproduced from [14].

Let

$$m_n = \frac{1}{\Delta E_g} \int\limits_{\Delta E_g} \mathrm{d}E \; \Sigma_t^n(E) = \int\limits_{\Delta\sigma} \mathrm{d}\sigma \; p(\sigma)\sigma^n, \tag{A.24a}$$

$$M_n = \sum_{i=1}^{N} P_i \sigma_i^n, \tag{A.24b}$$

$$\begin{aligned} F(z) &= \int\limits_{\Delta\sigma} \mathrm{d}\sigma \; p(\sigma) \frac{1}{1 - z\sigma} \\ &= \int\limits_{\Delta\sigma} \mathrm{d}\sigma \; p(\sigma) \left(1 + z\sigma + \ldots + z^k\sigma^k + \ldots\right) \\ &= m_0 + m_1 z + \ldots + m_{2N-1} z^{2N-1} + \mathfrak{R}\left(z^{2N}\right) \\ &= \frac{a_0 + a_1 z + \ldots + a_{N-1} z^{N-1}}{1 + b_1 z + \ldots + b_N z^N} + \mathfrak{R}'\left(z^{2N}\right) \\ &= \frac{P_{N-1}(z)}{Q_N(z)} + \mathfrak{R}'\left(z^{2N}\right) \\ &= \frac{P_{N-1}(z)}{\prod_{i=1}^{N}\left(1 - z/z_i\right)} + \mathfrak{R}'\left(z^{2N}\right) \\ &= \sum_{i=1}^{N} \frac{\omega_i}{1 - z/z_i} + \mathfrak{R}'\left(z^{2N}\right), \end{aligned} \tag{A.24c}$$

$$\begin{aligned} F(z) &= M_0 + M_1 z + \ldots + M_{2N-1} z^{2N-1} + \mathcal{R}\left(z^{2N}\right) \\ &= \sum_{i=1}^{N} P_i \left(1 + \sigma_i z + \sigma_i^2 z^2 + \ldots + \sigma_i^{2N-1} z^{2N-1}\right) + \mathcal{R}\left(z^{2N}\right) \\ &= \sum_{i=1}^{N} \frac{P_i}{1 - \sigma_i z} + \mathcal{R}'\left(z^{2N}\right), \end{aligned} \tag{A.24d}$$

where preservation of the desired moments, $n = 0, \ldots, 2N-1$, is used to equate $M_n = m_n$ in the first step of Eq. (A.24d).

Once the z_i and ω_i are known, it is simple to determine the quadrature weights

and abscissas. Equating Eq. (A.24c) and Eq. (A.24d), we find

$$P_i = \omega_i, \tag{A.24e}$$

$$\sigma_i = 1/z_i. \tag{A.24f}$$

Per Ribon and Maillard [14], using the Padé form introduces minimal errors in Eq. (A.24c) compared to the errors present in Eq. (A.24d):

$$\Re'\left(z^{2N}\right) \ll \mathcal{R}'\left(z^{2N}\right). \tag{A.24g}$$

The above derivation assumed $M^- = 0$. For more general M^-, we find, using $I = -M^-$ for consistency with Ribon and Maillard [14],

$$\begin{aligned} F(z) &= \int_{\Delta\sigma} \mathrm{d}\sigma\ p(\sigma)\sigma^I \frac{1}{1-z\sigma} \\ &= M_I + M_{I+1}z + \ldots + M_{I+2N-1}z^{2N-1} + \mathcal{R}\left(z^{2N}\right) \\ &= \sum_{i=1}^{N} P_i\sigma_i^I \left(1 + \sigma_i z + \sigma_i^2 z^2 + \ldots + \sigma_i^{2N-1} z^{2N-1}\right) + \mathcal{R}\left(z^{2N}\right) \\ &= \sum_{i=1}^{N} \frac{P_i\sigma_i^I}{1-\sigma_i z} + \mathcal{R}'\left(z^{2N}\right). \end{aligned} \tag{A.25a}$$

This in turn implies:

$$P_i = \omega_i\sigma_i^{-I}, \tag{A.25b}$$

$$\sigma_i = 1/z_i. \tag{A.25c}$$

We still need to determine the z_i and ω_i. The first step in this process is solving for the coefficients in $P_{N-1}(z)$ and $Q_N(z)$. The a_n and b_n in $P_{N-1}(z)$ and $Q_N(z)$,

respectively, may be found using one linear solve. The system is to determine the b_n is:

$$\begin{aligned} 0 &= m_N + m_{N-1}b_1 + \ldots + m_0 b_N, \\ &\vdots \\ 0 &= m_{2N-1} + m_{2N-2}b_1 + \ldots + m_{N-1}b_N. \end{aligned} \tag{A.26a}$$

Once the b_n are known, the a_n may be computed without an additional linear solve:

$$\begin{aligned} a_0 &= m_0, \\ a_1 &= m_1 + m_0 b_1, \\ &\vdots \\ a_{N-1} &= m_{N-1} + m_{N-2}b_1 + \ldots + m_0 b_{N-1}. \end{aligned} \tag{A.26b}$$

The roots, z_i, $i = 1, \ldots, N$, are the roots of $Q_N(z) = 1 + b_1 z + \ldots + b_N z^N$. There are many routines that can determine all the roots of polynomials. In this case the task is made simpler because the roots are real, there are no double roots and all the roots are known to be in $(1/\Sigma_{\max}, 1/\Sigma_{\min})$ (see below).

Once the roots are known, the ω_i can be calculated using another linear solve.

Coefficient matching is used to determine the matrix:

$$\begin{aligned}
\frac{P_{N-1}(z)}{\prod_{i=1}^{N}(1-z/z_i)} &= \sum_{i=1}^{N}\frac{\omega_i}{1-z/z_i}, \\
P_{N-1}(z) &= \sum_{i=1}^{N}\omega_i\left(\prod_{\substack{j=1\\ i\neq j}}^{N}1-\frac{z}{z_j}\right), \\
\sum_{k=0}^{N-1}a_k z^k &= \sum_{i=1}^{N}\omega_i\sum_{l=0}^{N-1}c_{i,l}z^l, \\
a_j &= \sum_{i=1}^{N}c_{i,j}\omega_i, \quad j=0,\ldots,N-1, \\
\mathcal{C}^{\mathsf{T}}\boldsymbol{\omega} &= \mathbf{a}, \qquad \text{(A.27a)}
\end{aligned}$$

with $(\mathcal{C})_{i,j} = c_{i,j}$. This is a system with N unknowns and N equations that is not singular so long as there are no repeated roots. Per Ribon and Maillard [14], repeated roots only occur if $p(\sigma)$ is composed of fewer than N Dirac measures and only this.

Combinatorics are used to determine the coefficients of the matrix:

$$c_{i,j} = \sum_{\boldsymbol{\alpha}\in\mathcal{S}_{i,j}}\frac{1}{z_1^{\alpha_1}z_2^{\alpha_2}\cdots z_{i-1}^{\alpha_{i-1}}z_{i+1}^{\alpha_{i+1}}\cdots z_N^{\alpha_N}}, \qquad \text{(A.27b)}$$

$$\mathcal{S}_{i,j} = \left\{\boldsymbol{\alpha} = \{\alpha_1,\ldots\alpha_N\} \mid \alpha_{k\neq i}\in\{0,1\}, \alpha_i = 0, \sum_{k=1}^{N}\alpha_k = j\right\}, \qquad \text{(A.27c)}$$

$$|\mathcal{S}_{i,j}| = \binom{N-1}{j} \qquad \text{(A.27d)}$$

For example, for $N = 4$,

$$
\begin{aligned}
c_{4,0} &= 1, \\
c_{4,1} &= -\left(\frac{1}{z_1} + \frac{1}{z_2} + \frac{1}{z_3}\right), \\
c_{4,2} &= \frac{1}{z_1 z_2} + \frac{1}{z_1 z_3} + \frac{1}{z_2 z_3}, \\
c_{4,3} &= -\frac{1}{z_1 z_2 z_3}.
\end{aligned}
$$

Solving Eq. (A.27a) allows one to determine the band probabilities, P_i. An alternative option, chosen by authors such as [15], is to instead get the P_i by preserving the N XS moments used for the partial XS but with the recently calculated total XS quadrature points:

$$
\langle \Sigma_t^m \rangle = \sum_{i=1}^{N} P_i \sigma_i^m, \quad m = -M'^{-}, \ldots, 0, \ldots, M'^{+}.
$$

Notice that if $m = 0$ is included, as shown above, that $1 = \sum_{i=1}^{N} P_i$ is preserved. Further notice that if the ω_i are not desired, the matrix $\mathcal{C}$ does not need to be formed (Eq. (A.27b)), nor do the a_n need to be calculated (Eq. (A.26b)).

Method 3 is characterized by a much stronger foundation in mathematical theory. The resultant quadrature, $\{p_n, \sigma_n\}$, has several notable properties, including

1. A quadrature with N points is exact for $2N$ moments,
2. If the moment $m = 0$ is used, the quadrature is conservative: $\sum_{n=1}^{N} p_n = 1$,
3. For everywhere-positive (physical) $p(\sigma)$, the weights are all positive: $p_n > 0$,
4. The quadrature points lie strictly within the domain: $\min_{\Delta E_g} \Sigma_t(E) < \sigma_n < \max_{\Delta E_g} \Sigma_t(E)$,

5. The probabilities, which act as normalized energy areas, are collocated with their quadrature points in the following sense:

   - Let S_i be such that $\int_{\Sigma_{t,\min}}^{S_1} \mathrm{d}\sigma\ p(\sigma) = p_1$, $\int_{S_1}^{S_2} \mathrm{d}\sigma\ p(\sigma) = p_2$, etc.
   - Then $\Sigma_{t,\min} < \sigma_1 < S_1 < \sigma_2 < S_2 < \ldots < S_{N-1} < \sigma_N < \Sigma_{t,\max}$

6. The quadrature is convergent and converges stably for physically accurate moments,

7. The quadrature is sensitive to noise, especially in the higher-order moments (see [14] for more details).

Notice that none of the above apply to the x_m, which are the expectation values of the partial XS. The Padé method used to determine the quadrature scheme does not have a straightforward multivariate extension. Ribon and Maillard [14] attempted to add in the partial XS moments to the main quadrature calculation without success. Future authors have determined the partial XS quadrature points after the main calculation to get the total XS quadrature points and weights, as is the done with Method 1 and Method 2. This requires a linear solve, though the resultant partial XS quadrature points have no guarantee of positivity.

Whereas $2N$ moments are used for the total XS quadrature points and probabilities calculation, only N moments are used for the partial XS calculation, implying an inconsistency. At the least, there is a choice for which subset of the $2N$ moments to use, leading to multiple valid sets of partial XS quadrature points. Some authors have used an L^2 fit to all $2N$ points in an attempt for maximum consistency. Others have thrown out the probabilities determined from the $2N$ moment calculation and instead recalculated probabilities to satisfy N moments of the total XS with known total XS quadrature points. The partial XS quadrature calculation uses these same

N moments for consistency. This latter method may produce negative probabilities.

Ribon and Maillard [14] did determine an algorithm to determine the macroscopic XS moments from microscopic XS moments which relies on using positive moments and invoking independence of moments:

$$\begin{aligned}
\langle \Sigma^n(E) \rangle &= \frac{1}{\Delta E_g} \int\limits_{\Delta E_g} \mathrm{d}E \; \Sigma^n(E) \\
&= \frac{1}{\Delta E_g} \int\limits_{\Delta E_g} \mathrm{d}E \; (N_1 \sigma_1(E) + N_2 \sigma_2(E))^n \\
&= \frac{1}{\Delta E_g} \int\limits_{\Delta E_g} \mathrm{d}E \; \sum_{i=0}^{n} \binom{n}{i} N_1^i \sigma_1^i(E) N_2^{n-i} \sigma_2^{n-i}(E) \\
&= \sum_{i=0}^{n} \binom{n}{i} N_1^i N_2^{n-i} \frac{1}{\Delta E_g} \int\limits_{\Delta E_g} \mathrm{d}E \; \sigma_1^i(E) \sigma_2^{n-i}(E) \\
&\simeq \sum_{i=0}^{n} \binom{n}{i} N_1^i N_2^{n-i} \left(\frac{1}{\Delta E_g} \int\limits_{\Delta E_g} \mathrm{d}E \; \sigma_1^i(E) \right) \left(\frac{1}{\Delta E_g} \int\limits_{\Delta E_g} \mathrm{d}E \; \sigma_2^{n-i}(E) \right) \\
&\simeq \sum_{i=0}^{n} \binom{n}{i} N_1^i N_2^{n-i} \langle \sigma_1^i \rangle \langle \sigma_2^{n-i} \rangle, \qquad \text{(A.28a)}
\end{aligned}$$

for $n = 0, 1, 2, \ldots$. This is easily extensible for macroscopic XS that have more than two components.

It is not straightforward how to apply this scheme when using negative moments. (If it were, we would have used it in Method 1 and Method 2.) One method that seems to be considered is to use

$$\Sigma^n(E) \equiv \left(N_1 \frac{1}{\sigma_1(E)} + N_2 \frac{1}{\sigma_2(E)} + \ldots \right)^{|n|}, \qquad \text{(A.28b)}$$

or something similar, instead of the proper

$$\Sigma^n(E) = \frac{1}{(N_1\sigma_1(E) + N_2\sigma_2(E) + \ldots)^{|n|}}, \tag{A.28c}$$

for $n = -1, -2, \ldots$ and then to use independence as in Eq. (A.28a).

Using Eq. (A.28b) would not preserve negative moments of the true macroscopic XS. Ribon and Maillard [14] do not see this as a difficulty, as the "the infinite series of the positive moments describe unambiguously the table considered." The negative moments seem to be a sort of hack to get better results and so may be treated approximately.

One way to treat the negative moments less approximately would be to use averaged XS for other nuclides as was done in Method 1 and Method 2:

$$\begin{aligned}\Sigma^n(E) &= \frac{1}{\left(\sum_i N_i\sigma_i(E)\right)^{|n|}} \\ &\simeq \sum_i \frac{w_i N_i^{-|n|}}{\left(\sigma_i(E) + \sum_{j\neq i}(N_j/N_i)\bar{\sigma}_j\right)^{|n|}}.\end{aligned} \tag{A.28d}$$

Backgroud/escape XS could additionally be added and λ_i's could be used as above in a Bondarenko iteration. As before, standard XS moments at several background XS values (and temperatures) could be calculated by a XS preparation code and interpolation used during the Bondarenko iteration. The disadvantage for the above treatment is that the w_i are completely arbitrary.

Using fractional XS moments has seen adoption in Japan. As mentioned concerning Method 1, the unshielded flux goes as $\psi(\Sigma_t(E)) \sim 1$ which corresponds to $m = 0$. The shielded flux goes as $\psi(\Sigma_t(E)) \sim 1/\Sigma_t(E)$ or $m = -1$. Preserving integrals of the flux thus requires the quadrature to have accuracy for XS moments

with $m \in [-1, 0]$. Integrating a reaction rate, the cross section multiplied by the flux, adds a power to m, meaning the quadrature should be accurate for $m \in [0, 1]$. This has led some authors to forego unit spacing between preserved moments and concentrate on XS moments within $m \in [-1, 1]$. We note much of the above theory no longer applies for this choice.

The difficulties of mixing microscopic XS or moments to macroscopic XS or moments are circumvented if HFG or CE XS are generated and used to define the XS moments.While eliminating the complexity of mixing the nuclide-specific moments, this introduces extra storage and calculational requirements. As with the previous methods, Method 3 was created specifically so that the energy-resolved resonances were not required during the band calculation and mixing. Only XS moments are needed for the standard band calculation algorithm. These moments take up little memory and can be calculated for each nuclide independently.

When using MC transport (Section A.5) or deterministic transport with more unknowns (Section A.6), creating a separate band structure for each nuclide independently is acceptable and may be desirable. In this case, no mixing algorithms or approximations are needed. The downside is that treating each nuclide independently ignores correlation effects, which are important in resonant nuclides such as ^{238}U, ^{235}U, ^{239}Pu and others. Defining self-consistent material-specific band parameters with HFG or CE XS would allow correct treatment of correlation within a material. However, correlation between materials would still be missing and there would be additional upfront cost of generating material-specific band parameters from HFG XS data. The ability to do "band tracking," wherein the band a particle interacts with is kept between collisions (even if the particle enters a different material) for within-nuclide correlation between materials, would additionally be lost if material-specific band structures were used (see Section A.5). For MC applications,

it is more desirable to use correlation matrices alongside nuclide-specific band structures, which would preserve band tracking and introduce correlation among nuclides within a material, or to try DED MB, which uses global energy structures and would provide automatic correlation.

Methods 1-3 all have the goal of accurately preserving reaction-rate-like quantities using macroscopic XS, not microscopic XS. Microscopic reaction rates matter in depletion applications. Nuclide-specific band calculations will produce optimal band parameters that preserve reaction rates for each nuclide. The cost is that these nuclide-specific band parameters are difficult to mix into macroscopic XS as each nuclide has its own within-group energy discretization (band structure). Non-correlation or explicit correlation can be used, but these are either approximations in the former case or add considerable complexity to the system in the latter case (e.g., adding unknowns, building correlation matrices, or building conditional probabilities). All of these problems may be solved with DED MB.

The DEDs in DED MB can be chosen to preserve nuclide-specific reaction rates. This is done by first splitting the within-group energy domain into "carriers" that represent invididual resonant nuclides or sets of resonant nuclides. Each carrier has its own DED. A band boundary calculation can be done on each carrier independently. The result is a set of non-overlapping DEDs that cover the group, automatically preserve correlation (the DEDs are global and do not change between materials), and are accurate for each resonant nuclide (or more correctly, each carrier).

FEDS is still preferable to a carrier-based scheme. FEDS defines energy elements to preserve the solution behavior in energy, not quantities such as microscopic XS that are correlated to solution behavior. One important feature of the solution not present in any cross section is the up-spikes from resonances of the scattering source. Additionally, the solution likely requires fewer unknowns to accurately discretize

than were all of the individual microscopic (partial) XS used.

A.4 Explicit Bands

BP MB is the same as DED MB, except the DEDs are calculated based on local HFG (or CE) macroscopic XS, not a global average XS. See my Master's Thesis or PHYSOR paper for further discussion of DED MB.

The BP MB as represented by [26] and [10] has its own mathematical framework that results in the expected definitions of bands. Cullen multiplies the transport equation by $p(\Sigma, E)$, the probability that $\Sigma_t = \Sigma$ at energy E.

A.4.1 Resolved resonance region

For the resolved resonance region (RRR), Σ_t is known at every energy. Hence, $p(\Sigma, E) = \delta(\Sigma - \Sigma_t(E))$. Notice this requires forming $\Sigma_t(E)$, which requires material information (esp. for neutronics) and XS information on a fine energy grid.

The transport equation is integrated over energy group and cross section band. For example,

$$\int_{\Delta E_g} \mathrm{d}E \int_{\Delta \Sigma_n} \mathrm{d}\Sigma \, p(\Sigma, E) \left[\mathbf{\Omega} \cdot \nabla \psi(\mathbf{r}, E, \mathbf{\Omega}) + \Sigma_t(E) \psi(\mathbf{r}, E, \mathbf{\Omega}) \right] =$$
$$\int_{\Delta E_g} \mathrm{d}E \int_{\Delta \Sigma_n} \mathrm{d}\Sigma \, p(\Sigma, E) \left[\frac{1}{4\pi} \int_0^\infty \mathrm{d}E' \, \Sigma_s(E' \to E) \phi(\mathbf{r}, E) + Q \right]. \tag{A.29a}$$

This defines band parameters,

$$\psi_{g,n}(\mathbf{r},\mathbf{\Omega}) = \int\limits_{\Delta E_g} \mathrm{d}E \int\limits_{\Delta\Sigma_n} \mathrm{d}\Sigma\ \delta(\Sigma - \Sigma_t(E))\psi(\mathbf{r},E,\mathbf{\Omega}), \tag{A.29b}$$

$$\Sigma_{x,g,n} = \frac{1}{F_{g,n}} \int\limits_{\Delta E_g} \mathrm{d}E \int\limits_{\Delta\Sigma_n} \mathrm{d}\Sigma\ \delta(\Sigma - \Sigma_t(E))\Sigma_x(E)f(E), \tag{A.29c}$$

etc.,

$$F_{g,n} = \int\limits_{\Delta E_g} \mathrm{d}E \int\limits_{\Delta\Sigma_n} \mathrm{d}\Sigma\ \delta(\Sigma - \Sigma_t(E))f(E), \tag{A.29d}$$

$$P_{g,n} = \frac{1}{\Delta E_g} \int\limits_{\Delta E_g} \mathrm{d}E \int\limits_{\Delta\Sigma_n} \mathrm{d}\Sigma\ \delta(\Sigma - \Sigma_t(E)), \tag{A.29e}$$

which are equivalent to DED MB band parameters, except with local band structures. Here, $f(E)$ is an approximation to the flux, usually 1 or $1/E$. The resultant transport equation,

$$\mathbf{\Omega}\cdot\nabla\psi_{g,n} + \Sigma_{t,g,n}\psi_{g,n} = \frac{1}{4\pi}\sum_{g'=1}^{G}\sum_{n'=1}^{N_g}\Sigma_{s,(g',n')\to(g,n)}\phi_{g',n'} + Q_{g,n} \tag{A.29f}$$

uses the usual MB definition of the scattering kernel (Eq. (A.8)).

A.4.2 Unresolved resonance region

In the URR, for each nuclide, ladders (realizations of the XS based on resonance distributions) are built and nuclide-specific band probabilities and XS are calculated for each ladder. These band parameters are averaged over the ladders. Nuclide-specific probabilities are combined using independence.

Band parameters are defined in the following sense. For the reference temperature, the microscopic total XS is split up into bands based on its value. This defines a set of DEDs in the same way as DED MB. Total and partial XS are averaged over

each band / DED. Band probabilities are simply the normalized energy areas of the DEDs. Flat or $1/E$ XS weighting is often used within a band because the bands themselves are generated to take care of the self-shielding.

There is one set of DEDs per nuclide and this set applies to all temperatures. This preserves correlation among temperatures. Particles in the same band correspond to the same energies for a given nuclide independent of temperature. This allows MC calculations to remember the band when streaming between multiple materials that share common nuclides, possibly at multiple temperatures (cf. Section A.5).

For the URR, Σ_t is only known in a distribution sense. Hence, $p(\Sigma, E)$ is a PDF. The math is simplified because this PDF depends weakly on energy: $p(\Sigma, E) \simeq p(\Sigma)$. Further, all the cross sections are physically uncorrelated, allowing $p(\Sigma)$ to be formed from the $p_i(\sigma)$ in a straightforward manner.

If $p_i(\sigma)$ is the probability that $\sigma_{t,i} = \sigma$ (barns), $\Sigma_t = \sum_i N_i \sigma_{t,i}$, and the p_i are independent, then it possible to define $p(\Sigma)$, the probability that $\Sigma_t = \Sigma$ (1/cm), inductively. Let $\Sigma_{t,j} = \sum_{i=1}^{j} N_i \sigma_{t,i}$ and let $\pi_j(\Sigma)$ be the probability that $\Sigma_{t,j} = \Sigma$. Then

$$\pi_j(\Sigma) = \int_0^{\Sigma} \mathrm{d}\alpha \;\; \pi_{j-1}(\alpha) \;\; p_j\left(\frac{\Sigma - \alpha}{N_j}\right). \tag{A.30a}$$

Note that the usual representation of the data for PT is a nuclide-wide set of band probabilities and total/partial XS in each band for each temperature. Data is stored in this histogram fashion, with correlation within a nuclide. Applying Eq. (A.30a) must be done with interpolation. A naïve approach would be to do each partial reaction separately, but this would decorrelate them from the total cross sections, which is undesirable. When the macroscopic XS is reconstructed from its microscopic components, temperature correlation information will be lost.

A better approach would be to build the expectation of the partial cross section in each band as the total cross section is built. That is

$$\sigma_{x,n} = \int\limits_{\Sigma_t \in \Delta\Sigma_{t,n}} \mathrm{d}\Sigma_t \; E(\sigma_x|\sigma_t)\; p(\sigma_t|\Sigma_t), \tag{A.30b}$$

$$p(\sigma_t|\Sigma_t) = \frac{p(\sigma_t \cap \Sigma_t)}{p(\Sigma_t)}, \tag{A.30c}$$

where the last result follows from Bayes' Theorem. To build the $p(\sigma_t \cap \Sigma_t)$ may require forming $\hat{\pi}_i(\Sigma)$, the probability that $\hat{\Sigma}_{t,i} = \Sigma$, where $\hat{\Sigma}_{t,i} = \sum_{j \neq i} N_j \sigma_{t,j}$, for each i.

The above process could conceivably be applied to the RRR by treating the XS as unresolved and forming band probabilities not from ladders, but from the actual $\sigma_{t,i}(E)$.

A.5 Treatment in CP and MC Codes

When using CP or MC calculations, one can use microscopic-based band structures along with correlation information between nuclides. NJOY can be used to compute RI for individual nuclides and all Σ's can be replaced by σ's for band determination purposes (cf. Section A.1.1, option C). For MC, one additional random number is needed to compute the microscopic total cross section for each resonant nuclide in a material.

The correlation information generally comes in two forms. The first is correlation matrices, which are suitable for sampling from MC routines. If the algorithm samples band 1 for ^{238}U, then it can sample using the Choleksy decomposition of the correlation matrix to determine which band of ^{235}U to pick when computing the total cross section. For CP routines, correlation information is often included in the form of conditional probabilities, which play essentially the same role.

For implementation details on PT in the URR in MCNP, see the (unrestricted, freely available) Volume 1 of the MCNP5 manual. Specifically, see Chapter 2 (Cross Sections), Section B: Particle Tracks for description of collision sampling (they need to form the full Σ_t, not just one $\sigma_{t,i}$) and Section C: Neutron Interactions (sampling of collision nuclide uses CDF of macroscopic cross sections from each nuclide and hence requires knowing $N_i\sigma_{t,i}$ for each nuclide in the region). See Chapter 3 (Physics), Section C (Neutron Interactions), Part 7: Probability Tables for the Unresolved Resonance Range (page 2-55 ff). They do not say how they sample the total cross sections for multiple resonant nuclides, though it is assumed that this is done independently. Once the collision nuclide is known, its table location must be kept until the next collision to allow proper correlation. This includes if the particle is split or enters a region of different temperature. Of note, they cite a paper written in 1999 that indicates use of PTs in the URR has a negligible impact unless systems have a "significant flux" in the URR and contain "large amounts" of ^{238}U.

A.6 Adding Unknowns in Deterministic Codes

There is a method which allows microscopic band-dependent XS and probabilities to be used (cf. Section A.1.1, option C) but which results in more unknowns. Depending on assumptions in correlation, the total number of unknowns may range from BN to B^N, where B is the number of bands per group and N is the number of resonant nuclides in a material or the entire problem. Effective nuclides could be used which represent several physical nuclides.

For the BN case, the idea is to have unknowns that correspond to the band-dependent fluxes in each of the resonant nuclides. A flux can now be identified with

a resonant nuclide and a DED (band) for that nuclide. The unknowns are

$$\psi_{g,i,b}, \quad g = 1, \ldots, G, \quad i = 1, \ldots, M_g, \quad b = 1, \ldots, B_{g,i} \tag{A.31a}$$

which is the integrated angular flux over band b of group g, for nuclide i. M_g has a group dependence because multiple nuclides only need to be tracked within resonance regions.

In general, $M_g = M_r + 1$, where M_r is the number of resonant nuclides or pseudo-nuclides being tracked. The other contribution, which we will call $i = 1$, is from all of the non-resonant nuclides in the current material. This implies $B_{g,1} = 1$.

The fluxes in Eq. (A.31a) interact with a macroscopic total cross section which uses the band-dependent total cross section of the current nuclide, and the average cross sections of the other nuclides:

$$\Sigma_{t,g,i,b} = N_i \sigma_{t,g,i,b} + \sum_{j \neq i} N_j \bar{\sigma}_{t,g,j}, \tag{A.31b}$$

where averaging is done in a Bondarenko-like manner as in Eq. (A.14c). Correlation may be taken into account by using band-specific values in the sum, though this requires mapping from one band structure to another. By default, non-correlation among nuclides is assumed.

Notice that unknowns for a given nuclide can be used in a material that does not contain that nuclide. In this case, $N_i = 0$ in Eq. (A.31b). This may be useful to preserve band information while particles are in transit between similar region, for example, when traveling in moderator between two fuel pins.

The first nuclide, corresponding to all non-resonant nuclides in the current region, is a pseudo-nuclide. N_1 is the sum of the non-resonant nuclide atom densities in

the region (which could be zero), and $\bar{\sigma}_{x,g,1} = \sigma_{x,g,1,1}$ is the atom-density-weighted average of the non-resonant nuclide cross sections in the region.

The band probabilities, which correspond to normalized areas in energy covered by the band in the group, are simply the band probabilities for the given nuclide:

$$P_{g,i,b} = (P_{g,b})_i = \frac{|\,(\Delta E_{g,b})_i\,|}{|\Delta E_g|}, \tag{A.31c}$$

$$1 = \sum_{b=1}^{B_{g,i}} P_{g,i,b} \quad i = 1, \ldots, M_g. \tag{A.31d}$$

The source terms have the same contributions for each nuclide:

$$S_{\text{scat},g,i,b} = \frac{1}{4\pi} P_{g,i,b} \sum_{g'=1}^{G} \sum_{i'=1}^{M_{g'}} N_{i'}\, T_{g' \to g,i'} \sum_{b'=1}^{B_{g',i'}} \sigma_{s,g',i',b'}\ \phi_{g',i',b'} = P_{g,i,b} S_{\text{scat},g}, \tag{A.31e}$$

$$S_{\text{fiss},g,i,b} = \frac{1}{4\pi k_{\text{eff}}} P_{g,i,b} \sum_{g'=1}^{G} \sum_{i'=1}^{M_{g'}} N_{i'}\, \chi_{g,i'} \sum_{b'=1}^{B_{g',i'}} \nu\sigma_{f,g',i',b'}\ \phi_{g',i',b'} = P_{g,i,b} S_{\text{fiss},g}. \tag{A.31f}$$

Notice these source terms have implicit non-correlation within a group. Using a nuclide- and band-specific transfer function, $T_{(g',i',b') \to (g,i,b)}$ would alleviate this but would increase complexity.

Interface conditions will depend on whether the flux unknowns are local to a material or if the same set of nuclides are used globally. In the former case, an averaging should be used, as in Eq. (A.10b), to signify non-correlation:

$$\psi_{g,i,b,\text{in}} = P_{g,i,b,\text{in}} \frac{1}{N_g} \sum_{b'=1}^{B_{g,i'}} \sum_{i'=1}^{M_g} \psi_{g,i',b',\text{out}}. \tag{A.31g}$$

In the latter case, correlation is preserved because the same fluxes are used for the

entire problem. In this case, Eq. (A.10a) is used with an added nuclide index:

$$\psi_{g,i,b,\text{in}} = \psi_{g,i,b,\text{out}}. \tag{A.31h}$$

In this latter case, temperature correlation may be kept, provided the same band structure is used for all temperatures of each nuclide.

One issue with adding more unknowns is that group-wise fluxes cease to be unique:

$$\phi_g = \sum_{b=1}^{B_{g,i}} \phi_{g,i,b}, \quad i = 1, \ldots, M_g. \tag{A.31i}$$

However, fluxes are normally not the desired end-result of a calculation, but rather reaction rates are. Reaction rates, and hence eigenvalues, are unique because they use the flux corresponding to the cross section used:

$$\text{RR}_{x,g,i,b} = \sigma_{x,g,i,b}\ \phi_{g,i,b}, \tag{A.31j}$$

$$\text{RR}_x = \sum_{g=1}^{G} \sum_{i=1}^{M_g} N_i \sum_{b=1}^{B_{g,i}} \sigma_{x,g,i,b}\ \phi_{g,i,b}. \tag{A.31k}$$

For the B^N case, the idea is not to assume independence of each (effective) nuclide, but rather to treat all possible permutations. There is a spectrum between BN and B^N, where only certain permutations are kept. This is beyond the scope of this overview.

For the B^N case, the unknowns are

$$\psi_{g,\mathbf{b}}, \quad g = 1, \ldots, G, \quad \forall\ \mathbf{b}, \tag{A.32a}$$

$$\mathbf{b} = \{b_1, \ldots, b_{M_g}\}, \quad b_i = 1, \ldots, B_{g,i}, \quad i = 1, \ldots, M_g. \tag{A.32b}$$

The unknown fluxes interact with a macroscopic total cross section which uses the band-dependent total cross sections of each nuclide:

$$\Sigma_{t,g,\mathbf{b}} = \sum_{i=1}^{M_g} N_i \sigma_{t,g,b_i}, \quad \forall\, b_i. \tag{A.32c}$$

Here $\forall\, b_i$ means over all B^N possible permutations of $\mathbf{b}$.

The band probabilities are products of the nuclides and are usually assumed to be independent:

$$P_{g,\mathbf{b}} = \prod_{i=1}^{M_g} (P_{g,b})_i = \prod_{i=1}^{M_g} \frac{|\,(\Delta E_{g,b})_i\,|}{|\Delta E_g|}, \quad \forall\, b_i \tag{A.32d}$$

This implies the flux $\psi_{g,\mathbf{b}}$ corresponds to the union energy space for bands $\{b_1, \ldots, b_{M_g}\}$ of the nuclides $\{1, \ldots, M_g\}$. The union definition renders the group-wise flux definition unique, as a sum over all $\mathbf{b}$ is necessary to cover the energy space within a group.

The source terms, which determine the RHS and the reaction rates, are now given by:

$$S_{x,g,\mathbf{b}} = \frac{1}{4\pi} P_{g,\mathbf{b}} \sum_{g'=1}^{G} \sum_{i'=1}^{M_{g'}} N_{i'}\, T_{g' \to g, i'} \sum_{b'_{i'}=1}^{B_{g',i'}} \sigma_{x,g',i',b'_{i'}}\ \phi_{g',i',b'_{i'}}, \tag{A.32e}$$

$$\phi_{g',i',b_{i'}} = \sum_{b_1=1}^{B_{g',1}} \cdots \sum_{b_{i'-1}=1}^{B_{g',i'-1}} \sum_{b_{i'+1}=1}^{B_{g',i'+1}} \cdots \sum_{b_{M_{g'}}=1}^{B_{g',M_{g'}}} \phi_{g',\mathbf{b}}. \tag{A.32f}$$

Notice Eq. (A.32f) assumes only the total flux within a nuclide's band matters, not its distribution. This is an approximation.

The BN or B^N framework allows us to make use of microscopic band-wise XS (option C in Section A.1.1). Resonance integrals (RI) can be computed for each

nuclide (or pseudo-nuclide) independently and combined to form band parameters independently. These nuclide-optimal band parameters may then be used as they are. The only coupling needed among nuclides is a Bondarenko-like treatment to get the background cross sections from the other nuclides (the $\bar{\sigma}$'s), and this is only necessary for the BN case.

The price paid for this simplicity and band optimality is additional unknowns and complexity. This method may not be cost-effective, especially the B^N case. In years past, XS preparation has been memory- and computation-limited and shortcuts were needed to avoid forming, storing, and operating on HFG or CE XS for more than one nuclide. Today, computer resources allow us to use the HFG or CE XS directly for 1-D problems. This means bands can be chosen — potentially constant across the entire problem — to be accurate and consistent for many nuclides, solving the problem of correlation and allowing a more first-principles approach to energy discretization. Such advances have been utilized when developing FEDS.

APPENDIX B

ADDENDUM TO SECTION 2

B.1 Energy Penalties

The minimization problem minimizes the variance of all observations within an energy element, where observations hold information about how the solution behaves. We use three types of observations: macroscopic total cross sections, infinite-medium fluxes (possibly with escape cross section), and energy itself. The last observation type is the energy penalty, which provides a mechanism to bound energy element extent in energy instead of flux. When multiple observations are used, which is often the case, they must be balanced in magnitude because the minimization problem sums over variances in individual observations using an unweighted norm. The magnitude of the energy penalty determines its relative importance. A magnitude of zero means no energy penalty. A magnitude much greater than the other observations will force contiguous energy elements that are equally spaced in lethargy. In this work, two separate energy penalty magnitude strategies were used.

For the cylindrical pincell problem, the energy penalty magnitude was determined by an α parameter and the observation for the energy penalty was:

$$O_{g,\text{energy, cyl.}} = (1 + \alpha) \log_{10} E_g, \tag{B.1}$$

for hyperfine group / point g.

The problem with this strategy is the magnitude of the energy penalty should be chosen to balance the magnitudes of the flux-based observations. Otherwise, applying the same energy penalty to two different problems or energy regions will

result in different penalty strengths. In practice, this strategy required manually tuning the energy penalty for each problem, which was undesirable. The values of energy penalty used for the cylindrical pincell problems were $\alpha = 0.65$ for problem 3, $\alpha = 0.45$ for problem 5 and the low-energy RRR, and $\alpha = -0.45$ for problem 5 and the medium-energy RRR. Sensitivity to the energy penalty magnitude was observed to be low, so long as an energy penalty with $\alpha > -1$ was used.

For the C5G$^\infty$ problem, a better strategy was devised, wherein a β parameter determined the energy penalty magnitude. The observation for the energy penalty was:

$$O_{g,\text{energy, C5}} = \beta \sqrt{N} \log_{10} \left[\frac{\phi_{\max}}{\phi_{\min}} \right] \frac{\log_{10} E_g}{\log_{10} \frac{E_{\max}}{E_{\min}}}, \tag{B.2}$$

where N is the number of other observations, and $\phi_{\max}/\phi_{\min}$ is the ratio of largest-to-smallest flux over the entire RRR. The square root was used because all minimization problems used an L^2 norm over the observations for computing distances and the energy penalty should balance the distance of the flux-based spectra.

With this strategy, the energy penalty strength relative to the other observations should depend solely on the choice of β and be insensitive to the magnitude of the other observations. A potential problem with the latter strategy is that the energy penalty is calculated before the coarse groups are formed, meaning different coarse groups may have different energy penalty strengths relative to the observation magnitudes within each group. The C5G$^\infty$ problem used $\beta = 0.36$ and two coarse groups with boundaries $[3, 54.7, 1060]$ eV. The slab pincell problems used an energy penalty with $\beta = 0.96$, but mostly relied on coarse groups for energy bounding. The TOF problem did not use an energy penalty.

One conclusion of this work is that using energy penalties to control element

extent in energy seems to be inferior to using coarse groups for this purpose. A major reason energy penalties were developed was to allow the minimization problem maximal freedom to determine where to put energy resolution. Using multiple coarse groups requires either manually determining how many energy unknowns to allocate to each coarse group or determining an algorithm to do this automatically. The former is undesirable. The latter was developed and is described in section 2.

B.2 Detailed Apportioning Algorithm

In previous subsections, various variance-like metrics were developed for automatic apportioning. The number of elements within a coarse group was said to be approximately proportional to the metric for a coarse group divided by the metric summed over all coarse groups multiplied by the total number of energy elements. Metrics were norms of observations over hyperfine groups and materials, and included the standard deviation metric, an L^1 difference metric, and a maximum ratio metric. This subsection details the precise implementation of the apportioning, given a metric and proves the algorithm has certain desirable properties.

Let

$$v_g = \text{metric in coarse group } g, \tag{B.3a}$$

$$G = \text{number of coarse groups}, \tag{B.3b}$$

$$N_{\text{tot}} = \text{total number of energy elements desired}, \tag{B.3c}$$

$$N_g = \text{number of energy elements in coarse group } g, \tag{B.3d}$$

$$v_{\text{tot}} \equiv \sum_g v_g = \text{total metric}. \tag{B.3e}$$

We desire that our apportioning satisfy

$$N_g \simeq \frac{v_g}{v_{\text{tot}}} N_{\text{tot}}, \tag{B.4a}$$

$$N_g \geq 1, \tag{B.4b}$$

$$\sum_g N_g = N_{\text{tot}}. \tag{B.4c}$$

Equation (B.4a) says we desire the number of elements per coarse group to be proportional to the relative metric in that coarse group. Equation (B.4b) says we require each coarse group to have at least one element, regardless of its metric. Equation (B.4c) says the sum of the elements per coarse group should equal the total number of elements. It turns out to be difficult to satisfy all three requirements simultaneously without requiring an iterative scheme.

Our apportioning strategy, which we later show satisfies Eq. (B.4), follows. Let

$$y_g \equiv \frac{v_g}{v_{\text{tot}}} N_{\text{tot}}, \tag{B.5a}$$

$$M_g \equiv \max\left(1, y_g\right), \tag{B.5b}$$

$$M_{\text{tot}} \equiv \sum_g M_g, \tag{B.5c}$$

$$\gamma_g \equiv \frac{M_g - 1}{M_{\text{tot}} - G}, \tag{B.5d}$$

$$\hat{N}_g \equiv \lfloor \gamma_g (N_{\text{tot}} - G) \rfloor + 1, \tag{B.5e}$$

$$\delta_g \equiv \big(\gamma_g (N_{\text{tot}} - G) + 1\big) - \hat{N}_g, \tag{B.5f}$$

$$\Delta = N_{\text{tot}} - \sum_g \hat{N}_g. \tag{B.5g}$$

Let a be the set that holds the g corresponding to the Δ largest δ_g. That is, a holds a list of coarse groups that have large remainders, δ_g, large being determined

such that there are Δ entries in a.

We define

$$N_g = \hat{N}_g \qquad \text{if } g \notin a, \tag{B.5h}$$

$$N_g = \hat{N}_g + 1 \qquad \text{if } g \in a. \tag{B.5i}$$

We now show our apportioning strategy, Eq. (B.5), achieves the properties in Eq. (B.4), assuming $N_{\text{tot}} \geq G$. By definition,

$$M_g \geq 1. \tag{B.6a}$$

Thus,

$$\gamma_g \geq 0. \tag{B.6b}$$

Also, by definition,

$$\sum_g \gamma_g = \frac{1}{M_{\text{tot}} - G} \sum_g M_g - 1 = \frac{M_{\text{tot}} - G}{M_{\text{tot}} - G} = 1 \tag{B.6c}$$

Continuing,

$$M_{\text{tot}} = \sum_g \max\left(1, \frac{v_g}{v_{\text{tot}}} N_{\text{tot}}\right) \geq \sum_g \frac{v_g}{v_{\text{tot}}} N_{\text{tot}} = N_{\text{tot}}, \tag{B.6d}$$

which implies

$$G \leq N_{\text{tot}} \leq M_{\text{tot}}. \tag{B.6e}$$

We use Eq. (B.6) to show

$$N_{\text{tot}} - G \geq 0, \tag{B.7a}$$

which implies

$$\lfloor \gamma_g (N_{\text{tot}} - G) \rfloor \geq 0, \tag{B.7b}$$

and hence

$$\hat{N}_g \geq 1, \tag{B.7c}$$

$$N_g \geq 1, \tag{B.7d}$$

proving Eq. (B.4b).

We use Eq. (B.6) to show

$$\sum_g \hat{N}_g = \sum_g \left(\lfloor \gamma_g (N_{\text{tot}} - G) \rfloor + 1 \right) \leq G + (N_{\text{tot}} - G) \sum_g \gamma_g = N_{\text{tot}}, \tag{B.8a}$$

which implies $\Delta \geq 0$ and our use of Δ is valid. Finally, by definition of the cardinality of a and of Δ,

$$\sum_g N_g = \Delta + \sum_g \hat{N}_g = N_{\text{tot}}, \tag{B.8b}$$

which proves Eq. (B.4c).

Finally, note that if the maximum in the definition of M_g is never needed, then

$$M_g = y_g, \tag{B.9a}$$

$$M_{\text{tot}} = \sum_g y_g = N_{\text{tot}} \sum_g \frac{v_g}{v_{\text{tot}}} = N_{\text{tot}}, \tag{B.9b}$$

$$N_g \simeq \gamma_g (N_{\text{tot}} - G) + 1 = \frac{M_g - 1}{M_{\text{tot}} - G}(N_{\text{tot}} - G) + 1 = M_g, \tag{B.9c}$$

that is,

$$N_g \simeq \frac{v_g}{v_{\text{tot}}} N_{\text{tot}}, \tag{B.9d}$$

proving Eq. (B.4a). The "$\simeq$" in Eq. (B.9c) follows from the definition of $\hat{N}_g$ and the way we distribute the final elements using the δ_g.

If the maximum in the definition of M_g is needed, we can still show the desired proportionality of the elements. We begin by noting that

$$N_g \simeq \frac{M_g - 1}{M_{\text{tot}} - G}(N_{\text{tot}} - G) + 1. \tag{B.10a}$$

We define

$$r \equiv \frac{N_{\text{tot}} - G}{M_{\text{tot}} - G}, \tag{B.10b}$$

and note that Eq. (B.6) implies that

$$0 \leq r \leq 1. \tag{B.10c}$$

r depends only on the number of times the maximum is used in Eq. (B.5b) and is generally near 1.

We divide N_g by N_{tot} and apply our definition of r to find:

$$N_g \simeq \frac{v_g}{v_{\text{tot}}} N_{\text{tot}}\, r + (1 - r)\, 1, \tag{B.11a}$$

$$\frac{N_g}{N_{\text{tot}}} \simeq \frac{v_g}{v_{\text{tot}}}\, r + (1 - r)\, \frac{1}{N_{\text{tot}}}. \tag{B.11b}$$

Equation (B.11) says the number of elements per coarse group approximately satisfies Eq. (B.4a) when r is close to 1 (when the maximum is used infrequently) and becomes closer to 1 as r becomes appreciably smaller than 1. This latter case occurs when a significant fraction of the coarse groups have little variance within themselves compared to the average variance per coarse group.

B.3 Comparing FEDS to PG-FEMG and MG

In much the same way as the PG-FEMG method before it, the FEDS method takes advantage of the low regularity requirements of the angular flux with respect to energy and generalizes the MG method to use a finite element in energy based on discontiguous energy elements. As with PG-FEMG, with FEDS, the support of each element is discontiguous (made up of multiple, unconnected energy ranges called subelements), no elements share support, and the union of the support of all elements is the entire energy domain. In FEDS, I refer to the mesh that describes the supports of the elements of the finite element space as the generalized energy mesh (GEM).

As with PG-FEMG, in FEDS, both basis and weight functions for the finite element method are $L^1((0, \infty))$ integrable. This is all that is required when working with the canonical neutral-particle transport equation, because the transport equation is integral with respect to the energy variable and because all the quantities of interest are energy-integrated flux moments. Basis and/or weight functions with

higher regularity would be required if derivatives in energy were desired or if it were required to have a continuous representation of the angular flux in energy.[1]

Unlike PG-FEMG, which used a band boundary calculation on a single, effective cross section, in FEDS, we generate the GEM using a clustering algorithm with multiple inputs. The clustering algorithm is fed variables that are correlated with the pointwise angular flux, such as local infinite-medium spectra, to determine which energy subelements contain particles that behave similarly over the entire problem. These subelements are clustered into elements.

The clustering is designed to minimize within-element variation of the angular flux in the problem. We note that the clustering algorithm minimizes the projection error between the angular flux (or a predictor thereof) and its finite element projection. This property provides important theoretical justification for the FEDS method.

In the limit that the flux is completely determined by one resonant cross section, the clustering algorithm will cluster based on the magnitude of that cross section. This is the typical MB behavior that works well for simple problems. For more complicated problems, the clustering generalizes MB and PG-FEMG, and overcomes the limitations of using a single input that are inherent to PG-FEMG.

It was mentioned above that if the cross sections were smooth within a group or element, then the MG method would work well. The same logic can be applied if the flux within an element were approximately constant. As mentioned previously, energy elements for FEDS are defined to maximize this property. Therefore, there is strong reason to believe the FEDS method should work well.

B.4 Relevant Problems for FEDS

The FEDS method is well-suited to problems for which

[1] N.B., MG does not provide a continuous representation of the flux in energy either.

1. There are a relatively small number of important components,
   where "component" refers to a collection of one or more nuclides that consistently appear in approximately the same relative densities.

   - For example: U-238 in LWR fuel, U-235 in LWR fuel, Pu's in LWR fuel, Zr in LWR clad, or Ag-In-Cd in LWR control rods
   - As a counter-example: Problems with large material motion, which shifts the effective resonance positions, making each spatial location act as a different resonance material

2. The total cross section or approximate spectra can be computed cheaply ahead of time (the minimization step requires hyperfine cross sections and fluxes defined on a hyperfine group structure).

3. The energy dependence of the cross sections are explicit.

   - For example: The resolved resonance region (RRR)
   - As a counter-example: The unresolved resonance region (URR)

4. The long-range energy dependencies may be easily approximated (cross sections must be flux-weighted over discontiguous energy domains. This requires knowledge of the flux not only within each subelement, but also relatively among subelements).

5. The solution depends on cross section values, not on energy explicitly.

   - Downscattering is an important counter-example, where the scattering kernel depends on energy lost.

- Time-dependence is another important counter-example, where groupwise velocities, which directly depend on energy, are used in the time derivative term.

The last two points do not need to be satisfied if the amount of discontiguity of the energy elements is somehow limited. Two straightforward ways to do this are to add in energy itself to the minimization inputs, effectively introducing an energy penalty term, and defining energy elements to live only within a coarse group, such as by forming the energy mesh out of several small pieces.

B.5 Running FEDS Problems

B.5.1 The workflow

Figure B.1 shows the workflow for solving a k-eigenvalue or time-dependent neutronics problem. Our workflow encompasses the entire range of the calculation, beginning with ENDF data and ending with a problem QOI. Other required inputs include the generalized energy mesh (GEM) — which we assume has already been computed — problem-specific materials and geometry information, solver-specific numerical and iterative method specifications / tolerances (not shown), and basis functions. The basis functions here are shape-function integrals over the subelements of the GEM and should be problem-dependent. We assume they have already been calculated. The workflow for solving a MG problem is the same, except that the GEM would contain contiguous elements and there may not be an element condensation in the GENDF reader step.

The first step in Fig. B.1 is to take evaluated nuclear data — ENDF/B-VII.1 in this case — and process it with NJOY [68]. NJOY is composed of a series of modules, each with a defined task. RECONR reconstructs point-wise cross sections from the ENDF data, expanding such things as resonance parameters. BROADR broadens

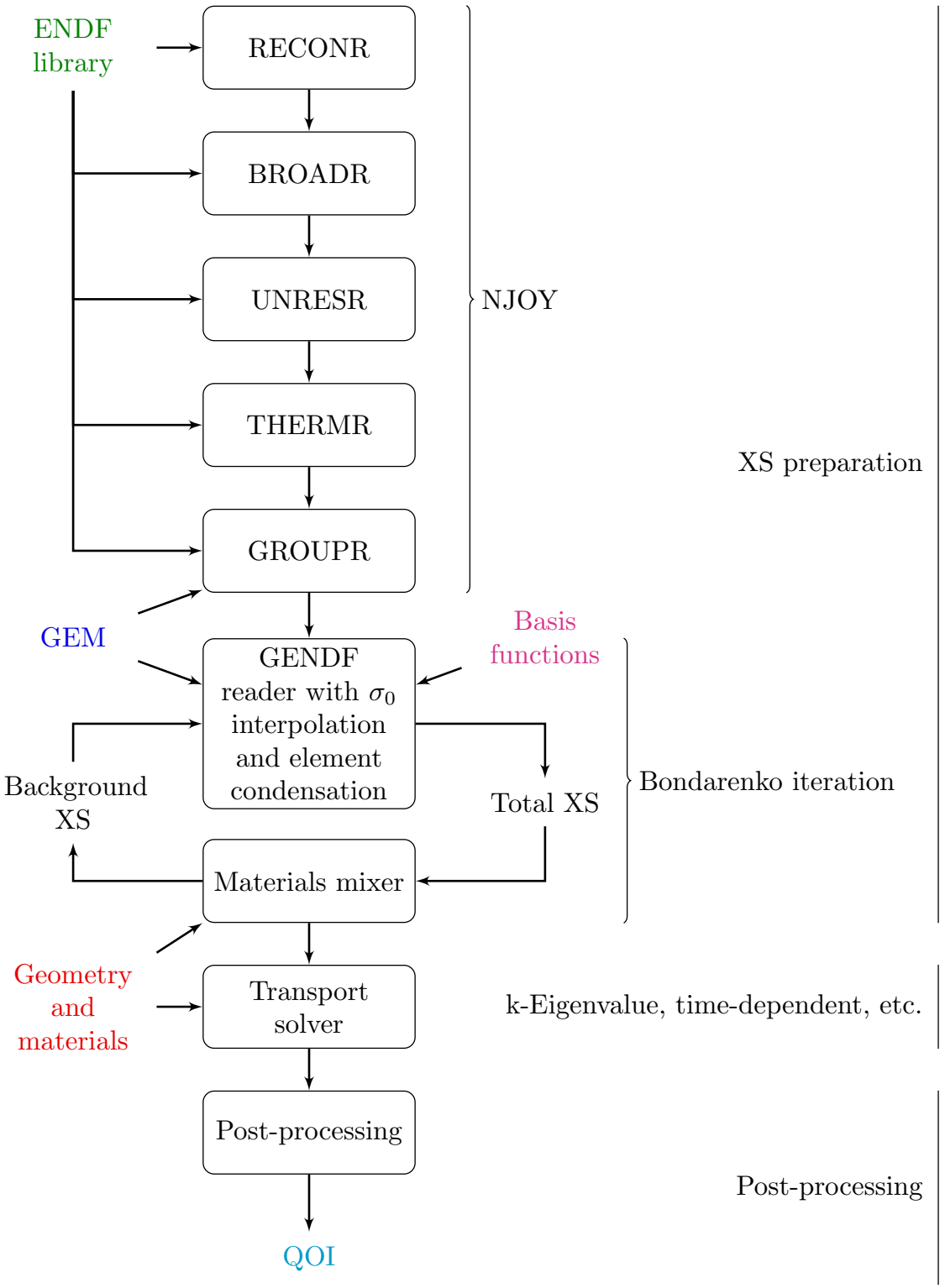

Figure B.1: Workflow for the FEDS method, from ENDF data to QOI.

the cross sections, important for resonances, to the desired temperatures. UNRESR deals with the unresolved resonance region (URR) and computes self-shielding in this range.[2] THERMR deals with thermal cross sections, where the neutron speeds become comparable to the nuclei speeds and neutron energies become comparable to lattice / molecular energies. These phenomena cause upscattering and add structure to the scattering cross sections within the thermal range. GROUPR groups the neutrons by their energies and computes flux-weighted averages of cross sections and transfer matrices. For our implementation, we give GROUPR the subelement energy boundaries, because subelements are contiguous and act exactly like MG groups. The result of this first step is a set of cross sections for each subelement of each reaction of each component / nuclide. Cross sections are given in a temperature-background cross section (σ_0) matrix.

The second step is to calculate element-wise cross sections for each component of each material, where a material is a user-defined combination of component nuclides at a user-defined temperature in a user-defined location (e.g., the inner ring of a UO_2 fuel pin). This involves interpolating in temperature and background cross-section space and condensing subelements into elements using the GEM. The condensation in subelements defines a cross section as the basis-function-weighted average of all the subelements within an energy element. The interpolation in background cross section involves a Bondarenko iteration, described below. All of the problems studied in this work used temperatures that were part of the temperature grid points in NJOY, meaning there was no approximation in temperature.

The third step is to solve a k-eigenvalue or time-dependent neutronics problem with a transport solver, using the FEDS cross sections produced in the second step

[2]In the URR, only a probabilistic distribution of the resonances are known, so cross sections at an energy represent an average that must be self-shielded to account for the presence of other cross sections.

as inputs. In this work, we use three types of transport solvers: SCDT, a one-dimensional, cylindrical, k-eigenvalue solver [1]; PDT, a two- or three-dimensional, cartesian, k-eigenvalue or time-dependent solver [71]; and an analytic long-characteristics in space-time, uncollided Python time-dependence solver. Notice that FEDS cross sections may be used in standard MG codes without modification.

There are four caveats. The first caveat is that some energy elements may contain large (resonance) cross sections, which forces either robust spatial methods or a fine spatial discretization. The second caveat is that the iterative method needs to be able to handle upscattering, as explained above. The third caveat is that, for time-dependent problems, the user must be able to manually specify group speeds for the elements as flux-weighted $1/v_e$. The final caveat is the user must be able to specify element-integrated sources, e.g., for the fission spectrum.

The last step is to post-process the output from the transport solver. The amount of required post-processing depends on the QOI. The k-eigenvalue requires no post-processing, nor do reaction rates. Expanding the finite element fluxes to show their true dependence on energy as a continuous variable requires knowing both the GEM and the continuous-energy basis functions. Condensing fluxes / reaction rates to a coarse group is trivial and does not require knowledge of basis functions or subelement locations, only which elements belong to the coarse group.

B.5.2 Within-subelement basis functions and between-subelement basis functions

NJOY has three options for determining the within-group (within-subelement) flux. Recall that the cross section for a subelement is a weighted average, where the weighting used is this flux. The first option, which we use, is to invoke the narrow-resonance (NR) approximation, which gives the within-sub-element flux for nuclide

i as:

$$\phi_i(\sigma_0, E) = M(E)\frac{1}{\sigma_i(E) + \sigma_0}, \tag{B.12}$$

where $M(E)$ is determined by the `iwt` parameter for GROUPR and is often $1/E$ in the RRR. The second option is to use a flux calculator that solves the slowing-down equation, but which only considers elastic scattering and an infinite medium composed of a background cross section, σ_0, and the current component's cross sections, $\sigma_{t,i}$ and $\sigma_{s,i}$. The third option is to use a user-supplied flux for $M(E)$ in Eq. (B.12). This flux is given as $E_i, \phi(E_i)$ pairs, and linear-linear interpolations are done for energies between supplied points. We chose to use the first option because it offers reasonable fidelity at low cost compared to the second option and because it allows us to run NJOY only once per nuclide, which is not necessarily the case for the third option. Future work may investigate using other options.

We note that using Eq. (B.12) for the within-subelement fluxes is tantamount to using approximate, nuclide-dependent basis functions for each component within a material. The fact that the continuous-energy basis functions become nuclide-dependent can be seen in Eq. (B.12), where the weighting flux used by NJOY depends on the nuclide. Notice that, if only one component nuclide has a varying σ_t within a subelement, or the variance within a subelement is small for all components, that Eq. (B.12) is equivalent to saying:

$$\phi_i(E) = M(E)\frac{1}{\sigma_i(E) + \sigma_0} \rightarrow M(E)\frac{1}{\Sigma_t(E) + \Sigma_e}, \tag{B.13}$$

which eliminates the nuclide dependence.

When condensing the subelements into elements during the second phase of

Fig. B.1, a consistent basis function is used for all components of a material. This basis function is the integral over a subelement of the continuous-energy basis function, which is the solution to an infinite-medium-equivalent, slowing-down problem with an analytic escape cross section. If small subelements are used, such that they resolve all of the desired resonances, it is the basis functions described here that are important. For all problems except the cylindrical pincell problems, subelements were large, being composed of all contiguous hyperfine groups belonging to the same element, so both basis functions described above were important.

B.5.3 The Bondarenko iteration

The Bondarenko iteration is one way to approximate the effect of other nuclides on the within-subelement spectrum. Our version of this iteration scheme used a narrow-resonance (NR) approximation (Eq. (B.12)) and an analytic escape cross section calculation, described below. A more in-depth exploration of Bondarenko iteration and its connection to NJOY is given in a future subsection. GROUPR uses the $\phi(\sigma_0, E)$ in Eq. (B.12) to flux-weight cross sections within each subelement on a grid of at most ten σ_0's.

When a cross section is desired for a given material, the correct σ_0 value for each element for each component nuclide is selected using a Bondarenko iteration on the σ_0's. This iteration has two steps. In the first step, for a given guess of $\sigma_0 = \sigma_{0,i}$ for nuclide i, the total cross section within each subelement is determined by interpolating the σ_0 grid. In the second step, σ_0 values are calculated for each subelement of each component nuclide using the σ_0 values for the other component nuclides within a material and the escape cross section:

$$\sigma_{0,g,i}^{k+1} = \frac{1}{N_i}\Sigma_e + \sum_{j \neq i} \frac{N_j}{N_i} \sigma_{t,g,j}(\sigma_{0,g,j}^{k}) \tag{B.14}$$

where k is the iteration index of the Bondarenko iteration, g is the subelement index, and Σ_e is the escape cross section. We use the approximate escape cross section of the chord length, which for a long cylinder of radius r is:

$$\Sigma_e \simeq \frac{\text{Surface area}}{4\,\text{Volume}} = \frac{1}{2r}. \tag{B.15}$$

In practice, the Bondarenko iteration converges quickly, often requiring fewer than ten iterations per material.

We justify using this form of the Bondarenko iteration by noting that this is a standard scheme for computing cross sections, though most practitioners use escape cross sections of higher fidelity that take into account square lattice effects and the transport cross section within a material region.[3]

B.6 Bondarenko Iterations and NJOY

B.6.1 Introduction

There are many ways to define multigroup (MG) cross sections. When generating MG cross sections directly from pointwise evaluated data, the common approach is to compute the cross sections as a flux-weighted average:

$$\sigma_g = \frac{\int\limits_{\Delta E_g} \mathrm{d}E\; f(E)\sigma(E)}{\int\limits_{\Delta E_g} \mathrm{d}E\; f(E)}, \tag{B.16}$$

for some spectrum $f(E)$.

To be accurate, the weighting spectrum, $f(E)$, should be close to the actual solution, $\psi(\mathbf{r}, E, \mathbf{\Omega})$. Because the energy dependence of ψ is tightly coupled with its spatial and directional dependence, it is in general not possible to factor out an

[3]Some practitioners even use transport calculations to inform their escape cross sections.

$f(E)$ that works in a pointwise sense. However, it is possible to define $f(E)$ that preserve the flux in some average sense. A common means of doing this is to employ an escape cross section and equivalence theory.

Equivalence theory allows us to define region-average escape cross sections, Σ_e's, that play the role of part of the leakage term in the transport equation. We begin by defining

$$J^+(E) \equiv \int_{\partial D} \mathrm{d}^3 r \int_{\mathbf{\Omega}\cdot\mathbf{n}\geq 0} \mathrm{d}\Omega \, |\mathbf{n}\cdot\mathbf{\Omega}| \psi(\mathbf{r},\mathbf{\Omega},E), \tag{B.17a}$$

$$J^-(E) \equiv \int_{\partial D} \mathrm{d}^3 r \int_{\mathbf{\Omega}\cdot\mathbf{n}<0} \mathrm{d}\Omega \, |\mathbf{n}\cdot\mathbf{\Omega}| \psi(\mathbf{r},\mathbf{\Omega},E), \tag{B.17b}$$

where $\mathbf{n}$ is the outward unit normal on the boundary of domain D.

We define our escape cross section, $\Sigma_e(E)$, as the ratio of the exiting partial current to the total flux within a region:

$$\Sigma_e(E) \equiv \frac{J^+(E)}{\phi(E)}. \tag{B.17c}$$

Equivalence theory treats leakage as though it were an absorption term with cross section $\Sigma_e(E)$.

Combining these definitions and assumptions, we find, ignoring time dependence

and lumping all local sources into one term, q:

$$[\nabla \cdot \mathbf{\Omega} + \Sigma_t(E)]\, \psi(\mathbf{r}, E, \mathbf{\Omega}) = q(\mathbf{r}, E, \mathbf{\Omega}), \tag{B.18a}$$

$$\int_D \mathrm{d}^3 r \int_{4\pi} \mathrm{d}\Omega\ [\nabla \cdot \mathbf{\Omega} + \Sigma_t(E)]\, \psi(\mathbf{r}, E, \mathbf{\Omega}) = \int_D \mathrm{d}^3 r \int_{4\pi} \mathrm{d}\Omega\ q(\mathbf{r}, E, \mathbf{\Omega}), \tag{B.18b}$$

$$J^+(E) - J^-(E) + \Sigma_t(E)\phi(E) = q(E), \tag{B.18c}$$

$$[\Sigma_e(E) + \Sigma_t(E)]\, \phi(E) = q(E) + J^-(E) = Q(E). \tag{B.18d}$$

Because of its weak dependence on energy, $\Sigma_e(E)$ is often approximated as Σ_e. The above derivation is to be applied separately for each material region.

This implies the flux is, to within a constant,

$$\phi(E) \simeq \frac{Q(E)}{\Sigma_e + \Sigma_t(E)}. \tag{B.19}$$

The narrow resonance approximation is often employed because it simplifies the flux to an analytic form. One of its assumptions is that resonances among different nuclides are well-separated and do not affect each other through self-shielding. When this is true, it is possible to represent the total cross section for a nuclide as the sum of background cross sections of other nuclides plus the local cross section. That is,

$$\Sigma_t(E) \simeq \left(\sigma_{t,i}(E) + \frac{1}{N_i} \sum_{j \neq i} N_j \bar{\sigma}_{t,j} \right) N_i. \tag{B.20}$$

The average cross sections and the escape cross section are often lumped together.

This allows us to represent the flux as

$$\phi_i(E) \simeq \frac{Q(E)}{\sigma_{t,i}(E) + \sigma_{0,i}}, \tag{B.21a}$$

$$\sigma_{0,i} \equiv \frac{1}{N_i}\left(\Sigma_e + \sum_{j \neq i} N_j \sigma_{t,j}\right). \tag{B.21b}$$

The upshot of this approach is it allows us to define a resonance-specific flux as a function of two parameters only: $Q(E)$ and σ_0.

For many light-water reactors made up of fuel pins, the incident partial current from the moderator is smoothed by the hydrogen and may be approximated as:

$$J^-(E) \simeq \frac{c}{E}. \tag{B.22}$$

This bolsters our approximation of using $Q(E) = 1/E$ in the resonance range.

We use Eq. (B.21a) with $Q(E) = 1/E$ as our spectra, $f(E)$, in Eq. (B.16). This allows us to define MG cross sections as a function of background cross sections, σ_0. The important point is that this process may be done independently for each nuclide. No information about other nuclides is required when doing the cross section preparation.

The NJOY processing code uses this technique and builds all cross sections for one nuclide on a σ_0 and temperature (T) grid. Later, cross sections can be properly mixed for each material by iteratively defining the average cross sections used in the background cross sections, the Bondarenko iteration. Analytic or simulated values are calculated for the escape cross sections.

We can estimate the magnitude of Σ_e from geometric considerations alone. If

$\psi(\mathbf{r}, \mathbf{\Omega}, E)$ is approximately constant within D, then

$$\phi(E) = \int_D \mathrm{d}^3 r \int_{4\pi} \mathrm{d}\Omega \; \psi(\mathbf{r}, E, \mathbf{\Omega}) \simeq 4\pi |D|, \tag{B.23a}$$

$$J^+(E) = \int_{\partial D} \mathrm{d}^3 r \int_{\mathbf{\Omega}\cdot\mathbf{n}\geq 0} \mathrm{d}\Omega \; |\mathbf{n}\cdot\mathbf{\Omega}| \psi(\mathbf{r}, \mathbf{\Omega}, E) \simeq \pi |\partial D|. \tag{B.23b}$$

If we define $\mathrm{V} \equiv |D|$ and $\mathrm{SA} \equiv |\partial D|$, we get back the chord length estimate of the escape cross section:

$$\Sigma_e \simeq \frac{\mathrm{SA}}{4\mathrm{V}}. \tag{B.23c}$$

The problem with the above method is it fails to account for resonance interference effects properly. For many nuclides of interest, e.g., U-238 and U-235, the resonances are sufficiently thick and numerous that they interfere with each other. The approximation in Eq. (B.20) is not appropriate, as $\sigma_{t,j}(E) \not\simeq \bar{\sigma}_{t,j}$ when $\sigma_{t,i}(E)$ has a resonance (is varying rapidly). For many reactors, U-238 is at a higher abundance than U-235, and more strongly determines the spectrum. The approximation in Eq. (B.20) therefore has more of an effect on the average cross section for U-235 than U-238 because the approximate spectrum for U-238 is closer to the true spectrum.

The solution in NJOY is to modify $Q(E)$ for the minor nuclides to account for the flux depressions that come from the major nuclides (major and minor here refering to relative atom densities). A spectrum, $f_{i,k}(E) = (1/E)[1/(\sigma_{t,i}(E) + \sigma_{0,k})]$, is saved from major nuclide i and used as the input to the group condensation for nuclide j

by saying

$$Q_j(E) \simeq f_{i,k}(E). \tag{B.24}$$

This implies the fluxes used for nuclides i and j are:

$$f_i(E) = \frac{1}{E}\frac{1}{\sigma_{t,i}(E) + \sigma_{0,i}}, \tag{B.25a}$$

$$f_{j,(i,k)}(E) = \frac{1}{E}\frac{1}{\sigma_{t,i}(E) + \sigma_{0,k}}\frac{1}{\sigma_{t,j}(E) + \sigma_{0,j}}. \tag{B.25b}$$

At first glance, this seems to be in error, as the correct spectrum is

$$f_j(E) = \frac{1}{E}\frac{1}{N_i\sigma_{t,i}(E) + N_j\sigma_{t,j}(E) + \ldots + \Sigma_e} \tag{B.26}$$

It can be shown that Eq. (B.25) yields better estimates of the average cross sections than using $Q(E) = 1/E$ for each nuclide, assuming proper values of $\sigma_{0,i}$, $\sigma_{0,j}$, and $\sigma_{0,k}$ may be found. The values of $\sigma_{0,i}$ and $\sigma_{0,j}$ may be found by using Bondarenko iteration as per normal.

The difficulty with this approach as it is implemented in NJOY lies with the definition of $\sigma_{0,k}$, because it requires an *a priori* estimate instead of an *a posteriori* calculation. That is, the flux cannot be given on a grid of $\sigma_{0,k}$ values and later interpolated without performing multiple NJOY runs for the second nuclide.

A reasonable approximation to the average cross section is the potential cross section, σ_p, which is the cross section a nuclide attains away from resonances. If fuel composition is approximately constant, we can calculate the $\sigma_{0,k}$ using analytic factors for the escape cross section, potential cross sections for the other nuclides, and average nuclide atom densities for the other nuclides' atom densities.

To prevent confusion, we call using $Q(E) = 1/E$ for all nuclides the "one-step approach" and using $Q_i(E) = 1/E$ for the major nuclide and $Q_j(E) = f_{i,k}(E)$ for the minor nuclides the "two-step approach." Although future subsections show the two-step approach to be superior to the one-step approach, we utilize the latter in our results in this work because the latter approach is a simpler workflow. This choice should affect the error coefficients but should not affect the error convergence rates for either MG and FEDS. This latter claim is backed up by results using reference-weighted basis functions in the cylindrical pincell tests.

B.6.2 Problem studied

We wish to ascertain the accuracy of the one-step and two-step approaches in calculating group-averaged cross sections. To do this, we have developed a mock problem wherein the major nuclide, which we now call f, has one large resonance at an energy of 10 eV and a potential cross section of 10 cm^{-1}.[4] In addition to the major nuclide, there is a minor nuclide, which we now call g, that also has one resonance. The resonance magnitude for g is a factor of 100 times smaller than for f. The nuclide g also has a potential cross section of 10 cm^{-1}.

We vary three parameters and study the accuracy of the MG cross section as a function of these parameters. The parameters are the location (in energy) of g's resonance, which determines resonance overlap between f and g; the "frozen background cross section," which corresponds to $\sigma_{0,k}$ in the above derivation; and the true escape cross section. Unlike the true escape cross section, which changes, the escape cross section we use when calculating the weighting function spectra will be fixed at the nominal value of the true escape cross section. Varying the true escape cross section mimics changing radii in the fuel pin. This last variation allows us to

[4] We are using partial macroscopic cross sections throughout to eliminate confusing divisions by atom density. The partial macroscopic cross section for nuclide i is $N_i\sigma_{t,i}$.

estimate how well our material- and energy-averaged cross sections approximate the true spatially varying energy-averaged cross sections.

B.6.3 Results

B.6.3.1 Nominal escape cross section

Figure B.2 shows the cross sections as functions of energy. The subfigures show different resonance positions for nuclide g with increasing amounts of overlap to the resonance of nuclide f.

Figure B.3 shows the fluxes used by the one-step process to weight the cross sections compared to the true flux. As expected, the one-step process produces poor flux estimates when resonances overlap.

Figure B.4 shows the fluxes used by the two-step process. The frozen flux is also shown, though it is in all cases overlapped by the flux for f, indicating we made a reasonable guess for the background cross section that defines the frozen flux (more on this later). The two-step flux for g does a much better job of tracking the true flux for all cases of overlap, which was expected. The two-step flux for f, which does not take into account any pointwise information about g, does not track the true flux well near resonances of g, which is also expected. The two-step flux for g seems to overestimate the shielding for complete overlap.

Figure B.5 shows the absolute errors in group-averaged cross sections for various fluxes as a function of the background cross section used to define the frozen flux. There are three interesting trends. The first is that it is possible to define a frozen flux that gets the average cross section for g exactly correct. However, this position is different for different overlap positions and furthermore is not knowable without knowing the true flux, and so is of limited use. The second point is that using the guess for background cross section of the frozen flux generally produces a better

estimate of the average cross section for nuclide g than is attainable with the single-step method. What was not anticipated was the error in average cross section for nuclide f can *also* be decreased using the two-step method, even though the spectrum for f has no knowledge of the pointwise spectrum of g. The reason is that f still contains a background cross section to which g contributes. The increase in fidelity for g feeds back into f. This effect is most apparent for the complete overlap case. The final point is to notice the absolute magnitudes of the errors. For the low overlap cases, the magnitude of the error is small for both nuclides, between 0.1 to 1.0 %. With the one-step method, as overlap increases, error increases. For the two-step method, error remains between 0.1 to 1.0 % or is reduced. The worst error occurs in the case of large but not complete overlap, where error approaches 1 %.

Figure B.6 shows the ratio of errors between the one-step method and two-step method as a function of the background cross section used to define the frozen flux. In general, the error for f is approximately the same using either the one- or two-step method. The error for g is generally better using the two-step method, though it can worsened if a poor background cross section for the frozen flux is used. The case where the error could get worse did have errors whose magnitudes were small.

B.6.3.2 Small escape cross section (inside pin)

This subsection examines the effect of drastically reducing the true escape cross section while still using a larger (region-average) escape cross section in the one- and two-step methods. This simulates fluxes and cross sections near the inside of a fuel pin and seeks to show that MG cross sections do not perform well in a pointwise sense.

Figure B.7 shows that the trends mentioned above hold, though the magnitude of the errors are increased because an incorrect escape cross section is used for the

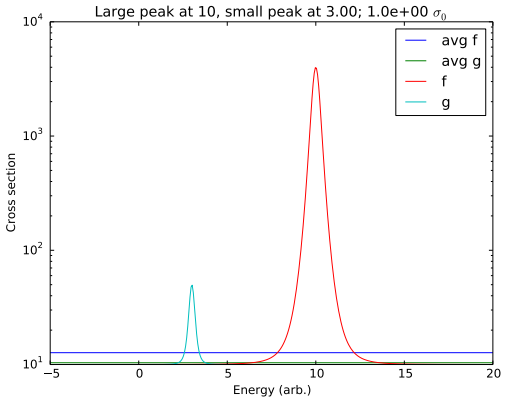

(a) No overlap

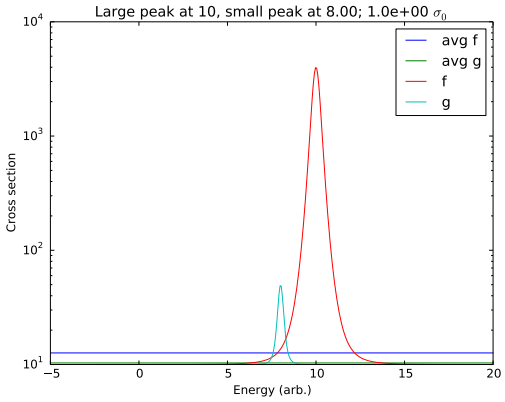

(b) Some overlap

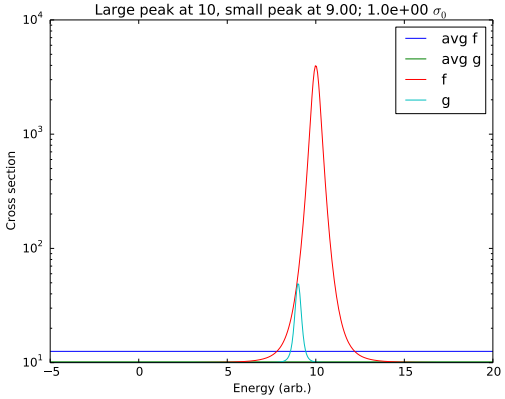

(c) Large overlap

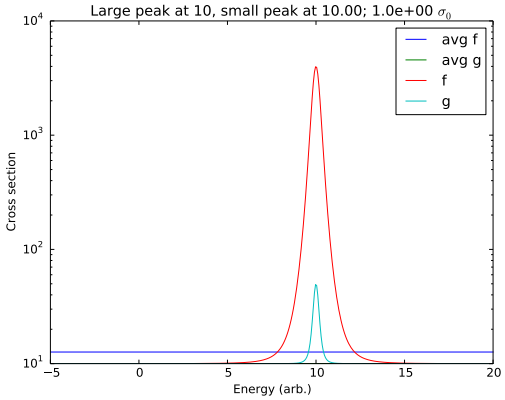

(d) Complete overlap

Figure B.2: Pointwise cross sections as a function of energy for varying resonance locations of nuclide g. Averages use the true average.

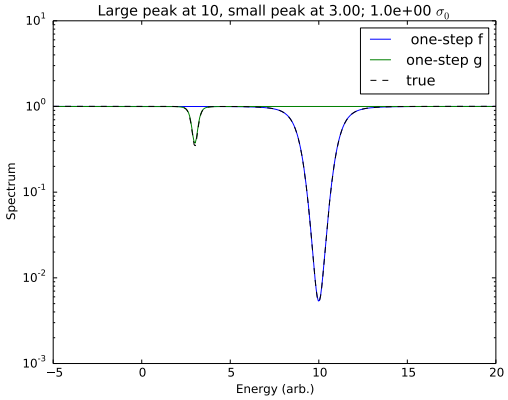

(a) No overlap

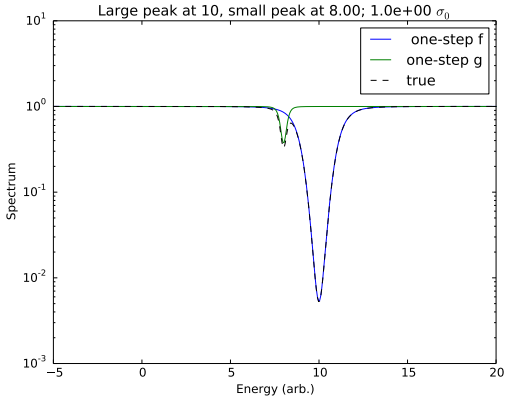

(b) Some overlap

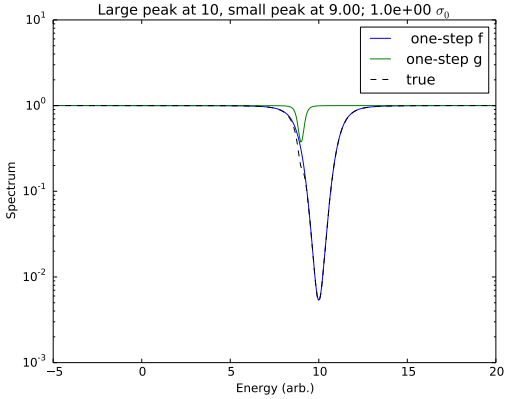

(c) Large overlap

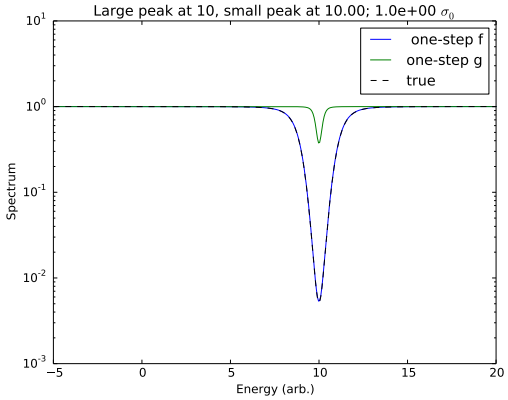

(d) Complete overlap

Figure B.3: One-step fluxes and true flux as a function of energy for varying resonance locations of nuclide g. $Q(E) = 1/E$ was used in the one-step process.

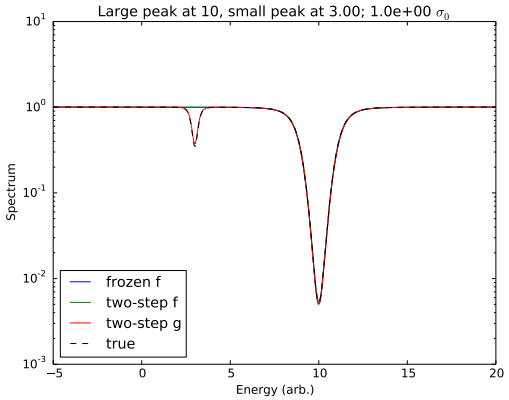

(a) No overlap

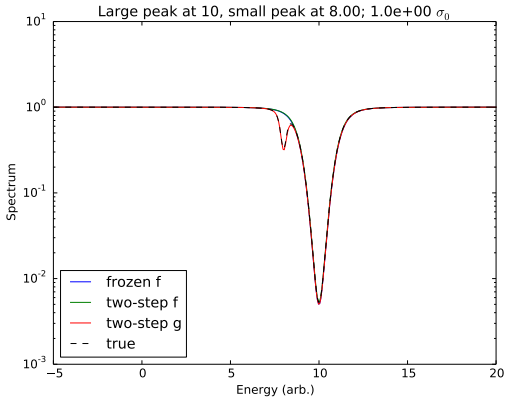

(b) Some overlap

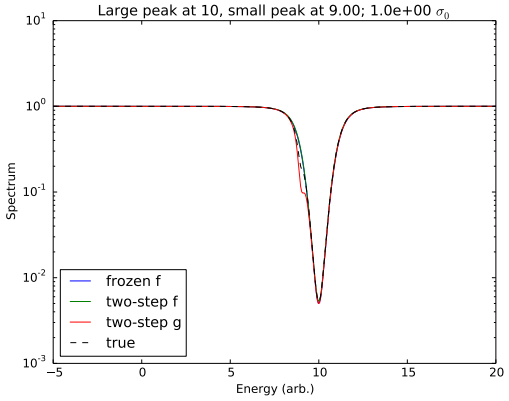

(c) Large overlap

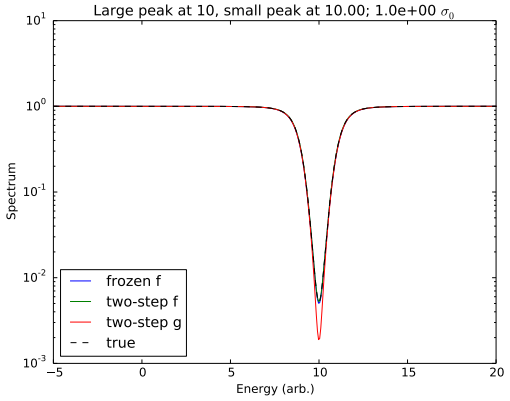

(d) Complete overlap

Figure B.4: Two-step, frozen, and true fluxes as a function of energy for varying resonance locations of nuclide g. The frozen flux is the $Q(E)$ used for g in the second step ($Q(E) = 1/E$ was used for f in the first step).

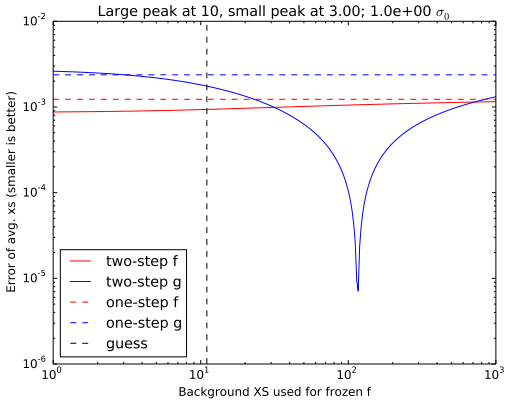

(a) No overlap

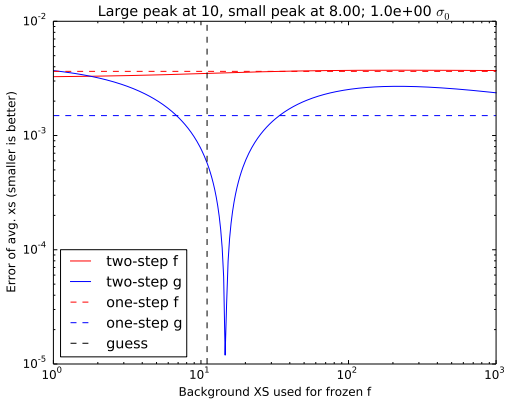

(b) Some overlap

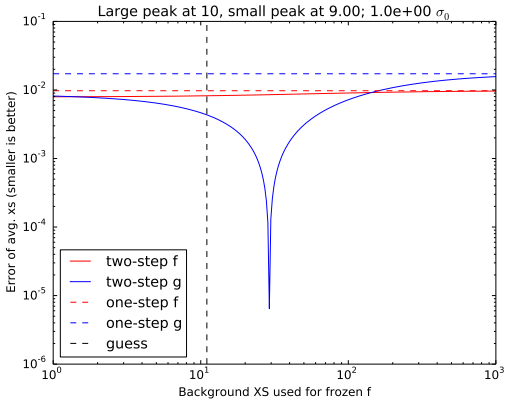

(c) Large overlap

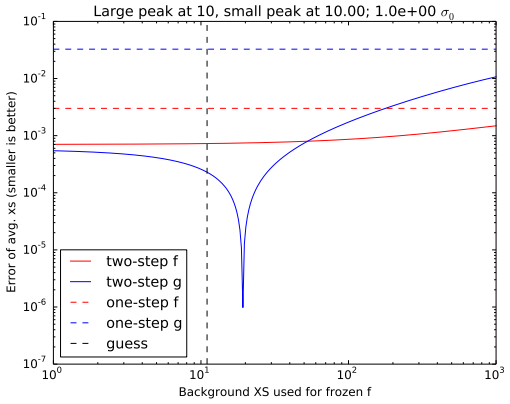

(d) Complete overlap

Figure B.5: Absolute errors in group-averaged cross sections using the one- and two-step methods as a function of the background cross section used in the frozen flux (i.e., as a function of $\sigma_{0,k}$). "Guess" refers to the background cross section that would be chosen from the *a priori* potential-cross section estimate.

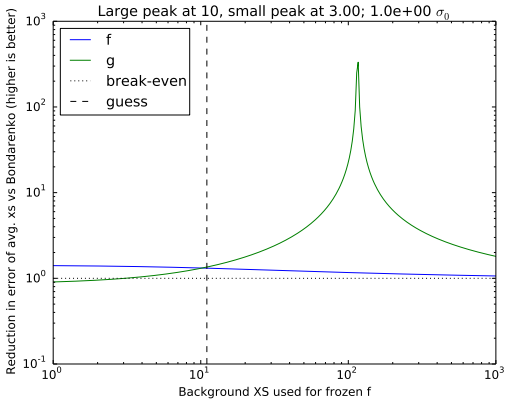

(a) No overlap

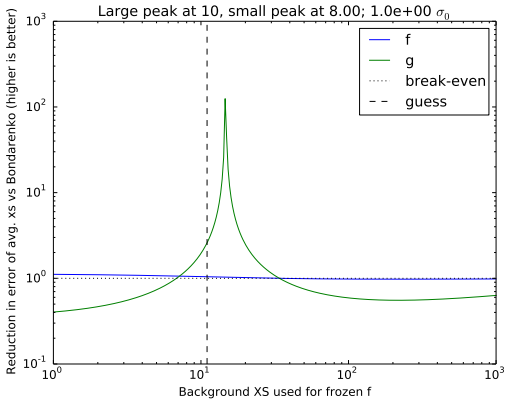

(b) Some overlap

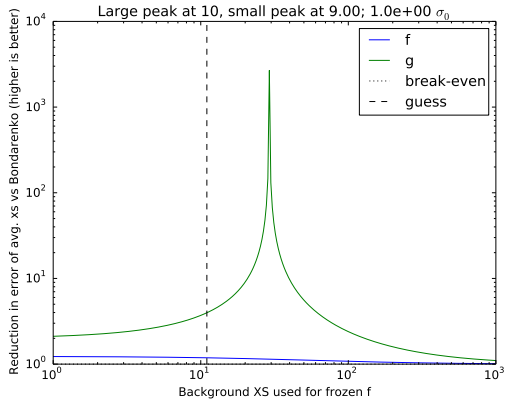

(c) Large overlap

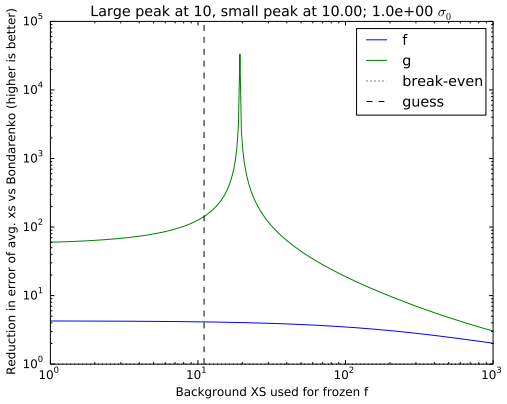

(d) Complete overlap

Figure B.6: Relative errors in group-averaged cross sections between the one- and two-step methods as a function of the background cross section used in the frozen flux (i.e., as a function of $\sigma_{0,k}$). "Guess" refers to the background cross section that would be chosen from the *a priori* potential-cross section estimate.

methods.

B.6.3.3 Moderate escape cross section (nearer to outside of pin)

In this subsection, a larger escape cross section is used in the true spectrum than in the Bondarenko iteration used in the one- and two-step methods.

Figure B.8 shows that the same trends occur as were given in the previous subsection: multigroup cross sections are sensitive to spectrum in the resonances, which in this case was modified by increasing the escape cross section.

B.6.3.4 Large escape cross section (outside of pin)

This subsection again varies the escape cross section used in the true spectrum to simulate the spectrum near the outside of a fuel pin. The escape cross section is now 1000 times that used in the one- and two-step methods.

Figure B.9 shows the pointwise cross section as a function of energy along with the averaged cross sections using the true flux. Notice how much larger the averaged cross sections are than in Fig. B.2.

Figure B.10 shows the one-step and true fluxes as functions of energy. For most cases, the one-step fluxes vastly over-shield because they are using the wrong escape cross section. Notice how the true flux does not dip at all due to nuclide g.

Figure B.11 shows the two-step and true fluxes as functions of energy. The two-step method produces more correct average fluxes, but the point under consideration is not near the average spectrum, so the two-step method does not do a good job estimating the fluxes.

Figure B.12 shows the absolute errors in energy-averaged cross sections when comparing region-averaged one-step and two-step fluxes against the pointwise (in space) true flux. The errors in the flux for nuclide g are less than 1 % because the resonance for nuclide g is small. The errors in the flux for nuclide f are large,

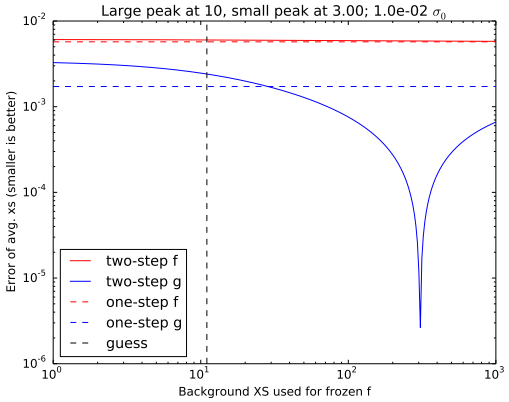

(a) No overlap

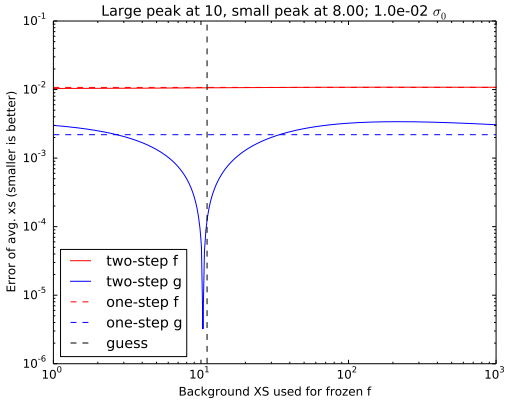

(b) Some overlap

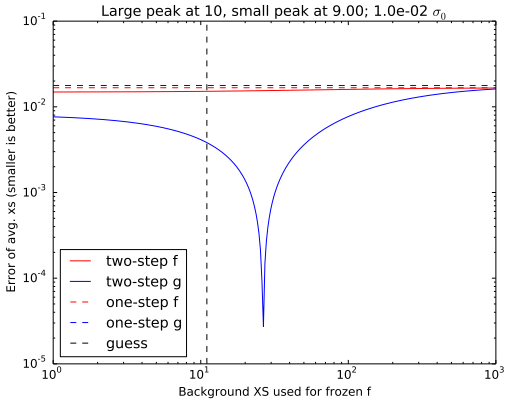

(c) Large overlap

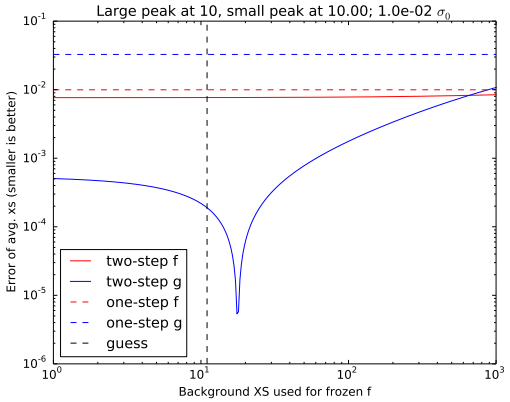

(d) Complete overlap

Figure B.7: Absolute errors in group-averaged cross sections using the one- and two-step methods as a function of the background cross section used in the frozen flux (i.e., as a function of $\sigma_{0,k}$) for small true escape cross section. "Guess" refers to the background cross section that would be chosen from the *a priori* potential-cross section estimate.

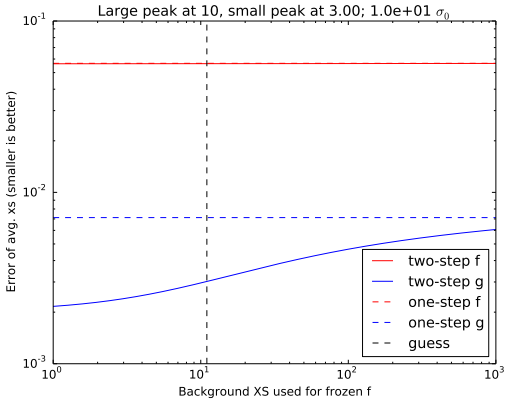

(a) No overlap

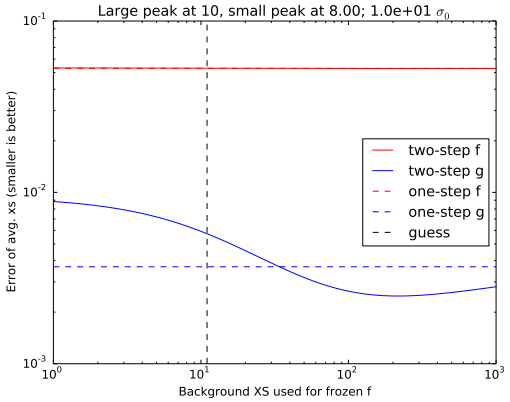

(b) Some overlap

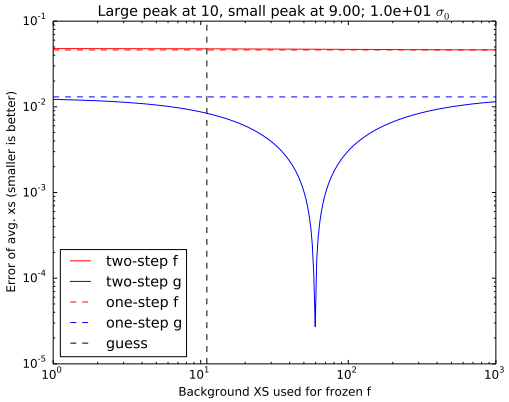

(c) Large overlap

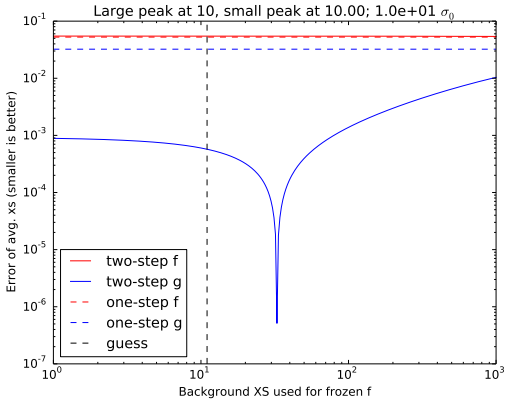

(d) Complete overlap

Figure B.8: Absolute errors in group-averaged cross sections using the one- and two-step methods as a function of the background cross section used in the frozen flux (i.e., as a function of $\sigma_{0,k}$) for moderate true escape cross section. "Guess" refers to the background cross section that would be chosen from the *a priori* potential-cross section estimate.

approaching 70 %!

This last point is important, because it gives us a sense of the error we incur in using a flat weighting flux ($f(E) = 1/E$). The error directly depends on the magnitude of the resonances.

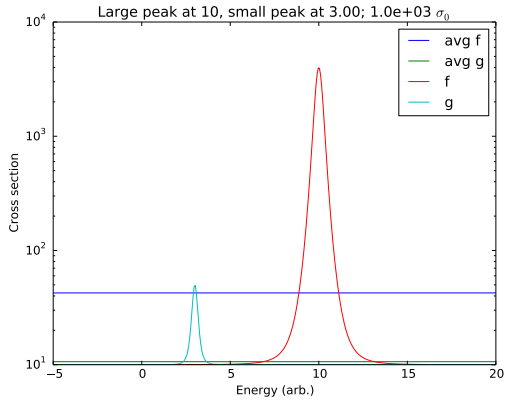

(a) No overlap

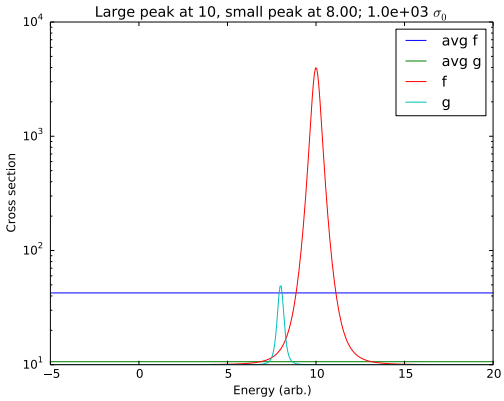

(b) Some overlap

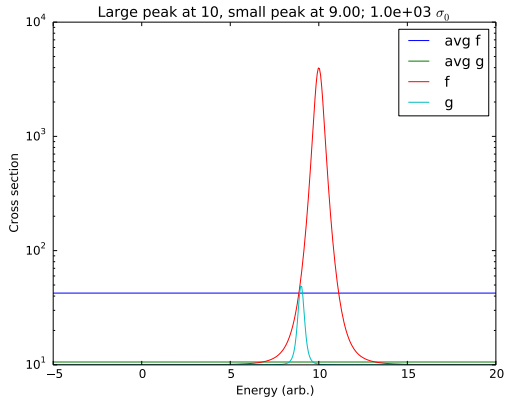

(c) Large overlap

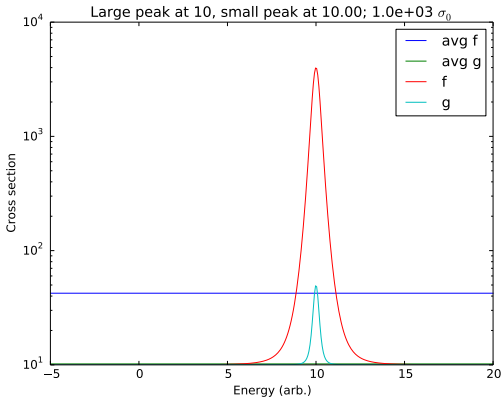

(d) Complete overlap

Figure B.9: Pointwise cross sections as a function of energy for varying resonance locations of nuclide g for large true escape cross section. Averages use the true average.

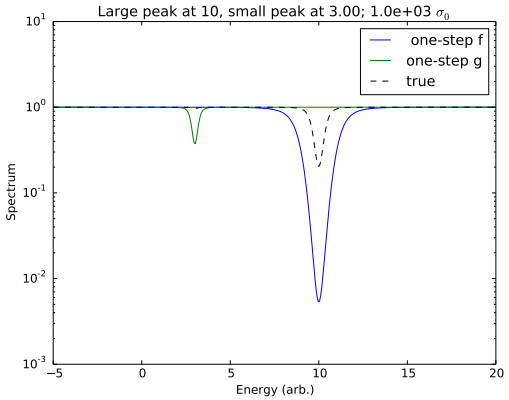

(a) No overlap

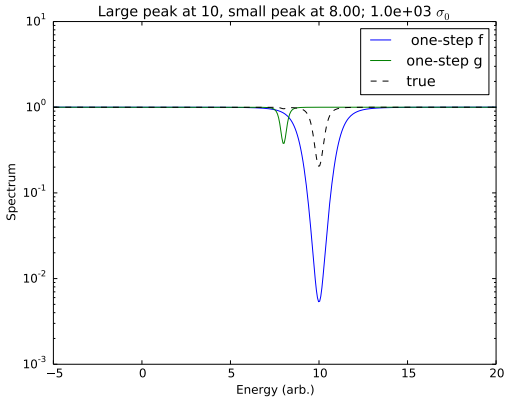

(b) Some overlap

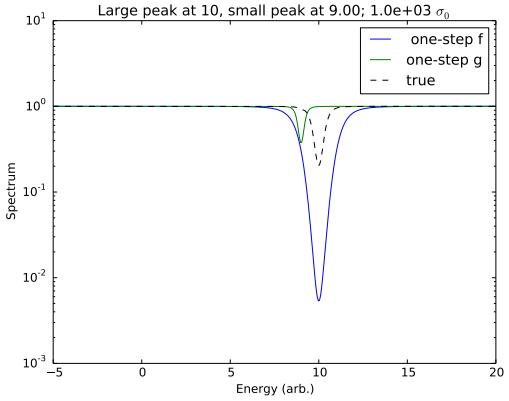

(c) Large overlap

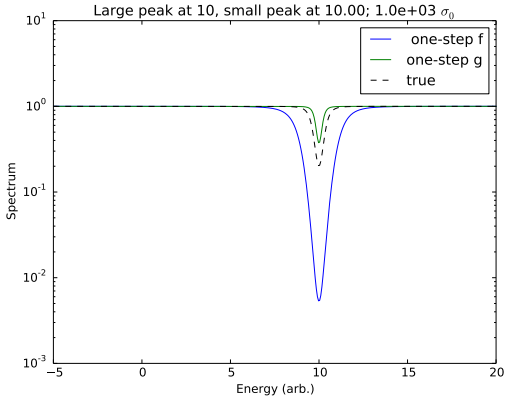

(d) Complete overlap

Figure B.10: One-step fluxes and true flux as a function of energy for varying resonance locations of nuclide g for large true escape cross section. $Q(E) = 1/E$ was used in the one-step process.

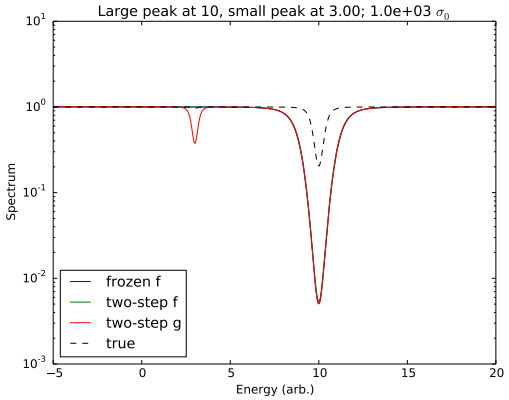

(a) No overlap

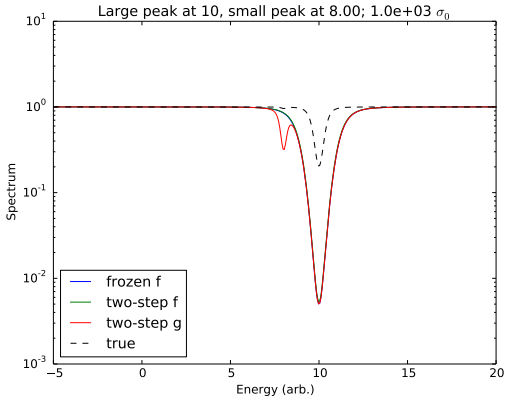

(b) Some overlap

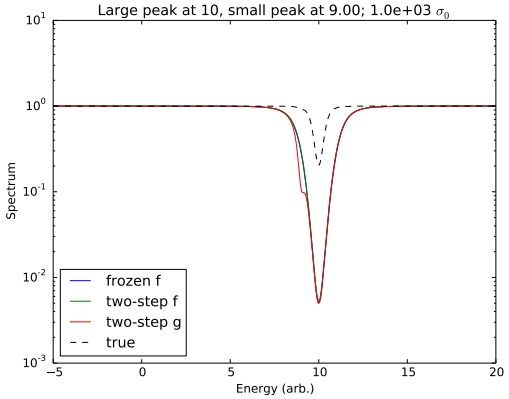

(c) Large overlap

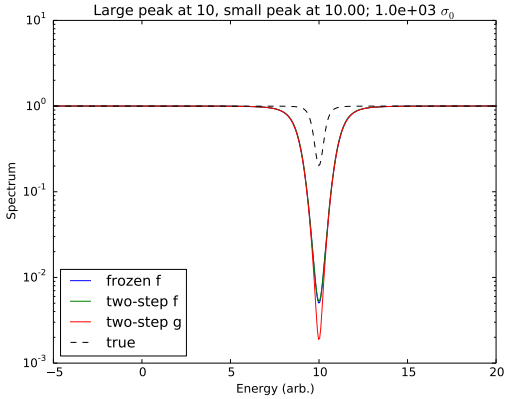

(d) Complete overlap

Figure B.11: Two-step, frozen, and true fluxes as a function of energy for varying resonance locations of nuclide g for large true escape cross section. The frozen flux is the $Q(E)$ used for g in the second step ($Q(E) = 1/E$ was used for f in the first step).

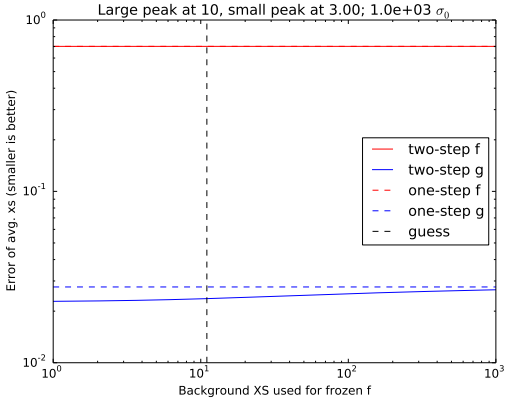

(a) No overlap

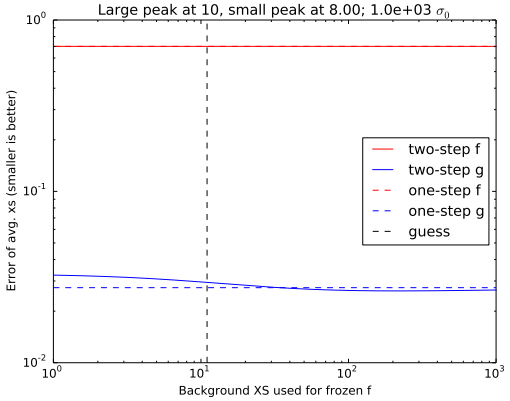

(b) Some overlap

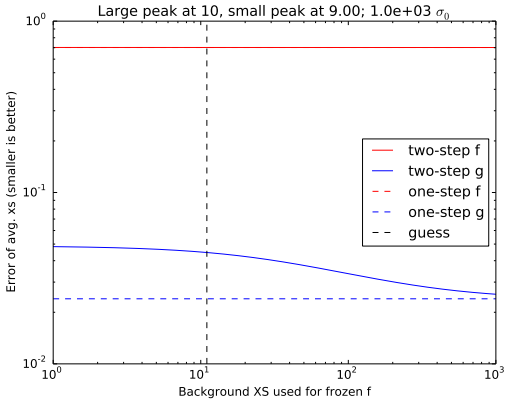

(c) Large overlap

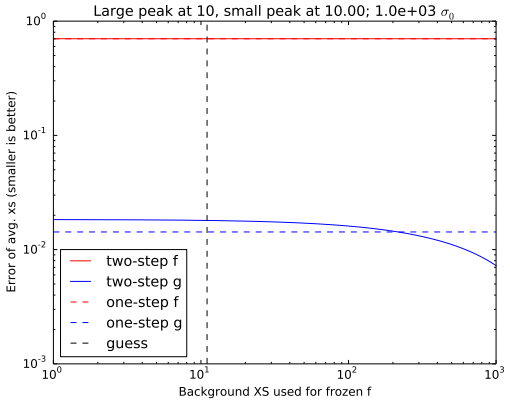

(d) Complete overlap

Figure B.12: Absolute errors in group-averaged cross sections using the one- and two-step methods as a function of the background cross section used in the frozen flux (i.e., as a function of $\sigma_{0,k}$) for large true escape cross section. "Guess" refers to the background cross section that would be chosen from the *a priori* potential-cross section estimate.

B.7 Calculating Total Cross Section on a Union Energy Grid

We use the following approach to generate spectra using Σ_t:

1. Choose the bounding materials list.

2. From the bounding materials, create a global nuclide set. Nuclides at different temperatures should be treated as separate nuclides.

3. Create a PENDF (or ACE) file for each nuclide and from it read in each σ_t.

4. Create a unionized energy grid over all nuclides in the global nuclide set that is the union of the energy grid of each σ_t.

5. For each material, compute Σ_t on the unionized energy grid.

6. Thin the energy grid using a linear interpolation criterion.
   Remove an energy grid point if the error made at that point using a linear interpolation of its neighbors is within a tolerance for all materials (all Σ_t). Do not remove multiple consecutive points during each thinning pass. Iterate until no points are removed.

7. Enrich the energy grid near strong gradients to bound cross section jump.
   The clustering algorithm and (FEDS-)MG in general uses a piecewise constant representation of the cross sections, while the cross sections are currently represented as piecewise linear. For a given range, add a midpoint if the relative difference between any two neighboring Σ_t is greater than some tolerance. Apply this recursively until no points are added.

8. Create an observation matrix (energy by material) equal to the logarithm of the Σ_t.

B.8 Calculating Infinite-Medium Flux Spectra on a Union Energy Grid

We use the following approach to create spectra from infinite-medium-equivalent fluxes. A difficulty in this approach is that both the infinite-medium fluxes and a suitable energy grid upon which they are to be defined are unknown *a priori*, and must be built together iteratively. We use a predictor-corrector scheme when building the mesh and its solution.

1. Choose the bounding materials list.

2. From the bounding materials, create a global nuclide set. Nuclides at different temperatures should be treated as separate nuclides.

3. Create a PENDF (or ACE) file for each nuclide and from it read in each σ_s and σ_t.

4. Choose which σ_s to keep. This may be done by relative atom fraction, atomic number, manually, etc.

5. Create a unionized energy grid over all nuclides in the global nuclide set that is the union of the energy grid of each σ_t. For each nuclide, σ_s and σ_t already have the same grid.

6. For each material, compute Σ_t on the unionized energy grid.

7. Thin the energy grid using a linear interpolation criterion.

   Remove an energy grid point if the error made at that point using a linear interpolation of its neighbors is within a tolerance for all Σ_t. Do not remove multiple consecutive points during each thinning pass. Iterate until no points are removed.

8. Enrich the energy grid to handle downscattering.

   Require a minimum grid spacing in lethargy that is some small constant times the downscatter distance off the heaviest nuclide. If two points are further away than this criterion, add a midpoint. Do this iteratively until no points are added.

9. Compute the infinite-medium flux, Q/Σ_t.

   Do this for each material, solving an infinite-medium-equivalent slowing-down equation, where Q includes a source from elastic down-scattering. See below for more details. When looking up σ_s values, use linear-linear interpolation from their original grid onto the union grid as needed.

10. Thin the energy grid using a linear interpolation criterion.

    Remove an energy grid point if the error made at that point using a linear interpolation of its neighbors is within a tolerance for all Q/Σ_t. Do not remove multiple consecutive points during each thinning pass. Iterate until no points are removed.

11. Enrich the energy grid near strong gradients of Q/Σ_t.

    The clustering algorithm and (FEDS-)MG in general uses a piecewise constant representation of the flux, while the flux on the union grid is represented as piecewise linear. For a given range, add a midpoint if the relative difference between any two neighboring Q/Σ_t is greater than some tolerance. Apply this iteratively until no points are added.

12. Enrich the energy grid in energy.

    To ensure a minimum lethargy resolution in the energy grid, add a midpoint between two energy points further away than a criterion lethargy spacing. Do

this iteratively until no points are added.

13. Create an observation matrix (energy by material) equal to the logarithm of the normalized infinite-medium flux.

We calculate the Q/Σ_t by solving an infinite-medium-equivalent, fixed-source, slowing-down equation. For thermal systems, a homogenized infinite medium includes hydrogen and hence a $1/E$ source in the resonance region. For fast systems, this contribution is neglected. For thermal systems, we take

$$\begin{aligned} q(E) = &\left[\frac{1}{E_{\text{thermal}}} + \frac{\chi(E_{\text{thermal}})}{E_{\text{fast}}\chi(E_{\text{fast}})}\right]\frac{M(E)}{M(E_{\text{thermal}})}\,(\text{if } E < E_{\text{thermal}}) + \\ &\left[\frac{1}{E} + \frac{\chi(E)}{E_{\text{fast}}\chi(E_{\text{fast}})}\right](\text{if } E_{\text{thermal}} \le E < E_{\text{high}}) + \\ &\left[\frac{1}{E_{\text{high}}} + \frac{\chi(E_{\text{high}})}{E_{\text{fast}}\chi(E_{\text{fast}})}\right](\text{if } E_{\text{high}} \le E), \end{aligned} \tag{B.27a}$$

where $M(E)$ is a Maxwellian, $\chi(E)$ is a Watt fission spectrum, E_{thermal} is around 0.1 eV, E_{fast} is around 50 keV and E_{high} is around 10 MeV. E_{high} is used to prevent the rapid decline of $\chi(E)$ at high energies. For fast systems, knowing nothing better, we take

$$\begin{aligned} q(E) = &\,1\,(\text{if } E < E_{\text{fast}}) + \\ &\frac{\chi(E)}{\chi(E_{\text{fast}})}\,(\text{if } E_{\text{fast}} \le E < E_{\text{high}}) + \\ &\frac{\chi(E_{\text{high}})}{\chi(E_{\text{fast}})}\,(\text{if } E_{\text{high}} \le E). \end{aligned} \tag{B.27b}$$

For a given escape cross section, Σ_e, we solve

$$\big[\Sigma_e + \Sigma_t(E)\big]\phi(E) = \sum_i \left[\frac{N_i}{1-\alpha_i}\int_E^{E/\alpha_i} \mathrm{d}E'\,\frac{\phi(E')\sigma_{s,i}(E')}{E'}\right] + q(E), \tag{B.28}$$

for $\phi(E)$, where i is the index over nuclide (for the nuclides to be included in the scattering source) and $\alpha_i = [(A_i - 1)/(A_i + 1)]^2$. We solve the equation for each grid point, which is like collocating on E. Using robust a trapezoidal approximation to the scattering source, we find, for a given E,

$$\int_E^{E/\alpha_i} \mathrm{d}E'\ \phi(E')\sigma_{s,i}(E') = \sum_{\{j|E\le E_j \cap E_{j+1}<E/\alpha_i\}} (E_{j+1} - E_j)\left[\left(\frac{E_j}{E_j + E_{j+1}}\right)\frac{\phi_j\sigma_{s,j}}{E_j} + \left(\frac{E_{j+1}}{E_j + E_{j+1}}\right)\frac{\phi_{j+1}\sigma_{s,j+1}}{E_{j+1}}\right] + (E/\alpha_i - E_k)\left[\left(\frac{E_k}{E_k + E/\alpha_i}\right)\frac{\phi_k\sigma_{s,k}}{E_k} + \left(\frac{E/\alpha_i}{E_k + E/\alpha_i}\right)\frac{\phi_{k+1}\sigma_{s,k+1}}{E_{k+1}}\right], \tag{B.29}$$

where k is defined such that $E_k < E/\alpha_i \le E_{k+1}$.

The equation may be solved without iteration by using backward substitution (starting at high energies and decreasing). As we are not interested in the thermal range, we do not solve past E_{thermal}, letting $\phi(E) = 1$ there.

Most weighting spectra, including those used in NJOY use a long-range shape of $1/E$. For thermal systems, weighting functions that look like $q(E)$ are often used. Let us define $f(E)$ as a crude but nonetheless useful approximation to the weighting spectrum. We approximate $f(E) \simeq q(E)$.

We compute the observations as $\log[\phi(E)/f(E)]$ and additively normalize them such that the median is zero. The division by $f(E)$ is important, as it removes long-range shape from the observations.

APPENDIX C

ADDENDUM TO SECTION 3

C.1 Differences Between FEDS and PG-FEMG

While the previous work developed the PG-FEMG method and demonstrated its efficacy, it focused on one-dimensional problems, used a simple algorithm to determine the generalized (discontiguous) energy mesh (GEM), and used either an accurate-but-expensive or inexpensive-but-inaccurate weighting spectrum for cross section condensation. In this work, we generalize the method to a larger class of problems, GEM-determining algorithms, and weighting spectra. We develop and test a more rigorous scheme for determining the GEMs that focuses on capturing the solution, not one effective total cross section, which is merely a proxy for the solution. Finally, we test weighting spectra for cross section condensation that are a middle ground between using the reference solution on the full problem and using a generic $1/E$ spectrum.

In previous work, [1], the GEMs were formed according to the magnitude of the total cross section using a band-boundary calculation (BBC), as in BP or DED MB. For problems with more than one material or temperature, an effective total cross section was used so the GEM would be the same for every nuclide in the problem. This effective total cross section was a weighted average of the macroscopic total cross section in each user-defined spatial region, with weighting being either straight or proportional to the region-averaged flux from a reference calculation.

BBC may not produce an optimal GEM. If only one resonant material is used, the BBC does not account for resonant downscattering off heavy nuclides, as its

energy elements are determined solely on the total cross section. If more than one resonant material is used, an additional approximation is made of basing the bands off a problem-averaged effective total cross section. It is not clear that simply averaging the disparate macroscopic total cross sections and forming bands based on that effective total cross section would preserve important resonant features in each material. Even if all resonant features were preserved in the limit of infinite bands per group, there would be no guarantee of GEM quality for moderate numbers of bands per group. It would be better to form a GEM that isolates resonant features of the total cross section for each material in addition to capturing resonant downscattering regions.

In previous work, we focused on providing bounding cases for flux weighting fidelity. Our low-fidelity weighting had no resonance shielding information and was $1/E$ in the resonance regions. Our high-fidelity weighting was the reference solution averaged over a material region.

For this work, we seek weighting spectra that are both inexpensive (not the reference weighting) and accurate (not the generic weighting). We care less about studying the sensitivity of the error to fidelity of the weighting spectrum and more about developing a practical method for determining weighting spectra that can be accurately and cheaply applied to multi-dimensional problems. Due to the fundamental similarities of FEDS and MG, we investigate weighting spectrum generation methods used by MG for cross section condensation.

There are many schemes to determine weighting spectra for the MG method. One common example is invoking the narrow-resonance (NR) approximation or its kin. These are not appropriate in the resolved resonance region and may contribute substantial error. Higher fidelity options include using hyperfine-group (HFG) or continuous-energy (CE) calculations to determine weighting spectra. Such options

often are not practical for multi-dimensional systems due to cost. When these options are exercised on zero- or one-dimensional sub-problems, heterogeneity information is lost or is approximated using equivalence theory, which may also introduce errors. In this work, we focus on solving the infinite-medium slowing-down equations with equivalence theory to account for heterogeneity with an escape cross section and using these solutions as the weighting spectra within each material region.

While many of the above weighting spectrum generation methods require severe approximations, we note PG-FEMG has previously been shown to be less sensitive to weighting spectrum than MG. Both FEDS and PG-FEMG before it have separate DOF for energies that are most sensitive to spatially and angularly induced changes in the spectrum. In previous work, we found that we could get acceptable errors in our quantities of interest (QOI) by increasing the number of bands per group, even when we weighted the cross sections with $1/E$. We will show that a similar emphasis here allows us to focus on generation of the GEM and use a crude method to get our weighting spectra.

We find FEDS to be superior to PG-FEMG for these pincell problems. Our FEDS implementation is able to use more elements per resonance than our PG-FEMG implementation, which allows FEDS to achieve lower errors at lower total DOF count, especially when the new, medium-fidelity basis functions are used. Error convergence rates, while not always smooth, demonstrate first-order convergence over long ranges of energy element unknown counts that were unattainable in previous PG-FEMG studies. Future sections introduce coarse groups and show FEDS to be an attractive method for more complicated problems and against more convincing reference solutions.

C.2 Additional Results

Figures C.1 and C.2 give errors for each QOI for hierarchical agglomerative clustering for problem 3 with the low-energy portion of the resonance range resolved. Errors are given for varying basis function fidelities (the three cases) as a function of the number of energy elements in the resolved resonance range (RRR).

Figures C.3 and C.4 give errors for each QOI for k-means clustering for problem 3 with the low-energy portion of the resonance range resolved.

Figures C.5 and C.6 give errors for each QOI for αMG for problem 3 with the low-energy portion of the resonance range resolved.

Figures C.7 and C.8 give errors for each QOI for sMG for problem 3 with the low-energy portion of the resonance range resolved.

Figures C.9 – C.11 give errors for each QOI for hierarchical agglomerative clustering for problem 3 with the medium-energy portion of the resonance range resolved.

Figures C.12 – C.14 give errors for each QOI for hierarchical agglomerative clustering for problem 5 with the low-energy portion of the resonance range resolved.

Figures C.15 and C.16 give errors for each QOI for hierarchical aggl. clustering for problem 5 with the medium-energy portion of the resonance range resolved.

Figures C.17 and C.18 give errors for each QOI for k-means clustering for problem 5 with the medium-energy portion of the resonance range resolved.

Figures C.19 and C.20 give errors for each QOI for αMG for problem 5 with the medium-energy portion of the resonance range resolved.

Figures C.21 and C.22 give errors for each QOI for sMG for problem 5 with the medium-energy portion of the resonance range resolved.

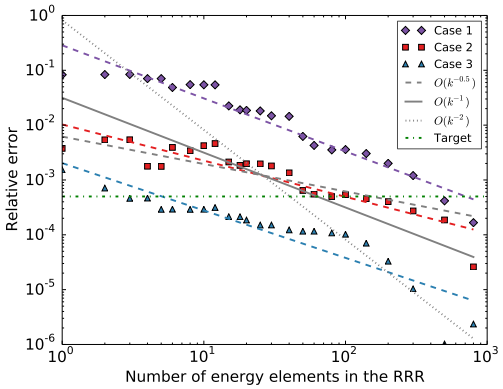

(a) Absorption rate in inner (hottest) Pu-239

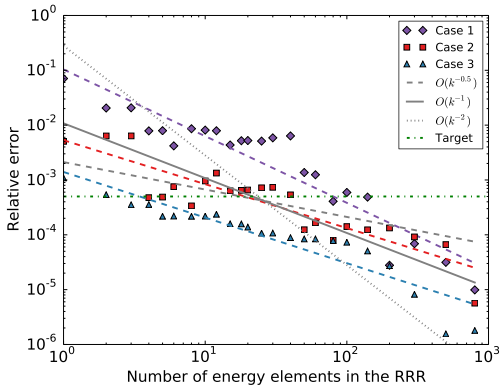

(b) Fission production rate in inner Pu-239

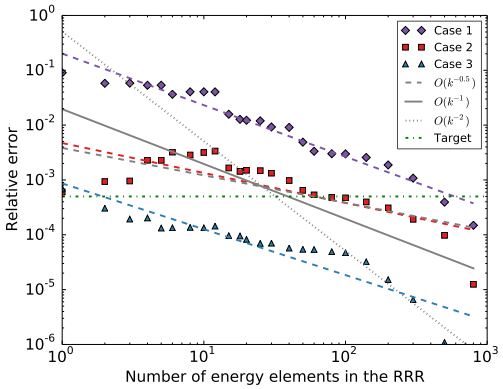

(c) Absorption rate in middle Pu-239

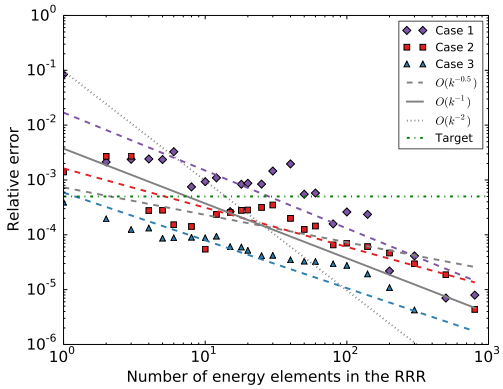

(d) Fission production rate in middle Pu-239

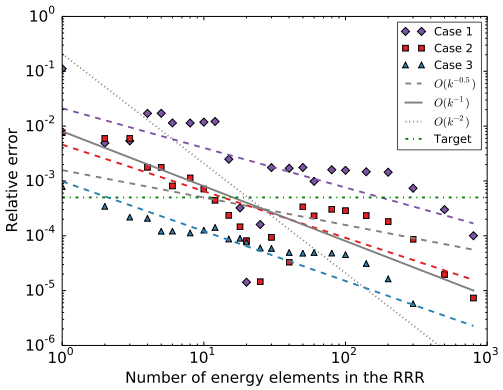

(e) Absorption rate in outer (coolest) Pu-239

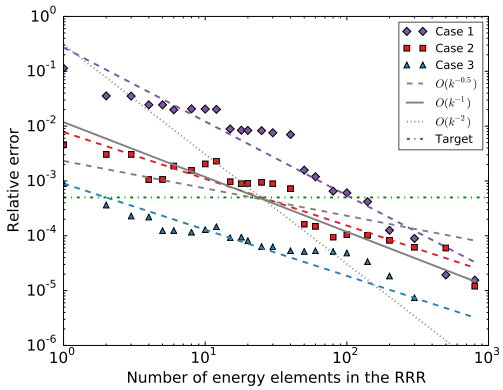

(f) Fission production rate in coolest Pu-239

Figure C.1: Errors for individual QOI as a function of energy elements for problem 3 in the low-energy RRR for all cases and the hierarchical agglomerative clustering method.

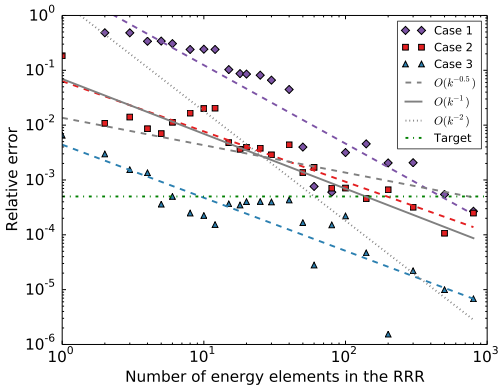

(a) Absorption rate in inner U-238

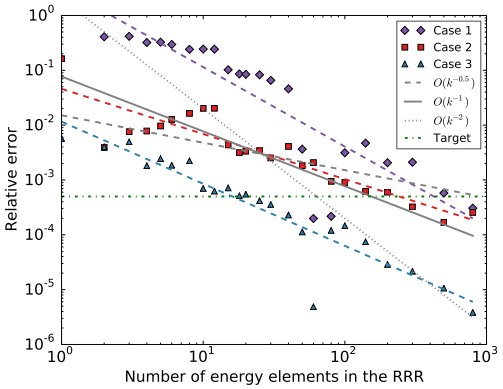

(b) Absorption rate in middle U-238

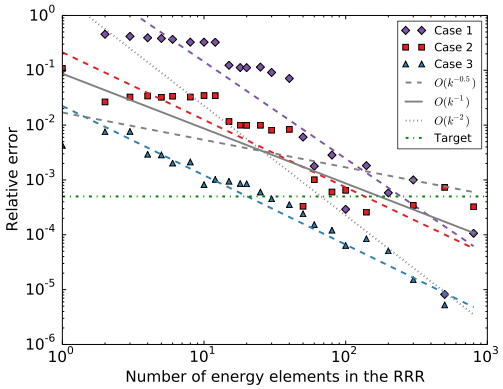

(c) Absorption rate in outer U-238

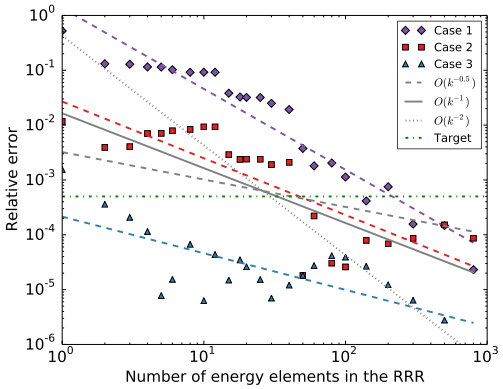

(d) Criticality eigenvalue

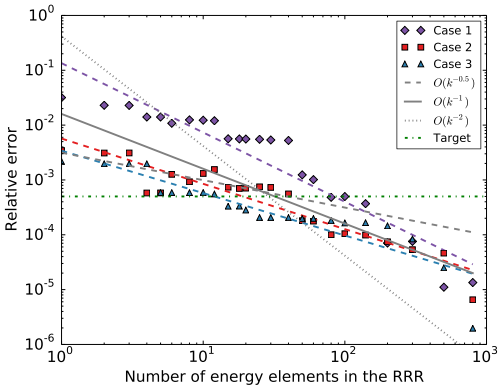

(e) Power shape

Figure C.2: Errors for individual QOI as a function of energy elements for problem 3 in the low-energy RRR for all cases and the hierarchical agglomerative clustering method (cont.).

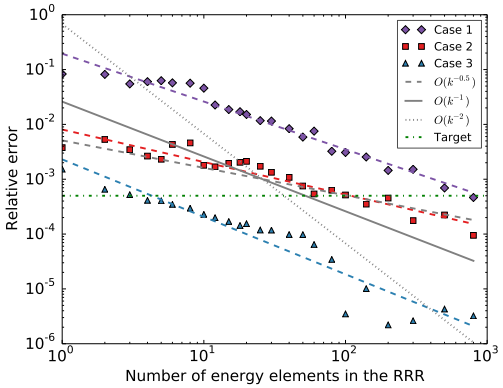

(a) Absorption rate in inner (hottest) Pu-239

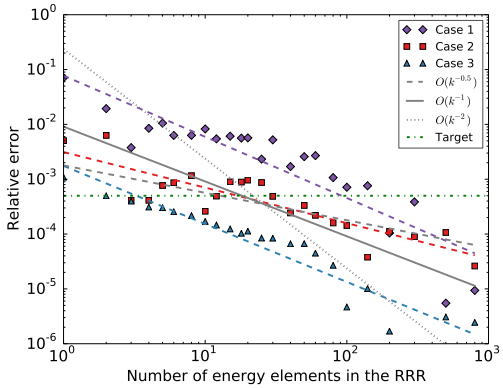

(b) Fission production rate in inner Pu-239

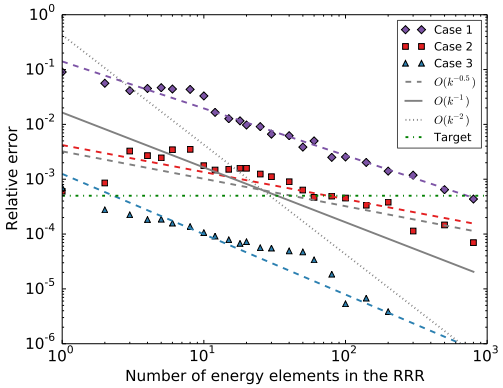

(c) Absorption rate in middle Pu-239

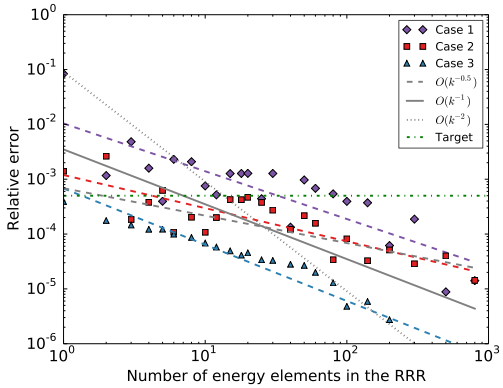

(d) Fission production rate in middle Pu-239

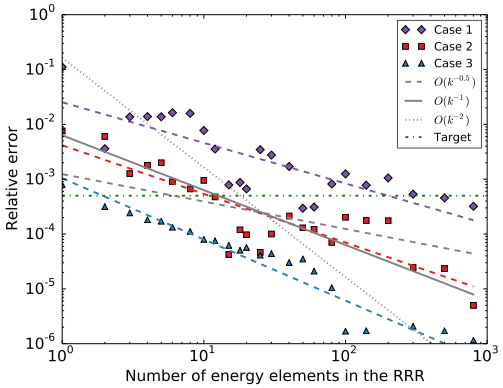

(e) Absorption rate in outer (coolest) Pu-239

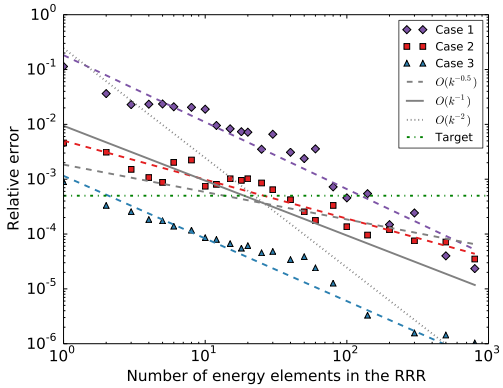

(f) Fission production rate in coolest Pu-239

Figure C.3: Errors for individual QOI as a function of energy elements for problem 3 in the low-energy RRR for all cases and the k-means clustering method.

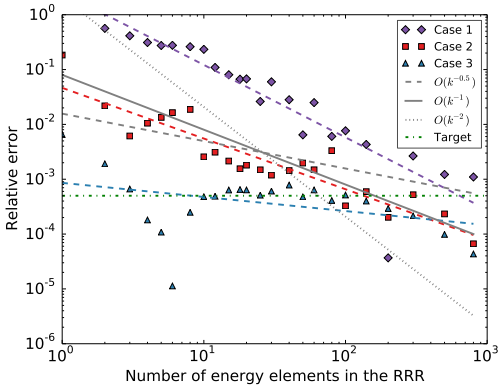

(a) Absorption rate in inner U-238

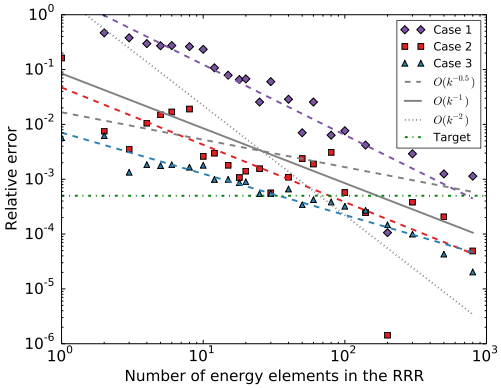

(b) Absorption rate in middle U-238

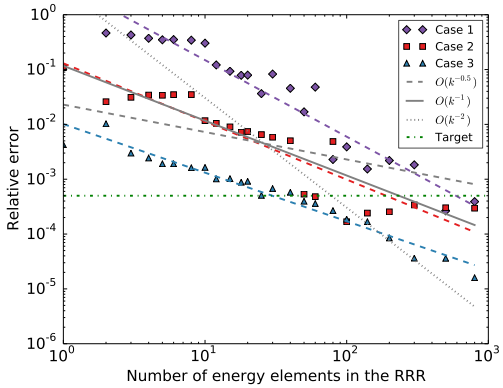

(c) Absorption rate in outer U-238

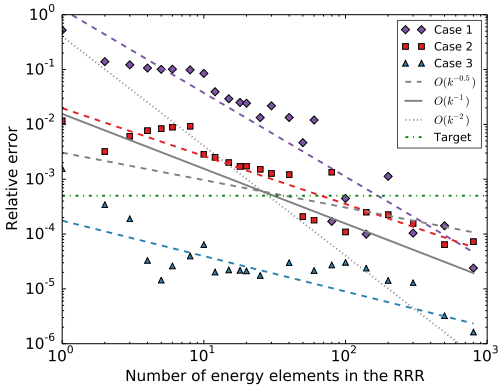

(d) Criticality eigenvalue

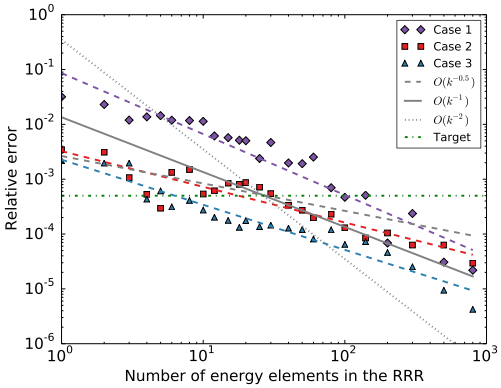

(e) Power shape

Figure C.4: Errors for individual QOI as a function of energy elements for problem 3 in the low-energy RRR for all cases and the k-means clustering method (cont.).

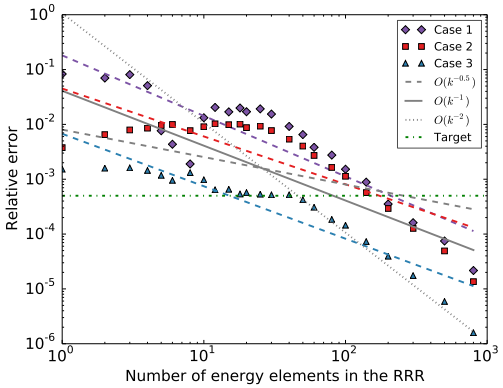

(a) Absorption rate in inner (hottest) Pu-239

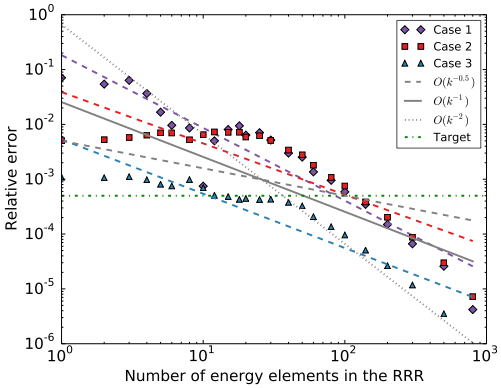

(b) Fission production rate in inner Pu-239

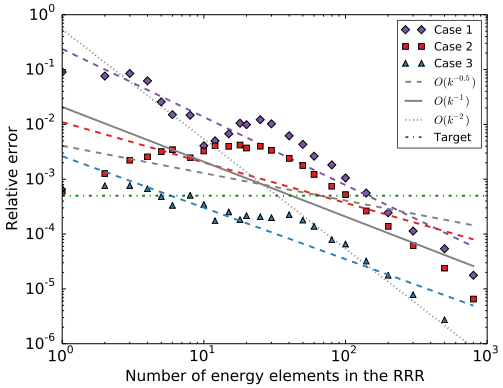

(c) Absorption rate in middle Pu-239

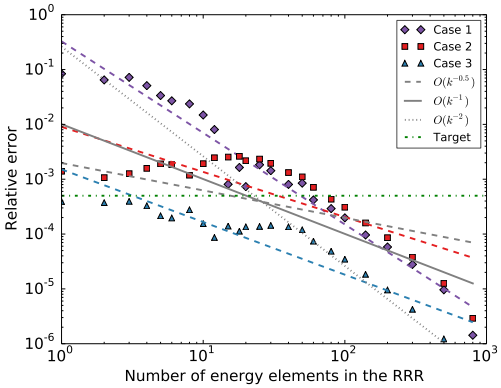

(d) Fission production rate in middle Pu-239

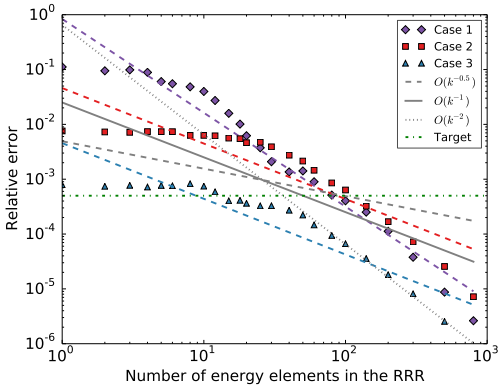

(e) Absorption rate in outer (coolest) Pu-239

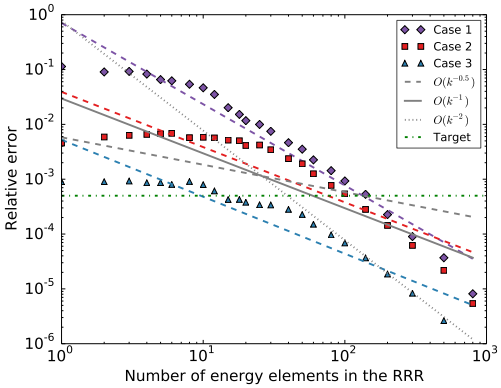

(f) Fission production rate in coolest Pu-239

Figure C.5: Errors for individual QOI as a function of energy elements for problem 3 in the low-energy RRR for all cases and the αMG clustering method.

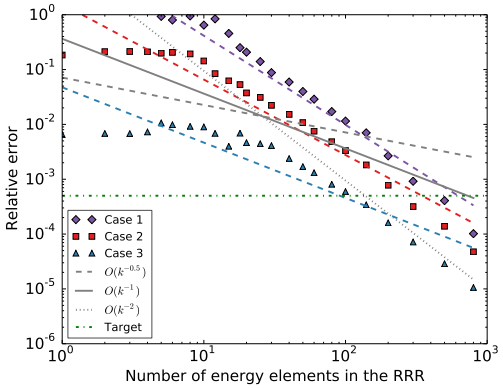

(a) Absorption rate in inner U-238

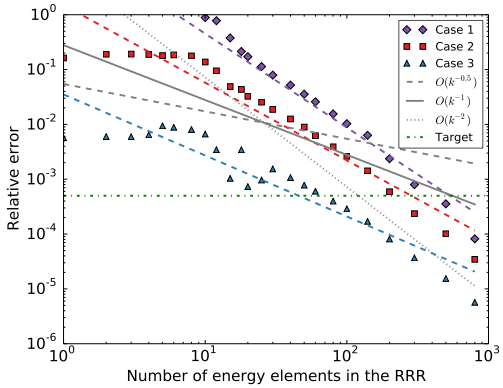

(b) Absorption rate in middle U-238

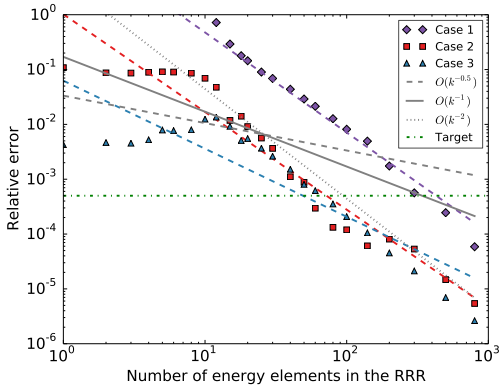

(c) Absorption rate in outer U-238

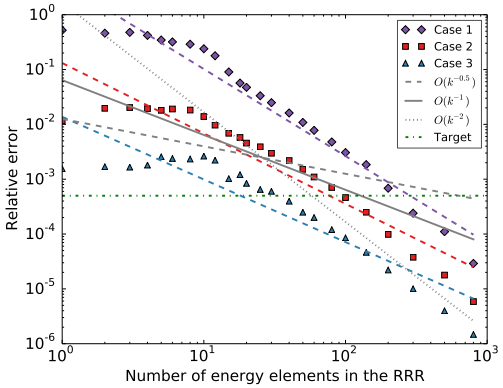

(d) Criticality eigenvalue

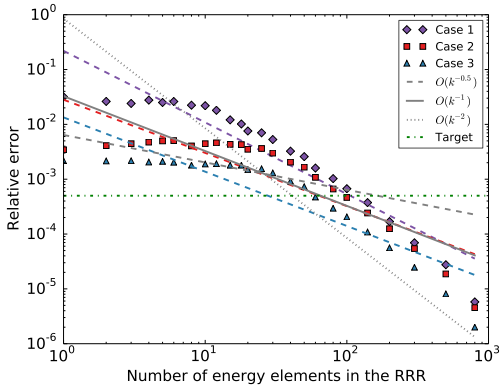

(e) Power shape

Figure C.6: Errors for individual QOI as a function of energy elements for problem 3 in the low-energy RRR for all cases and the αMG clustering method (cont.).

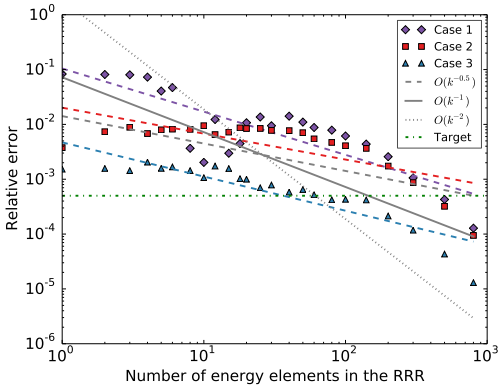

(a) Absorption rate in inner (hottest) Pu-239

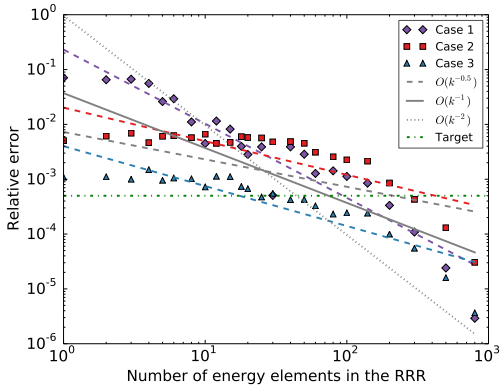

(b) Fission production rate in inner Pu-239

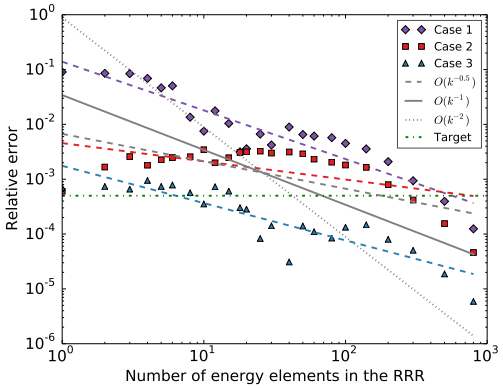

(c) Absorption rate in middle Pu-239

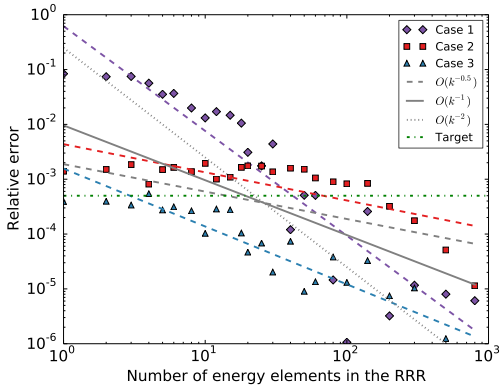

(d) Fission production rate in middle Pu-239

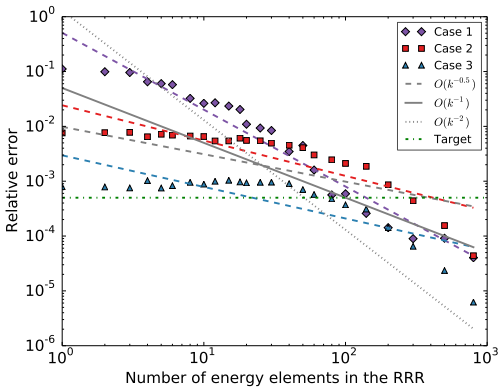

(e) Absorption rate in outer (coolest) Pu-239

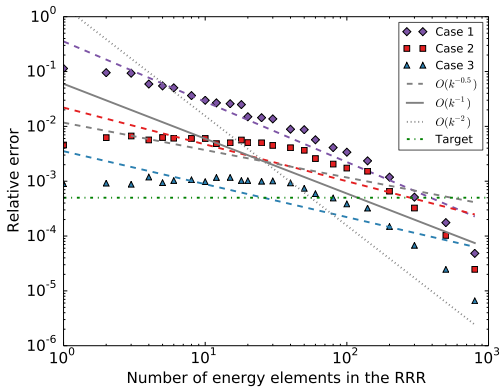

(f) Fission production rate in coolest Pu-239

Figure C.7: Errors for individual QOI as a function of energy elements for problem 3 in the low-energy RRR for all cases and the sMG group structure.

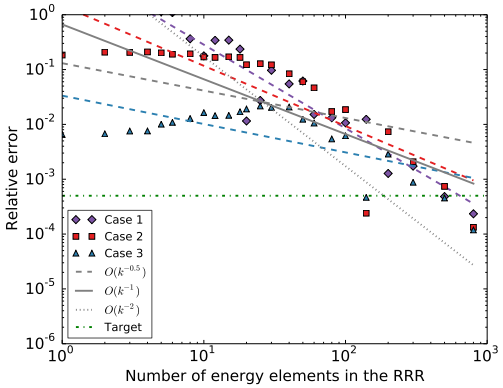

(a) Absorption rate in inner U-238

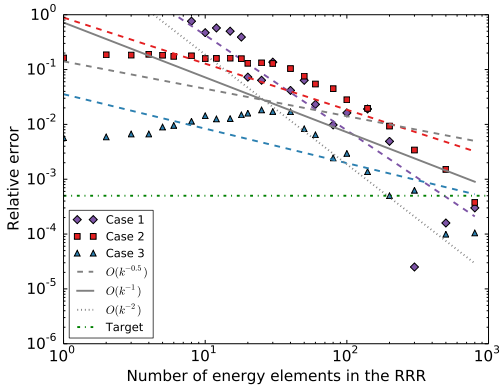

(b) Absorption rate in middle U-238

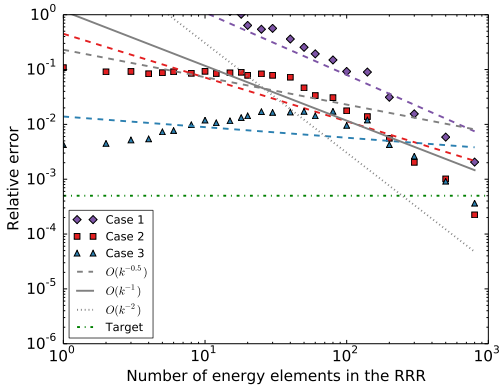

(c) Absorption rate in outer U-238

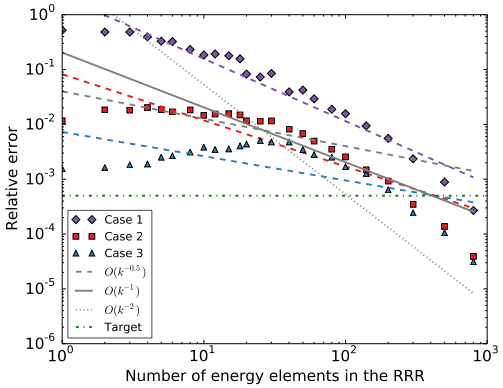

(d) Criticality eigenvalue

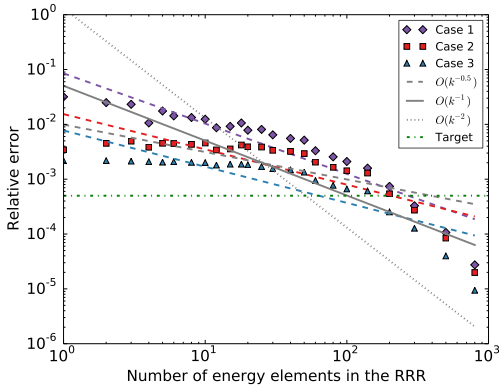

(e) Power shape

Figure C.8: Errors for individual QOI as a function of energy elements for problem 3 in the low-energy RRR for all cases and the sMG group structure (cont.).

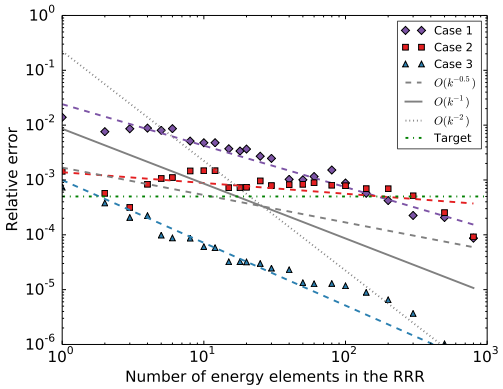

(a) Absorption rate in inner (hottest) Pu-239

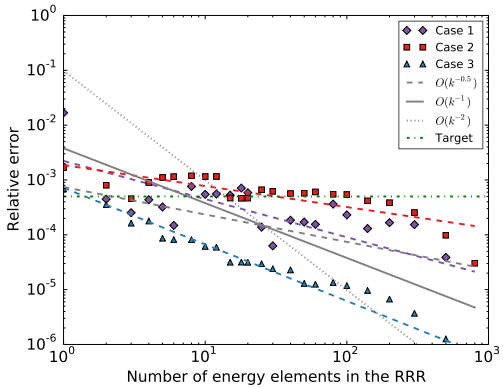

(b) Fission production rate in inner Pu-239

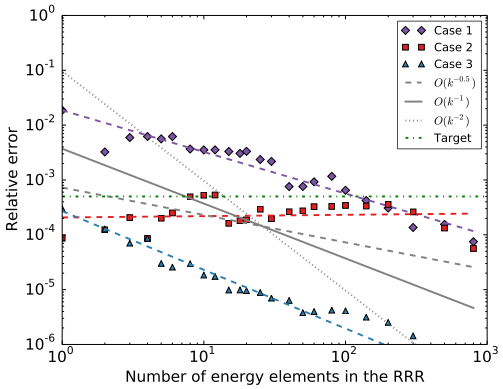

(c) Absorption rate in middle Pu-239

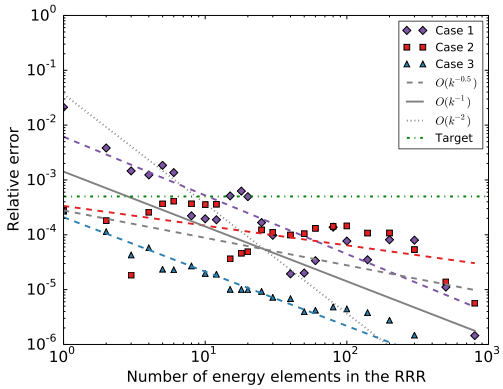

(d) Fission production rate in middle Pu-239

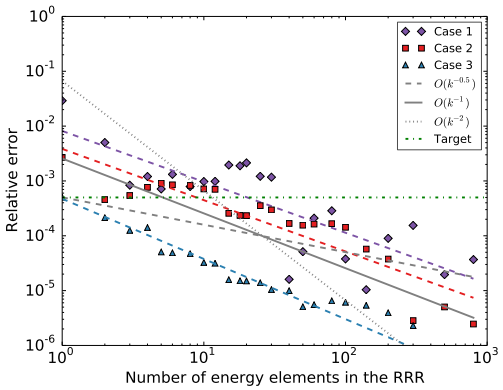

(e) Absorption rate in outer (coolest) Pu-239

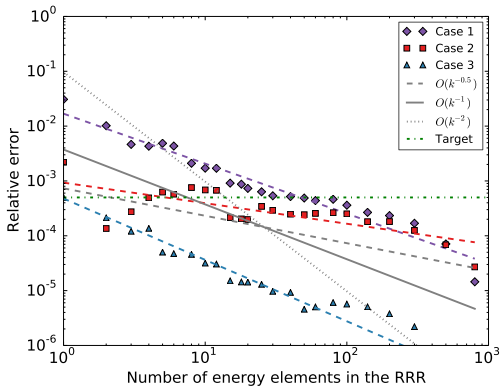

(f) Fission production rate in coolest Pu-239

Figure C.9: Errors for individual QOI as a function of energy elements for problem 3 in the medium-energy RRR for all cases and the hierarchical agglomerative clustering method.

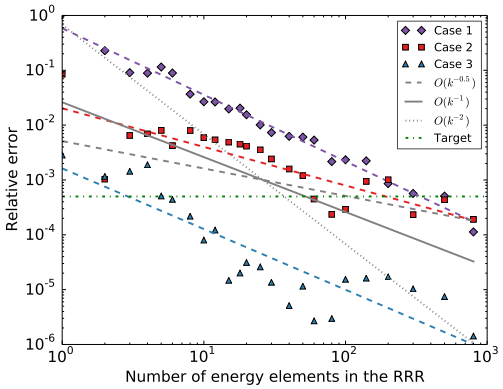

(a) Absorption rate in inner U-238

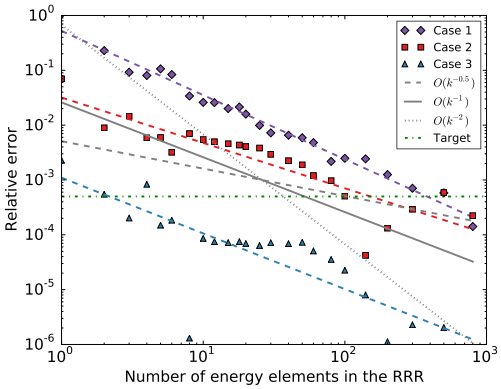

(b) Absorption rate in middle U-238

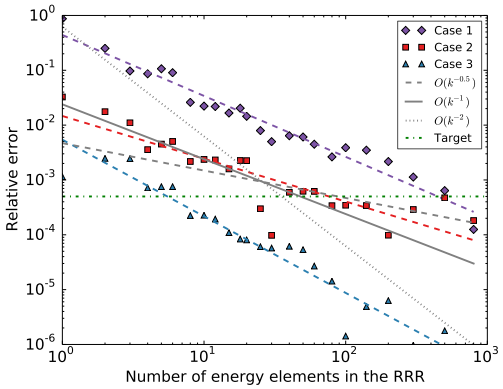

(c) Absorption rate in outer U-238

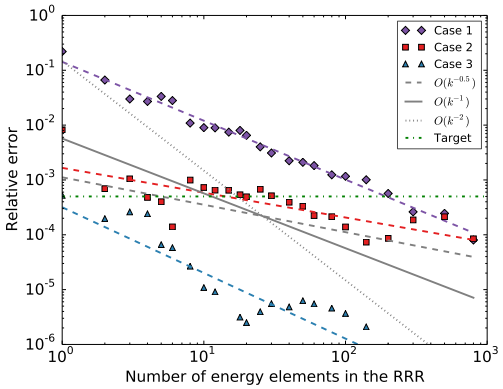

(d) Criticality eigenvalue

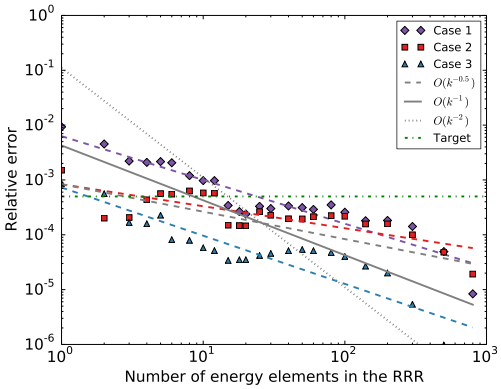

(e) Power shape

Figure C.10: Errors for individual QOI as a function of energy elements for problem 3 in the medium-energy RRR for all cases and the hierarchical agglomerative clustering method (cont.).

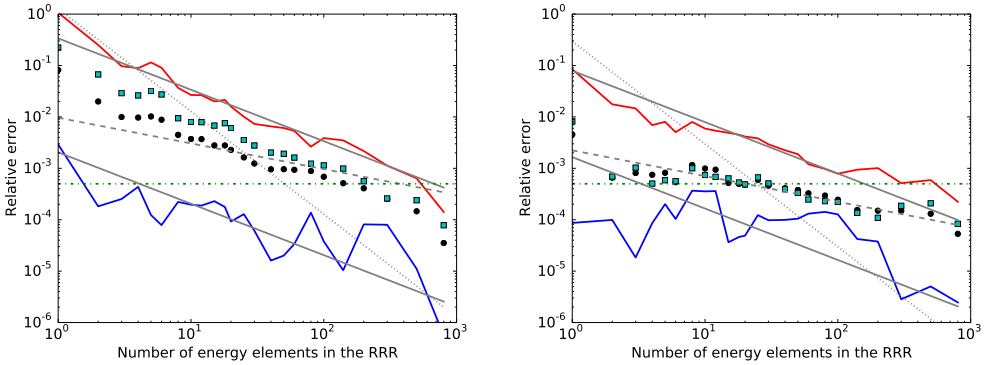

(a) Case 1

(b) Case 2

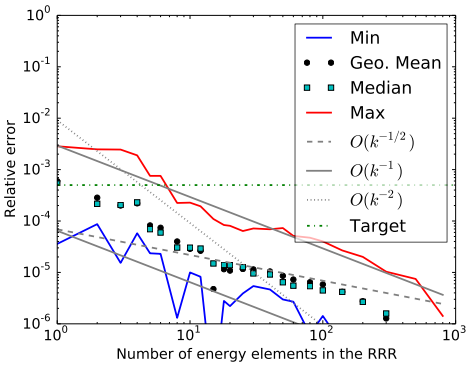

(c) Case 3

Figure C.11: Errors for all QOI as a function of energy elements for problem 3 in the medium-energy RRR for each case and the hierarchical agglomerative clustering method.

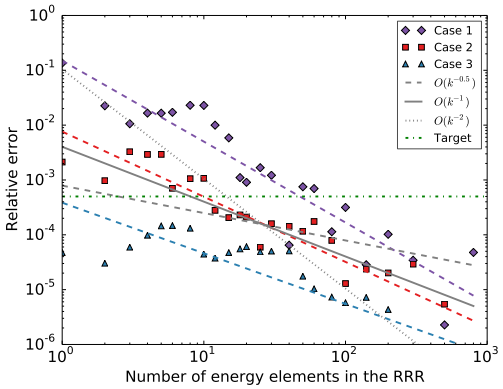

(a) Absorption rate in inner Pu-239

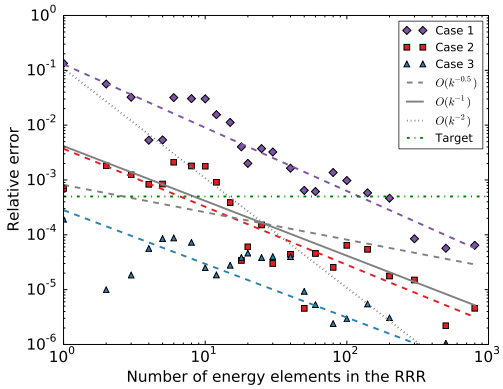

(b) Fission production rate in inner Pu-239

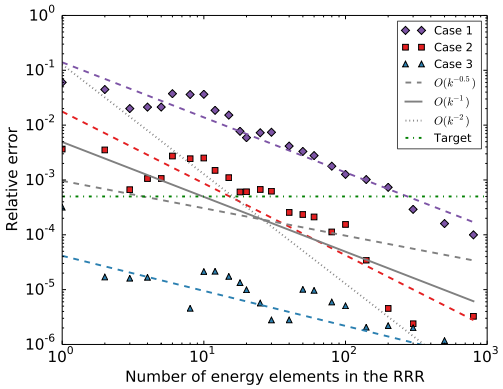

(c) Absorption rate in outer U-235

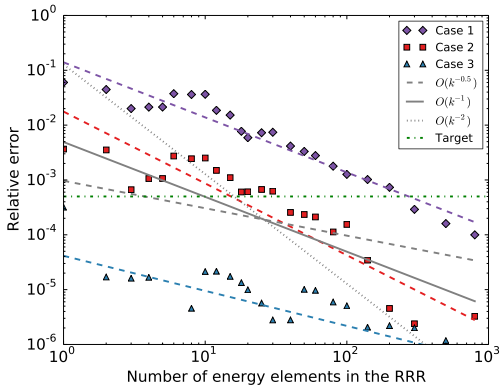

(d) Fission production rate in outer U-235

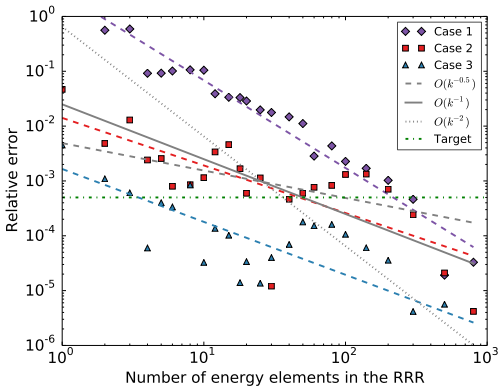

(e) Absorption rate in inner U-238

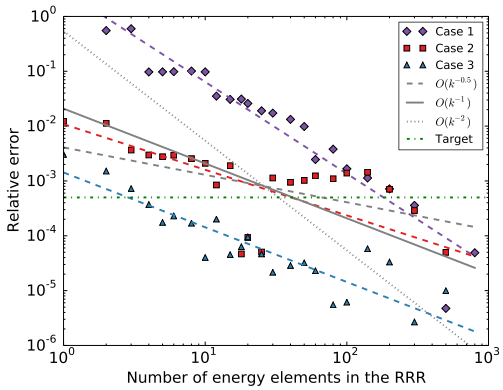

(f) Absorption rate in outer U-238

Figure C.12: Errors for individual QOI as a function of energy elements for problem 5 in the low-energy RRR for all cases and the hierarchical agglomerative clustering method.

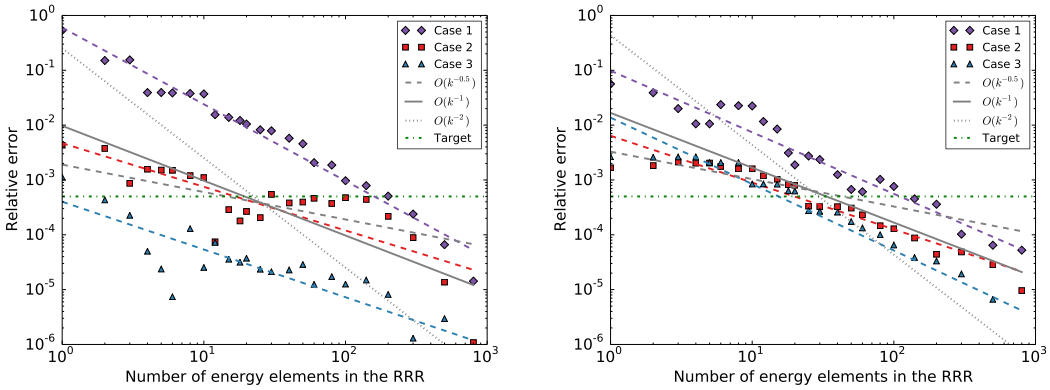

(a) Criticality eigenvalue

(b) Power shape

Figure C.13: Errors for individual QOI as a function of energy elements for problem 5 in the low-energy RRR for all cases and the hierarchical agglomerative clustering method (cont.).

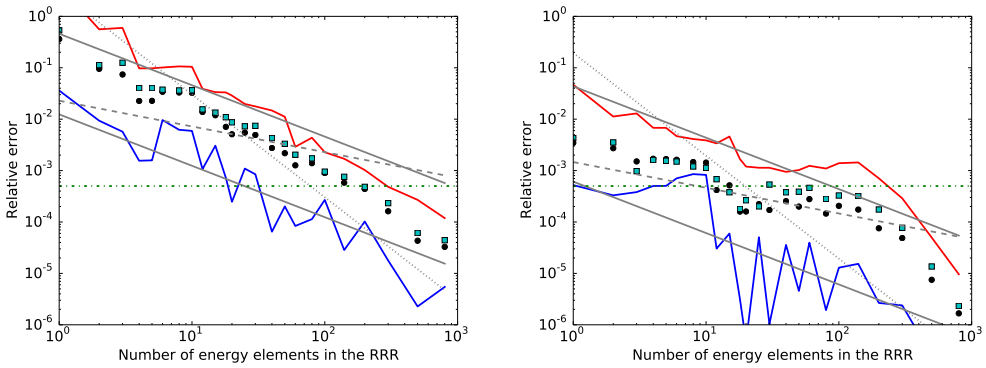

(a) Case 1

(b) Case 2

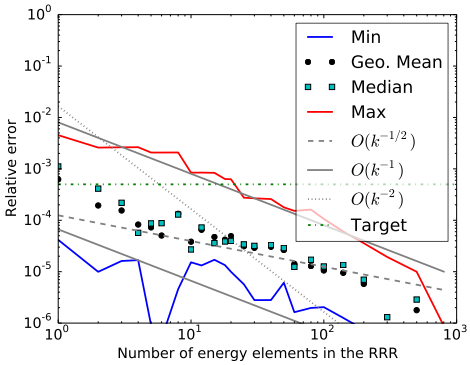

(c) Case 3

Figure C.14: Errors for all QOI as a function of energy elements for problem 5 in the low-energy RRR for each case and the hierarchical agglomerative clustering method.

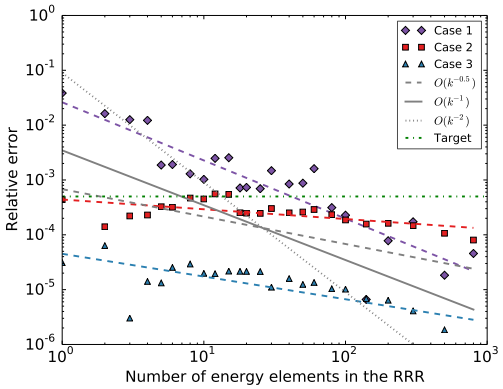

(a) Absorption rate in inner Pu-239

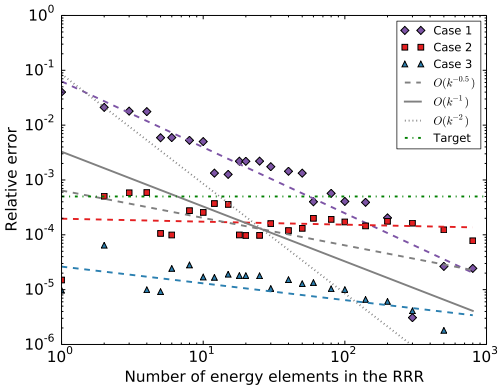

(b) Fission production rate in inner Pu-239

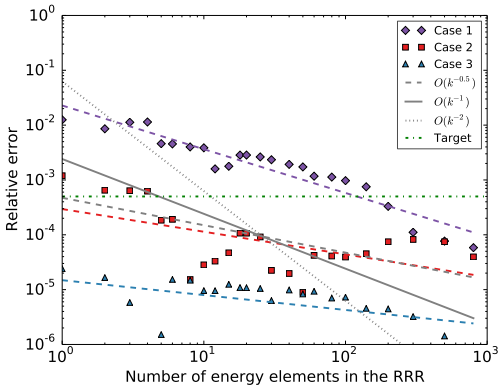

(c) Absorption rate in outer U-235

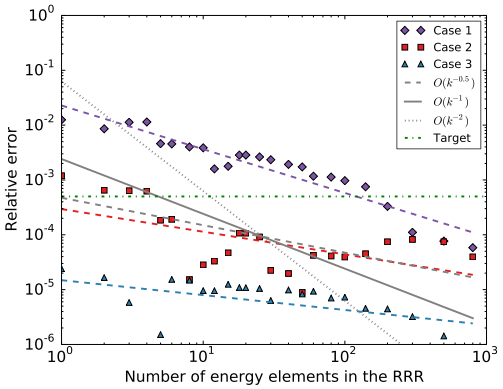

(d) Fission production rate in outer U-235

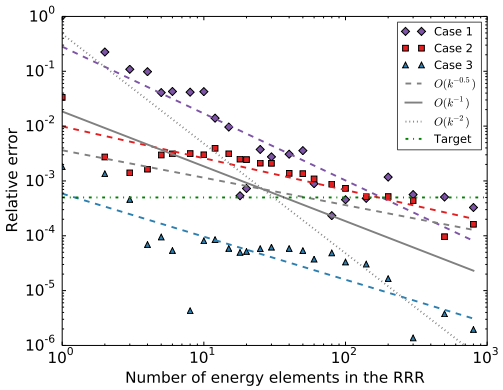

(e) Absorption rate in inner U-238

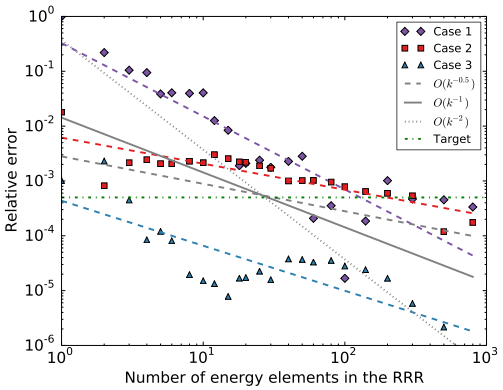

(f) Absorption rate in outer U-238

Figure C.15: Errors for individual QOI as a function of energy elements for problem 5 in the medium-energy RRR for all cases and the hierarchical agglomerative clustering method.

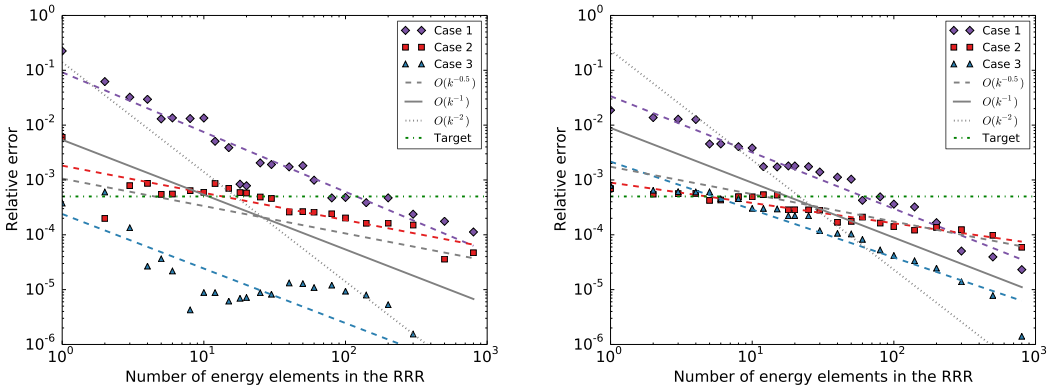

(a) Criticality eigenvalue

(b) Power shape

Figure C.16: Errors for individual QOI as a function of energy elements for problem 5 in the medium-energy RRR for all cases and the hierarchical agglomerative clustering method (cont.).

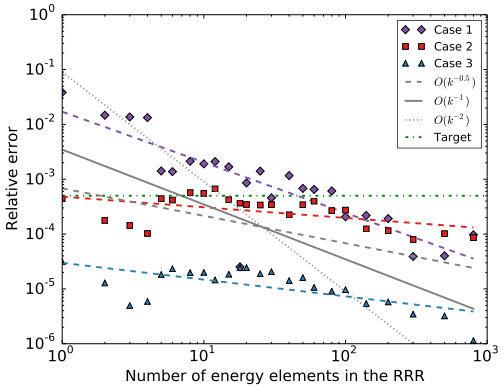

(a) Absorption rate in inner Pu-239

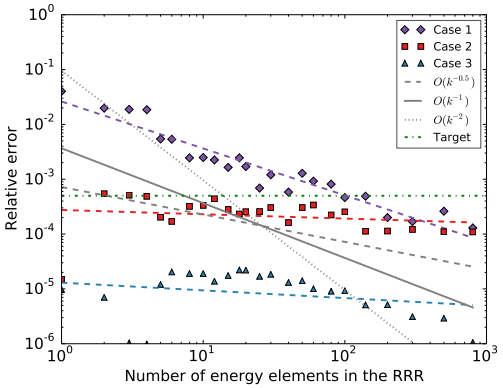

(b) Fission production rate in inner Pu-239

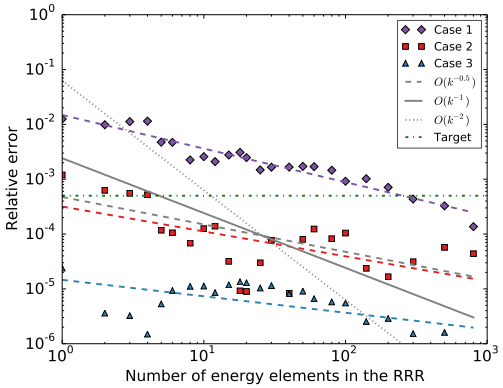

(c) Absorption rate in outer U-235

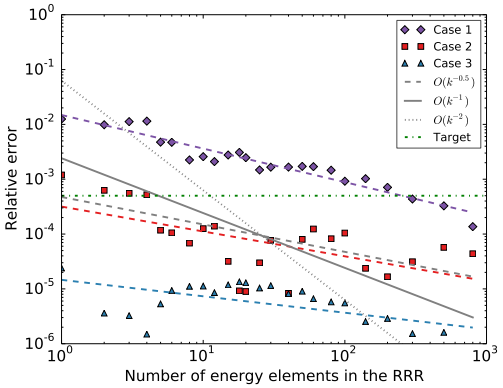

(d) Fission production rate in outer U-235

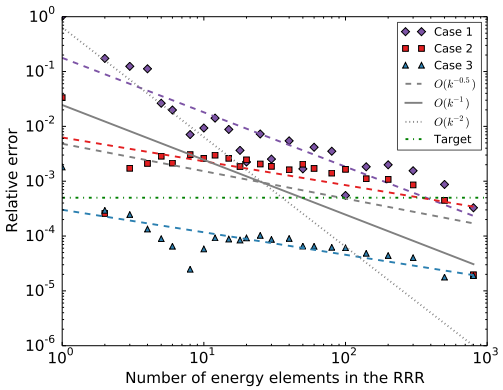

(e) Absorption rate in inner U-238

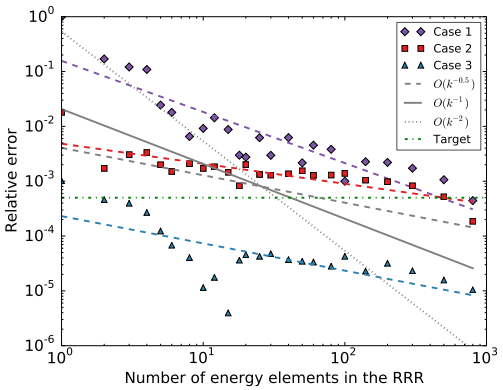

(f) Absorption rate in outer U-238

Figure C.17: Errors for individual QOI as a function of energy elements for problem 5 in the medium-energy RRR for all cases and the k-means clustering method.

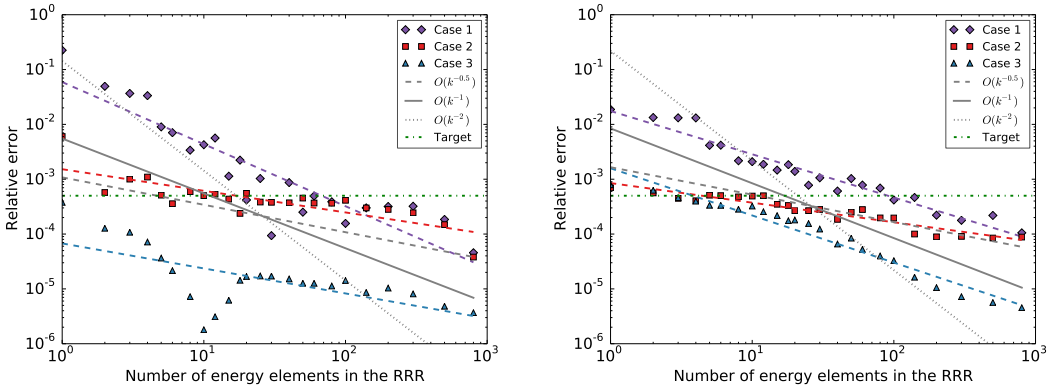

(a) Criticality eigenvalue

(b) Power shape

Figure C.18: Errors for individual QOI as a function of energy elements for problem 5 in the medium-energy RRR for all cases and the k-means clustering method (cont.).

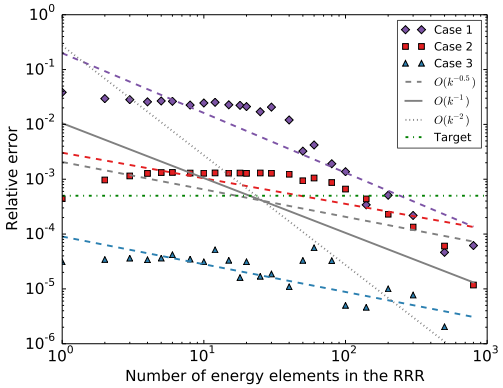

(a) Absorption rate in inner Pu-239

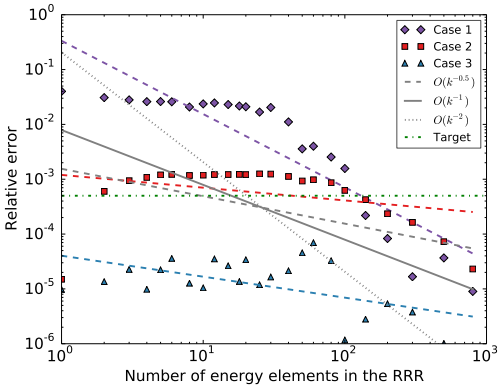

(b) Fission production rate in inner Pu-239

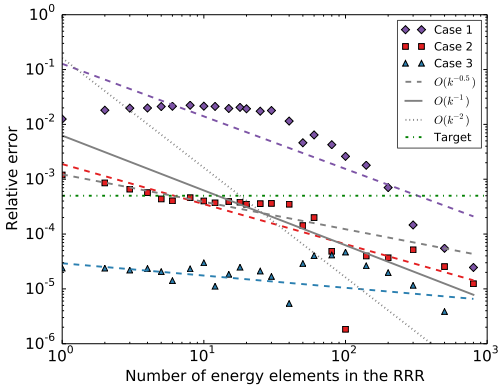

(c) Absorption rate in outer U-235

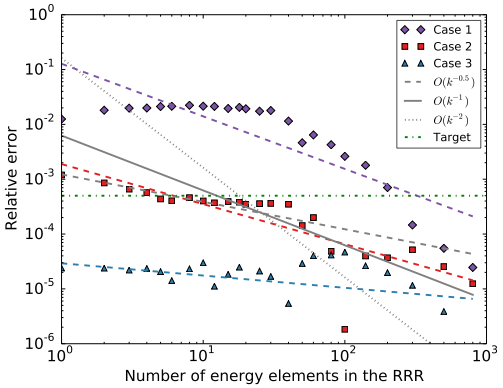

(d) Fission production rate in outer U-235

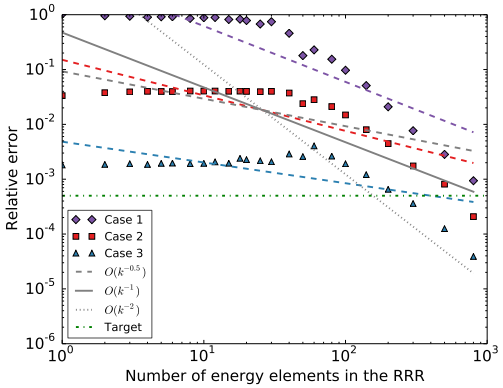

(e) Absorption rate in inner U-238

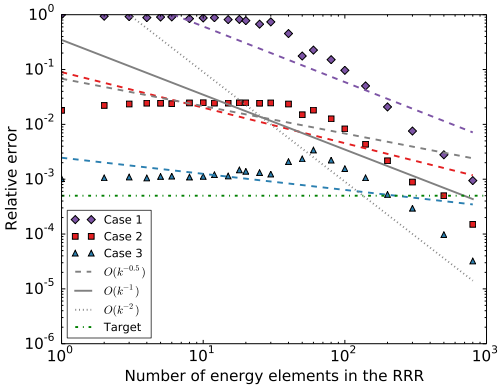

(f) Absorption rate in outer U-238

Figure C.19: Errors for individual QOI as a function of energy elements for problem 5 in the medium-energy RRR for all cases and the αMG clustering method.

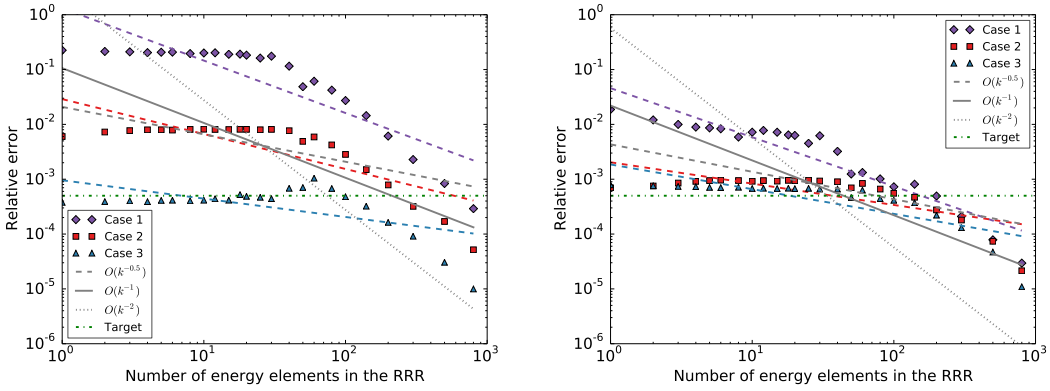

(a) Criticality eigenvalue

(b) Power shape

Figure C.20: Errors for individual QOI as a function of energy elements for problem 5 in the medium-energy RRR for all cases and the αMG clustering method (cont.).

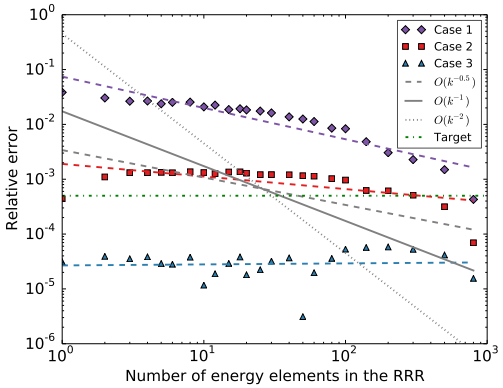

(a) Absorption rate in inner Pu-239

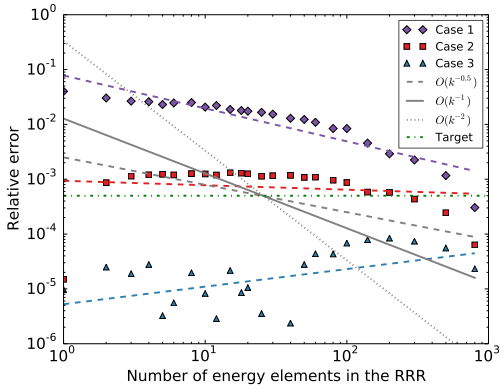

(b) Fission production rate in inner Pu-239

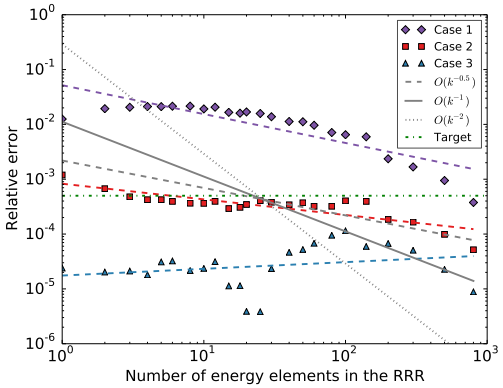

(c) Absorption rate in outer U-235

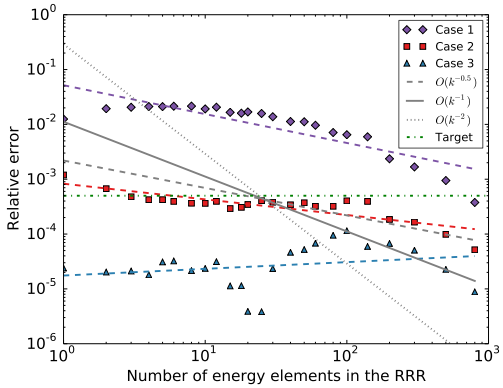

(d) Fission production rate in outer U-235

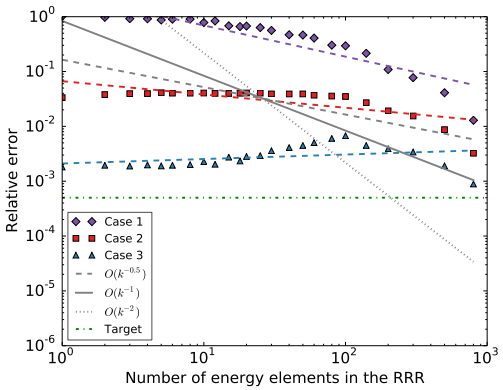

(e) Absorption rate in inner U-238

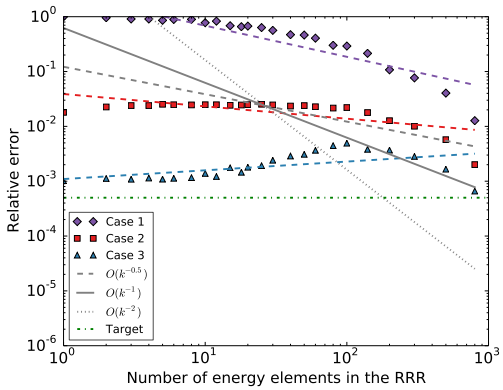

(f) Absorption rate in outer U-238

Figure C.21: Errors for individual QOI as a function of energy elements for problem 5 in the medium-energy RRR for all cases and the sMG group structure.

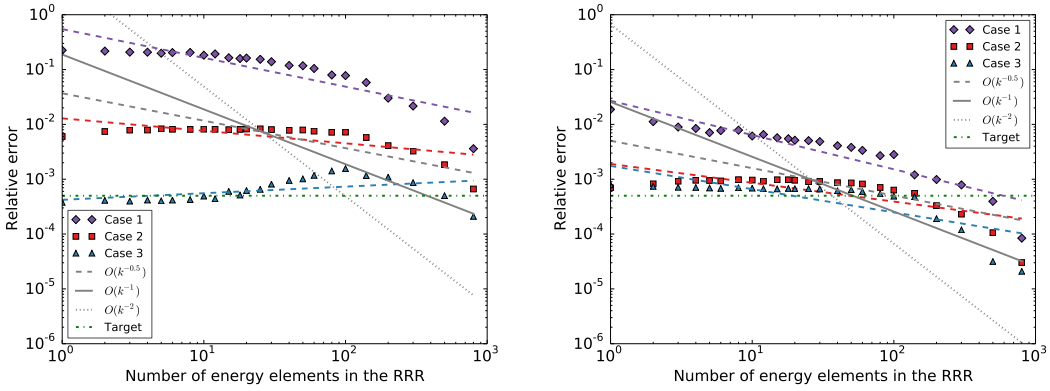

(a) Criticality eigenvalue

(b) Power shape

Figure C.22: Errors for individual QOI as a function of energy elements for problem 5 in the medium-energy RRR for all cases and the sMG group structure (cont.).

APPENDIX D

ADDENDUM TO SECTION 4

D.1 Wynn-Epsilon Acceleration

The formula for the Wynn-epsilon extrapolation we used is:

$$q_r^{s+1} = q_{r-1}^{s-1} + \frac{1}{q_r^s - q_{r-1}^s} \tag{D.1}$$

where q_r^s is the QOI extrapolation at resolution r and Wynn-epsilon stage s. Equation (D.1) is the lower-diagonal formulation of the Wynn-epsilon acceleration technique. The q_r^0 are 0. The q_r^1 are the unextrapolated / original QOI values. The values for odd stage counts converge while the values for even stage counts diverge. The value at the highest resolution and odd stage is taken for the extrapolation.

For our FEDS reference solution, we used a maximum stage of $s = 5$ and resolutions of $\{27, 43, 59, 91, 219\}$ energy elements in the RRR from the FEDS solutions. Using fewer than 5 stages was found to provide insufficient acceleration. Using more than 5 stages required using QOI at low energy unknown counts. Other Wynn-epsilon extrapolation flavors were tried, and found to be inferior. Wynn-epsilon extrapolation was applied to each QOI separately to determine the FEDS reference.

D.2 Additional Results

Figures D.1 and D.2 show error plotted against the inverse energy DOF. If the error is first-order in energy resolution, then the error in these plots should be a straight line that goes through the origin. A lower slope means lower error constant for Figs. D.1 and D.2.

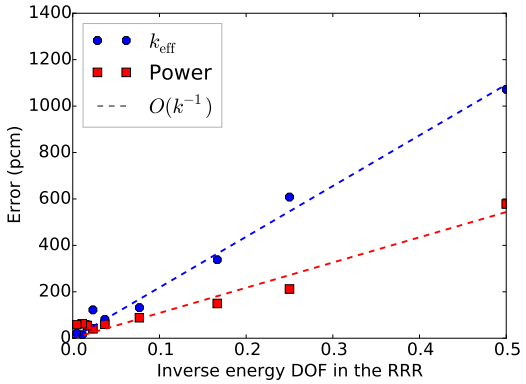

(a) FEDS with MG reference

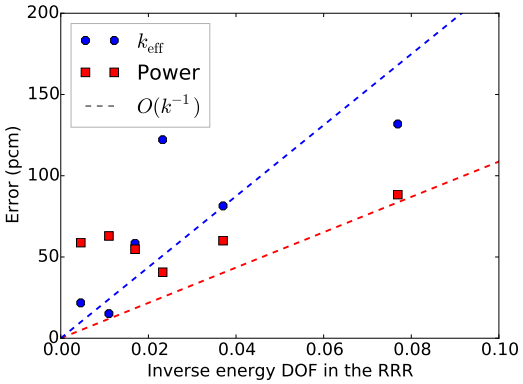

(b) FEDS with MG reference (zoom)

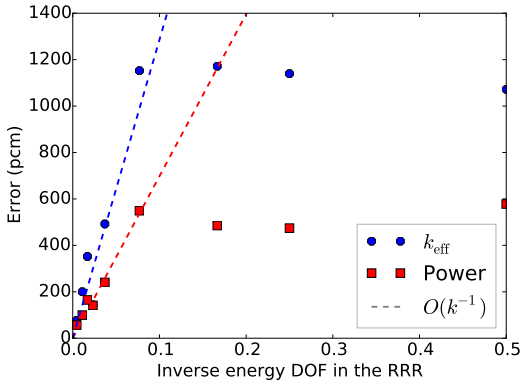

(c) αMG with MG reference

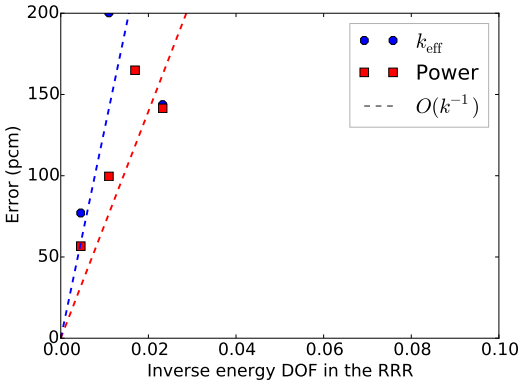

(d) αMG with MG reference (zoom)

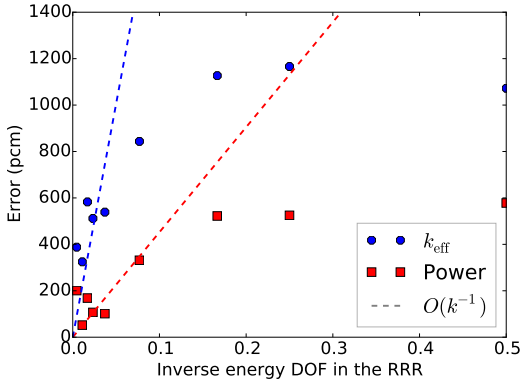

(e) sMG with MG reference

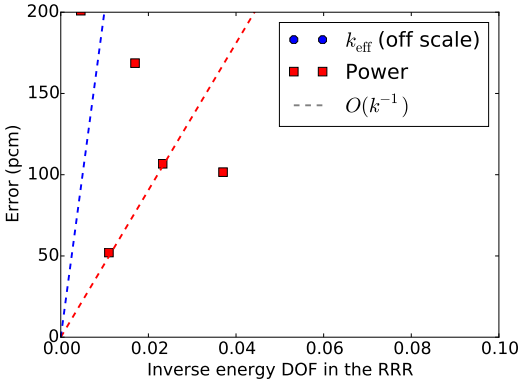

(f) sMG with MG reference (zoom)

Figure D.1: Errors for selected QOI as a function of inverse energy element number for the C5 problem and the MG reference

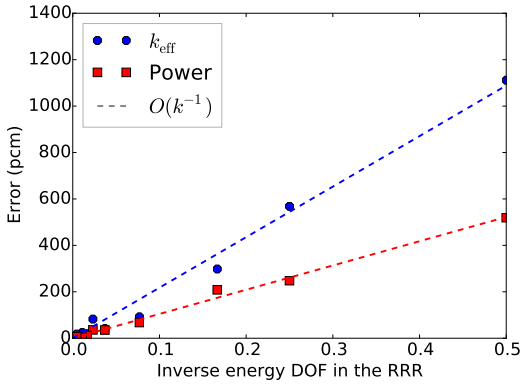

(a) FEDS with FEDS reference

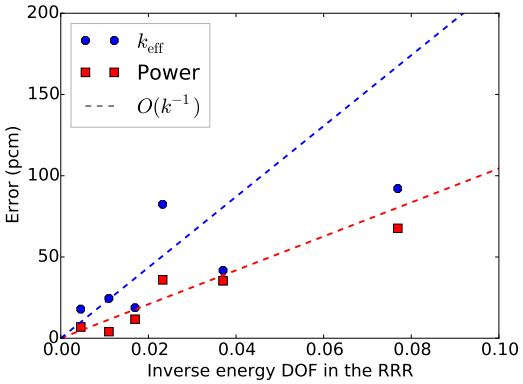

(b) FEDS with FEDS reference (zoom)

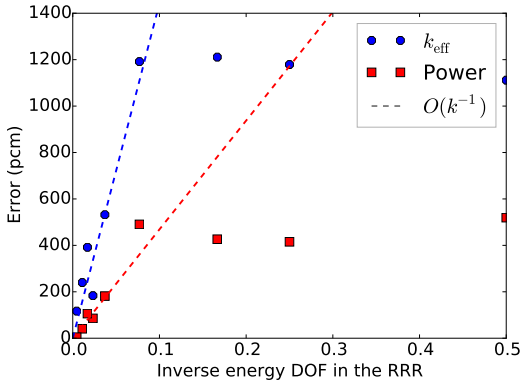

(c) αMG with FEDS reference

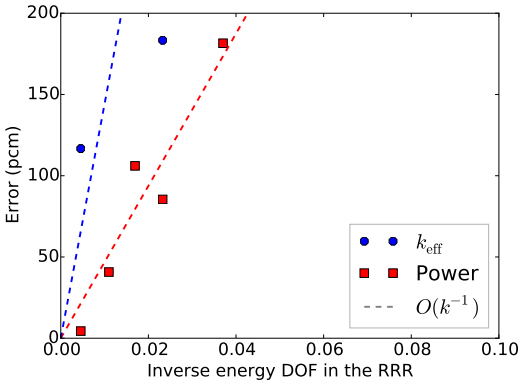

(d) αMG with FEDS reference (zoom)

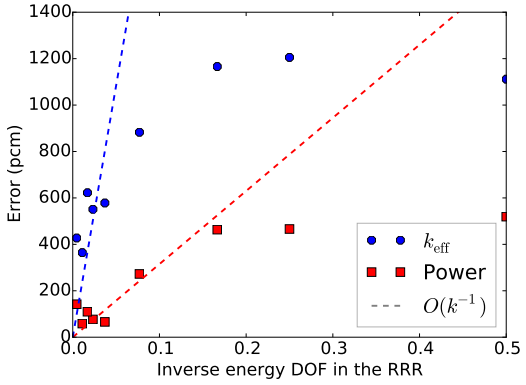

(e) sMG with FEDS reference

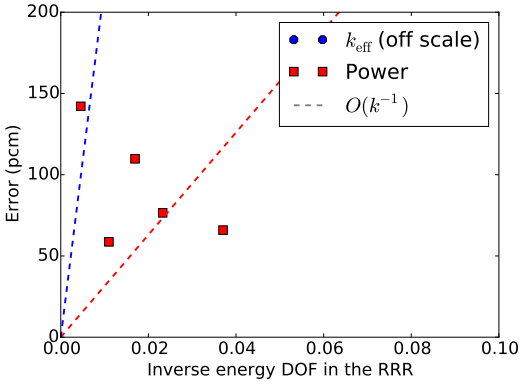

(f) sMG with FEDS reference (zoom)

Figure D.2: Errors for selected QOI as a function of inverse energy element number for the C5 problem with the FEDS reference

APPENDIX E

ADDENDUM TO SECTION 5

E.1 Apportioning Distributions

The ratio of total energy elements to number of coarse groups alone is insufficient to describe the distribution of energy elements to coarse groups because elements are not distributed uniformly. Figure E.1 shows the number of energy elements per coarse group as a function of energy. Figure E.2 shows histograms of these distributions for the TOF problem. The abscissa is the number of elements per coarse group. The ordinate is the number of times the abscissa occurs, that is, the number of coarse groups that have that number of elements. The legends show four numbers: the percentage of coarse groups that have one element, and the 50th, 75th, and 90th percentiles of number of elements per coarse group. The percentiles are computed over the subset of coarse groups with more than one element. Apportioning for αMG was proportional to relative L^1 norm per coarse group, while apportioning for FEDS was based on relative standard deviation per coarse group.

E.2 TOF Results

Tables E.1 – E.6 give QOI error for standard MG (sMG) and adaptive MG (αMG) compared to a reference solution with 10,000 fine groups and 2,000 coarse groups.

Tables E.7 – E.12 give QOI error for standard MG (a.k.a., sMG) and FEDS compared to a reference solution with 10,000 fine groups and 2,000 coarse groups.

E.3 Testing the Reference Solution

It is difficult to find a high-fidelity reference solution. NJOY 99 is limited to using fewer than 15,000 groups. Using this number of equally-spaced groups would not be

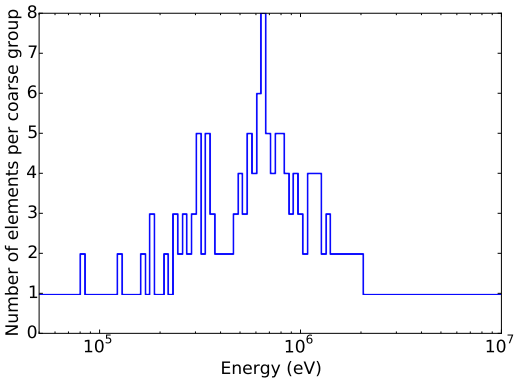

(a) 200 groups, $r = 2$, αMG

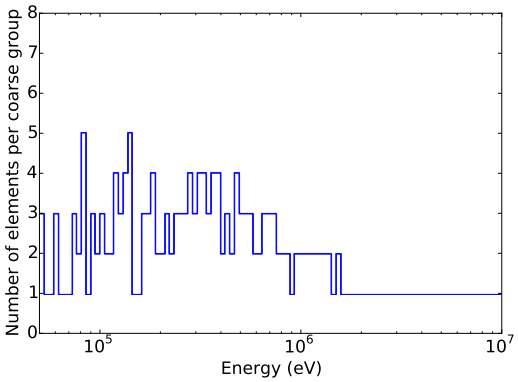

(b) 200 groups, $r = 2$, FEDS

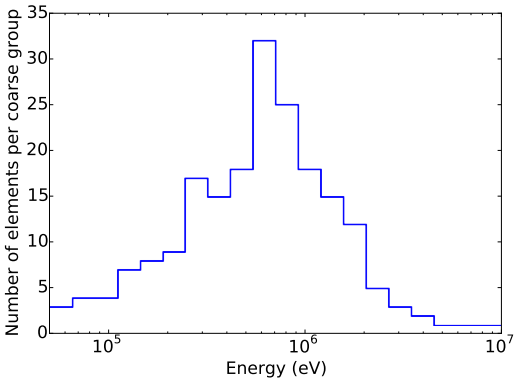

(c) 200 groups, $r = 10$, αMG

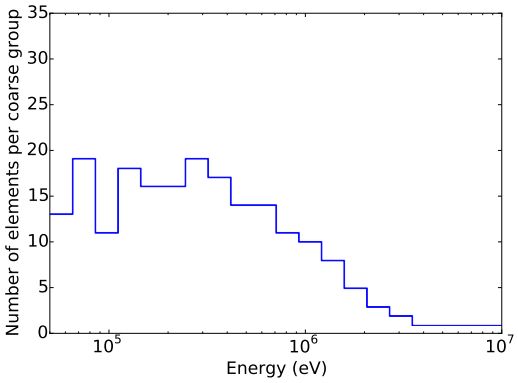

(d) 200 groups, $r = 10$, FEDS

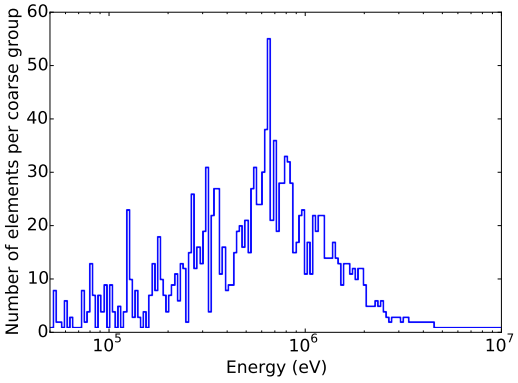

(e) 1600 groups, $r = 10$, αMG

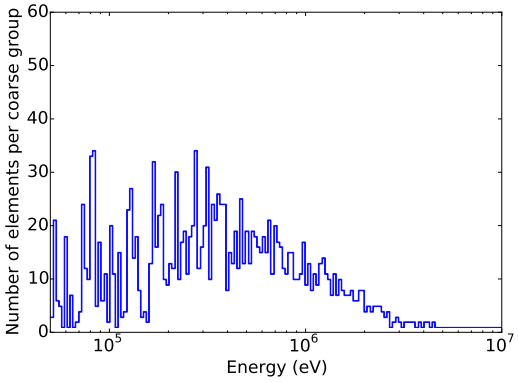

(f) 1600 groups, $r = 10$, FEDS

Figure E.1: Number of energy elements per coarse group as a function of energy for various numbers of coarse groups and ratios.

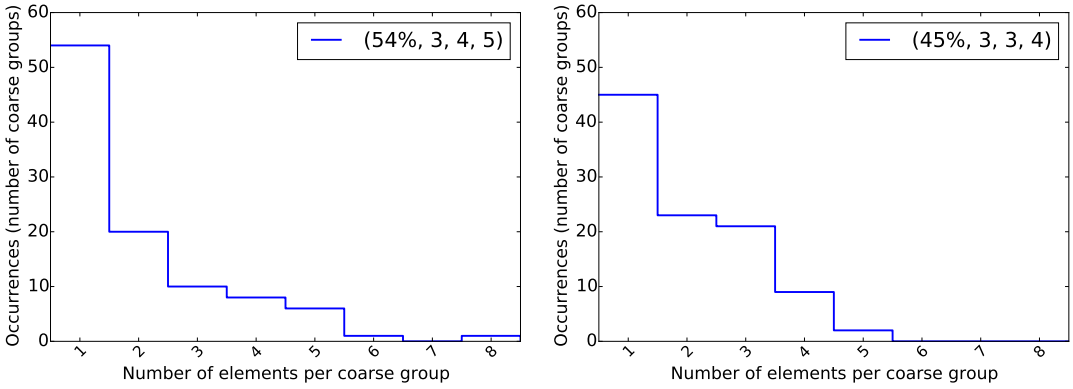

(a) 200 groups, $r = 2$, αMG

(b) 200 groups, $r = 2$, FEDS

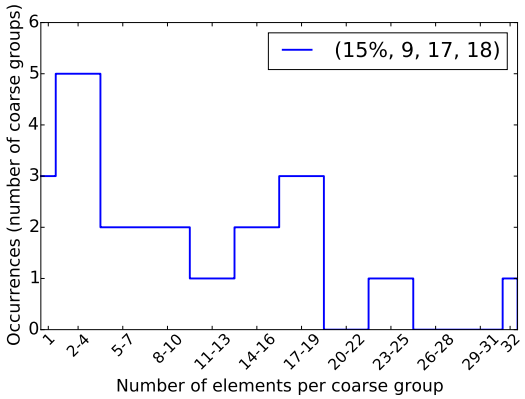

(c) 200 groups, $r = 10$, αMG

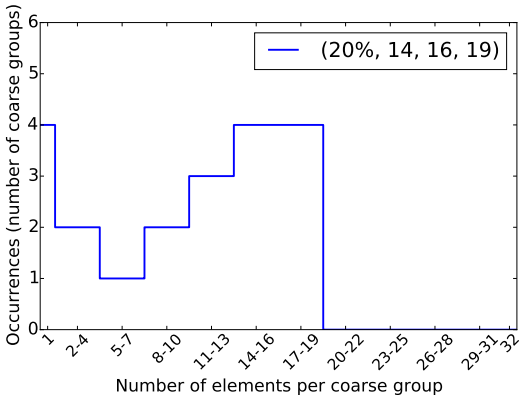

(d) 200 groups, $r = 10$, FEDS

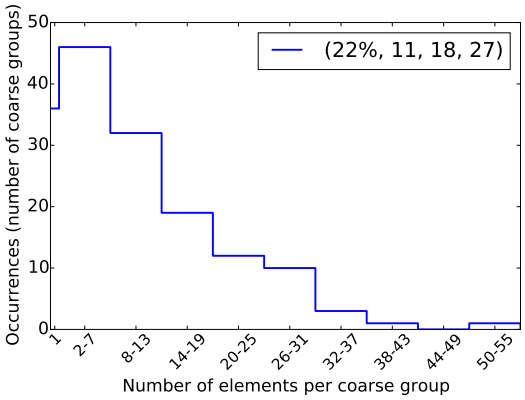

(e) 1600 groups, $r = 10$, αMG

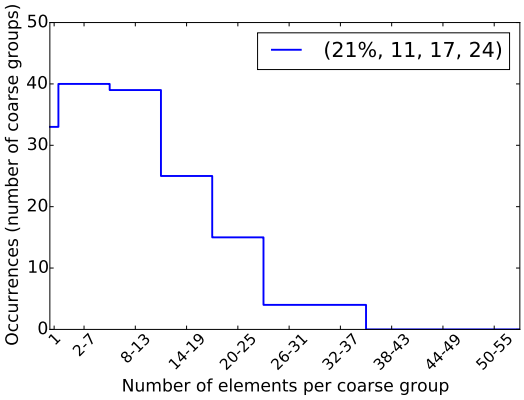

(f) 1600 groups, $r = 10$, FEDS

Figure E.2: Histogram of the distribution of energy unknowns to coarse groups for various numbers of coarse groups and ratios.

enough to resolve the fine resonances, which is necessary to get accurate absorption and transmission QOIs. Any fidelity spent on the fine resonances is fidelity that cannot be used to resolve the speeds, which is necessary to get accurate time-binned detector-response QOIs.

Table E.13 gives the errors for several numbers of coarse and fine groups for a possible reference solution. Each entry was compared against an energy mesh with 10,000 coarse groups and 14,500 fine groups (ratio of 1.45). Since the most difficult case was a large distance with fine time bins, Table E.13 uses a distance of 10 m and 10,000 time bins.

All cases of the detector response error (error 3) are smaller by an order of magnitude than are found in the MG and FEDS cases tested. The magnitudes of error 1 are the same as the most-resolved FEDS case tested. For these reasons, it was decided to use a reference solution of 2,000 coarse groups and 10,000 fine groups for the reference solution for all other cases.

E.4 Testing the Escape Cross Section

A Bondarenko iteration with escape cross section is used to approximate the flux seen by the iron from the source. This subsection looks at the impact of the escape cross section on the errors.

Say the thickness of the iron is M. The absorbed fraction in and the transmission fraction through the iron for a neutron of energy E normalized to a source shape of

$q(E)$ is:

$$\frac{a(E)}{q(E)} = \int_0^M \mathrm{d}x\ \Sigma_t(E) e^{-\Sigma_t(E)x} = 1 - e^{-\Sigma_t(E)M} \simeq \frac{\Sigma_t(E)M}{1+\Sigma_t(E)M} = \frac{\Sigma_t(E)}{\Sigma_e + \Sigma_t(E)}, \tag{E.1a}$$

$$\frac{t(E)}{q(E)} = e^{-\Sigma_t(E)M} \simeq \frac{1}{1+\Sigma_t(E)M} = \frac{\Sigma_e}{\Sigma_e + \Sigma_t(E)}, \tag{E.1b}$$

$$\Sigma_e \equiv \frac{1}{M}, \tag{E.1c}$$

where the approximate equality for the absorption is accurate to 30 %, and maximum relative deviation occurs around 1.8 mean free paths. Since the absorption rate, $a(E)$, is the flux multiplied by the total cross section, and the transmission rate, $t(E)$, is proportional to the flux, both indicate that a reasonable energy shape for the flux / basis function is

$$\phi(E) \simeq q(E) \frac{1}{\Sigma_e + \Sigma_t(E)}, \tag{E.1d}$$

which is what is assumed with the Bondarenko iteration.

To determine the effect of the background cross section on the errors, we compared two sets of cross sections. The first, (100 and 400) used escape cross sections of $1/M$. The second (101 and 401) used escape cross sections of infinity. The escape cross section seems to provide approximately a factor of 2 in fidelity for the cross section for both the FEDS and standard MG, with sMG being more sensitive than FEDS.

Table E.1: TOF QOI errors for vacuum distance 10 cm and 50 time bins

Method	Ratio	Coarse Groups	Total DOF	Error 1 (abs.)	Error 2 (cumul. det.)	Error 3 (det.)
sMG	1	100	100	4.90×10^{-3}	4.77×10^{-3}	5.59×10^{-3}
αMG	1.25	80		4.79×10^{-3}	4.65×10^{-3}	5.61×10^{-3}
	1.6	62		4.22×10^{-3}	4.12×10^{-3}	7.59×10^{-3}
	2	50		4.62×10^{-3}	4.48×10^{-3}	6.34×10^{-3}
	4	25		4.42×10^{-3}	4.28×10^{-3}	6.31×10^{-3}
	10	10		4.28×10^{-3}	4.31×10^{-3}	4.59×10^{-2}
sMG	1	200	200	4.07×10^{-3}	4.02×10^{-3}	4.50×10^{-3}
αMG	1.25	160		3.99×10^{-3}	3.94×10^{-3}	4.44×10^{-3}
	1.6	125		3.54×10^{-3}	3.52×10^{-3}	4.02×10^{-3}
	2	100		3.62×10^{-3}	3.56×10^{-3}	4.30×10^{-3}
	4	50		3.29×10^{-3}	3.25×10^{-3}	5.09×10^{-3}
	10	20		3.26×10^{-3}	3.20×10^{-3}	4.85×10^{-3}
sMG	1	400	400	3.06×10^{-3}	3.07×10^{-3}	3.48×10^{-3}
αMG	1.25	320		3.01×10^{-3}	3.02×10^{-3}	3.50×10^{-3}
	1.6	250		2.67×10^{-3}	2.69×10^{-3}	3.14×10^{-3}
	2	200		2.56×10^{-3}	2.58×10^{-3}	3.08×10^{-3}
	4	100		2.48×10^{-3}	2.50×10^{-3}	3.25×10^{-3}
	10	40		2.30×10^{-3}	2.33×10^{-3}	3.01×10^{-3}
sMG	1	800	800	2.32×10^{-3}	2.33×10^{-3}	2.71×10^{-3}
αMG	1.25	640		2.10×10^{-3}	2.13×10^{-3}	2.58×10^{-3}
	1.6	500		1.83×10^{-3}	1.87×10^{-3}	2.31×10^{-3}
	2	400		1.78×10^{-3}	1.81×10^{-3}	2.24×10^{-3}
	4	200		1.56×10^{-3}	1.60×10^{-3}	1.99×10^{-3}
	10	80		1.48×10^{-3}	1.52×10^{-3}	1.94×10^{-3}
sMG	1	1600	1600	1.50×10^{-3}	1.51×10^{-3}	1.78×10^{-3}
αMG	1.25	1280		1.22×10^{-3}	1.25×10^{-3}	1.59×10^{-3}
	1.6	1000		1.11×10^{-3}	1.13×10^{-3}	1.49×10^{-3}
	2	800		1.00×10^{-3}	1.03×10^{-3}	1.35×10^{-3}
	4	400		8.96×10^{-4}	9.22×10^{-4}	1.19×10^{-3}
	10	160		8.45×10^{-4}	8.69×10^{-4}	1.13×10^{-3}

Table E.2: TOF QOI errors for vacuum distance 10 cm and 10,000 time bins

Method	Ratio	Coarse Groups	Total DOF	Error 1 (abs.)	Error 2 (cumul. det.)	Error 3 (det.)
sMG	1	100	100	4.90×10^{-3}	4.75×10^{-3}	3.68×10^{-2}
αMG	1.25	80		4.79×10^{-3}	4.63×10^{-3}	4.01×10^{-2}
	1.6	62		4.22×10^{-3}	4.11×10^{-3}	4.35×10^{-2}
	2	50		4.62×10^{-3}	4.48×10^{-3}	5.21×10^{-2}
	4	25		4.42×10^{-3}	4.27×10^{-3}	6.31×10^{-2}
	10	10		4.28×10^{-3}	4.27×10^{-3}	1.09×10^{-1}
sMG	1	200	200	4.07×10^{-3}	4.02×10^{-3}	1.55×10^{-2}
αMG	1.25	160		3.99×10^{-3}	3.94×10^{-3}	1.82×10^{-2}
	1.6	125		3.54×10^{-3}	3.52×10^{-3}	1.97×10^{-2}
	2	100		3.62×10^{-3}	3.56×10^{-3}	2.20×10^{-2}
	4	50		3.29×10^{-3}	3.24×10^{-3}	3.58×10^{-2}
	10	20		3.26×10^{-3}	3.19×10^{-3}	4.66×10^{-2}
sMG	1	400	400	3.06×10^{-3}	3.07×10^{-3}	5.38×10^{-3}
αMG	1.25	320		3.01×10^{-3}	3.02×10^{-3}	6.65×10^{-3}
	1.6	250		2.67×10^{-3}	2.69×10^{-3}	7.52×10^{-3}
	2	200		2.56×10^{-3}	2.58×10^{-3}	9.59×10^{-3}
	4	100		2.48×10^{-3}	2.50×10^{-3}	1.67×10^{-2}
	10	40		2.30×10^{-3}	2.33×10^{-3}	2.23×10^{-2}
sMG	1	800	800	2.32×10^{-3}	2.33×10^{-3}	2.85×10^{-3}
αMG	1.25	640		2.10×10^{-3}	2.13×10^{-3}	2.69×10^{-3}
	1.6	500		1.83×10^{-3}	1.87×10^{-3}	2.78×10^{-3}
	2	400		1.78×10^{-3}	1.81×10^{-3}	3.35×10^{-3}
	4	200		1.56×10^{-3}	1.60×10^{-3}	6.97×10^{-3}
	10	80		1.48×10^{-3}	1.52×10^{-3}	1.00×10^{-2}
sMG	1	1600	1600	1.50×10^{-3}	1.51×10^{-3}	1.81×10^{-3}
αMG	1.25	1280		1.22×10^{-3}	1.25×10^{-3}	1.61×10^{-3}
	1.6	1000		1.11×10^{-3}	1.14×10^{-3}	1.57×10^{-3}
	2	800		1.00×10^{-3}	1.03×10^{-3}	1.47×10^{-3}
	4	400		8.96×10^{-4}	9.23×10^{-4}	2.23×10^{-3}
	10	160		8.45×10^{-4}	8.70×10^{-4}	4.38×10^{-3}

Table E.3: TOF QOI errors for vacuum distance 1 m and 50 time bins

Method	Ratio	Coarse Groups	Total DOF	Error 1 (abs.)	Error 2 (cumul. det.)	Error 3 (det.)
sMG	1	100	100	4.90×10^{-3}	4.89×10^{-3}	2.17×10^{-2}
αMG	1.25	80		4.79×10^{-3}	4.61×10^{-3}	1.64×10^{-2}
	1.6	62		4.22×10^{-3}	4.20×10^{-3}	3.05×10^{-2}
	2	50		4.62×10^{-3}	4.64×10^{-3}	3.60×10^{-2}
	4	25		4.42×10^{-3}	4.98×10^{-3}	7.18×10^{-2}
	10	10		4.28×10^{-3}	5.43×10^{-3}	6.51×10^{-2}
sMG	1	200	200	4.07×10^{-3}	4.04×10^{-3}	5.83×10^{-3}
αMG	1.25	160		3.99×10^{-3}	3.95×10^{-3}	6.60×10^{-3}
	1.6	125		3.54×10^{-3}	3.55×10^{-3}	6.48×10^{-3}
	2	100		3.62×10^{-3}	3.57×10^{-3}	9.27×10^{-3}
	4	50		3.29×10^{-3}	3.41×10^{-3}	2.91×10^{-2}
	10	20		3.26×10^{-3}	3.33×10^{-3}	3.45×10^{-2}
sMG	1	400	400	3.06×10^{-3}	3.08×10^{-3}	3.87×10^{-3}
αMG	1.25	320		3.01×10^{-3}	3.02×10^{-3}	3.84×10^{-3}
	1.6	250		2.67×10^{-3}	2.70×10^{-3}	3.75×10^{-3}
	2	200		2.56×10^{-3}	2.60×10^{-3}	3.96×10^{-3}
	4	100		2.48×10^{-3}	2.48×10^{-3}	4.14×10^{-3}
	10	40		2.30×10^{-3}	2.33×10^{-3}	8.12×10^{-3}
sMG	1	800	800	2.32×10^{-3}	2.33×10^{-3}	2.76×10^{-3}
αMG	1.25	640		2.10×10^{-3}	2.13×10^{-3}	2.66×10^{-3}
	1.6	500		1.83×10^{-3}	1.87×10^{-3}	2.41×10^{-3}
	2	400		1.78×10^{-3}	1.82×10^{-3}	2.49×10^{-3}
	4	200		1.56×10^{-3}	1.61×10^{-3}	2.58×10^{-3}
	10	80		1.48×10^{-3}	1.51×10^{-3}	3.22×10^{-3}
sMG	1	1600	1600	1.50×10^{-3}	1.51×10^{-3}	1.79×10^{-3}
αMG	1.25	1280		1.22×10^{-3}	1.25×10^{-3}	1.60×10^{-3}
	1.6	1000		1.11×10^{-3}	1.14×10^{-3}	1.51×10^{-3}
	2	800		1.00×10^{-3}	1.03×10^{-3}	1.38×10^{-3}
	4	400		8.96×10^{-4}	9.27×10^{-4}	1.52×10^{-3}
	10	160		8.45×10^{-4}	8.74×10^{-4}	1.32×10^{-3}

Table E.4: TOF QOI errors for vacuum distance 1 m and 10,000 time bins

Method	Ratio	Coarse Groups	Total DOF	Error 1 (abs.)	Error 2 (cumul. det.)	Error 3 (det.)
sMG	1	100	100	4.90×10^{-3}	4.81×10^{-3}	3.88×10^{-1}
αMG	1.25	80		4.79×10^{-3}	4.70×10^{-3}	4.18×10^{-1}
	1.6	62		4.22×10^{-3}	4.21×10^{-3}	4.44×10^{-1}
	2	50		4.62×10^{-3}	4.64×10^{-3}	5.30×10^{-1}
	4	25		4.42×10^{-3}	4.82×10^{-3}	6.80×10^{-1}
	10	10		4.28×10^{-3}	5.76×10^{-3}	8.42×10^{-1}
sMG	1	200	200	4.07×10^{-3}	4.02×10^{-3}	1.67×10^{-1}
αMG	1.25	160		3.99×10^{-3}	3.94×10^{-3}	1.74×10^{-1}
	1.6	125		3.54×10^{-3}	3.53×10^{-3}	1.72×10^{-1}
	2	100		3.62×10^{-3}	3.57×10^{-3}	2.04×10^{-1}
	4	50		3.29×10^{-3}	3.35×10^{-3}	4.00×10^{-1}
	10	20		3.26×10^{-3}	3.48×10^{-3}	4.93×10^{-1}
sMG	1	400	400	3.06×10^{-3}	3.07×10^{-3}	8.00×10^{-2}
αMG	1.25	320		3.01×10^{-3}	3.02×10^{-3}	8.80×10^{-2}
	1.6	250		2.67×10^{-3}	2.69×10^{-3}	8.80×10^{-2}
	2	200		2.56×10^{-3}	2.58×10^{-3}	1.19×10^{-1}
	4	100		2.48×10^{-3}	2.51×10^{-3}	1.39×10^{-1}
	10	40		2.30×10^{-3}	2.35×10^{-3}	2.16×10^{-1}
sMG	1	800	800	2.32×10^{-3}	2.33×10^{-3}	3.56×10^{-2}
αMG	1.25	640		2.10×10^{-3}	2.13×10^{-3}	4.16×10^{-2}
	1.6	500		1.83×10^{-3}	1.87×10^{-3}	4.60×10^{-2}
	2	400		1.78×10^{-3}	1.81×10^{-3}	5.09×10^{-2}
	4	200		1.56×10^{-3}	1.60×10^{-3}	7.76×10^{-2}
	10	80		1.48×10^{-3}	1.52×10^{-3}	1.05×10^{-1}
sMG	1	1600	1600	1.50×10^{-3}	1.51×10^{-3}	1.37×10^{-2}
αMG	1.25	1280		1.22×10^{-3}	1.25×10^{-3}	1.68×10^{-2}
	1.6	1000		1.11×10^{-3}	1.14×10^{-3}	2.07×10^{-2}
	2	800		1.00×10^{-3}	1.03×10^{-3}	2.32×10^{-2}
	4	400		8.96×10^{-4}	9.23×10^{-4}	4.14×10^{-2}
	10	160		8.45×10^{-4}	8.70×10^{-4}	5.09×10^{-2}

Table E.5: TOF QOI errors for vacuum distance 10 m and 50 time bins

Method	Ratio	Coarse Groups	Total DOF	Error 1 (abs.)	Error 2 (cumul. det.)	Error 3 (det.)
sMG	1	100	100	4.90×10^{-3}	4.98×10^{-3}	4.39×10^{-2}
αMG	1.25	80		4.79×10^{-3}	5.14×10^{-3}	7.71×10^{-2}
	1.6	62		4.22×10^{-3}	4.37×10^{-3}	4.33×10^{-2}
	2	50		4.62×10^{-3}	4.86×10^{-3}	5.59×10^{-2}
	4	25		4.42×10^{-3}	5.14×10^{-3}	1.02×10^{-1}
	10	10		4.28×10^{-3}	6.87×10^{-3}	1.53×10^{-1}
sMG	1	200	200	4.07×10^{-3}	4.16×10^{-3}	3.54×10^{-2}
αMG	1.25	160		3.99×10^{-3}	3.93×10^{-3}	1.49×10^{-2}
	1.6	125		3.54×10^{-3}	3.60×10^{-3}	2.16×10^{-2}
	2	100		3.62×10^{-3}	3.72×10^{-3}	3.13×10^{-2}
	4	50		3.29×10^{-3}	3.85×10^{-3}	4.81×10^{-2}
	10	20		3.26×10^{-3}	3.61×10^{-3}	5.09×10^{-2}
sMG	1	400	400	3.06×10^{-3}	3.09×10^{-3}	1.35×10^{-2}
αMG	1.25	320		3.01×10^{-3}	3.04×10^{-3}	8.22×10^{-3}
	1.6	250		2.67×10^{-3}	2.74×10^{-3}	1.28×10^{-2}
	2	200		2.56×10^{-3}	2.68×10^{-3}	2.27×10^{-2}
	4	100		2.48×10^{-3}	2.65×10^{-3}	2.42×10^{-2}
	10	40		2.30×10^{-3}	2.51×10^{-3}	2.70×10^{-2}
sMG	1	800	800	2.32×10^{-3}	2.34×10^{-3}	4.54×10^{-3}
αMG	1.25	640		2.10×10^{-3}	2.13×10^{-3}	3.79×10^{-3}
	1.6	500		1.83×10^{-3}	1.88×10^{-3}	6.94×10^{-3}
	2	400		1.78×10^{-3}	1.85×10^{-3}	8.86×10^{-3}
	4	200		1.56×10^{-3}	1.69×10^{-3}	1.39×10^{-2}
	10	80		1.48×10^{-3}	1.58×10^{-3}	1.18×10^{-2}
sMG	1	1600	1600	1.50×10^{-3}	1.51×10^{-3}	2.02×10^{-3}
αMG	1.25	1280		1.22×10^{-3}	1.24×10^{-3}	2.08×10^{-3}
	1.6	1000		1.11×10^{-3}	1.13×10^{-3}	2.32×10^{-3}
	2	800		1.00×10^{-3}	1.04×10^{-3}	2.53×10^{-3}
	4	400		8.96×10^{-4}	9.54×10^{-4}	4.99×10^{-3}
	10	160		8.45×10^{-4}	8.93×10^{-4}	4.70×10^{-3}

Table E.6: TOF QOI errors for vacuum distance 10 m and 10,000 time bins

Method	Ratio	Coarse Groups	Total DOF	Error 1 (abs.)	Error 2 (cumul. det.)	Error 3 (det.)
sMG	1	100	100	4.90×10^{-3}	5.04×10^{-3}	1.99×10^{0}
αMG	1.25	80		4.79×10^{-3}	4.96×10^{-3}	2.07×10^{0}
	1.6	62		4.22×10^{-3}	4.51×10^{-3}	2.09×10^{0}
	2	50		4.62×10^{-3}	4.98×10^{-3}	2.28×10^{0}
	4	25		4.42×10^{-3}	5.27×10^{-3}	2.61×10^{0}
	10	10		4.28×10^{-3}	6.29×10^{-3}	2.99×10^{0}
sMG	1	200	200	4.07×10^{-3}	4.10×10^{-3}	1.34×10^{0}
αMG	1.25	160		3.99×10^{-3}	4.03×10^{-3}	1.42×10^{0}
	1.6	125		3.54×10^{-3}	3.64×10^{-3}	1.47×10^{0}
	2	100		3.62×10^{-3}	3.71×10^{-3}	1.55×10^{0}
	4	50		3.29×10^{-3}	3.62×10^{-3}	1.87×10^{0}
	10	20		3.26×10^{-3}	3.83×10^{-3}	2.03×10^{0}
sMG	1	400	400	3.06×10^{-3}	3.09×10^{-3}	8.55×10^{-1}
αMG	1.25	320		3.01×10^{-3}	3.05×10^{-3}	9.26×10^{-1}
	1.6	250		2.67×10^{-3}	2.72×10^{-3}	9.60×10^{-1}
	2	200		2.56×10^{-3}	2.63×10^{-3}	1.04×10^{0}
	4	100		2.48×10^{-3}	2.62×10^{-3}	1.27×10^{0}
	10	40		2.30×10^{-3}	2.52×10^{-3}	1.36×10^{0}
sMG	1	800	800	2.32×10^{-3}	2.33×10^{-3}	4.50×10^{-1}
αMG	1.25	640		2.10×10^{-3}	2.14×10^{-3}	5.29×10^{-1}
	1.6	500		1.83×10^{-3}	1.87×10^{-3}	5.63×10^{-1}
	2	400		1.78×10^{-3}	1.82×10^{-3}	6.20×10^{-1}
	4	200		1.56×10^{-3}	1.64×10^{-3}	8.08×10^{-1}
	10	80		1.48×10^{-3}	1.59×10^{-3}	9.07×10^{-1}
sMG	1	1600	1600	1.50×10^{-3}	1.51×10^{-3}	1.49×10^{-1}
αMG	1.25	1280		1.22×10^{-3}	1.25×10^{-3}	1.69×10^{-1}
	1.6	1000		1.11×10^{-3}	1.14×10^{-3}	2.22×10^{-1}
	2	800		1.00×10^{-3}	1.03×10^{-3}	2.81×10^{-1}
	4	400		8.96×10^{-4}	9.33×10^{-4}	4.72×10^{-1}
	10	160		8.45×10^{-4}	8.97×10^{-4}	5.69×10^{-1}

Table E.7: TOF QOI errors for vacuum distance 10 cm and 50 time bins

Method	Ratio	Coarse Groups	Total DOF	Error 1 (abs.)	Error 2 (cumul. det.)	Error 3 (det.)
sMG	1	100	100	4.90×10^{-3}	4.77×10^{-3}	5.59×10^{-3}
FEDS	1.25	80		4.08×10^{-3}	4.08×10^{-3}	5.51×10^{-3}
	1.6	62		2.88×10^{-3}	2.92×10^{-3}	6.52×10^{-3}
	2	50		2.22×10^{-3}	2.26×10^{-3}	8.01×10^{-3}
	4	25		1.49×10^{-3}	1.63×10^{-3}	2.25×10^{-2}
	10	10		3.38×10^{-4}	5.09×10^{-3}	1.90×10^{-1}
sMG	1	200	200	4.07×10^{-3}	4.02×10^{-3}	4.50×10^{-3}
FEDS	1.25	160		3.29×10^{-3}	3.33×10^{-3}	4.39×10^{-3}
	1.6	125		2.45×10^{-3}	2.50×10^{-3}	3.37×10^{-3}
	2	100		2.16×10^{-3}	2.20×10^{-3}	3.77×10^{-3}
	4	50		9.70×10^{-4}	1.02×10^{-3}	6.65×10^{-3}
	10	20		3.13×10^{-4}	1.42×10^{-3}	4.75×10^{-2}
sMG	1	400	400	3.06×10^{-3}	3.07×10^{-3}	3.48×10^{-3}
FEDS	1.25	320		2.45×10^{-3}	2.50×10^{-3}	3.24×10^{-3}
	1.6	250		1.89×10^{-3}	1.94×10^{-3}	2.58×10^{-3}
	2	200		1.59×10^{-3}	1.63×10^{-3}	2.22×10^{-3}
	4	100		8.25×10^{-4}	8.47×10^{-4}	2.38×10^{-3}
	10	40		2.43×10^{-4}	4.03×10^{-4}	8.11×10^{-3}
sMG	1	800	800	2.32×10^{-3}	2.33×10^{-3}	2.71×10^{-3}
FEDS	1.25	640		1.68×10^{-3}	1.72×10^{-3}	2.21×10^{-3}
	1.6	500		1.30×10^{-3}	1.33×10^{-3}	1.73×10^{-3}
	2	400		1.03×10^{-3}	1.07×10^{-3}	1.42×10^{-3}
	4	200		5.66×10^{-4}	5.84×10^{-4}	8.87×10^{-4}
	10	80		1.74×10^{-4}	1.92×10^{-4}	2.19×10^{-3}
sMG	1	1600	1600	1.50×10^{-3}	1.51×10^{-3}	1.78×10^{-3}
FEDS	1.25	1280		9.75×10^{-4}	1.00×10^{-3}	1.34×10^{-3}
	1.6	1000		7.82×10^{-4}	8.06×10^{-4}	1.07×10^{-3}
	2	800		6.19×10^{-4}	6.38×10^{-4}	8.28×10^{-4}
	4	400		3.30×10^{-4}	3.41×10^{-4}	4.39×10^{-4}
	10	160		9.50×10^{-5}	1.01×10^{-4}	3.47×10^{-4}

Table E.8: TOF QOI errors for vacuum distance 10 cm and 10,000 time bins

Method	Ratio	Coarse Groups	Total DOF	Error 1 (abs.)	Error 2 (cumul. det.)	Error 3 (det.)
sMG	1	100	100	4.90×10^{-3}	4.75×10^{-3}	3.68×10^{-2}
FEDS	1.25	80		4.08×10^{-3}	4.09×10^{-3}	4.64×10^{-2}
	1.6	62		2.88×10^{-3}	2.93×10^{-3}	6.05×10^{-2}
	2	50		2.22×10^{-3}	2.26×10^{-3}	7.59×10^{-2}
	4	25		1.49×10^{-3}	1.88×10^{-3}	1.51×10^{-1}
	10	10		3.38×10^{-4}	6.06×10^{-3}	3.47×10^{-1}
sMG	1	200	200	4.07×10^{-3}	4.02×10^{-3}	1.55×10^{-2}
FEDS	1.25	160		3.29×10^{-3}	3.33×10^{-3}	2.03×10^{-2}
	1.6	125		2.45×10^{-3}	2.50×10^{-3}	2.67×10^{-2}
	2	100		2.16×10^{-3}	2.20×10^{-3}	3.47×10^{-2}
	4	50		9.70×10^{-4}	1.03×10^{-3}	7.04×10^{-2}
	10	20		3.13×10^{-4}	1.36×10^{-3}	1.53×10^{-1}
sMG	1	400	400	3.06×10^{-3}	3.07×10^{-3}	5.38×10^{-3}
FEDS	1.25	320		2.45×10^{-3}	2.50×10^{-3}	7.34×10^{-3}
	1.6	250		1.89×10^{-3}	1.94×10^{-3}	1.00×10^{-2}
	2	200		1.59×10^{-3}	1.63×10^{-3}	1.34×10^{-2}
	4	100		8.25×10^{-4}	8.41×10^{-4}	3.06×10^{-2}
	10	40		2.43×10^{-4}	4.43×10^{-4}	7.97×10^{-2}
sMG	1	800	800	2.32×10^{-3}	2.33×10^{-3}	2.85×10^{-3}
FEDS	1.25	640		1.68×10^{-3}	1.72×10^{-3}	2.30×10^{-3}
	1.6	500		1.30×10^{-3}	1.33×10^{-3}	2.48×10^{-3}
	2	400		1.03×10^{-3}	1.07×10^{-3}	3.72×10^{-3}
	4	200		5.66×10^{-4}	5.84×10^{-4}	1.18×10^{-2}
	10	80		1.74×10^{-4}	1.97×10^{-4}	3.51×10^{-2}
sMG	1	1600	1600	1.50×10^{-3}	1.51×10^{-3}	1.81×10^{-3}
FEDS	1.25	1280		9.75×10^{-4}	1.00×10^{-3}	1.36×10^{-3}
	1.6	1000		7.82×10^{-4}	8.07×10^{-4}	1.21×10^{-3}
	2	800		6.19×10^{-4}	6.38×10^{-4}	1.07×10^{-3}
	4	400		3.30×10^{-4}	3.41×10^{-4}	2.89×10^{-3}
	10	160		9.50×10^{-5}	9.90×10^{-5}	1.30×10^{-2}

Table E.9: TOF QOI errors for vacuum distance 1 m and 50 time bins

Method	Ratio	Coarse Groups	Total DOF	Error 1 (abs.)	Error 2 (cumul. det.)	Error 3 (det.)
sMG	1	100	100	4.90×10^{-3}	4.89×10^{-3}	2.17×10^{-2}
FEDS	1.25	80		4.08×10^{-3}	4.09×10^{-3}	2.55×10^{-2}
	1.6	62		2.88×10^{-3}	3.43×10^{-3}	6.22×10^{-2}
	2	50		2.22×10^{-3}	3.37×10^{-3}	6.91×10^{-2}
	4	25		1.49×10^{-3}	4.09×10^{-3}	1.13×10^{-1}
	10	10		3.38×10^{-4}	1.15×10^{-2}	4.73×10^{-1}
sMG	1	200	200	4.07×10^{-3}	4.04×10^{-3}	5.83×10^{-3}
FEDS	1.25	160		3.29×10^{-3}	3.28×10^{-3}	7.26×10^{-3}
	1.6	125		2.45×10^{-3}	2.65×10^{-3}	1.31×10^{-2}
	2	100		2.16×10^{-3}	2.35×10^{-3}	2.05×10^{-2}
	4	50		9.70×10^{-4}	2.54×10^{-3}	6.03×10^{-2}
	10	20		3.13×10^{-4}	5.73×10^{-3}	1.92×10^{-1}
sMG	1	400	400	3.06×10^{-3}	3.08×10^{-3}	3.87×10^{-3}
FEDS	1.25	320		2.45×10^{-3}	2.50×10^{-3}	3.29×10^{-3}
	1.6	250		1.89×10^{-3}	1.94×10^{-3}	4.52×10^{-3}
	2	200		1.59×10^{-3}	1.63×10^{-3}	3.98×10^{-3}
	4	100		8.25×10^{-4}	1.06×10^{-3}	1.80×10^{-2}
	10	40		2.43×10^{-4}	2.01×10^{-3}	7.22×10^{-2}
sMG	1	800	800	2.32×10^{-3}	2.33×10^{-3}	2.76×10^{-3}
FEDS	1.25	640		1.68×10^{-3}	1.72×10^{-3}	2.28×10^{-3}
	1.6	500		1.30×10^{-3}	1.33×10^{-3}	1.90×10^{-3}
	2	400		1.03×10^{-3}	1.07×10^{-3}	2.17×10^{-3}
	4	200		5.66×10^{-4}	5.87×10^{-4}	3.17×10^{-3}
	10	80		1.74×10^{-4}	7.35×10^{-4}	2.24×10^{-2}
sMG	1	1600	1600	1.50×10^{-3}	1.51×10^{-3}	1.79×10^{-3}
FEDS	1.25	1280		9.75×10^{-4}	1.00×10^{-3}	1.35×10^{-3}
	1.6	1000		7.82×10^{-4}	8.06×10^{-4}	1.09×10^{-3}
	2	800		6.19×10^{-4}	6.40×10^{-4}	8.67×10^{-4}
	4	400		3.30×10^{-4}	3.45×10^{-4}	1.16×10^{-3}
	10	160		9.50×10^{-5}	1.49×10^{-4}	3.73×10^{-3}

Table E.10: TOF QOI errors for vacuum distance 1 m and 10,000 time bins

Method	Ratio	Coarse Groups	Total DOF	Error 1 (abs.)	Error 2 (cumul. det.)	Error 3 (det.)
sMG	1	100	100	4.90×10^{-3}	4.81×10^{-3}	3.88×10^{-1}
FEDS	1.25	80		4.08×10^{-3}	4.23×10^{-3}	5.05×10^{-1}
	1.6	62		2.88×10^{-3}	3.39×10^{-3}	6.46×10^{-1}
	2	50		2.22×10^{-3}	3.22×10^{-3}	7.53×10^{-1}
	4	25		1.49×10^{-3}	5.62×10^{-3}	1.13×10^{0}
	10	10		3.38×10^{-4}	1.19×10^{-2}	1.32×10^{0}
sMG	1	200	200	4.07×10^{-3}	4.02×10^{-3}	1.67×10^{-1}
FEDS	1.25	160		3.29×10^{-3}	3.34×10^{-3}	1.98×10^{-1}
	1.6	125		2.45×10^{-3}	2.53×10^{-3}	2.62×10^{-1}
	2	100		2.16×10^{-3}	2.29×10^{-3}	3.60×10^{-1}
	4	50		9.70×10^{-4}	2.38×10^{-3}	6.98×10^{-1}
	10	20		3.13×10^{-4}	6.45×10^{-3}	1.06×10^{0}
sMG	1	400	400	3.06×10^{-3}	3.07×10^{-3}	8.00×10^{-2}
FEDS	1.25	320		2.45×10^{-3}	2.50×10^{-3}	1.00×10^{-1}
	1.6	250		1.89×10^{-3}	1.94×10^{-3}	1.27×10^{-1}
	2	200		1.59×10^{-3}	1.63×10^{-3}	1.52×10^{-1}
	4	100		8.25×10^{-4}	1.01×10^{-3}	3.05×10^{-1}
	10	40		2.43×10^{-4}	2.72×10^{-3}	7.34×10^{-1}
sMG	1	800	800	2.32×10^{-3}	2.33×10^{-3}	3.56×10^{-2}
FEDS	1.25	640		1.68×10^{-3}	1.72×10^{-3}	4.57×10^{-2}
	1.6	500		1.30×10^{-3}	1.33×10^{-3}	5.55×10^{-2}
	2	400		1.03×10^{-3}	1.07×10^{-3}	6.70×10^{-2}
	4	200		5.66×10^{-4}	5.94×10^{-4}	1.29×10^{-1}
	10	80		1.74×10^{-4}	8.18×10^{-4}	3.76×10^{-1}
sMG	1	1600	1600	1.50×10^{-3}	1.51×10^{-3}	1.37×10^{-2}
FEDS	1.25	1280		9.75×10^{-4}	1.00×10^{-3}	1.78×10^{-2}
	1.6	1000		7.82×10^{-4}	8.07×10^{-4}	2.28×10^{-2}
	2	800		6.19×10^{-4}	6.38×10^{-4}	2.78×10^{-2}
	4	400		3.30×10^{-4}	3.42×10^{-4}	5.66×10^{-2}
	10	160		9.50×10^{-5}	1.61×10^{-4}	1.27×10^{-1}

Table E.11: TOF QOI errors for vacuum distance 10 m and 50 time bins

Method	Ratio	Coarse Groups	Total DOF	Error 1 (abs.)	Error 2 (cumul. det.)	Error 3 (det.)
sMG	1	100	100	4.90×10^{-3}	4.98×10^{-3}	4.39×10^{-2}
FEDS	1.25	80		4.08×10^{-3}	4.89×10^{-3}	9.56×10^{-2}
	1.6	62		2.88×10^{-3}	3.55×10^{-3}	6.54×10^{-2}
	2	50		2.22×10^{-3}	4.15×10^{-3}	9.94×10^{-2}
	4	25		1.49×10^{-3}	4.75×10^{-3}	1.32×10^{-1}
	10	10		3.38×10^{-4}	1.33×10^{-2}	5.45×10^{-1}
sMG	1	200	200	4.07×10^{-3}	4.16×10^{-3}	3.54×10^{-2}
FEDS	1.25	160		3.29×10^{-3}	3.33×10^{-3}	2.11×10^{-2}
	1.6	125		2.45×10^{-3}	2.63×10^{-3}	2.78×10^{-2}
	2	100		2.16×10^{-3}	2.50×10^{-3}	4.04×10^{-2}
	4	50		9.70×10^{-4}	3.68×10^{-3}	8.05×10^{-2}
	10	20		3.13×10^{-4}	8.02×10^{-3}	2.35×10^{-1}
sMG	1	400	400	3.06×10^{-3}	3.09×10^{-3}	1.35×10^{-2}
FEDS	1.25	320		2.45×10^{-3}	2.53×10^{-3}	8.81×10^{-3}
	1.6	250		1.89×10^{-3}	1.96×10^{-3}	1.57×10^{-2}
	2	200		1.59×10^{-3}	1.84×10^{-3}	3.03×10^{-2}
	4	100		8.25×10^{-4}	1.48×10^{-3}	3.96×10^{-2}
	10	40		2.43×10^{-4}	3.35×10^{-3}	1.15×10^{-1}
sMG	1	800	800	2.32×10^{-3}	2.34×10^{-3}	4.54×10^{-3}
FEDS	1.25	640		1.68×10^{-3}	1.72×10^{-3}	4.55×10^{-3}
	1.6	500		1.30×10^{-3}	1.41×10^{-3}	9.01×10^{-3}
	2	400		1.03×10^{-3}	1.12×10^{-3}	1.28×10^{-2}
	4	200		5.66×10^{-4}	1.00×10^{-3}	2.96×10^{-2}
	10	80		1.74×10^{-4}	1.42×10^{-3}	5.07×10^{-2}
sMG	1	1600	1600	1.50×10^{-3}	1.51×10^{-3}	2.02×10^{-3}
FEDS	1.25	1280		9.75×10^{-4}	1.00×10^{-3}	1.57×10^{-3}
	1.6	1000		7.82×10^{-4}	7.94×10^{-4}	1.87×10^{-3}
	2	800		6.19×10^{-4}	6.48×10^{-4}	3.04×10^{-3}
	4	400		3.30×10^{-4}	4.19×10^{-4}	6.09×10^{-3}
	10	160		9.50×10^{-5}	4.64×10^{-4}	1.57×10^{-2}

Table E.12: TOF QOI errors for vacuum distance 10 m and 10,000 time bins

Method	Ratio	Coarse Groups	Total DOF	Error 1 (abs.)	Error 2 (cumul. det.)	Error 3 (det.)
sMG	1	100	100	4.90×10^{-3}	5.04×10^{-3}	1.99×10^{0}
FEDS	1.25	80		4.08×10^{-3}	4.58×10^{-3}	2.23×10^{0}
	1.6	62		2.88×10^{-3}	3.96×10^{-3}	2.48×10^{0}
	2	50		2.22×10^{-3}	3.95×10^{-3}	2.69×10^{0}
	4	25		1.49×10^{-3}	6.46×10^{-3}	3.45×10^{0}
	10	10		3.38×10^{-4}	1.24×10^{-2}	3.74×10^{0}
sMG	1	200	200	4.07×10^{-3}	4.10×10^{-3}	1.34×10^{0}
FEDS	1.25	160		3.29×10^{-3}	3.47×10^{-3}	1.51×10^{0}
	1.6	125		2.45×10^{-3}	2.80×10^{-3}	1.70×10^{0}
	2	100		2.16×10^{-3}	2.70×10^{-3}	1.88×10^{0}
	4	50		9.70×10^{-4}	3.14×10^{-3}	2.30×10^{0}
	10	20		3.13×10^{-4}	6.99×10^{-3}	2.74×10^{0}
sMG	1	400	400	3.06×10^{-3}	3.09×10^{-3}	8.55×10^{-1}
FEDS	1.25	320		2.45×10^{-3}	2.53×10^{-3}	9.81×10^{-1}
	1.6	250		1.89×10^{-3}	2.01×10^{-3}	1.11×10^{0}
	2	200		1.59×10^{-3}	1.77×10^{-3}	1.21×10^{0}
	4	100		8.25×10^{-4}	1.60×10^{-3}	1.56×10^{0}
	10	40		2.43×10^{-4}	3.40×10^{-3}	2.11×10^{0}
sMG	1	800	800	2.32×10^{-3}	2.33×10^{-3}	4.50×10^{-1}
FEDS	1.25	640		1.68×10^{-3}	1.73×10^{-3}	5.60×10^{-1}
	1.6	500		1.30×10^{-3}	1.35×10^{-3}	6.56×10^{-1}
	2	400		1.03×10^{-3}	1.10×10^{-3}	7.44×10^{-1}
	4	200		5.66×10^{-4}	8.33×10^{-4}	1.02×10^{0}
	10	80		1.74×10^{-4}	1.53×10^{-3}	1.40×10^{0}
sMG	1	1600	1600	1.50×10^{-3}	1.51×10^{-3}	1.49×10^{-1}
FEDS	1.25	1280		9.75×10^{-4}	1.00×10^{-3}	1.87×10^{-1}
	1.6	1000		7.82×10^{-4}	8.09×10^{-4}	2.64×10^{-1}
	2	800		6.19×10^{-4}	6.44×10^{-4}	3.44×10^{-1}
	4	400		3.30×10^{-4}	4.11×10^{-4}	6.30×10^{-1}
	10	160		9.50×10^{-5}	6.35×10^{-4}	9.19×10^{-1}

Table E.13: TOF QOI errors for differing reference solutions for a vacuum distance of 10 m and 10,000 time bins

Method	Ratio	Coarse Groups	Total DOF	Error 1 (abs.)	Error 2 (cumul. det.)	Error 3 (det.)
sMG	1	10000	10000	1.68×10^{-4}	1.72×10^{-4}	2.41×10^{-3}
αMG	1.25	8000		8.45×10^{-5}	8.70×10^{-5}	7.86×10^{-3}
	2	5000		6.42×10^{-5}	6.67×10^{-5}	1.42×10^{-2}
	5	2000		6.59×10^{-5}	6.95×10^{-5}	4.83×10^{-2}
αMG	1.8125	8000	14500	6.11×10^{-7}	1.74×10^{-6}	7.34×10^{-3}
	2.9	5000		4.89×10^{-6}	6.32×10^{-6}	1.31×10^{-2}
	7.25	2000		7.49×10^{-6}	7.88×10^{-6}	4.15×10^{-3}

Table E.14: TOF QOI errors for differing escape cross sections for various vacuum distances and numbers of time bins

Method	Ratio	Coarse Groups	Total DOF	Error 1 (abs.)	Error 2 (cumul. det.)	Error 3 (det.)
			$d = 10$ cm, $b = 10,000$			
FEDS	2	50	100	2.28×10^{-3}	2.32×10^{-3}	7.59×10^{-2}
			101	4.80×10^{-3}	4.67×10^{-3}	7.53×10^{-2}
sMG	1	100	100	4.97×10^{-3}	4.82×10^{-3}	3.68×10^{-2}
			101	1.11×10^{-2}	1.01×10^{-2}	3.64×10^{-2}
FEDS	2	200	400	1.65×10^{-3}	1.70×10^{-3}	1.34×10^{-2}
			401	2.77×10^{-3}	2.73×10^{-3}	1.36×10^{-2}
sMG	1	400	400	3.13×10^{-3}	3.14×10^{-3}	5.42×10^{-3}
			401	7.55×10^{-3}	7.11×10^{-3}	8.06×10^{-3}
			$d = 1$ m, $b = 10,000$			
FEDS	2	50	100	2.28×10^{-3}	3.27×10^{-3}	7.53×10^{-1}
			101	4.80×10^{-3}	5.20×10^{-3}	7.51×10^{-1}
sMG	1	100	100	4.97×10^{-3}	4.88×10^{-3}	3.88×10^{-1}
			101	1.11×10^{-2}	1.01×10^{-2}	3.69×10^{-1}
FEDS	2	200	400	1.65×10^{-3}	1.70×10^{-3}	1.52×10^{-1}
			401	2.77×10^{-3}	2.73×10^{-3}	1.50×10^{-1}
sMG	1	400	400	3.13×10^{-3}	3.14×10^{-3}	8.00×10^{-2}
			401	7.55×10^{-3}	7.11×10^{-3}	7.88×10^{-2}
			$d = 10$ m, $b = 10,000$			
FEDS	2	50	100	2.28×10^{-3}	3.99×10^{-3}	2.70×10^{0}
			101	4.80×10^{-3}	5.68×10^{-3}	2.71×10^{0}
sMG	1	100	100	4.97×10^{-3}	5.10×10^{-3}	1.99×10^{0}
			101	1.11×10^{-2}	1.02×10^{-2}	1.93×10^{0}
FEDS	2	200	400	1.65×10^{-3}	1.83×10^{-3}	1.22×10^{0}
			401	2.77×10^{-3}	2.82×10^{-3}	1.21×10^{0}
sMG	1	400	400	3.13×10^{-3}	3.16×10^{-3}	8.60×10^{-1}
			401	7.55×10^{-3}	7.12×10^{-3}	8.49×10^{-1}
			$d = 10$ m, $b = 50$			
FEDS	2	50	100	2.28×10^{-3}	4.18×10^{-3}	9.93×10^{-2}
			101	4.80×10^{-3}	6.24×10^{-3}	1.52×10^{-1}
sMG	1	100	100	4.97×10^{-3}	5.04×10^{-3}	4.39×10^{-2}
			101	1.11×10^{-2}	1.03×10^{-2}	4.75×10^{-2}
FEDS	2	200	400	1.65×10^{-3}	1.90×10^{-3}	3.04×10^{-2}
			401	2.77×10^{-3}	2.86×10^{-3}	3.01×10^{-2}
sMG	1	400	400	3.13×10^{-3}	3.16×10^{-3}	1.35×10^{-2}
			401	7.55×10^{-3}	7.13×10^{-3}	1.14×10^{-2}

APPENDIX F

ADDENDUM TO SECTION 6

F.1 Additional Slab Pincell Errors

Figures F.1 – F.4 give additional absolute errors (in pcm) for component QOIs for problems A and B. Figures F.5 – F.13 give relative errors (in percent) for problems A, B, and D. The corresponding absolute errors are in section 6.

F.2 SHEM group structures

Tables F.1 – F.3 give the group boundaries for the SHEM-166, SHEM-244, and SHEM-361 structures, respectively. The SHEM-361 boundaries are taken from [56]. The SHEM-166 and SHEM-244 boundaries are manual coarsenings I created.

Table F.1: Energy boundaries for the SHEM-166 group structure in eV.

2.00000×10^{7}	7.06511×10^{5}	2.61001×10^{4}	9.50002×10^{0}	2.33006×10^{0}	1.07799×10^{0}	2.31192×10^{-1}
1.49182×10^{7}	5.78443×10^{5}	2.49991×10^{4}	8.59597×10^{0}	2.27299×10^{0}	1.03499×10^{0}	2.09610×10^{-1}
1.38403×10^{7}	4.94002×10^{5}	2.26994×10^{4}	7.77796×10^{0}	2.21709×10^{0}	1.02101×10^{0}	1.90005×10^{-1}
1.16183×10^{7}	4.56021×10^{5}	1.43872×10^{4}	7.03779×10^{0}	2.15695×10^{0}	1.00904×10^{0}	1.61895×10^{-1}
9.99999×10^{6}	4.12501×10^{5}	9.11881×10^{3}	6.36805×10^{0}	2.07010×10^{0}	9.96501×10^{-1}	1.37999×10^{-1}
9.04836×10^{6}	3.83884×10^{5}	5.57526×10^{3}	5.76205×10^{0}	1.98992×10^{0}	9.81959×10^{-1}	1.19995×10^{-1}
8.18730×10^{6}	3.20646×10^{5}	3.40872×10^{3}	5.21372×10^{0}	1.90008×10^{0}	9.63960×10^{-1}	1.04298×10^{-1}
7.40817×10^{6}	2.67826×10^{5}	2.08410×10^{3}	4.71757×10^{0}	1.77997×10^{0}	9.44022×10^{-1}	8.97968×10^{-2}
6.70319×10^{6}	2.30014×10^{5}	1.32800×10^{3}	4.21983×10^{0}	1.66895×10^{0}	9.19978×10^{-1}	7.64969×10^{-2}
6.06530×10^{6}	1.95008×10^{5}	8.46204×10^{2}	4.00000×10^{0}	1.58803×10^{0}	8.80024×10^{-1}	6.51999×10^{-2}
4.96585×10^{6}	1.64999×10^{5}	5.39204×10^{2}	3.88217×10^{0}	1.51998×10^{0}	8.00371×10^{-1}	5.54982×10^{-2}
4.06569×10^{6}	1.40000×10^{5}	3.55228×10^{2}	3.71209×10^{0}	1.44397×10^{0}	7.19999×10^{-1}	4.73019×10^{-2}
3.32871×10^{6}	1.22773×10^{5}	2.34025×10^{2}	3.54307×10^{0}	1.41001×10^{0}	6.24999×10^{-1}	4.02999×10^{-2}
2.72531×10^{6}	1.15624×10^{5}	1.54176×10^{2}	3.14211×10^{0}	1.38098×10^{0}	5.94993×10^{-1}	3.43998×10^{-2}
2.23130×10^{6}	9.46645×10^{4}	1.07171×10^{2}	2.88405×10^{0}	1.33095×10^{0}	5.54990×10^{-1}	2.92989×10^{-2}
1.90139×10^{6}	8.22974×10^{4}	7.44972×10^{1}	2.77512×10^{0}	1.29304×10^{0}	5.20011×10^{-1}	2.49394×10^{-2}
1.63654×10^{6}	6.73794×10^{4}	5.17847×10^{1}	2.74092×10^{0}	1.25094×10^{0}	4.75017×10^{-1}	2.00104×10^{-2}
1.40577×10^{6}	5.51656×10^{4}	4.21301×10^{1}	2.71990×10^{0}	1.21397×10^{0}	4.31579×10^{-1}	1.48300×10^{-2}
1.33694×10^{6}	4.99159×10^{4}	3.42754×10^{1}	2.70012×10^{0}	1.16999×10^{0}	3.90001×10^{-1}	1.04505×10^{-2}
1.28696×10^{6}	4.08677×10^{4}	2.78852×10^{1}	2.64004×10^{0}	1.14797×10^{0}	3.52994×10^{-1}	7.14526×10^{-3}
1.16205×10^{6}	3.69786×10^{4}	2.24906×10^{1}	2.62005×10^{0}	1.12997×10^{0}	3.25008×10^{-1}	4.55602×10^{-3}
1.05115×10^{6}	3.34596×10^{4}	1.81396×10^{1}	2.59009×10^{0}	1.11605×10^{0}	3.05012×10^{-1}	2.49990×10^{-3}
9.51119×10^{5}	2.92810×10^{4}	1.46303×10^{1}	2.55000×10^{0}	1.10395×10^{0}	2.79989×10^{-1}	1.00000×10^{-5}
8.60006×10^{5}	2.73944×10^{4}	1.18000×10^{1}	2.46994×10^{0}	1.09198×10^{0}	2.54997×10^{-1}	

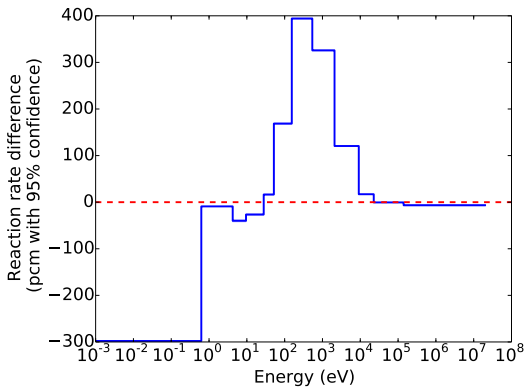

(a) Inner fuel U-238 absorption differences

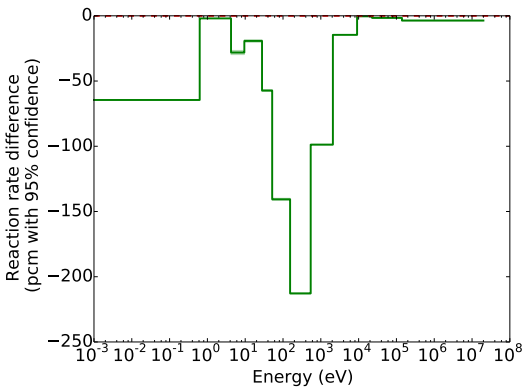

(b) Outer fuel U-238 absorption differences

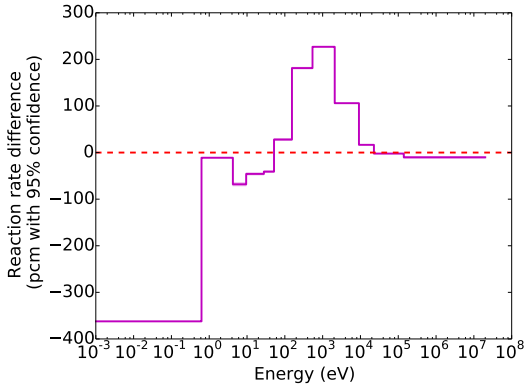

(c) Total fuel U-238 absorption differences

Figure F.1: Component errors between MCNP and PDT using the 361-group SHEM structure for problem A (cf. Table 6.1) in pcm, normalized to the total absorption or fission rate.

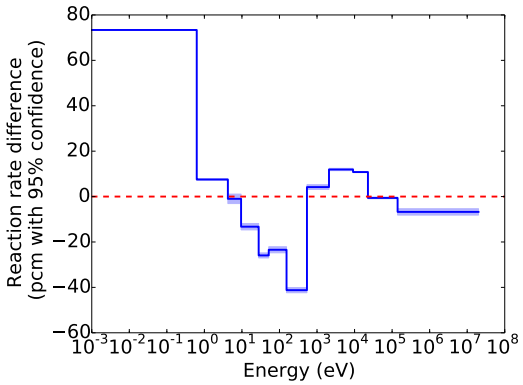

(a) Inner fuel U-238 absorption differences

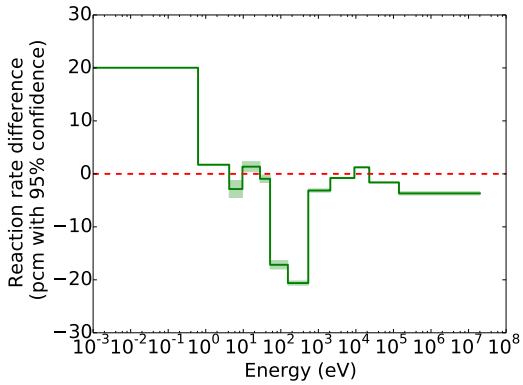

(b) Outer fuel U-238 absorption differences

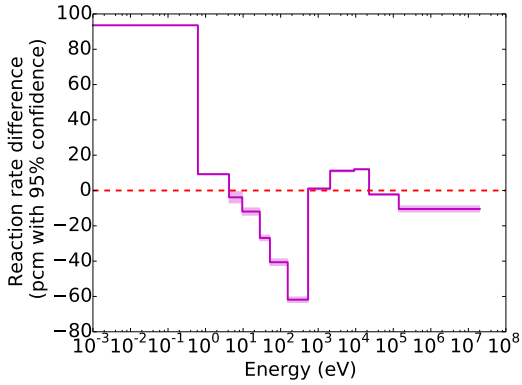

(c) Total fuel U-238 absorption differences

Figure F.2: Component errors between MCNP and PDT using the $R_{4,d}$ structure for problem A in pcm, normalized to the total absorption or fission rate.

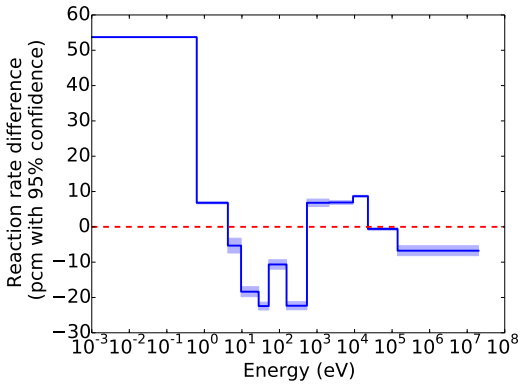

(a) Inner fuel U-238 absorption differences

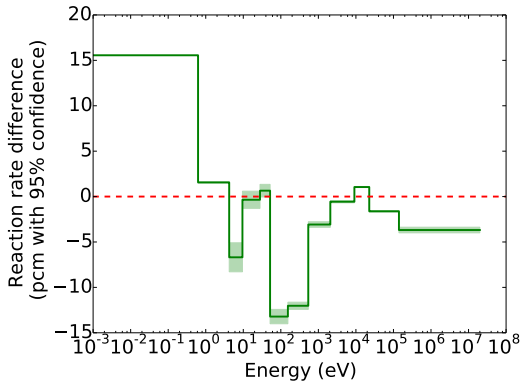

(b) Outer fuel U-238 absorption differences

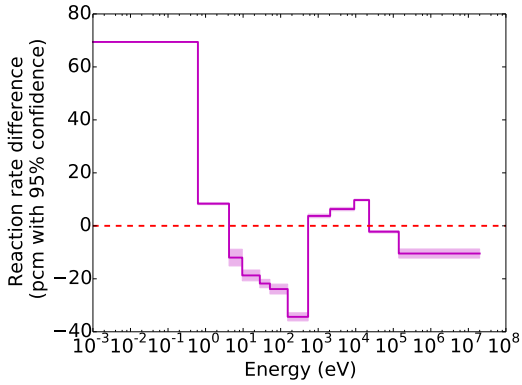

(c) Total fuel U-238 absorption differences

Figure F.3: Component errors between MCNP and PDT using the $R_{4,e}$ structure for problem A in pcm, normalized to the total absorption or fission rate.

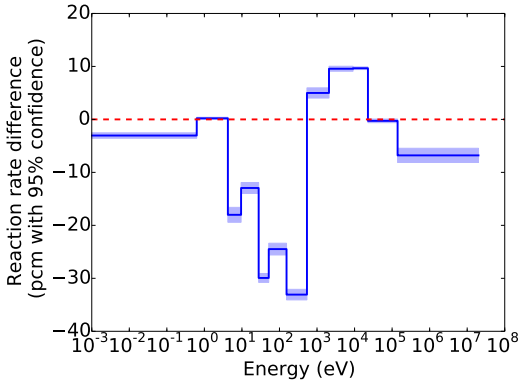

(a) Inner fuel U-238 absorption differences

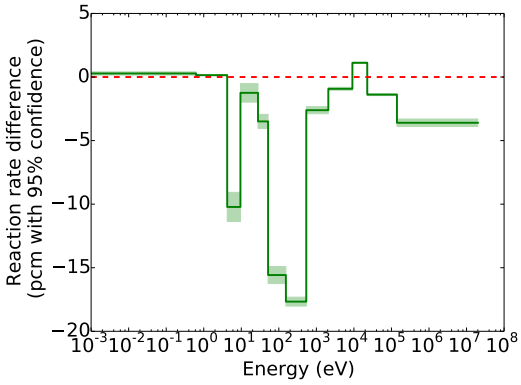

(b) Outer fuel U-238 absorption differences

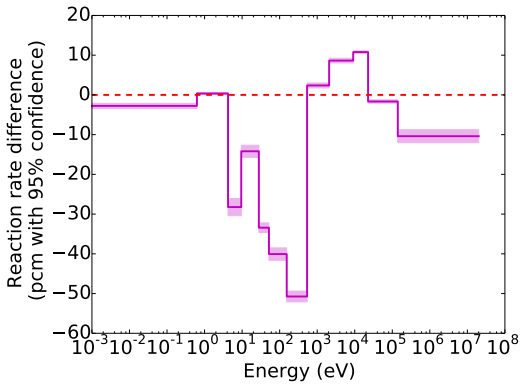

(c) Total fuel U-238 absorption differences

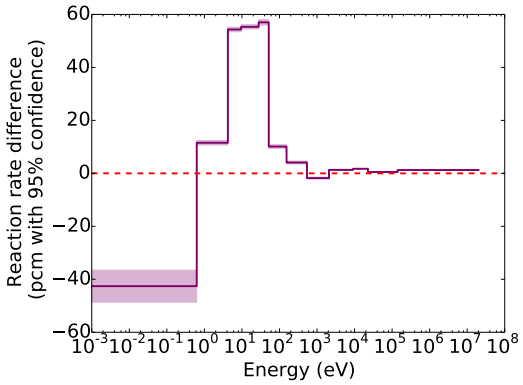

(d) Total fuel U-235 absorption differences

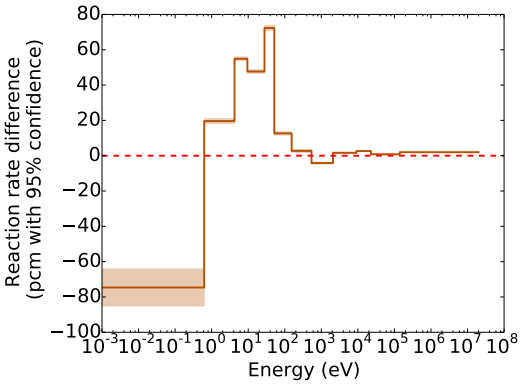

(e) Total fuel U-235 fission differences

Figure F.4: Component errors between MCNP and PDT using the $R_{4,d}$ structure for problem B in pcm, normalized to the total absorption or fission rate.

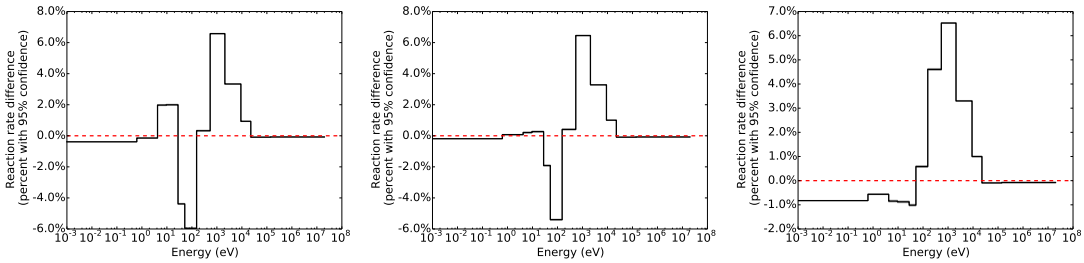

(a) SHEM-166 (b) SHEM-244 (c) SHEM-361

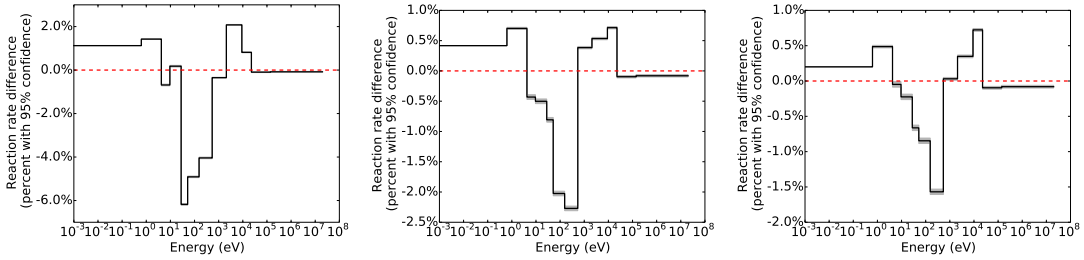

(d) $R_{1,d}$ (e) $R_{3,d}$ (f) $R_{4,d}$

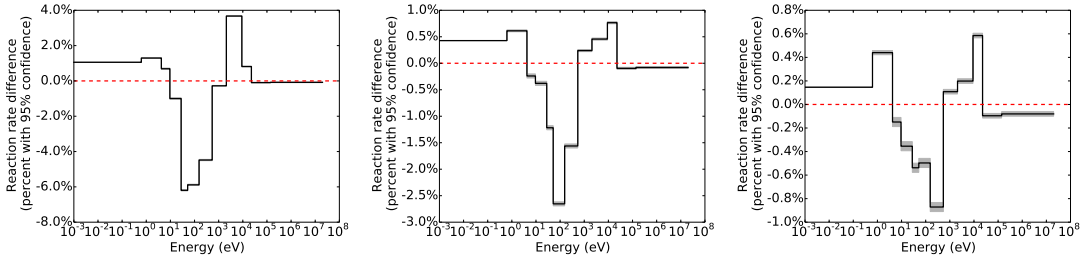

(g) $R_{1,e}$ (h) $R_{3,3}$ (i) $R_{4,e}$

Figure F.5: Relative total absorption errors between MCNP and PDT for different energy structures for problem A

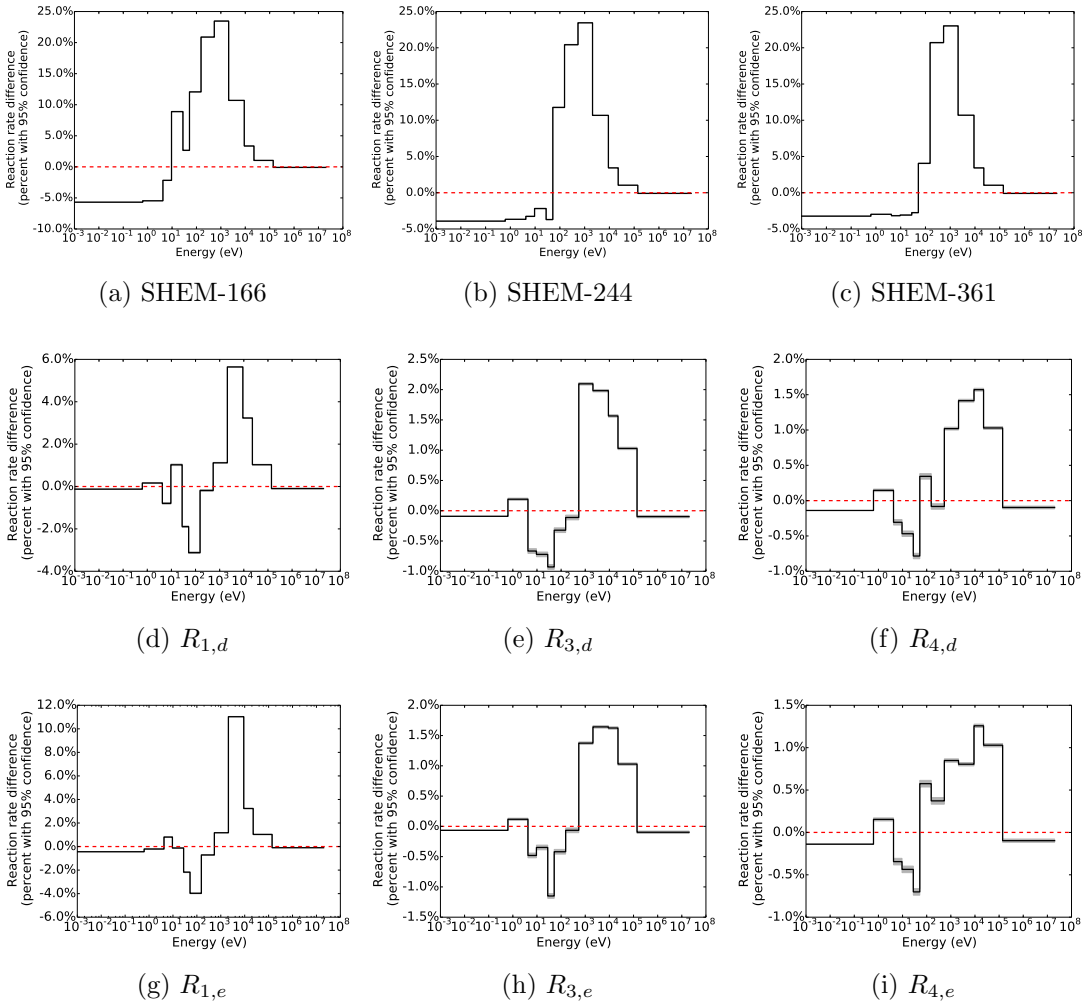

(a) SHEM-166 (b) SHEM-244 (c) SHEM-361

(d) $R_{1,d}$ (e) $R_{3,d}$ (f) $R_{4,d}$

(g) $R_{1,e}$ (h) $R_{3,e}$ (i) $R_{4,e}$

Figure F.6: Relative total absorption errors between MCNP and PDT for different energy structures for problem D

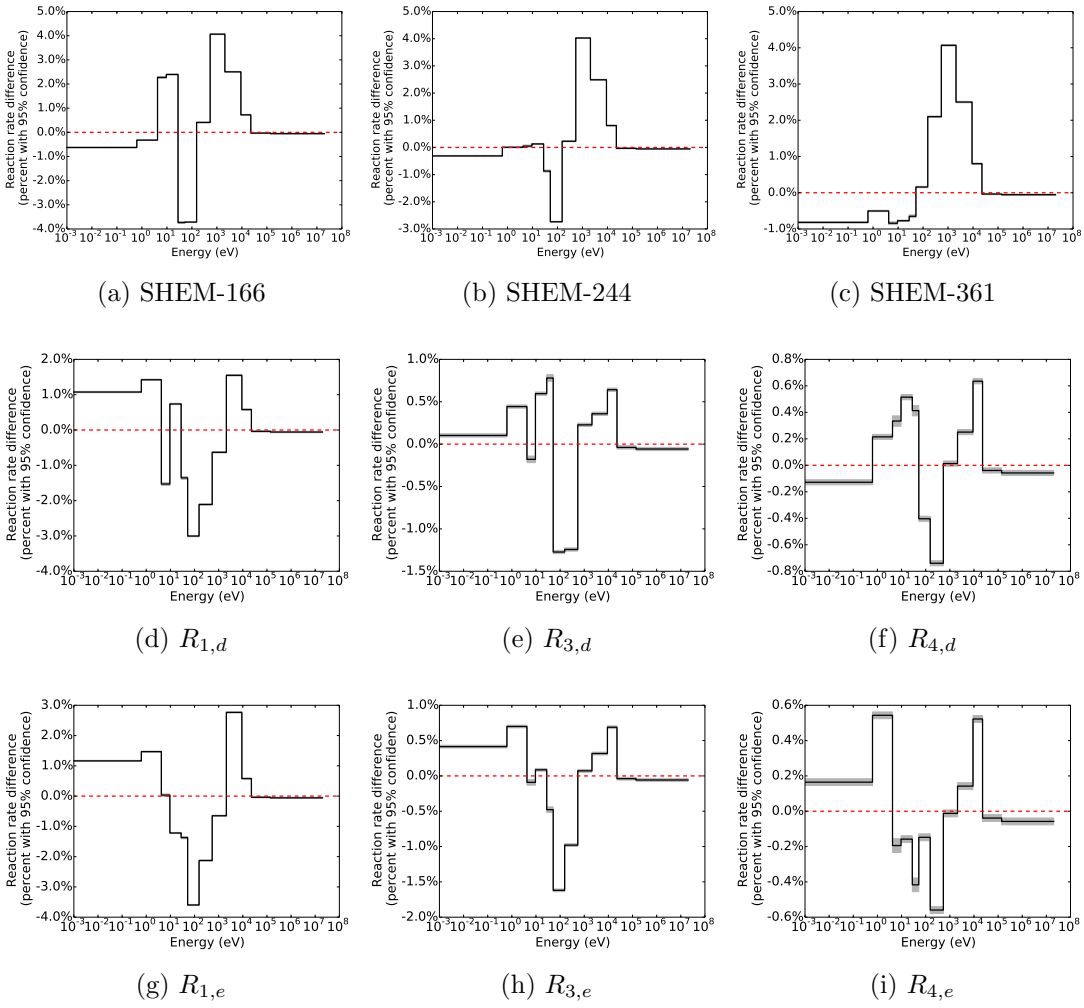

(a) SHEM-166 (b) SHEM-244 (c) SHEM-361

(d) $R_{1,d}$ (e) $R_{3,d}$ (f) $R_{4,d}$

(g) $R_{1,e}$ (h) $R_{3,e}$ (i) $R_{4,e}$

Figure F.7: Relative total absorption errors between MCNP and PDT for different energy structures for problem B

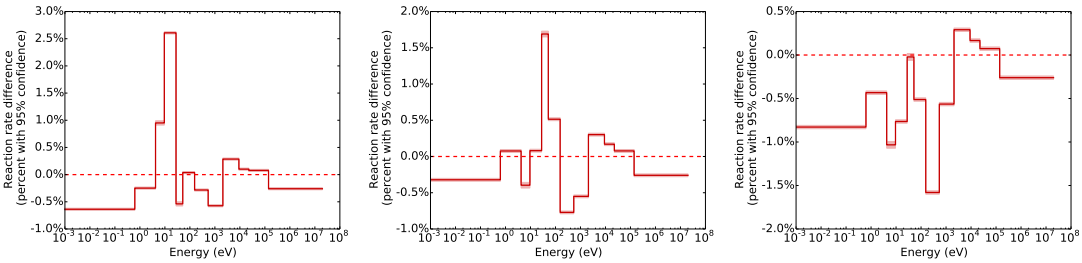

(a) SHEM-166 (b) SHEM-244 (c) SHEM-361

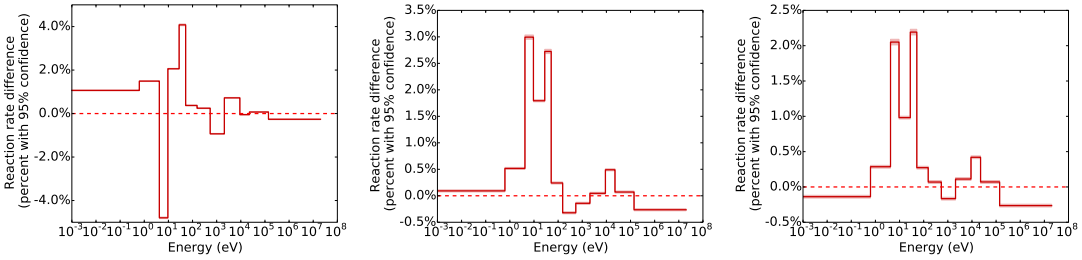

(d) $R_{1,d}$ (e) $R_{3,d}$ (f) $R_{4,d}$

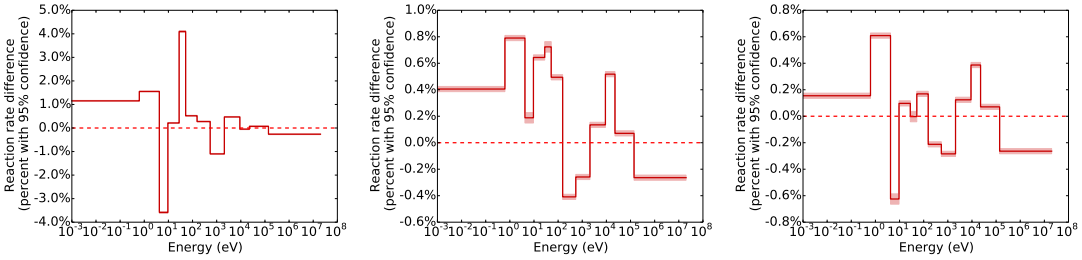

(g) $R_{1,e}$ (h) $R_{3,e}$ (i) $R_{4,e}$

Figure F.8: Relative total fission errors between MCNP and PDT for different energy structures for problem B.

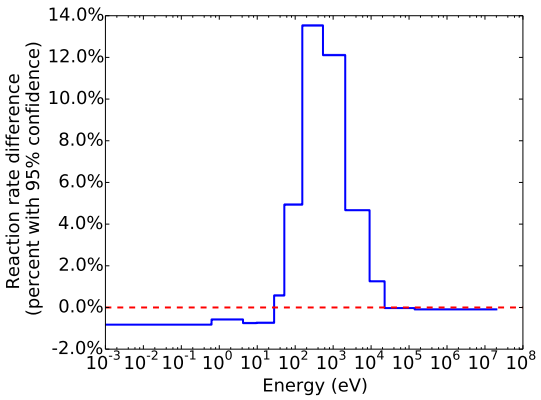

(a) Inner fuel U-238 absorption differences

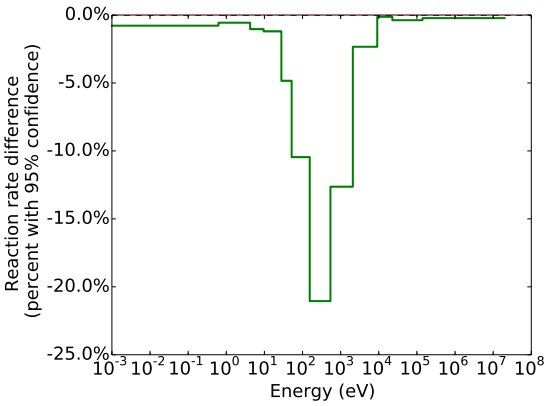

(b) Outer fuel U-238 absorption differences

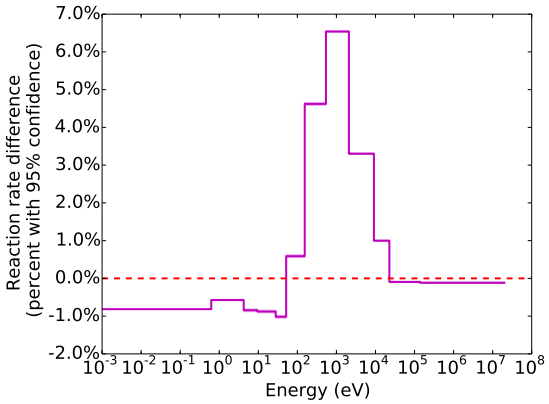

(c) Total fuel U-238 absorption differences

Figure F.9: Relative component errors between MCNP and PDT using the 361-group SHEM structure for problem A.

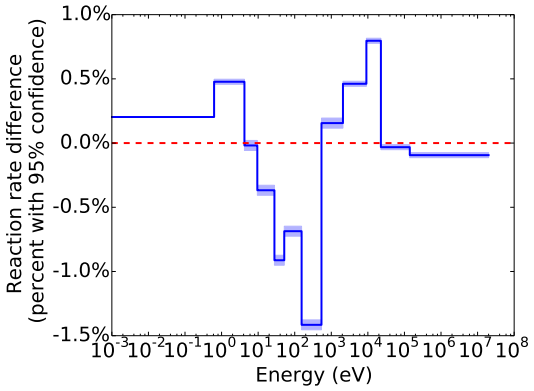

(a) Inner fuel U-238 absorption differences

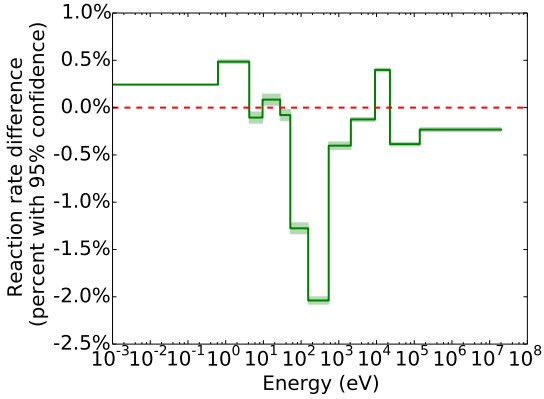

(b) Outer fuel U-238 absorption differences

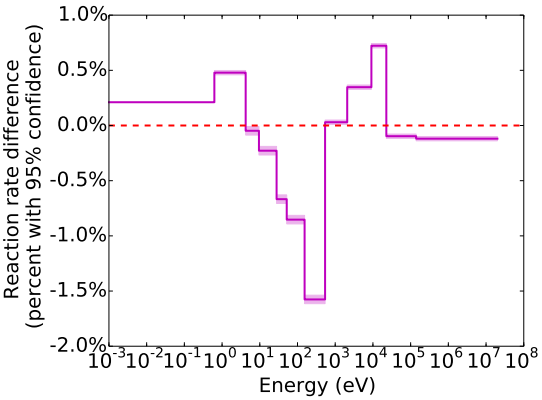

(c) Total fuel U-238 absorption differences

Figure F.10: Relative component errors between MCNP and PDT using the $R_{4,d}$ structure for problem A.

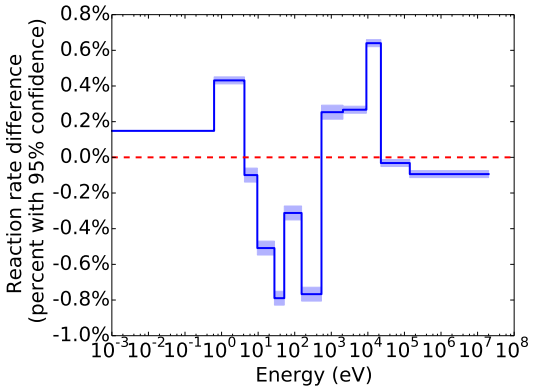

(a) Inner fuel U-238 absorption differences

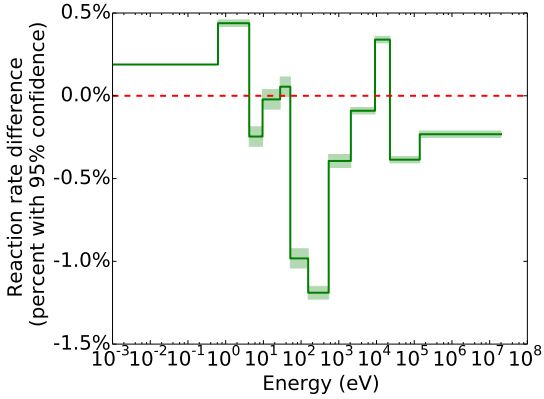

(b) Outer fuel U-238 absorption differences

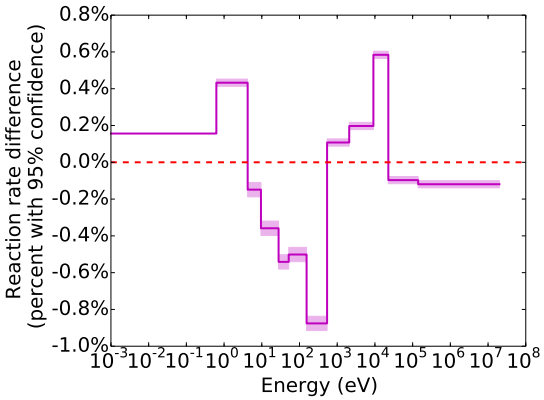

(c) Total fuel U-238 absorption differences

Figure F.11: Relative component errors between MCNP and PDT using the $R_{4,e}$ structure for problem A.

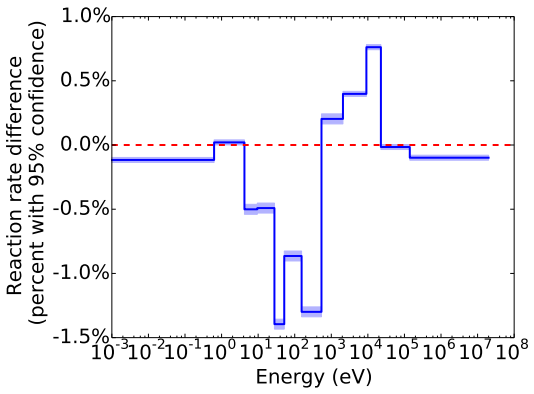

(a) Inner fuel U-238 absorption differences

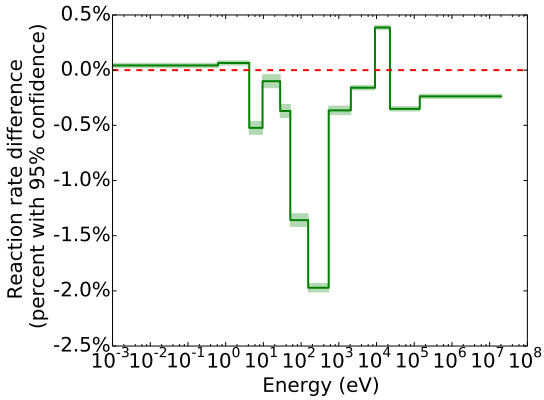

(b) Outer fuel U-238 absorption differences

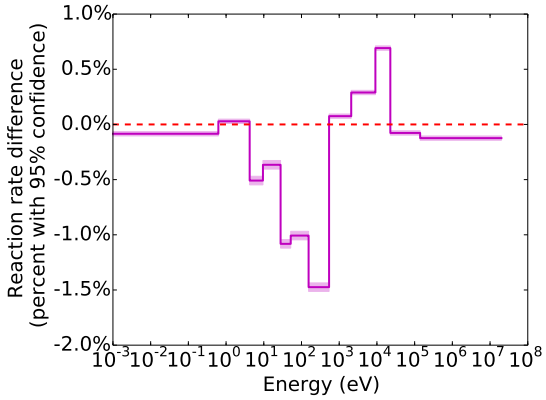

(c) Total fuel U-238 absorption differences

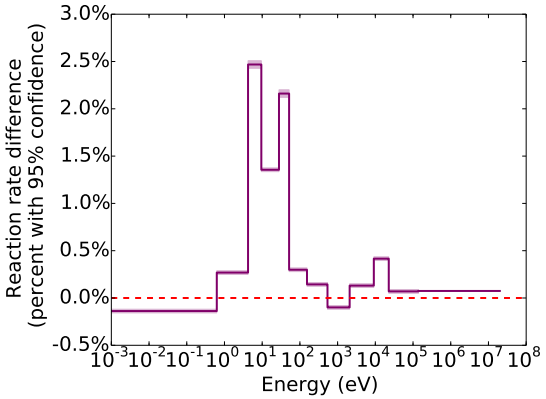

(d) Total fuel U-235 absorption differences

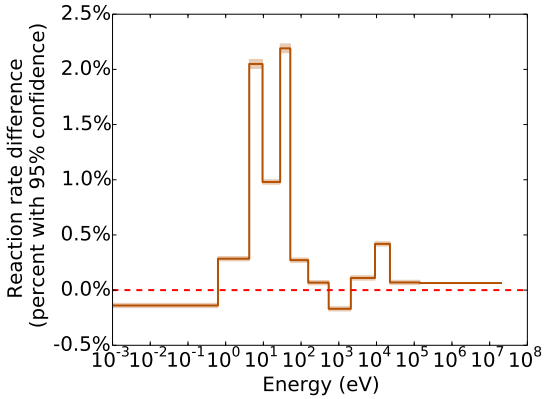

(e) Total fuel U-235 fission differences

Figure F.12: Relative component errors between MCNP and PDT using the $R_{4,d}$ structure for problem B.

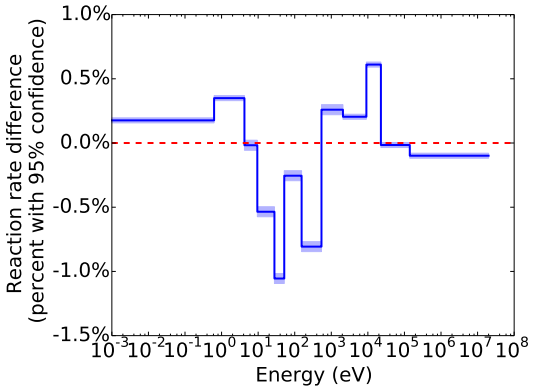

(a) Inner fuel U-238 absorption differences

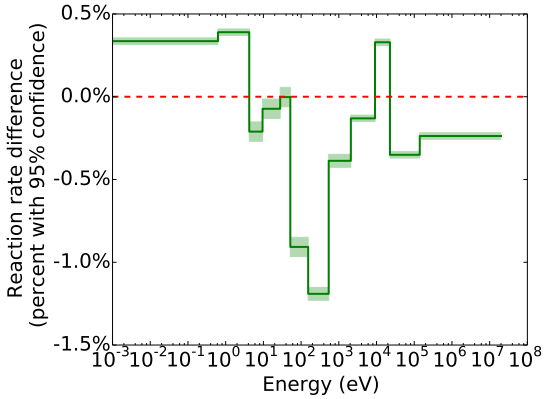

(b) Outer fuel U-238 absorption differences

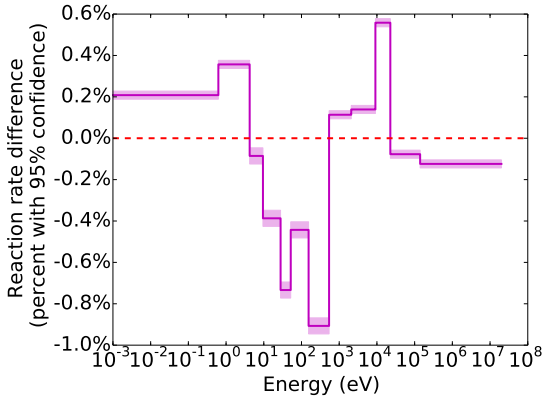

(c) Total fuel U-238 absorption differences

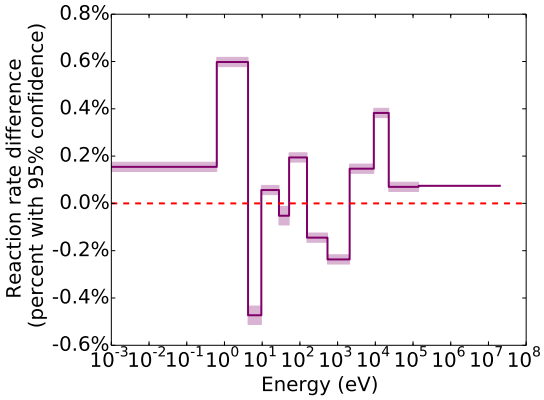

(d) Total fuel U-235 absorption differences

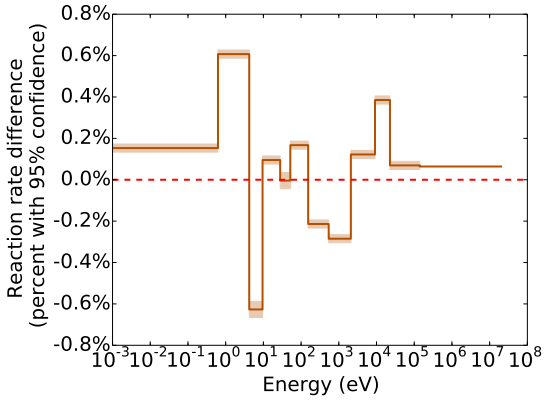

(e) Total fuel U-235 fission differences

Figure F.13: Relative component errors between MCNP and PDT using the $R_{4,e}$ structure for problem B.

Table F.2: Energy boundaries for the SHEM-244 group structure in eV.

2.00000×10^{7}	1.40000×10^{5}	5.39204×10^{2}	1.75314×10^{1}	6.75778×10^{0}	2.27299×10^{0}	6.24999×10^{-1}
1.49182×10^{7}	1.22773×10^{5}	4.37070×10^{2}	1.70491×10^{1}	6.58302×10^{0}	2.21709×10^{0}	5.94993×10^{-1}
1.38403×10^{7}	1.15624×10^{5}	3.54282×10^{2}	1.65800×10^{1}	6.41279×10^{0}	2.15695×10^{0}	5.54990×10^{-1}
1.16183×10^{7}	9.46645×10^{4}	2.87176×10^{2}	1.61238×10^{1}	6.24695×10^{0}	2.07010×10^{0}	5.20011×10^{-1}
9.99999×10^{6}	8.22974×10^{4}	2.32780×10^{2}	1.56802×10^{1}	6.08541×10^{0}	1.98992×10^{0}	4.75017×10^{-1}
9.04836×10^{6}	6.73794×10^{4}	1.88688×10^{2}	1.52487×10^{1}	5.92804×10^{0}	1.90008×10^{0}	4.31579×10^{-1}
8.18730×10^{6}	5.51656×10^{4}	1.54176×10^{2}	1.48292×10^{1}	5.77474×10^{0}	1.77997×10^{0}	3.90001×10^{-1}
7.40817×10^{6}	4.99159×10^{4}	1.28779×10^{2}	1.44212×10^{1}	5.62541×10^{0}	1.66895×10^{0}	3.52994×10^{-1}
6.70319×10^{6}	4.08677×10^{4}	1.07565×10^{2}	1.40244×10^{1}	5.47994×10^{0}	1.58803×10^{0}	3.25008×10^{-1}
6.06530×10^{6}	3.69786×10^{4}	8.98458×10^{1}	1.36385×10^{1}	5.33823×10^{0}	1.51998×10^{0}	3.05012×10^{-1}
4.96585×10^{6}	3.34596×10^{4}	7.50455×10^{1}	1.32632×10^{1}	5.20018×10^{0}	1.44397×10^{0}	2.79989×10^{-1}
4.06569×10^{6}	2.92810×10^{4}	6.14420×10^{1}	1.28983×10^{1}	5.06571×10^{0}	1.41001×10^{0}	2.54997×10^{-1}
3.32871×10^{6}	2.73944×10^{4}	5.17847×10^{1}	1.25434×10^{1}	4.93471×10^{0}	1.38098×10^{0}	2.31192×10^{-1}
2.72531×10^{6}	2.61001×10^{4}	4.50195×10^{1}	1.21983×10^{1}	4.80710×10^{0}	1.33095×10^{0}	2.09610×10^{-1}
2.23130×10^{6}	2.49991×10^{4}	3.97295×10^{1}	1.18627×10^{1}	4.68279×10^{0}	1.29304×10^{0}	1.90005×10^{-1}
1.90139×10^{6}	2.26994×10^{4}	3.85276×10^{1}	1.15363×10^{1}	4.56169×10^{0}	1.25094×10^{0}	1.61895×10^{-1}
1.63654×10^{6}	1.85847×10^{4}	3.73257×10^{1}	1.12189×10^{1}	4.44373×10^{0}	1.21397×10^{0}	1.37999×10^{-1}
1.40577×10^{6}	1.62005×10^{4}	3.61239×10^{1}	1.09102×10^{1}	4.32882×10^{0}	1.16999×10^{0}	1.19995×10^{-1}
1.33694×10^{6}	1.36037×10^{4}	3.49220×10^{1}	1.06100×10^{1}	4.21983×10^{0}	1.14797×10^{0}	1.04298×10^{-1}
1.28696×10^{6}	1.11377×10^{4}	3.37201×10^{1}	1.03181×10^{1}	4.00000×10^{0}	1.12997×10^{0}	8.97968×10^{-2}
1.16205×10^{6}	9.11881×10^{3}	2.78852×10^{1}	1.00342×10^{1}	3.88217×10^{0}	1.11605×10^{0}	7.64969×10^{-2}
1.05115×10^{6}	7.46585×10^{3}	2.46578×10^{1}	9.75809×10^{0}	3.71209×10^{0}	1.10395×10^{0}	6.51999×10^{-2}
9.51119×10^{5}	6.11252×10^{3}	2.42334×10^{1}	9.50002×10^{0}	3.54307×10^{0}	1.09198×10^{0}	5.54982×10^{-2}
8.60006×10^{5}	5.00451×10^{3}	2.38089×10^{1}	9.25435×10^{0}	3.14211×10^{0}	1.07799×10^{0}	4.73019×10^{-2}
7.06511×10^{5}	4.09735×10^{3}	2.33845×10^{1}	9.01504×10^{0}	2.88405×10^{0}	1.03499×10^{0}	4.02999×10^{-2}
5.78443×10^{5}	3.35462×10^{3}	2.29600×10^{1}	8.78191×10^{0}	2.77512×10^{0}	1.02101×10^{0}	3.43998×10^{-2}
4.94002×10^{5}	2.74653×10^{3}	2.25356×10^{1}	8.55481×10^{0}	2.74092×10^{0}	1.00904×10^{0}	2.92989×10^{-2}
4.56021×10^{5}	2.39729×10^{3}	2.19155×10^{1}	8.33359×10^{0}	2.71990×10^{0}	9.96501×10^{-1}	2.49394×10^{-2}
4.12501×10^{5}	2.08410×10^{3}	2.13126×10^{1}	8.11808×10^{0}	2.70012×10^{0}	9.81959×10^{-1}	2.00104×10^{-2}
3.83884×10^{5}	1.71487×10^{3}	2.07262×10^{1}	7.90815×10^{0}	2.64004×10^{0}	9.63960×10^{-1}	1.48300×10^{-2}
3.20646×10^{5}	1.41105×10^{3}	2.01559×10^{1}	7.70365×10^{0}	2.62005×10^{0}	9.44022×10^{-1}	1.04505×10^{-2}
2.67826×10^{5}	1.16106×10^{3}	1.96013×10^{1}	7.50443×10^{0}	2.59009×10^{0}	9.19978×10^{-1}	7.14526×10^{-3}
2.30014×10^{5}	9.55364×10^{2}	1.90620×10^{1}	7.31037×10^{0}	2.55000×10^{0}	8.80024×10^{-1}	4.55602×10^{-3}
1.95008×10^{5}	7.86107×10^{2}	1.85375×10^{1}	7.12133×10^{0}	2.46994×10^{0}	8.00371×10^{-1}	2.49990×10^{-3}
1.64999×10^{5}	6.46836×10^{2}	1.80275×10^{1}	6.93717×10^{0}	2.33006×10^{0}	7.19999×10^{-1}	1.00000×10^{-5}

Table F.3: Energy boundaries for the SHEM-361 group structure in eV.

2.00000×10^{7}	1.62005×10^{4}	1.88877×10^{2}	4.41721×10^{1}	1.40496×10^{1}	5.96014×10^{0}	1.11605×10^{0}
1.49182×10^{7}	1.48997×10^{4}	1.87559×10^{2}	4.31246×10^{1}	1.35460×10^{1}	5.80021×10^{0}	1.10395×10^{0}
1.38403×10^{7}	1.36037×10^{4}	1.86251×10^{2}	4.21441×10^{1}	1.33297×10^{1}	5.72015×10^{0}	1.09198×10^{0}
1.16183×10^{7}	1.11377×10^{4}	1.84952×10^{2}	4.12270×10^{1}	1.26000×10^{1}	5.61979×10^{0}	1.07799×10^{0}
9.99999×10^{6}	9.11881×10^{3}	1.83295×10^{2}	3.97295×10^{1}	1.24721×10^{1}	5.53004×10^{0}	1.03499×10^{0}
9.04836×10^{6}	7.46585×10^{3}	1.75229×10^{2}	3.87874×10^{1}	1.23086×10^{1}	5.48817×10^{0}	1.02101×10^{0}
8.18730×10^{6}	6.11252×10^{3}	1.67519×10^{2}	3.77919×10^{1}	1.21302×10^{1}	5.41025×10^{0}	1.00904×10^{0}
7.40817×10^{6}	5.00451×10^{3}	1.63056×10^{2}	3.73038×10^{1}	1.19795×10^{1}	5.38003×10^{0}	9.96501×10^{-1}
6.70319×10^{6}	4.09735×10^{3}	1.54176×10^{2}	3.68588×10^{1}	1.18153×10^{1}	5.32011×10^{0}	9.81959×10^{-1}
6.06530×10^{6}	3.48107×10^{3}	1.46657×10^{2}	3.64191×10^{1}	1.17094×10^{1}	5.21008×10^{0}	9.63960×10^{-1}
4.96585×10^{6}	2.99618×10^{3}	1.39504×10^{2}	3.60568×10^{1}	1.15894×10^{1}	5.10997×10^{0}	9.44022×10^{-1}
4.06569×10^{6}	2.70024×10^{3}	1.32701×10^{2}	3.56980×10^{1}	1.12694×10^{1}	4.93323×10^{0}	9.19978×10^{-1}
3.32871×10^{6}	2.39729×10^{3}	1.26229×10^{2}	3.45392×10^{1}	1.10529×10^{1}	4.76785×10^{0}	8.80024×10^{-1}
2.72531×10^{6}	2.08410×10^{3}	1.20554×10^{2}	3.30855×10^{1}	1.08038×10^{1}	4.41980×10^{0}	8.00371×10^{-1}
2.23130×10^{6}	1.81183×10^{3}	1.17577×10^{2}	3.16930×10^{1}	1.05793×10^{1}	4.30981×10^{0}	7.19999×10^{-1}
1.90139×10^{6}	1.58620×10^{3}	1.16524×10^{2}	2.78852×10^{1}	9.50002×10^{0}	4.21983×10^{0}	6.24999×10^{-1}
1.63654×10^{6}	1.34358×10^{3}	1.15480×10^{2}	2.46578×10^{1}	9.14031×10^{0}	4.00000×10^{0}	5.94993×10^{-1}
1.40577×10^{6}	1.13467×10^{3}	1.12854×10^{2}	2.25356×10^{1}	8.97995×10^{0}	3.88217×10^{0}	5.54990×10^{-1}
1.33694×10^{6}	1.06432×10^{3}	1.10288×10^{2}	2.23788×10^{1}	8.80038×10^{0}	3.71209×10^{0}	5.20011×10^{-1}
1.28696×10^{6}	9.82494×10^{2}	1.05646×10^{2}	2.21557×10^{1}	8.67369×10^{0}	3.54307×10^{0}	4.75017×10^{-1}
1.16205×10^{6}	9.09681×10^{2}	1.03038×10^{2}	2.20011×10^{1}	8.52407×10^{0}	3.14211×10^{0}	4.31579×10^{-1}
1.05115×10^{6}	8.32218×10^{2}	1.02115×10^{2}	2.17018×10^{1}	8.30032×10^{0}	2.88405×10^{0}	3.90001×10^{-1}
9.51119×10^{5}	7.48517×10^{2}	1.01605×10^{2}	2.14859×10^{1}	8.13027×10^{0}	2.77512×10^{0}	3.52994×10^{-1}
8.60006×10^{5}	6.77287×10^{2}	1.01098×10^{2}	2.13360×10^{1}	7.97008×10^{0}	2.74092×10^{0}	3.25008×10^{-1}
7.06511×10^{5}	6.46837×10^{2}	1.00594×10^{2}	2.12296×10^{1}	7.83965×10^{0}	2.71990×10^{0}	3.05012×10^{-1}
5.78443×10^{5}	6.12834×10^{2}	9.73287×10^{1}	2.11448×10^{1}	7.73994×10^{0}	2.70012×10^{0}	2.79989×10^{-1}
4.94002×10^{5}	6.00099×10^{2}	9.33256×10^{1}	2.10604×10^{1}	7.60035×10^{0}	2.64004×10^{0}	2.54997×10^{-1}
4.56021×10^{5}	5.92941×10^{2}	8.87741×10^{1}	2.09763×10^{1}	7.38015×10^{0}	2.62005×10^{0}	2.31192×10^{-1}
4.12501×10^{5}	5.77146×10^{2}	8.39393×10^{1}	2.07676×10^{1}	7.13987×10^{0}	2.59009×10^{0}	2.09610×10^{-1}
3.83884×10^{5}	5.39204×10^{2}	7.93679×10^{1}	2.06847×10^{1}	6.99429×10^{0}	2.55000×10^{0}	1.90005×10^{-1}
3.20646×10^{5}	5.01746×10^{2}	7.63322×10^{1}	2.06021×10^{1}	6.91778×10^{0}	2.46994×10^{0}	1.61895×10^{-1}
2.67826×10^{5}	4.53999×10^{2}	7.35595×10^{1}	2.05199×10^{1}	6.87021×10^{0}	2.33006×10^{0}	1.37999×10^{-1}
2.30014×10^{5}	4.19094×10^{2}	7.18869×10^{1}	2.04175×10^{1}	6.83526×10^{0}	2.27299×10^{0}	1.19995×10^{-1}
1.95008×10^{5}	3.90760×10^{2}	6.90682×10^{1}	2.02751×10^{1}	6.81070×10^{0}	2.21709×10^{0}	1.04298×10^{-1}
1.64999×10^{5}	3.71703×10^{2}	6.68261×10^{1}	2.00734×10^{1}	6.79165×10^{0}	2.15695×10^{0}	8.97968×10^{-2}
1.40000×10^{5}	3.53575×10^{2}	6.64929×10^{1}	1.95974×10^{1}	6.77605×10^{0}	2.07010×10^{0}	7.64969×10^{-2}
1.22773×10^{5}	3.35323×10^{2}	6.61612×10^{1}	1.93927×10^{1}	6.75981×10^{0}	1.98992×10^{0}	6.51999×10^{-2}
1.15624×10^{5}	3.19928×10^{2}	6.58312×10^{1}	1.91997×10^{1}	6.74225×10^{0}	1.90008×10^{0}	5.54982×10^{-2}
9.46645×10^{4}	2.95922×10^{2}	6.55029×10^{1}	1.90848×10^{1}	6.71668×10^{0}	1.77997×10^{0}	4.73019×10^{-2}
8.22974×10^{4}	2.88327×10^{2}	6.50460×10^{1}	1.79591×10^{1}	6.63126×10^{0}	1.66895×10^{0}	4.02999×10^{-2}
6.73794×10^{4}	2.84888×10^{2}	6.45923×10^{1}	1.77590×10^{1}	6.60611×10^{0}	1.58803×10^{0}	3.43998×10^{-2}
5.51656×10^{4}	2.76468×10^{2}	6.36306×10^{1}	1.75648×10^{1}	6.58829×10^{0}	1.51998×10^{0}	2.92989×10^{-2}
4.99159×10^{4}	2.68297×10^{2}	6.23083×10^{1}	1.74457×10^{1}	6.57184×10^{0}	1.44397×10^{0}	2.49394×10^{-2}
4.08677×10^{4}	2.56748×10^{2}	5.99250×10^{1}	1.68305×10^{1}	6.55609×10^{0}	1.41001×10^{0}	2.00104×10^{-2}
3.69786×10^{4}	2.41796×10^{2}	5.70595×10^{1}	1.65501×10^{1}	6.53907×10^{0}	1.38098×10^{0}	1.48300×10^{-2}
3.34596×10^{4}	2.35590×10^{2}	5.40600×10^{1}	1.60498×10^{1}	6.51492×10^{0}	1.33095×10^{0}	1.04505×10^{-2}
2.92810×10^{4}	2.24325×10^{2}	5.29895×10^{1}	1.57792×10^{1}	6.48178×10^{0}	1.29304×10^{0}	7.14526×10^{-3}
2.73944×10^{4}	2.12108×10^{2}	5.17847×10^{1}	1.48662×10^{1}	6.43206×10^{0}	1.25094×10^{0}	4.55602×10^{-3}
2.61001×10^{4}	2.00958×10^{2}	4.92591×10^{1}	1.47301×10^{1}	6.35978×10^{0}	1.21397×10^{0}	2.49990×10^{-3}
2.49991×10^{4}	1.95996×10^{2}	4.75173×10^{1}	1.45952×10^{1}	6.28016×10^{0}	1.16999×10^{0}	1.00000×10^{-5}
2.26994×10^{4}	1.93078×10^{2}	4.62053×10^{1}	1.44702×10^{1}	6.16011×10^{0}	1.14797×10^{0}	
1.85847×10^{4}	1.90204×10^{2}	4.52904×10^{1}	1.42505×10^{1}	6.05991×10^{0}	1.12997×10^{0}	

APPENDIX G

TIME-OF-FLIGHT ANALYTIC DERIVATIONS

This appendix derives the various analytic expressions used in the time-of-flight calculations, including the time-dependent, speed-quantized, scattering-free (uncollided), time-of-flight problem, and the analytic advection of a FEDS / MG flux in space-time from a point source emitting uniformly over a timestep to a point detector.

G.1 Derivation of the Angular Flux at the Right Edge of the Source

In this subsection we derive an expression for the angular flux that is exact and analytic in space, angle, and time for one energy point or energy group for the pulsed-source, neutron time-of-flight problem. We begin with the time-dependent neutron-transport equation in the $\mathbf{\Omega} = \hat{\mathbf{x}}$ direction, suppressing the energy dependence:

$$\frac{1}{v}\frac{\partial}{\partial t}\,\psi(x,t) + \frac{\partial}{\partial x}\,\psi(x,t) + \Sigma(x)\,\psi(x,t) = Q(x,t), \quad x > 0, \quad t > 0, \tag{G.1a}$$

$$\psi(x,0) = 0, \qquad \text{(Initial Condition)}, \tag{G.1b}$$

$$\psi(0,t) = 0, \qquad \text{(Boundary Condition)}. \tag{G.1c}$$

Let

$$\begin{pmatrix} x \\ t \end{pmatrix} = \begin{pmatrix} x_0 \\ t_0 \end{pmatrix} + s \begin{pmatrix} 1 \\ \frac{1}{v} \end{pmatrix}. \tag{G.2a}$$

This implies

$$\frac{\mathrm{d}}{\mathrm{d}s} = \frac{\partial x}{\partial s}\frac{\partial}{\partial x} + \frac{\partial t}{\partial s}\frac{\partial}{\partial t} \tag{G.2b}$$

$$= \frac{\partial}{\partial x} + \frac{1}{v}\frac{\partial}{\partial t}. \tag{G.2c}$$

Our transport equation becomes:

$$\frac{\mathrm{d}\psi(s)}{\mathrm{d}s} + \Sigma(s)\psi(s) = Q(s). \tag{G.3a}$$

If $s = 0$ is chosen such that $(x_0, t_0) = (x > 0, 0)$ or $(0, t > 0)$, that is, a boundary crossed in space or time, then s picks up an implicit dependence on (x, t) and the boundary and initial conditions merge to become:

$$\psi(s = 0) = 0. \tag{G.3b}$$

If we restrict ourselves to regions in (x, t) for which $\Sigma(x)$ and $Q(x, t)$ are constant, the solution to our transport equation, Eq. (G.3), is

$$\psi(x,t) = \psi_{\mathrm{bdr}}\big(s(x,t)\big)\, e^{-\Sigma s(x,t)} + \frac{Q}{\Sigma}\left(1 - e^{-\Sigma s(x,t)}\right). \tag{G.4a}$$

In this subsection, we derive $\psi(X, t)$ where X is the width of the source region. The source in turned on for $t \in [0, \tau)$. We encounter two setups with five different regions each. A region is a set of locations/times where material properties are constant and we can apply Eq. (G.4).

1. Long source in time ($\frac{X}{v} \leq \tau$)

   (a) Negative times ($t < 0$)

We include this region for completeness and because later transformations may land us here. In this region,

$$\psi\left(X, t < 0\right) = 0. \tag{G.5}$$

(b) Early times ($0 \leq t < \frac{X}{v}$)

In this region, $Q(x,t) = q$, $\Sigma(x) = \sigma$, and ψ_{bdr} occurs at $t = 0$ and has value 0. We use Eq. (G.2a) and find

$$s = vt,$$

which implies

$$\psi\left(X, 0 \leq t < \frac{X}{v}\right) = \frac{q}{\sigma}\left(1 - e^{-\sigma v t}\right). \tag{G.6}$$

(c) Moderate times ($\frac{X}{v} \leq t < \tau$)

In this region, $Q(x,t) = q$, $\Sigma(x) = \sigma$, and ψ_{bdr} occurs at $x = 0$ and has value 0. We use Eq. (G.2a) and find

$$s = x = X,$$

which implies

$$\psi\left(X, \frac{X}{v} \leq t < \tau\right) = \frac{q}{\sigma}\left(1 - e^{-\sigma X}\right). \tag{G.7}$$

(d) Late times ($\tau \leq t < \tau + \frac{X}{v}$)

In this region, $\Sigma(x) = \sigma$. The source has been turned off by the time

particles reach the boundary, but particles born while the source was on continue to advect from inside the source to its boundary. These particles exhibit exponential attenuation within the source region for times $\tau \leq t$. The neutron path may be split into path with the source: $\psi(x = 0, t) = 0$ to $\psi(x, t = \tau)$ with $Q(x, t) = q$; and path without the source: $\psi(x, t = \tau)$ to $\psi(x = X, t)$ with $Q(x, t) = 0$. The amount of path with the source is

$$s_{\text{src}} = X - (t - \tau)v.$$

The rest of the path experiences only attenuation:

$$s_{\text{atten}} = X - s_{\text{src}} = (t - \tau)v.$$

Upon dual application of Eq. (G.3), we find

$$\psi\left(X, \tau \leq t < \tau + \frac{X}{v}\right) = \frac{q}{\sigma}\left(1 - e^{-\sigma[X-(t-\tau)v]}\right) e^{-\sigma(t-\tau)v}. \tag{G.8}$$

(e) Tardy times ($t < 0$)

We include this region for completeness and because later transformations may land us here. In this region, all particles produced by the source have made it to the right boundary of the source region. Hence,

$$\psi\left(X, \tau + \frac{X}{v} \leq t\right) = 0. \tag{G.9}$$

2. Long source in space ($\tau < \frac{X}{v}$)

(a) Negative times ($t < 0$)

We include this region for completeness and because later transformations

may land us here. In this region,

$$\psi\left(X, t < 0\right) = 0. \tag{G.10}$$

(b) Early times ($0 \leq t < \tau$)

In this region, $Q(x,t) = q$, $\Sigma(x) = \sigma$, and ψ_{bdr} occurs at $t = 0$ and has value 0. We use Eq. (G.2a) and find

$$s = vt,$$

which implies

$$\psi\left(X, 0 \leq t < \tau\right) = \frac{q}{\sigma}\left(1 - e^{-\sigma v t}\right). \tag{G.11}$$

(c) Moderate times ($\tau \leq t < \frac{X}{v}$)

In this region, $\Sigma(x) = \sigma$. The source has been turned off by the time particles reach the boundary, but particles born while the source was on continue to advect from inside the source to its boundary. These particles exhibit exponential attenuation within the source region for times $\tau \leq t$. The neutron path may be split into path with the source: $\psi(x, t = 0) = 0$ to $\psi(x, t = \tau)$ with $Q(x,t) = q$; and path without the source: $\psi(x, t = \tau)$ to $\psi(x = X, t)$ with $Q(x,t) = 0$. The amount of path with the source is

$$s_{\text{src}} = \tau v.$$

The rest of the path experiences only attenuation:

$$s_{\text{atten}} = t - s_{\text{src}} = (t - \tau)v.$$

Upon dual application of Eq. (G.3), we find

$$\psi\left(X, \tau \leq t < \frac{X}{v}\right) = \frac{q}{\sigma}\left(1 - e^{-\sigma\tau v}\right) e^{-\sigma(t-\tau)v}. \tag{G.12}$$

(d) Late times ($\frac{X}{v} \leq t < \tau + \frac{X}{v}$)

In this region, $\Sigma(x) = \sigma$. The source has been turned off by the time particles reach the boundary, but particles born while the source was on continue to advect from inside the source to its boundary. These particles exhibit exponential attenuation within the source region for times $\tau \leq t$. The neutron path may be split into path with the source: $\psi(x = 0, t) = 0$ to $\psi(x, t = \tau)$ with $Q(x, t) = q$; and path without the source: $\psi(x, t = \tau)$ to $\psi(x = X, t)$ with $Q(x, t) = 0$. The amount of path with the source is

$$s_{\text{src}} = X - (t - \tau)v.$$

The rest of the path experiences only attenuation:

$$s_{\text{atten}} = X - s_{\text{src}} = (t - \tau)v.$$

Upon dual application of Eq. (G.3), we find

$$\psi\left(X, \frac{X}{v} \leq t < \tau + \frac{X}{v}\right) = \frac{q}{\sigma}\left(1 - e^{-\sigma[X-(t-\tau)v]}\right) e^{-\sigma(t-\tau)v}. \tag{G.13}$$

(e) Tardy times ($t < 0$)

We include this region for completeness and because later transformations may land us here. In this region, all particles produced by the source have made it to the right boundary of the source region. Hence,

$$\psi\left(X, \tau + \frac{X}{v} \leq t\right) = 0. \tag{G.14}$$

G.2 Derivation of the Time-Integrated Angular Flux at the Detector Location

We desire integrals in time of the angular flux at the location of the detector. The previous subsection yielded the angular flux at the right boundary of the source. Between this boundary and the detector, the neutrons stream through iron and then vacuum. In the iron,

$$\frac{\mathrm{d}\psi(s)}{\mathrm{d}s} + \sigma_m(s)\psi(s) = 0, \tag{G.15a}$$

where σ_m is the (macroscopic) cross section of natural iron, and the iron has total mean-free path thickness of $\alpha_m = M\sigma_m$, whose dependence on energy we are suppressing in our derivation. The boundary conditions to the iron are $\psi_{\mathrm{bdr}} = \psi(x = X, t)$, which we use even if this leads to negative times. In the vacuum,

$$\frac{\mathrm{d}\psi(s)}{\mathrm{d}s} = 0, \tag{G.15b}$$

and boundary conditions are $\psi_{\mathrm{bdr}} = \psi(x = X + M, t)$, which we use even if this leads to negative times.

We can relate the time-integrated angular flux at the detector ($x = X_d$) to the

time-differential angular flux at the right boundary of the source using Eq. (G.15):

$$\psi(X_d, t) = e^{-\alpha_m}\ \psi\left(X,\ t - \frac{X_d - X}{v}\right), \tag{G.16a}$$

$$\int_{t_0'}^{t_1'} \mathrm{d}t\ \psi(X_d, t) = e^{-\alpha_m} \int_{t_0' - \frac{X_d - X}{v}}^{t_1' - \frac{X_d - X}{v}} \mathrm{d}t\ \psi\left(X, t\right), \tag{G.16b}$$

for region of integration $t \in [t_0', t_1']$. Complete treatment of the boundaries, including negative times, in the derivation in the previous subsection allow us to investigate all times for $\psi(X, t)$.

For ease of notation, we define

$$t_0 \equiv t_0' - \frac{X_d - X}{v}, \tag{G.16c}$$

$$t_1 \equiv t_1' - \frac{X_d - X}{v}, \tag{G.16d}$$

$$I(t_0, t_1) \equiv \int_{t_0}^{t_1} \mathrm{d}t\ \psi\left(X, t\right), \tag{G.16e}$$

$$\Rightarrow \int_{t_0'}^{t_1'} \mathrm{d}t\ \psi(X_d, t) = e^{-\alpha_m}\ I(t_0, t_1). \tag{G.16f}$$

The following assume both t_0 and t_1 are in one time region. If they encompass multiple regions, the time domain of interest may be split on the region boundaries and each region may be looked up independently. The total integral is the sum of the integrals for the individual regions. This approach was taken in my implementation, which used the `searchsorted` and `bincount` functions in Numpy.

We now show analytic expressions for $I(t_0, t_1)$ as a function of (t_0, t_1).

1. Long source in time $\left(\frac{X}{v} \leq \tau\right)$

   (a) Negative times $((t_0, t_1) < 0)$

The time at the detector is too early to see any particles from the source.

$$I(t_0, t_1) = 0. \tag{G.17}$$

(b) Early times $\left(0 \leq (t_0, t_1) < \frac{X}{v}\right)$

$$I(t_0, t_1) = \frac{q}{\sigma}(t_1 - t_0) - \frac{q}{\sigma^2 v}\, e^{-\sigma v t_0} \left(1 - e^{-\sigma v (t_1 - t_0)}\right). \tag{G.18}$$

(c) Moderate times $\left(\frac{X}{v} \leq (t_0, t_1) < \tau\right)$

$$I(t_0, t_1) = \frac{q}{\sigma} \left(1 - e^{-\sigma X}\right) (t_1 - t_0). \tag{G.19}$$

(d) Late times $\left(\tau \leq (t_0, t_1) < \tau + \frac{X}{v}\right)$

$$I(t_0, t_1) = \frac{q}{\sigma^2 v} e^{-\sigma v (t_0 - \tau)} \left(1 - e^{-\sigma v (t_1 - t_0)}\right) - \frac{q}{\sigma} e^{-\sigma X} (t_1 - t_0). \tag{G.20}$$

(e) Tardy times $\left(\tau + \frac{X}{v} \leq (t_0, t_1)\right)$

The time at the detector is too late to see any particles from the source.

$$I(t_0, t_1) = 0. \tag{G.21}$$

2. Long source in space $(\tau < \frac{X}{v})$

(a) Negative times $((t_0, t_1) < 0)$

The time at the detector is too early to see any particles from the source.

$$I(t_0, t_1) = 0. \tag{G.22}$$

(b) Early times $(0 \leq (t_0, t_1) < \tau)$

$$I(t_0, t_1) = \frac{q}{\sigma}(t_1 - t_0) - \frac{q}{\sigma^2 v}\, e^{-\sigma v t_0} \left(1 - e^{-\sigma v (t_1 - t_0)}\right). \tag{G.23}$$

(c) Moderate times $\left(\tau \leq (t_0, t_1) < \frac{X}{v}\right)$

$$I(t_0, t_1) = \frac{q}{\sigma^2 v} e^{-\sigma v (t_0 - \tau)} \left(1 - e^{-\sigma v \tau}\right) \left(1 - e^{-\sigma v (t_1 - t_0)}\right). \tag{G.24}$$

(d) Late times $\left(\frac{X}{v} \leq (t_0, t_1) < \tau + \frac{X}{v}\right)$

$$I(t_0, t_1) = \frac{q}{\sigma^2 v} e^{-\sigma v (t_0 - \tau)} \left(1 - e^{-\sigma v (t_1 - t_0)}\right) - \frac{q}{\sigma} e^{-\sigma X} (t_1 - t_0). \tag{G.25}$$

(e) Tardy times $\left(\tau + \frac{X}{v} \leq (t_0, t_1)\right)$

The time at the detector is too late to see any particles from the source.

$$I(t_0, t_1) = 0. \tag{G.26}$$

In this subsection, we have derived an analytic solution to the pulsed-source, neutron time-of-flight problem for one energy and one angle. These results are easily generalized to rays not traveling in $\mathbf{\Omega} = \hat{\mathbf{x}}$: simply replace all distance quantities such

as X by $X/(\mathbf{\Omega}\cdot\hat{\mathbf{x}})$. A cone of angles may be approximated using a quadrature scheme in angle. These results may be applied independently for each energy point or group and a quadrature scheme used to integrate over the points / groups. Equation (G.16e) may be applied for each time bin independently. A finite detector thickness may be approximated by using a quadrature of spatial locations, X_d. Scattering is more difficult to add to these results, though they could be used as an uncollided flux source for another calculation.

APPENDIX H

APPLICATIONS OF FEDS TO MONTE CARLO

This appendix looks into applying discontiguous energy elements as a lossy data compression mechanism for pointwise cross sections used in Monte Carlo applications. I call the method cross section compression (XSC).

The following is my implementation of XSC in OpenMC [75], available at `https://github.com/attom/openmc.git`. It is comprised of two steps. In the first, the pointwise cross section data is compressed using clustering algorithms. In the second, the compressed data is used during normal cross section lookup during particle tracking.

I Cluster Data

1 Read in pointwise nuclear data

2 Loop over all nuclides with resonances

3 Determine resolved resonance range (RRR) for the nuclide

For ease of implementation, make upper RRR energy boundary lower than the lowest threshold reaction

4 Create observations from the cross sections: $O_{x,g} = \log \sigma_{x,g}$

for $x \in \{t, s, f\}$ and g the energy index

5 Guess the initial cluster centers as existing data points

Use every G^{th} energy point such that N initial cluster centers are specified

6 Perform Lloyd's method to implement the k-means algorithm

7 Store the centroid cross section values, subelement boundaries, and labels of which centroid each subelement corresponds to

II Use Clustered Data

1 When computing Σ_t, loop over all nuclides present in the material

2 Determine the cross section index corresponding to the energy of the particle

3 If the particle energy is inside the RRR of the nuclide, use the cross section index and an offset to look up which element that subelement corresponds to

4 Use the partial and total cross section values of the element instead of the pointwise cross section values

5 If an interaction produces secondary particles, do the normal lookups and computations for the scattering kernel

Comparisons of the XSC method to FEDS follow.

Usage

FEDS	XSC
Minimize varaince over infinite-medium spectra that are snapshots of the solution.	Compress microscopic partial and total cross section data directly.
Use one energy mesh for all nuclides.	Use a different energy mesh for each nuclide, but the same mesh for all partial cross sections for one nuclide.
Use a spectrum that approximates the solution to flux-weight the cross sections within each element.	Use a flat spectrum (no weighting) when averaging the cross sections within each element.
Average over the secondary distribution for scattering.	Keep continuous-energy secondary distribution information.
Discard subelement-to-element labels and subelement energy boundary list during transport solve.	Keep and use subelement-to-element labels and subelement energy boundary list during particle tracking.

Properties

FEDS	XSC
Akin to a physics-based compression of the solution, or at least snapshots of it.	Akin to a physics-based compression of the individual component cross sections themselves.
Solves the correlation issue[1] by using one energy mesh and applying it to all nuclides, and by consistently treating element-to-element scattering.	Solves the correlation issue by keeping track of particle energy explicitly, and only approximating the cross section for each nuclide on its own mesh, while using the same scattering kinematics (secondary treatment) as continuous-energy Monte Carlo.
Able to achieve low errors with relatively few degrees of freedom (DOF) in energy because the solution is often low-dimensional, in the sense that the variance in the solution within a coarse group is well-explained by a small number of resonant nuclides.	Requires substantially more DOF because the dimensionality of the cross section data is greater (high fidelity for all partial cross sections for all resonant nuclides) and because the method does not make assumptions about the solution spectrum when doing cross section averaging.

There are many possible generalizations of XSC that could be done in the future. The first would be to use a different energy mesh for each partial cross section for

[1]MB is plagued by a correlation isue wherein correlation of bands of disparate nuclides / materials /reactions / temperatures is often ignored.

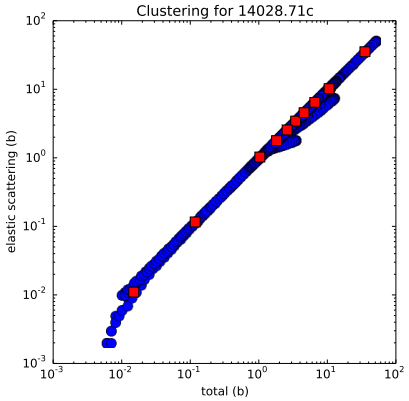

(a) Si-28 with 10 elements (s vs t)

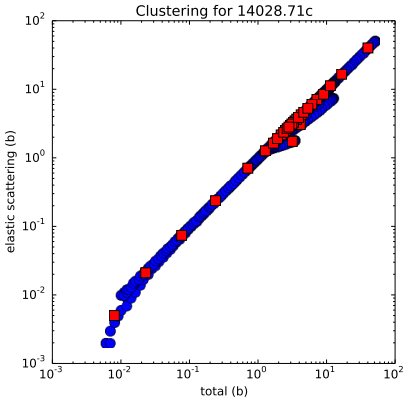

(b) Si-28 with 30 elements (s vs t)

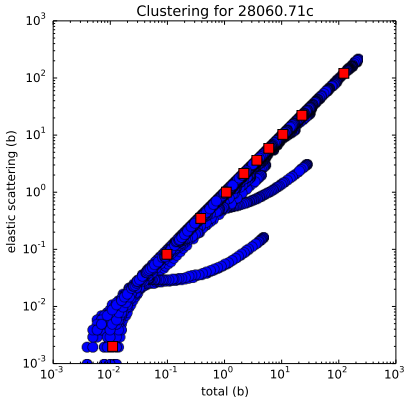

(c) Ni-60 with 10 elements (s vs t)

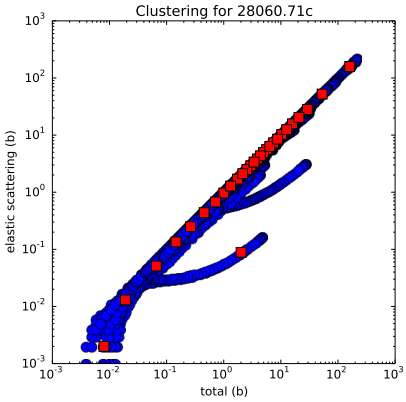

(d) Ni-60 with 30 elements (s vs t)

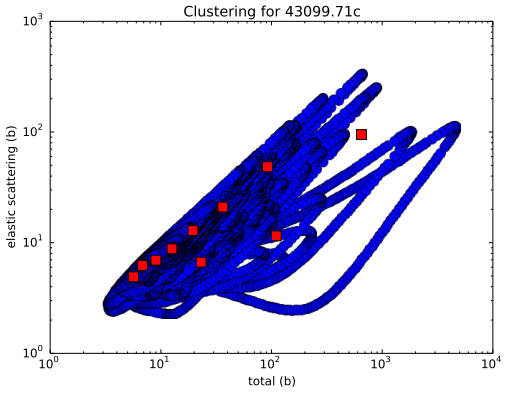

(e) Tc-99 with 10 elements (s vs t)

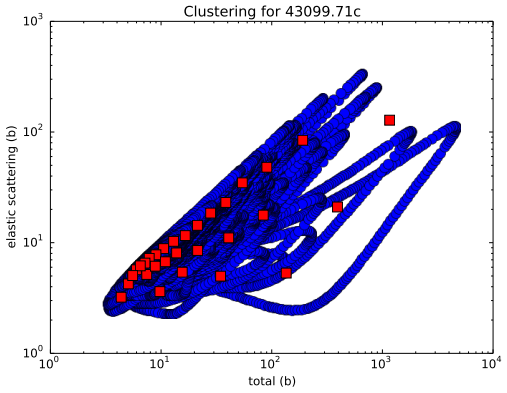

(f) Tc-99 with 30 elements (s vs t)

Figure H.1: Cross section clustering example with various numbers of elements for various low-Z nuclides

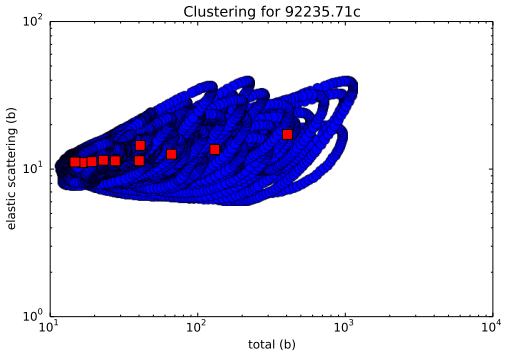

(a) U-235 with 10 elements (s vs t)

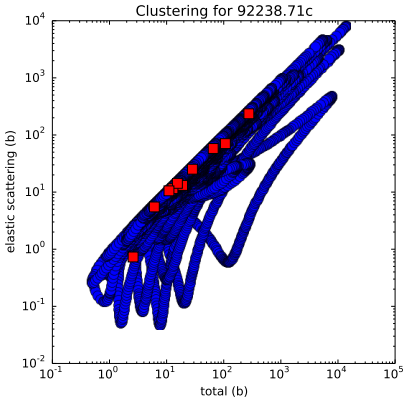

(b) U-238 with 10 elements (s vs t)

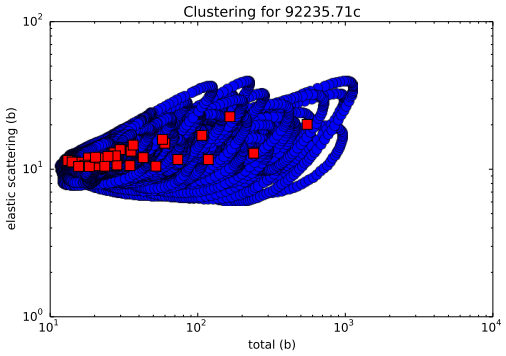

(c) U-235 with 30 elements (s vs t)

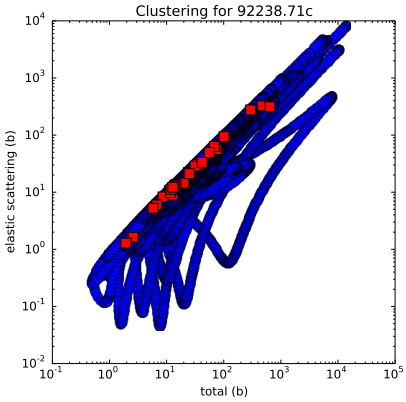

(d) U-238 with 30 elements (s vs t)

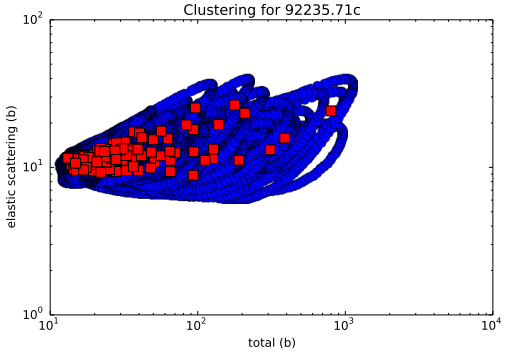

(e) U-235 with 100 elements (s vs t)

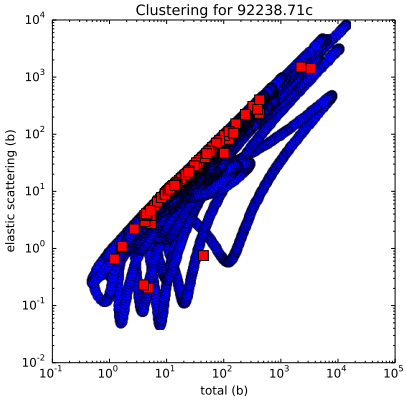

(f) U-238 with 100 elements (s vs t)

Figure H.2: Cross section clustering example with variable number of total elements for various high-Z nuclides

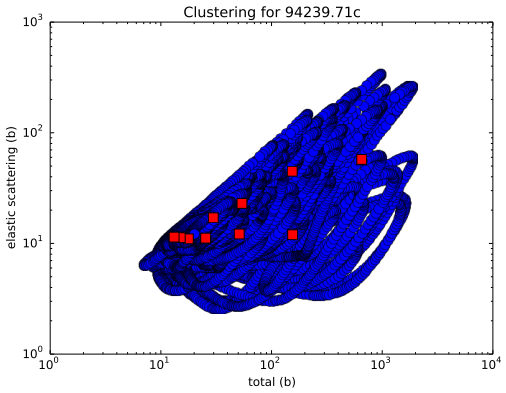

(a) Pu-239 (s vs t)

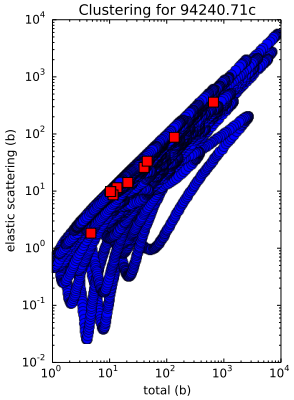

(b) Pu-240 (s vs t)

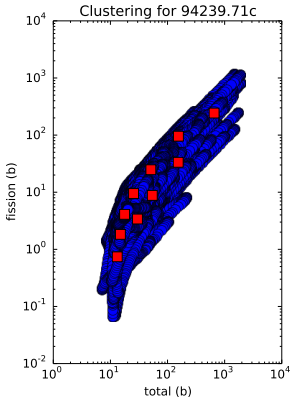

(c) Pu-239 (f vs t)

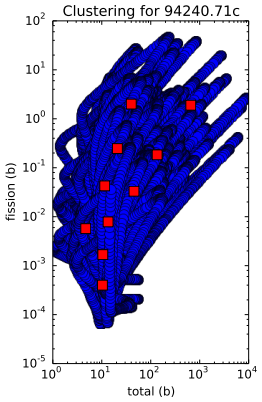

(d) Pu-240 (f vs t)

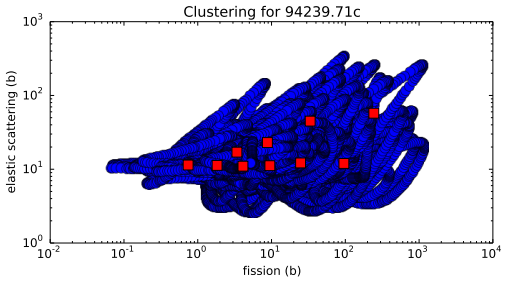

(e) Pu-239 (s vs f)

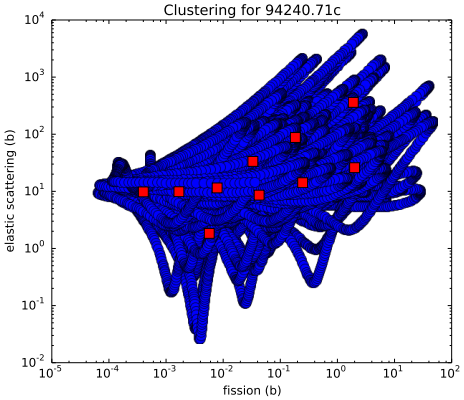

(f) Pu-240 (s vs f)

Figure H.3: Cross section clustering example with 10 total elements for various partial cross sections for high-Z nuclides

each nuclide. This would increase memory by at least a factor of $2-3$, depending on the fraction of fissionable nuclides. Because XSC was designed to minimize memory, this may not be desirable.

Another generalization would be to use coarse groups and clustering within each coarse group separately. If coarse groups with approximately equal lethargy width were used, this would increase the relative resolution of the low-lying resonances, as most of the data points would be in the higher-energy coarse groups but apportioning of clusters to coarse groups would be based on average cross section variance within a coarse group.

The partial cross sections are not correlated as simply with the total cross section as one might think. This is shown in Figs. H.1 – H.3, where each pointwise cross section is a blue dot and each element-averaged cross section is a red square. Most of the data points are restricted to a small range of the cross section space, which is why the red squares are clustered together. There are outlying resonances, often from thicker low-lying resonances, whose structure is not captured by the element centroids for low numbers of final elements. This makes it difficult to accurately compress the data using k-means, which does a good job of minimizing the L^2 error between the distance between the data points and their centroids, but not as good of a job with the L^∞ error. Instead of giving each data point in energy equal weight, we could try weighting by reaction rate, which would require either an approximate solution or an adjoint.

For a pointwise cross section representation, the value of a cross section in the RRR is equal to a linear interpolationbetween points. For XSC, the value of a cross section in the RRR is equal to the average value of the cross section in the corresponding element. This gives the pointwise representation an advantage in that it can use less memory to store the same amount of information. XSC could

be reformulated to store not the integer of the element for each subelement, but something with slope information as well.

Pointwise cross section grids are built for linear-linear interpolation, but the desired input (fine) grid for XSC would be one made for histogram lookups. The original grid could be thickened such that constant lookup error is bounded for each point. This larger grid could be passed into the clustering algorithm.

There are over one hundred resonant nuclides that must be treated simultaneously for depletion problems. This constitutes a large amount of data. One could imagine classifying nuclides based on their importance to the solution, either based on impact to the spectrum or on reaction rates. This classification could be done within each coarse group. More important nuclides (in more important coarse groups) could be given higher-fidelity compression treatments with more elements. Retaining accuracy for the unresolved nuclides may require a problem- or region-specific flux weighting, which might defeat the purposes of using XSC as an *ab initio* method and of trying to save memory space.

Requiring the upper-bound for the RRR to be below the lowest threshold energy for all threshold reactions can be a limiting assumption in practice for the lighter nuclides that have resonances at higher energies. If an energy cannot be treated as existing in the RRR, it must be stored as pointwise in our implementation of XSC. Relaxing this requirement may involve significant code refactoring and make the implementation of XSC more expensive.

We developed XSC for two reasons. The first and foremost reason was as a means of reducing the data storage requirements for Monte Carlo to enable code performance measurements with arbitrary cross section sizes while still using approximately correct physics, i.e., cross sections. The second reason was to study the feasbility of XSC for a more general implementation. We found the first objective

was achieved but there is still more work required before we can conclusively judge the second. Preliminary analysis shows XSC as it is implemented here to be either inaccurate (too few elements, not enough cross section fidelity) or too expensive (too many elements, too much requirement memory). Continuous-energy Monte Carlo is hard to beat.